Karlsruhe Institute of Technology

Development of novel ozone sensors for medical therapy

Zur Erlangung des akademischen Grades einer

Doktorin der Ingenieurwissenschaften (Dr.-Ing.)

von der KIT-Fakultät für Maschinenbau des
Karlsruher Instituts für Technologie (KIT)

angenommene

Dissertation

von

M.Sc. Lisa Petani

aus Freiburg im Breisgau

Hauptreferent:	Prof. Dr. med. Christian Pylatiuk
Koreferentinnen:	Prof. Dr. Jasmin Aghassi-Hagmann
	Prof. Dr.-Ing. Barbara Deml
Tag der mündlichen Prüfung:	15. Dezember 2023

Lisa Petani
Development of novel ozone sensors for medical therapy
Doctoral Thesis,
Reviewers: Prof. Dr. med. Christian Pylatiuk, Prof. Dr. Jasmin Aghassi-Hagmann, and Prof. Dr.-Ing. Barbara Deml
Supervisor: Prof. Dr. med. Christian Pylatiuk

Karlsruhe Institute of Technology (KIT)
Biomedical Engineering & Robotics (BER)
Institute for Automation and Applied Informatics (IAI)
Department of Mechanical Engineering
Hermann-von-Helmholtz-Platz 1
76344 Eggenstein-Leopoldshafen

Abstract

Medical gases, such as ozone (O_3), are used for their effectiveness and minimal side effects, making them an alternative to surgery or medication in therapies like ozone therapy for herniated disks. However, to perform ozone therapy safely and effectively, it is necessary to accurately measure the ozone concentration before and during the therapy. This thesis focuses on the design and evaluation of novel sensors that can measure ozone concentrations, thus overcoming current challenges in ozone therapy. First, reference systems are developed to enable the calibration, characterisation, and evaluation of novel ozone sensors. The developed reference systems serve as the foundation for further development of novel sensors and provide a benchmark to evaluate their performance. Subsequently, the biocompatibility of materials for exemplary inkjet-printed amperometric, impedimetric, and optical absorption ozone sensor structures is assessed. Also, various novel sensor prototypes, based on electrochemical and optical absorption measurement principles, are manufactured. For the sensor prototypes based on the optical absorption measurement principle, miniaturisation is investigated mainly through a reduction of components. For investigating the miniaturisation of the sensor prototypes based on the electrochemical measurement principle, an exemplary inkjet-printed structure of an oxygen (O_2) sensor is manufactured. This is an important step towards small and flexible sensors that can be integrated into medical devices. In addition, for developing electrochemical ozone sensors and investigating alternative ways of manufacturing ozone sensors, commercial electrodes are modified to serve as ozone sensors. Furthermore, experiments are conducted to explore the effect of ozone on bacterial cultures, such as *Escherichia coli*, and to investigate other use cases for ozone in medical therapy. Thus, insights into the potential mechanisms and action of ozone in the medical treatment of, e.g., chronic wounds are provided. Overall, this thesis represents a foundation for the measurement of ozone concentration during medical therapy, which has the potential to broaden the use of ozone in medicine and improve patient outcomes.

Kurzfassung

Medizinische Gase, wie z.B. Ozon (O_3), werden aufgrund ihrer Wirksamkeit und minimalen Nebenwirkungen als Alternative zu Operationen oder Medikamenten bei Therapien wie der Ozontherapie von Bandscheibenvorfällen eingesetzt. Um die Ozontherapie sicher und effektiv durchführen zu können, ist es jedoch notwendig, die Ozonkonzentration genau zu messen. Diese Dissertation befasst sich mit der Entwicklung neuartiger Ozonsensoren, um damit die derzeitigen Herausforderungen in der Ozontherapie zu überwinden. Zunächst werden Referenzsysteme entwickelt, um die Kalibrierung, Charakterisierung und Bewertung neuartiger Ozonsensoren zu ermöglichen. Anschließend wird die Biokompatibilität von Materialien für beispielhafte inkjet-gedruckte amperometrische, impedimetrische und optische Absorptionssensorstrukturen für Ozon untersucht. Außerdem werden verschiedene neuartige Sensorprototypen hergestellt, die auf den elektrochemischen und optischen absorptionsbasierten Messprinzipien basieren. Für die Sensorprototypen, die auf dem optischen Absorptionsmessprinzip basieren, wird die Miniaturisierung hauptsächlich durch eine Reduzierung der Komponenten untersucht. Zur Untersuchung der Miniaturisierung der auf dem elektrochemischen Messprinzip basierenden Sensorprototypen wird eine inkjet-gedruckte Struktur eines Sensors für Sauerstoff (O_2) hergestellt. Darüber hinaus werden zur Entwicklung elektrochemischer Ozonsensoren und zur Untersuchung alternativer Herstellungsmethoden für Ozonsensoren handelsübliche Elektroden so modifiziert, dass sie als Ozonsensoren eingesetzt werden können. Außerdem werden Experimente zur Erforschung der Wirkung von Ozon auf Bakterienkulturen, wie z. B. *Escherichia coli*, durchgeführt, um weitere Anwendungsfälle für Ozon in der medizinischen Therapie zu untersuchen. Auf diese Weise werden Einblicke in die möglichen Mechanismen und Wirkungen von Ozon bei der medizinischen Behandlung von z.B. chronischen Wunden gewonnen. Insgesamt stellt diese Dissertation eine Grundlage für die Messung der Ozonkonzentration während der medizinischen Therapie dar, die das Potenzial hat, den Einsatz von Ozon in der Medizin auszuweiten und die Ergebnisse für die Patienten zu verbessern.

Acknowledgements

I am sincerely grateful to all the individuals whose support and contributions have been instrumental in enabling me to successfully complete this thesis.

Foremost, my deepest appreciation goes to my supervisor, Christian Pylatiuk, for his guidance, encouragement, and steadfast support throughout this challenging journey. I would also like to thank Veit Hagenmeyer, head of the institute, for providing me the opportunity to conduct my research work at the Institute for Automation and Applied Informatics (IAI). I also owe special gratitude to Barbara Deml for being a reviewer of my thesis, to Jasmin Aghassi-Hagmann for stepping in as an additional reviewer at the eleventh hour, and to Christian Greiner, who served as the thesis committee chair.

In addition, I would like to thank Liane Koker and Ulrich Gengenbach for their co-supervision and constructive criticism, which have improved the quality of my research work, as well as Ralf Mikut, head of the research area Automated Image and Data Analysis (AIDA), and Markus Reischl, the group leader during the initial two years of my doctoral work in the group Machine Learning for High-Throughput Methods and Mechatronics (ML4HOME). My dissertation also would not have been possible without the invaluable organisational support provided by Andreas Hofmann, the scientific administrative manager of the institute, and Bernadette Lehmann. Without the financial support, undertaking this doctoral journey would not have been possible and I would therefore like to thank the Federal Ministry for Economic Affairs and Climate Action (BMWK) for their support under grant ZF4717901SK9.

One of the highlights of my doctoral studies was my research stay at Keio University. I would like to thank Yasuaki Einaga for hosting me and providing invaluable guidance and insightful suggestions during my stay as well as the Karlsruhe House of Young Scientists (KHYS) for their financial support. A huge shout-out goes to all the members of the Einaga group, particularly Andrea Fiorani, Atsushi Otake, Genki Ogata, Irkham, Kana Asai, Kazumi Akai, Michiko Maeda, Michio Murata, Miwa Yoshii, Risa Ogawa, Tatsumi Yusuke, and Zhen Peng, for their collective spirit that made my stay truly memorable.

Finally, I am truly thankful for all my colleagues at the IAI and the Karlsruhe Institute of Technology (KIT) who have contributed to this work in various ways, directly or indirectly. To my colleagues within the Biomedical Engineering & Robotics (BER) group, including Lorenz, Onur, Nathalie, Hossein, and Damyan, thank you for the coffee breaks, the laughs, and the support through challenging times. Also, thank you to all of my collaborators and students who worked with me during my doctoral journey – I wouldn't have made it without your help. To my peers at the IAI and the KIT, especially Alex, Andy, Angelo, André, Benedikt, Claudia, Daniel, David, Dominique, Dorina, Friedrich, Hawo, Ilona, Ines, Ingo, Jan, Johannes, Julian, Kaleb, Katharina, Klaus-Martin, Liyu, Luca, Marcel, Marian, Martha, Martin, Matthias, Maximilian, Moritz, Navid, Nils, Oli, Rafael, Rebecca, Richard, Roman, Sebastian, Simon, Stefan, Stephan, Tim, Tobias, and Zehua, your support and encouragement have cultivated a lively and thriving academic atmosphere.

Beyond the academic realm, my deepest appreciation extends to Kaleb, my friends, and my family, who stood by me during this challenging journey. Your encouragement, understanding, and shared moments of respite have been a source of strength.

Contents

1

Introduction

Ozone therapy has gained increasing attention in the medical field for its potential therapeutic effects in various conditions, such as chronic wounds, infections, inflammations, circulatory disorders, and immune diseases [1]. Several studies have reported its efficacy in treating, e.g., herniated disks, knee osteoarthritis, and avulsed teeth [2]–[5]. The procedure during ozone therapy is shown in Fig. 1.1. Ozone is injected with a needle into the herniated disk. As a result of the treatment of herniated disks with ozone, the leaked part of the nucleus pulposus recedes, and inflammation of the surrounding tissue is reduced [6], [7].

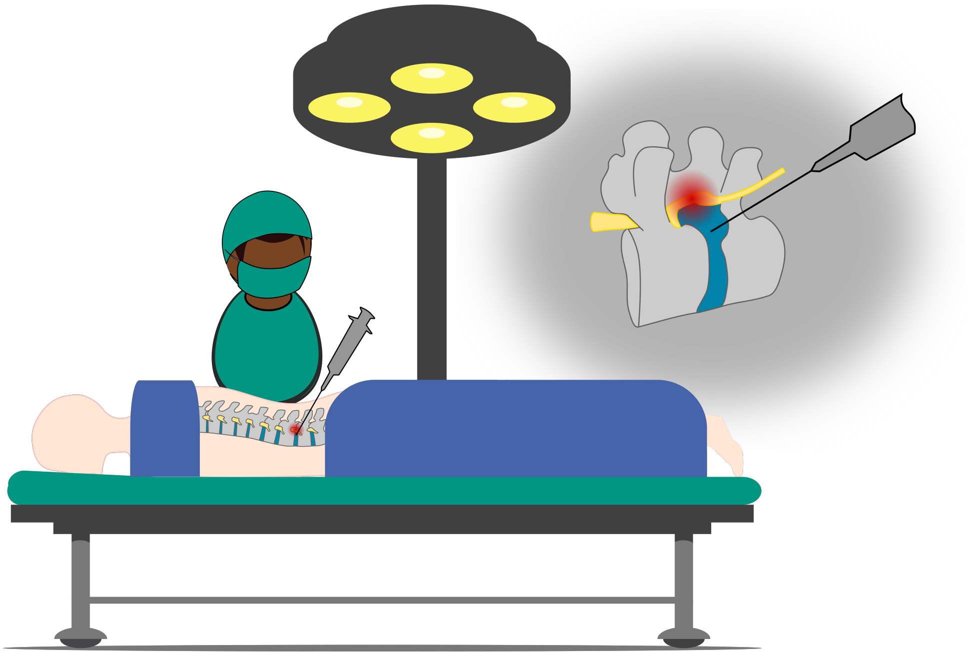

Fig. 1.1: Shows the procedure during ozone therapy for treating a herniated disk and depicts a detailed view of the ozone therapy procedure. Thereby, the challenge for this application is to measure the ozone concentration at the tip of the injection needle during the complete therapy.

Ozone dispersed in oil or water is an additional potential application that shows promise for treating skin infections [8]. The safe and effective application of ozone therapy in clinical practice requires the development of suitable medical sensors that can measure the ozone concentration before, during, and after treatment [9], [10]. This is a significant challenge due to the lack of sensors that can accurately measure ozone concentrations at the point of injection [10]. Further research is necessary to establish ozone measurement and analysis methods that can enable the widespread use of ozone therapy in clinical settings [4]. The development and evaluation of such sensors require specialised reference systems that can provide accurate and reproducible measurements of ozone concentrations over a wide range of concentration values. One promising technology for developing such sensors is functional inkjet-printing, as it enables fabrication on flexible substrates and enhances miniaturisation. Biocompatibility and reliable measurement are important objectives in the development of these sensors [11], [12]. Also, more research needs to be conducted on the potential of ozone as an antibacterial agent for the treatment of chronic wounds. Chronic wounds are a serious global healthcare challenge that can result in high morbidity and mortality [13]. Thus, it is essential to explore novel, efficient therapies for chronic wounds.

In order to address these challenges, this thesis focuses on designing and assessing novel dissolved and ozone gas sensors for medical therapy, as well as the possibility of ozone as a treatment for chronic wounds. The design of these sensors and their successful application in clinical settings may allow the broad application of ozone for a variety of medical therapies, giving patients a secure and efficient course of treatment.

1.1 Research questions and objectives

In the following, the research questions (RQs), that are the main focus in this thesis, are outlined.

- RQ1: How can novel dissolved and ozone gas sensors be referenced for their calibration, characterisation, and evaluation?
- RQ2: How can novel dissolved and ozone gas sensors be realised as electrochemical or optical sensors?

- RQ3: Can ozone be further used in medicine as an antibacterial agent for the treatment of, e.g., chronic wounds?

The first research question, RQ1, is about the development of novel methods to measure and quantify dissolved ozone and ozone gas concentrations in a reliable and accurate manner. The emphasis is on finding effective reference methods that can be used to calibrate and validate novel sensors. This research question is essential to ensure that the sensors developed are reliable and accurate in measuring ozone concentrations in different environments.

The second research question, RQ2, is focused on the development of novel sensors that can detect dissolved ozone or ozone gas. For RQ2 it is also important to assess the biocompatibility of the used materials. The emphasis is on exploring different types of sensors and their feasibility for detecting ozone in different environments. This research question is essential to develop new and improved low-cost sensors that can detect ozone concentrations with high accuracy, high selectivity, and a compact design.

The third research question, RQ3, is about exploring the potential of ozone as a novel therapeutic agent for the treatment of chronic wounds, which are a major challenge in the healthcare system. There is a need for novel and effective therapeutic agents for their treatment. The focus is on assessing ozone's efficacy as an antibacterial agent and its potential for clinical application.

In summary, the focused RQs investigates challenges that are essential for the design and application of novel ozone sensors for medical therapy, as well as for the potential application of ozone for the treatment of chronic wounds. Thus, this thesis focuses on the challenges that need to be addressed to widely use ozone therapy in medicine. Thereby, one of the key challenges is the absence of accurate and reliable techniques for determining ozone concentration at the point of injection. An essential field of research is the design of innovative sensors for the detection of ozone. This thesis addresses a number of challenges regarding the design, evaluation, and reference of novel dissolved and ozone gas sensors in medicine, as well as regarding the application of ozone for the treatment of chronic wounds. Thus, this thesis provides new insights and solutions to address these challenges, which have important implications for various fields, including medical therapy and environmental monitoring.

1.2 Thesis outline

In the following, this thesis is outlined:

Chapter 2 presents an overview of the medical applications of ozone. This chapter explores different ways in which ozone is used in the medical field to treat a range of conditions, such as disk herniations, artery diseases, and chronic wounds. Furthermore, the antibacterial effects of ozone in medicine are elaborated. In addition, ozone sensing in the context of medical ozone therapy is investigated.

Chapter 3 discusses the importance of ozone measurement and analysis methods in medical ozone therapy. This chapter explores the challenges of measuring ozone concentrations at the injection point and the need for the development of suitable medical sensors to measure ozone concentrations before, during, and after treatment. Furthermore, conventional manufacturing and inkjet-printing of ozone sensors are investigated.

Part I (Referencing novel ozone sensors) includes two chapters, **Chapter 4** and **Chapter 5**, which both focus on RQ1. These chapters provide a reference for the sensor properties and characteristics of ozone gas concentrations and dissolved ozone concentrations in water. They serve as a foundation for the subsequent parts of this thesis.

Part II (Biocompatibility of medical ozone sensors) includes **Chapter 6**, which discusses the importance of biocompatibility in the development of ozone sensors for medical therapy. Thereby, this part focuses on the first part of RQ2. This chapter explores different materials and fabrication methods used in the development of ozone sensors that are biocompatible and can provide accurate and reproducible measurements of ozone over a wide range of concentration values.

Part III (Ozone sensing in medicine) includes three chapters, **Chapter 7**, **Chapter 8**, and **Chapter 9**, which complement Part II and thus RQ2. Part III discusses the development and evaluation of novel ozone gas and dissolved ozone sensors for medical therapy. These chapters explore the different sensing techniques, such as electrochemical and optical methods, and evaluate their performance in measuring ozone concentrations.

Part IV (Antibacterial effects of ozone) includes **Chapter 10**, which investigates RQ3. Thus, this chapter assesses the potential of ozone as an antibacterial agent for the treatment of chronic wounds.

Chapter 11 concludes this thesis by summarising the findings of the work presented in the previous chapters and discussing their implications for the development and application of ozone therapy in medical treatment. This chapter also highlights the potential future directions for research in this area.

2

Ozone for medical therapy

Parts of this chapter are based on: L. Petani, L. Koker, J. Herrmann, V. Hagenmeyer, U. Gengenbach, and C. Pylatiuk, “Recent developments in ozone sensor technology for medical applications”, *Micromachines*, vol. 11, no. 6, 2020. DOI: `10.3390/mi11060624`.

This chapter is supplemented by findings from: [12], [14]–[16]

Since at least the time of World War I, ozone has proven its effectiveness as a therapeutic agent for treating chronic wounds, including ulcers [17]. Since then, several additional applications using ozone have been explored and thoroughly investigated. Fig. 2.1 provides an overview of ozone applications currently applied in medical therapy. Over the past century, life expectancy and daily sitting time have increased in industrialised nations [18]. This includes the possibility of developing physical health issues, such as back pain, diabetes mellitus, cancer, heart disease, and stroke [19], [20]. The cost of chronic pain treatment in the United States alone ranges from 560 to 635 billion dollars [21]. Therefore, more research is needed to effectively prevent and treat chronic pain. Treating chronic pain, including low back pain, coronary artery disease, osteoarthritis, and peripheral artery disease, is currently a significant societal and economic burden [22]–[24]. Muscle strain, arthritis, or disk herniation are possible causes of back pain, which is a significant health concern [25]. Conventional treatment for pain resulting from a herniated disk or joint osteoarthritis typically involves repeated injections of anti-inflammatory drugs, including corticosteroids, immunosuppressive drugs, and analgesics [26]–[28]. However, these drugs have limited and temporary effectiveness and may cause potential side effects. In some cases, they may even fail to alleviate the pain.

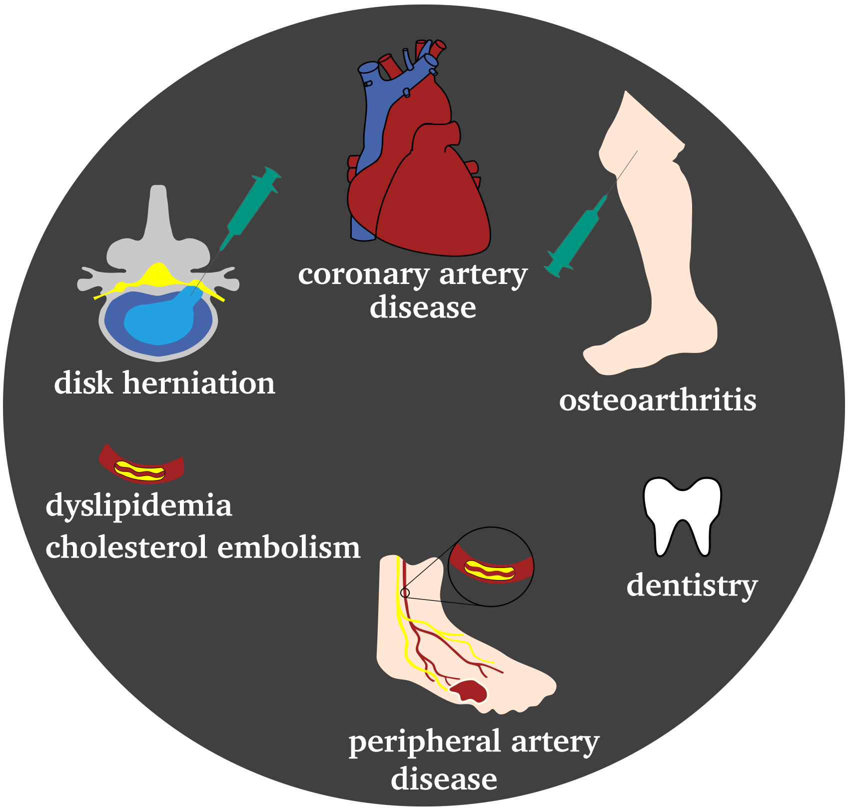

Fig. 2.1: Illustrates the potential uses of ozone treatment in medical therapy, including treating conditions such as disk herniation, osteoarthritis, coronary and peripheral artery disease, dyslipidemia, cholesterol embolism, and in dentistry. [10]

Due to the limitations of conventional pain treatments, new methods have emerged for pain therapy and related conditions that are already used in clinical practice. For instance, subcutaneous carbon dioxide is used to alleviate muscle pain, while nitrous oxide is used as an anaesthetic for obstetrics and prostate exams [29], [30]. Other gases that have potential therapeutic benefits include ozone [2], [4], [5], [7], [26], [31], [32] and xenon [33]. However, further clinical studies are required to determine the effectiveness of xenon as a therapy [33]. Ozone has already been shown to be effective in multiple clinical trials for pain related to conditions such as herniated disks and osteoarthritis [2], [7], [26]. Ozone has also been studied for potential use in dentistry and other applications [4], [5], [31], [32]. Apart from medical therapy, ozone is also used for a variety of purposes, including treating wastewater, odour removal, and processing food [10], [34], [35]. Generally, for different applications, ozone mixtures with various concentrations are used. For example, to treat wastewater, mixtures containing oxygen and ozone with an ozone concentration of around 0.01 vol% are utilised [36]. For odour removal, higher concentrations of 0.14 vol% of ozone are used [37]. In food processing, ozone concentrations of about 1.61 vol% are applied [34]. The highest ozone concentrations of up to 1.89 vol% are required for the treatment of disk herniations [14], [38], [39]. In the following, medical applications of ozone, especially the treatment of disk herniations, are focused.

2.1 Application examples for medical ozone therapy

Depending on the medical application, the administration of ozone takes place in different ways: For superficial treatment, the skin can be directly exposed to an ozone-containing atmosphere [40]. Inside the body, for example, subcutaneously in joints or muscles, small bubbles of the oxygen-ozone mixture can be introduced, which subsequently dissolve in the tissue [41]. Internal mucous membranes, such as the colon, can be brought into contact with oxygen-ozone with the help of a catheter [42]. In addition to the gas mixture, administration can also take the form of autologous blood treatment, where up to 200 ml of blood is drawn from the patient, enriched with ozone, and re-injected [42]. In the following, various application examples for medical ozone therapy are presented. A schematic of a disk herniation and a healed disk herniation are shown in Fig. 2.2. The inner gel-like centre, known as the nucleus pulposus of a spinal disk, protrudes through the outer fibrous ring, called the annulus fibrosus, which may put pressure on the spinal nerve [43]. Conventional treatments for disk herniation include surgery, heat therapy, and physiotherapy [44]. As surgery carries inherent risks and physiotherapy and heat treatment are effective only for mild disk herniation, the use of ozone therapy appears to be a viable and minimally invasive alternative [7], [26]. By an injection needle, medical oxygen-ozone is therefore applied under computer tomography (CT) guidance and injected into surrounding tissue [45] or the disk [7]. As a result, the intervertebral disk undergoes chemonucleolysis, and the nucleus pulposus, the inner part of the disk, gradually loses volume [7]. As a result, the patient’s pain from the pressure on the spinal nerve is reduced. In addition to its therapeutic effects, ozone therapy has been shown to boost the immune system and reduce oxidative stress, which refers to an imbalance between the production, accumulation, and detoxification of reactive oxygen species [46].

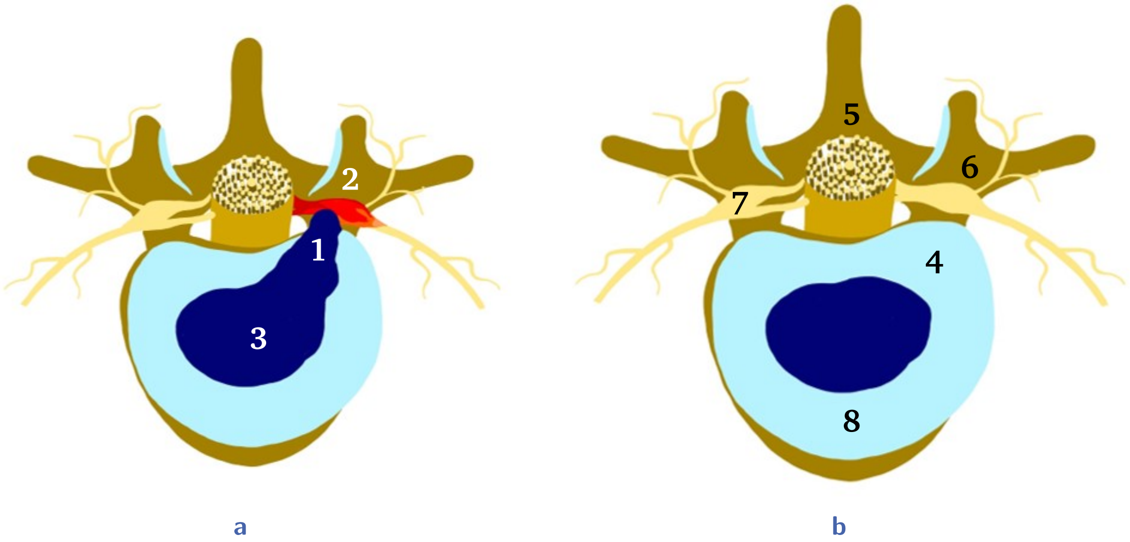

Fig. 2.2: (a) Shows a herniated disk (1) with a pinched nerve (2). The nucleus pulposus (3), the inner part of the disk, puts pressure on the nerve in the presence of a disk herniation. (b) Depicts a previously herniated disk (4) that is healed. Thereby, (5) shows the spinal cord, (6) the spondylophyt (a bony projection), (7) the spinal nerve, and (8) the annulus fibrosus. [12]

Also, intra-articular injections of oxygen-ozone for the treatment of knee osteoarthritis result in long-lasting analgesic effects and improved mobility [2]. Ozone also has an anti-inflammatory impact that is important for both intradiscal and intra-articular injections [2].

The extracorporeal blood oxygenation and ozonation (EBOO) therapy, shown in Fig. 2.3, is another medicinal procedure that applies ozone. EBOO may be used to treat peripheral artery disease, coronary artery disease, dyslipidemia, and cholesterol embolism [31], [32]. During the treatment, the patient's venous blood is drawn and enhanced with oxygen—ozone. After that, the patient receives a re-infusion of the oxygen-ozone-enhanced blood.

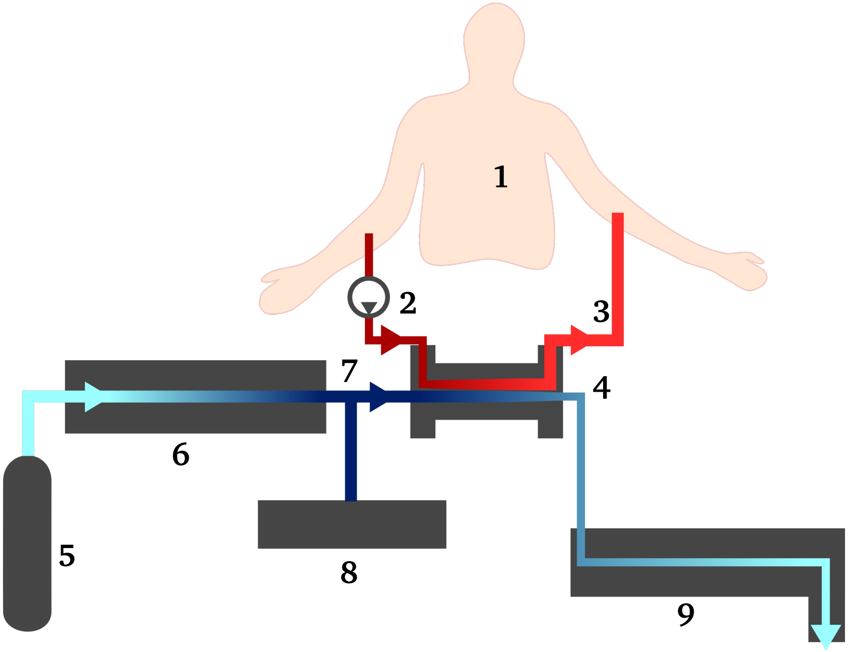

Fig. 2.3: The blood of the patient (1) is drawn with a blood pump (2) and enriched with oxygen-ozone, while it passes through the blood circuit (3). The blood circuit is enriched with ozone through contact with the gas circuit (4). The gas circuit consists of oxygen supply (5), ozone generator (6), an ozone supply (7), an ozone sensor (8), and an ozone destructor (9).

Ozone is additionally used in dentistry. Using oxygen-ozone prior to applying dental sealants is one strategy that has strong supporting data [4]. Using ozonated water to treat avulsed teeth is another use case [5].

For the treatment of a disk herniation with oxygen-ozone injection, 10 ml of oxygen-ozone with ozone concentrations between 25 $\mathrm{mg\,l^{-1}}$ and 30 $\mathrm{mg\,l^{-1}}$ are injected [47]. Lower doses are used in other applications, such as oxygen-ozone injection for the treatment of knee osteoarthritis and antimicrobial ozone therapy in dentistry. In order to treat knee osteoarthritis, 5 ml to 10 ml of oxygen-ozone are used, with ozone concentrations ranging from 5 $\mathrm{mg\,l^{-1}}$ to 15 $\mathrm{mg\,l^{-1}}$ [2], [3]. The lowest ozone concentrations (4 $\mathrm{mg\,l^{-1}}$) for the considered medical applications are used in dentistry, whereby 30 ml of oxygen-ozone are applied [48]. For the treatment of herniated disks with ozone, different concentrations are listed in the literature (see Tab. 2.1).

Monitoring the ozone concentration at the injection point is essential due to its rapid decay and the potential for variation in the amount present between production, in the

Tab. 2.1: Overview of oxygen-ozone injection volumes and ozone concentrations for the treatment of herniated disks. [14]

reference	ozone concentration [$\mathrm{mg\,l^{-1}}$]	injection volume [ml]
[49]	27	12
[50]	30	3-4
[51]	27	10-14
[7]	30	10
[47]	25-30	10
[6]	30	3-10

injection syringe, and during treatment. In an ideal situation, ozone therapy involves measuring the concentration at the point of injection and the concentration in the intervertebral disk tissue. It is important to maintain a safe and effective concentration that can effectively treat the disk herniation without harming the patient. Although this concentration has not yet been measurable, the following analysis takes into account the theoretical concentration at the point of injection. The volume of the disk (Tab. 2.2) and the amount of injected ozone (Tab. 2.1) are taken into account in order to calculate the theoretical concentration in the intervertebral disk immediately following injection.

Tab. 2.2: Overview of intervertebral disk volumes for determining the theoretical ozone concentration inside the disk after injection. Thereby, L stands for the lumbar part of the spinal column and S for the sacral region. [14]

reference	average volume [ml]	intervertebral disk
[52]	9.19	L3/4, L4/5, L5/S1
[53]	6.1	L1/2, L2/3, L3/4, L4/5, L5/S1
[54]	8.6	L1/2, L2/3, L3/4, L4/5
[7]	17.37 ± 4.7	L1/2, L2/3, L3/4, L4/5, L5/S1
[55]	15 ± 3	L2/3, L3/4, L4/5

According to earlier studies [6], [47], 90 µg to 300 µg of pure ozone are administered at a concentration of $30\,\mathrm{mg\,l^{-1}}$. In contrast, the largest volume of ozone (14 ml, see Tab. 2.1) with the highest concentration is injected ($30\,\mathrm{mg\,l^{-1}}$, see Tab. 2.1), in the smallest disk volume (6.1 ml, see Tab. 2.2), to produce the highest and, consequently, most critical theoretical concentration inside the disk. Pure ozone in the amount of 420 µg is applied for an injection of 14 ml at the prescribed concentration. With a minimum disk volume of

6.1 ml, a maximum oxygen-ozone mixture concentration of 30 mg l^{-1}, and a maximum injection volume of 14 ml, a theoretical ozone concentration of 68.85 mg l^{-1} is reached in the disk instantly following injection.

2.2 Antibacterial effects of ozone in medicine

Over the past few decades, bacterial resistance to antibiotics has developed into a significant challenge [56], [57]. Antibiotics, used to treat bacterial infections, are becoming less effective, leading to serious disease progressions, mostly in hospital settings [56], [57]. Due to its disinfecting and antibacterial qualities, ozone can be a powerful substitute for conventional treatments based on antibiotics and anti-inflammatory drugs [8]. However, using ozone comes with a number of challenges, including the need for special storage facilities, the dangers of inhalation, and the difficulty of transferring ozonated gas to wounds [58]. As a result, ozone is typically used in clinical settings [59]. Ozonated oils, which are simpler to use and store, offer an alternative. Numerous clinical investigations have demonstrated that ozonated oils are among the best topical disinfectants for chronic wounds, inactivating not only bacteria but also viruses and fungi [58]. Fig. 2.4a shows a chronic wound, while Fig. 2.4b demonstrates a previously chronic wound that is healed.

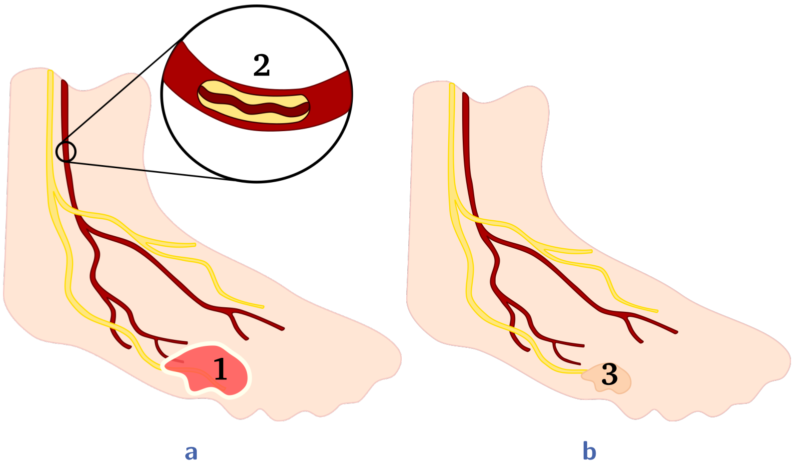

Fig. 2.4: **(a)** Shows a chronic wound with an ulcer (1) that results in reduced blood flow (2). **(b)** Depicts a previously chronic wound (3) that is healed.

2.3 Ozone sensors in the context of medical ozone therapy

Ozone is an unstable gas that rapidly decays into oxygen. As a result, it must be generated immediately before its application. In medical treatments, ozone is generated using ultra-pure medical oxygen as the input for the generator, which produces a mixture of oxygen and ozone for further use. Since medical-grade oxygen is used instead of air for ozone production, the effect of humidity interference can be neglected when measuring ozone gas for medical purposes. An extensive literature search has shown that it is not yet possible to measure the ozone concentration during medical therapy in human body liquids and tissues at the point of injection. There are many different treatment methods, and it is essential that the ozone concentration be monitored to avoid under- or over-dosing. For instance, during EBOO it is only possible to monitor the ozone concentration before ozonation in the gas phase or by indirect measurement using markers that correlate with the ozone concentration in blood [32]. Additionally, accurate dosing and regulation are not possible. This is especially important for the treatment of herniated disks, because only small volumes of oxygen-ozone are used. Health-critical amounts may be administered without monitoring the ozone concentration, while on the other hand, a concentration of ozone that is too low may not be effective. In order to support various treatment modalities, it is essential to incorporate ozone sensors into medical and bioanalytical instruments [9]. Thus, to prevent exceeding health-critical limits, this enables automatic deactivation. Monitoring also enables to approach the limit more closely, enhancing the therapeutic effect without exceeding it.

Depending on the application, a medical ozone sensor must meet unique specifications, whereby an overview is shown in Table 2.3. Ozone's half-life in bodily fluids and tissues makes a fast response and recovery time extremely important. With the exception of bones, human tissues normally contain a high proportion of water. Ozone decomposes in water at a temperature of 40 °C in about 25 min, while the water has a pH value of 7 and an agitation speed of 100 rpm [60]. Ozone, in contrast, disintegrates in blood within a short period of time of a few minutes [61]. As a result, it is unfeasible to use sensors with a response time of several minutes. The sensor reaction time for oxygen-ozone injection in cases of herniated disks must be less than the injection time, which ranges between 10 s and 15 s [7]. In order to prevent tissue damage, sensors that come into direct contact with blood should not be heated over 40 °C. Ozone sensors can also be used in medical settings without coming into contact with biological fluids or tissues; hence, in the following, sensors with greater measuring temperatures are also covered. The use of ozone therapy to treat a herniated disk is one example. A gas sensor may be used for this application to monitor the concentration inside the injection needle while the treatment is conducted. Therefore, a medical use does not necessitate that the sensor be implanted in a person's body. Medical temperature sensors, as an illustration, often gauge body temperature externally. In order to integrate the sensor inside the injection needle, the sensor's size must also be small enough. The root-mean-square percentage error (RMSPE) should also be as low as possible, but at least below 10%.

Tab. 2.3: Overview of the most important requirements for a medical ozone sensor

parameter	requirement
measurement temperature	below 40 °C
response time	below 15 s
recovery time	below 15 s
measurement substance	ozone gas and dissolved in body liquids and tissues
wavelength	no UV light
size	needs to be integrated in a 22-gauge spinal needle
substrate	flexible to enable the integration into the needle
used materials	need to be biocompatible and/or encapsulated
measurement range	dissolved: up to $70\,\mathrm{mg\,l^{-1}}$, gas: up to $30\,\mathrm{mg\,l^{-1}}$
selectivity	high selectivity against oxygen
sensitivity	average sensitivity is sufficient
in-line measurement	needs to be enabled for continuous measurement
long-term stability	average long-term stability is sufficient
RMSPE	below 10%

3

Overview of ozone measurement

Parts of this chapter are based on: L. Petani, L. Koker, J. Herrmann, V. Hagenmeyer, U. Gengenbach, and C. Pylatiuk, “Recent developments in ozone sensor technology for medical applications”, *Micromachines*, vol. 11, no. 6, 2020. DOI: `10.3390/mi11060624`.

This chapter is supplemented by findings from: [12], [15]

For the design of sensors, there are numerous measurement methods and sensing components, as given in [10], [62]–[64]. In the following, the measurement methods are subdivided into electrochemical, optical, and volumetric. Amperometry and impedimetry are subcategories of electrochemical methods. Optical absorption, photoluminescence, and colorimetry are subcategories of optical methods. Titration-based methods are part of the volumetric measurement methods. Fig. 3.1 depicts a fundamental sensor structure and materials used for sensor setups. The decisive factor in the development of a sensor is its intended, specific application and the associated requirements. The application, in turn, also determines the sensor’s mode of operation and the materials used. The materials and operating method are selected to guarantee their integration with medical and bioanalytical devices. The sensing material is typically applied to a substrate. The sensitive area of a metal-oxide sensor, for instance, is built upon an indium oxide (In_2O_3) thin film on a silicon substrate. For instance, the electrodes in an amperometric sensor are printed with gold nanoparticle (AuNP) and silver nanoparticle (AgNP) inks. A membrane ensures selectivity, allowing only those substances to come into contact with the sensing material that do not interfere with the desired measurement.

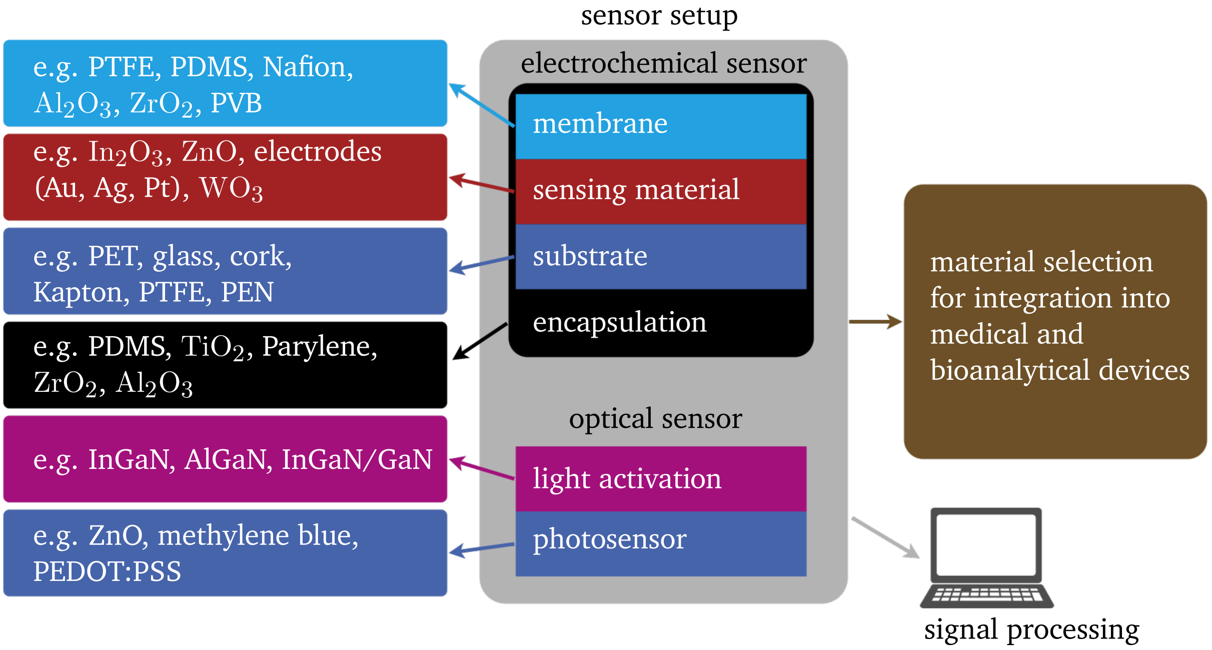

Fig. 3.1: A membrane, sensing material, substrate, and encapsulation yield the basic sensor assembly for an electrochemical sensor, shown in the schematic. For an optical sensor, the basic sensor assembly consists of a light activation element and a photosensor. (Modified according to [10])

Encapsulation is required to ensure the biocompatibility of sensors that come into contact with bodily fluids and tissues. It is essential that the encapsulation has no impact on the measurement method and the substances intended for the measurement can still pass through the encapsulation.

An overview of the various measurement methods is provided in Tab. 3.1. According to Section 2.3, the response time is one key parameter for medical applications. The half-life of ozone in water, bodily fluids, and tissues makes a fast response time extremely important. Response times for amperometric sensors range from 15 s to 3 min [65]–[69]. The response times of the summarised impedimetric sensors, in contrast, range from 4 s to 15.5 min [70]–[72]. Impedimetric sensors that use carbon nanotubes (CNTs) as their sensing material exhibit a slow response time of approximately 15.5 min [72]. In contrast, impedimetric metal-oxide sensors require light activation or high measurement temperatures to achieve a faster response time [73]. The response time for light-activated sensors falls within the range of 13 s to 12.9 min, while heated metal-oxide sensors have response times ranging from 4 s to 10 min [36], [71], [74], [75]. Optical absorption sensors are typically able to provide a real-time response, whereas photoluminescence

Tab. 3.1: Overview of the measurement methods used for sensing ozone, including various criteria such as measurement temperature and response time. Ozone is either measured with the sensors as gas or dissolved in water. [10]

method	sensing	ozone	T [°C]	t_{Response}	λ [nm]
amperometric	electrodes	gas	–30 - 90	15 s - 3 min	NA
		dissolved	–5 - 50	15 s - 3 min	NA
impedimetric	metal-oxide	gas	0 - 350	4 s - 10 min	NA
	metal-oxide	gas	25 - 26	13 s - 12.9 min	LA[a]
	nanotubes	gas	25 - 75	15.5 min	NA
colourimetric	photosensor	dissolved	T_{Room}	2.5 min	NR
optical	photosensor	gas	T_{Room}	real-time	190 - 800
absorption	photosensor	dissolved	5 - 40	real-time	190 - 900
PL	photosensor	gas	25	10 - 20 min	500 - 800
titration	volume	dissolved	T_{Room}	NR	NA

[a] In case of an impedimetric metal-oxide sensor, the light activation of the sensor surface allows a significant reduction of the response time at low measurement temperatures.; LA: light activation; NA: not applicable; NR: not reported; PL: photoluminescence.

sensors have reported response times between 10 min and 20 min [76]–[78]. Colourimetric measurement methods have a response time of 2.5 min, while the response time for titration-based methods is not available [79]–[81]. Dissolved ozone and ozone gas can be measured with amperometric and optical absorption methods [65], [82]–[84]. For ozone gas sensors, impedimetric and photoluminescence methods can be utilised, while for dissolved ozone measurements, titration and colourimetric methods [78]–[81], [85] are applied. Hydrophobic membranes can allow gas sensors to be used for dissolved ozone measurements [10]. Additionally, gas stripping, as shown in Fig. 3.2, can be used to preprocess dissolved ozone measurements and enable gas measurements. Gas stripping is a process in which dissolved ozone measurement is converted into a gas measurement [86]. This involves separating ozone gas from a liquid solution through a mass transfer process, in which a gas stream is passed over a liquid stream. The mass transfer between the gas and the liquid is dependent on their relative concentrations and temperatures and is facilitated by the concentration difference between them. The gas concentration is then measured by a gas sensor, such as a photosensor or heated metal-oxide sensor, and the dissolved concentration of the liquid solution is subsequently determined [87]. Compared to measuring dissolved ozone, measuring ozone gas in combination with gas stripping has the advantage of not being affected by particles or organic substances, making it suitable for use with non-pure water samples [86], [87]. However, it's important to note that the gas stripping method for measuring ozone requires more complex equipment and setup, potentially leading to higher initial costs and size requirements, which could be considered a disadvantage in certain budget-constrained or size-limited scenarios.

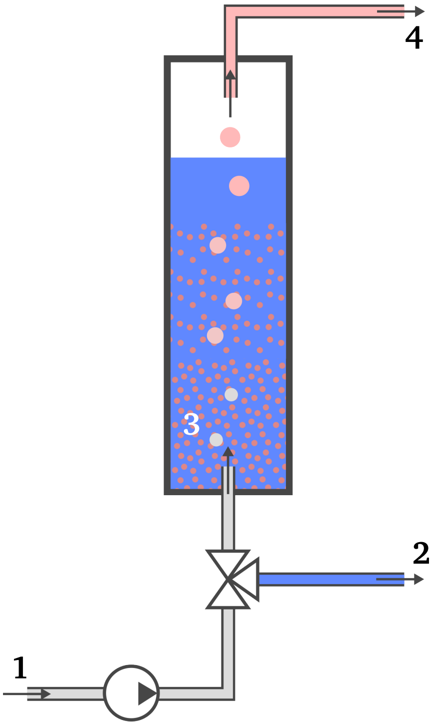

Fig. 3.2: Shows the procedure during gas stripping, including stripping gas (1), liquid (2), measurement substance (3), and target gas (4).

3.1 Electrochemical measurement

The electrochemical measurement of ozone is either possible with amperometric or impedimetric measurement methods. Both of these measurement methods are explained and summarised in the following.

3.1.1 Amperometric measurement

Amperometry is an electrochemical method used for measurement of gases and dissolved gases [62], [73]. The basic structure of the sensor is presented in Fig. 3.3, which includes a working electrode (WE), a counter electrode (CE), a reference electrode (RE), an electrolyte, and a membrane. The sensor is surrounded by the substance to be measured, which can be either a gas or a liquid solution. The sensor is enclosed by the combination of the membrane material and the outer surface of the chamber around the electrolyte. A constant voltage is applied over time between the WE and RE. Ozone permeates through the membrane and causes a reduction reaction at the WE. The resulting current is measured at the WE, and the concentration is calculated from the measured current value, which is proportional to the concentration.

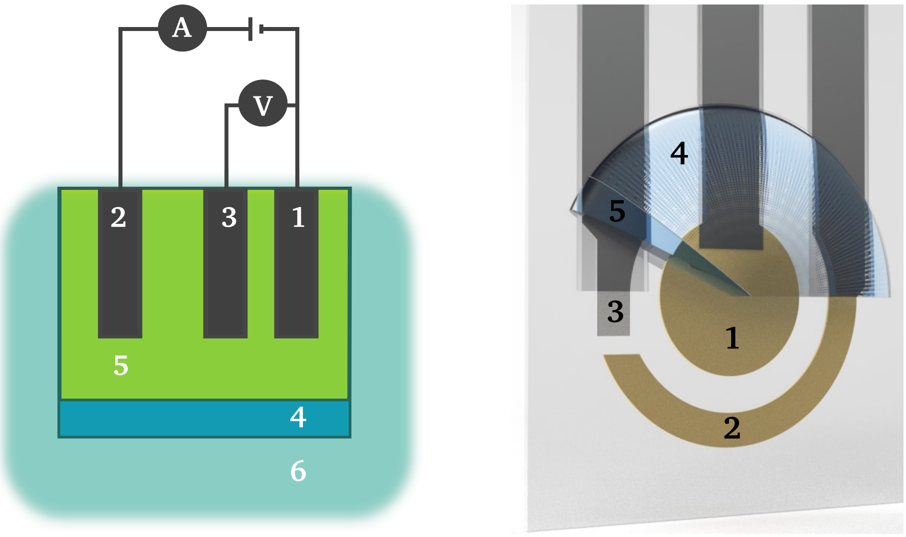

a

b

Fig. 3.3: **(a)** Amperometric sensor schematic. [10] **(b)** Computer-aided design (CAD) model, including WE (1), CE (2), RE (3), membrane (4), and electrolyte (5). Depending on the ozone concentration present as gas or dissolved in liquid in the measurement substance (6), the current changes. [12]

Amperometric sensors can either be used for gaseous or liquid measurement substances. In the following and in Tab. 3.3, the properties of amperometric ozone gas sensors are summarised. The sensing electrodes utilised in amperometric gas sensors are typically made of gold (Au), silver (Ag), or platinum (Pt), and the substrates commonly encountered include polyethylene (PE), polyvinyl chloride (PVC), and polypropylene (PP). Measurements are taken at temperatures ranging from $-30\,°\mathrm{C}$ and $90\,°\mathrm{C}$, with measurement ranges between 0.23 parts per billion (ppb) and 5×10^4 ppb. The minimum response time and recovery time that are provided are 15 s and 180 s.

Additionally to sensors for gas measurement, Tab. 3.5 compares the properties of different dissolved ozone sensors. Amperometric dissolved ozone sensors that have been reported use various types of electrodes, such as Au, Ag, Pt, and boron-doped diamond (BDD), to detect substances. The temperature range for measurements is typically between $-5\,°\mathrm{C}$ and $50\,°\mathrm{C}$, and the measurement range is between $0.05\,\mathrm{mg\,l^{-1}}$ and $20\,\mathrm{mg\,l^{-1}}$. The response and recovery times of these sensors are typically 15 s and 1 s, respectively.

Amperometric sensors typically have a membrane that filters out interfering substances. In the case of ozonated water, oxygen must be filtered because it is also an oxidising substance that reacts with the WE. The main drawback of using a membrane is that it increases the sensor's response time as ozone needs to diffuse through it. There are different materials that can be used as a membrane, resulting in varying ozone transfer rates and response times. Ceramic membranes made of aluminium oxide have an ozone transfer rate of $0.35\,\mathrm{g\,m^{-2}\,h^{-1}}$, zirconium oxide has an ozone transfer rate of $10\,\mathrm{g\,m^{-2}\,h^{-1}}$, and porous polytetrafluoroethene (PTFE) has an ozone transfer rate of $4\,\mathrm{g\,m^{-2}\,h^{-1}}$ [88]. Zoumpouli et al. [89] reported that ozone mass transfer coefficients for polydimethylsiloxane (PDMS), PTFE, and polyvinylidene difluoride (PVDF) are of the same order of magnitude. They also suggest that other membranes, such as polyethersulfone (PES) and polyetherimide (PEI), react with ozone, leading to membrane decomposition. Shanbhag et al. [90] noted that the permeability of ozone through PDMS is four times higher than the permeability of oxygen. Zhang et al. [91] compared the permeability of several gases through PDMS and found that oxygen has a permeability that is approximately twice as great as that of nitrogen. Furthermore, Zhang et al. [91] reported more information about the permeability of PDMS membranes as a function of factors such as thickness and area. Shanbhag et al. [90] investigated PDMS membranes with varying thicknesses (ranging from 165 µm to 419 µm) and permeation areas (ranging from 6900 mm^2 to 29900 mm^2).

Previous work [71], [92] has also discussed amperometric sensors that do not require membranes and instead use a WE made of BDD material. These microelectrodes are fabricated by depositing the BDD film on silicon wafers or tungsten needles with a diameter of 20 µm [71]. The use of BDD WEs provides selectivity without the need for a membrane since they are insensitive to reduction reactions with oxygen [71]. The CE used is Pt, while Ag/silver chloride (AgCl) is used for the RE. Due to the low background current, there is no need for an electrolyte.

3.1.2 Impedimetric measurement

Impedimetry is also an electrochemical measurement method for the measurement of gases and dissolved gases [62]. Impedimetric sensors, as depicted in Fig. 3.4, are composed of electrodes, sensing material, substrate, and a heat or light activation component.

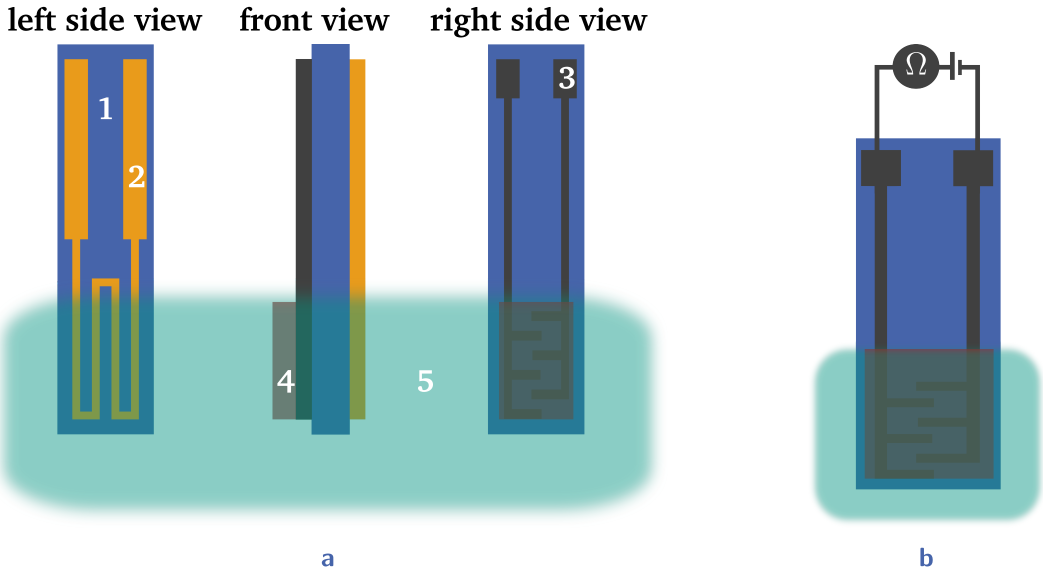

Fig. 3.4: **(a)** Illustrating an impedimetric sensor, including substrate (1), heater (2), electrodes (3), and sensing material (4). **(b)** Enlarged view of the impedimetric sensor. The resistance Ω of the sensing material (measured in Ohms) is changed in the presence of ozone within the gaseous measurement substance (5). [10]

Some variants incorporate a heater to maintain a specific temperature of the sensing material, while others utilise light activation to allow for room temperature (RT) sensing or a decrease in measurement temperature while maintaining fast response times [93]. Impedimetric sensors require a long recovery time after each exposure [94]. When the sensor is immersed in a gaseous measurement substance, any exposed electrode surfaces not covered by the sensing material must be coated with a dielectric material.

Impedimetric sensors are comprised of two types of sensors, including resistive sensors for measuring direct currents and impedance sensors for measuring alternating currents. When the target substance is present, the resistance or impedance value of the sensing material changes, and the concentration can be calculated based on this value. For these types of sensors, the measurement temperature corresponds to the temperature of the sensing material. When operating at RT, the sensing material is not heated and remains at the same temperature as the surrounding measurement substance. The most commonly used materials as sensing materials for impedimetric ozone gas sensors are In_2O_3, zinc oxide (ZnO), CNTs, and tungsten trioxide [70], [72], [74], [85], [93], [95]–[110]. Different nanostructures, such as nanoparticles (NPs) [72], [98]–[101], nanocolumns [95], platelets [74], [106], nanorods [93], [103], nanothin films [96], [97], [107]–[110], nanoislands [70], nanotubes [85], [104], nanosheets [102], nanowires [101], and thick films [105], are utilised as the sensing layer morphology. The substrate materials commonly applied include aluminium oxide (Al_2O_3), silicon dioxide/silicon, glass, quartz, and aluminium (Al), while Au, Pt, copper (Cu), and titanium (Ti) are commonly used as electrodes [72], [93], [95], [101]–[103], [106], [111]. The thickness of the electrode varies between 100 nm [72], [93], [95], [101], [103], [106], [111] and 300 nm [102], while the distance between two opposing electrodes ranges from 5 µm [109] to 50 mm [72], [95], [100]. The temperature range for measurement is 0 °C to 350 °C. To decrease the response time at low temperatures, some sensors utilise light activation of the sensor surface, with a wavelength typically between 254 nm and 490 nm, as shown in Tab. 3.3. Reported measurement ranges vary between 0.5 ppb and 10^6 ppb. The lowest response and recovery time presented is 4 s.

Korotcenkov et al. [112] explored the impact of materials and structural parameters on impedimetric ozone gas sensors, focusing on In_2O_3 and tin dioxide. The authors found that thin films with a thickness of 60 nm to 80 nm exhibited a response time of no more than 1 s to 2 s at 200 °C. They also observed that a smaller film thickness and crystallite size, as well as a larger pore size, led to a greater sensor response amplitude.

One of the key advantages of impedimetric ozone sensors is their high selectivity towards ozone, without the need for membranes to filter out interfering substances. To achieve high selectivity and sensitivity, Korotcenkov et al. [112] identified several important factors, including: the superior ozone selectivity of In_2O_3 over tin dioxide sensors [113]; the use of sensor arrays instead of a single sensor to analyse the sensor response [114]; and the enhancement of selectivity through surface modification or bulk doping [115].

3.2 Optical measurement

The optical measurement of the ozone concentration is possible with colourimetric, optical absorption, and photoluminescence measurement methods, which are explained in the following. The colourimetric measurement method can be applied for the measurement of dissolved ozone, the photoluminescence measurement method for ozone gas, and optical absorption for dissolved ozone and ozone gas.

3.2.1 Colourimetric measurement

Colourimetric measurement is a well-established optical method for measuring ozone concentrations ranging from $0.05\,\mathrm{mg\,l^{-1}}$ to $2\,\mathrm{mg\,l^{-1}}$ [79], [80]. This measurement method uses the method of optical absorption, based on Lambert-Beer's law, which is explained in Section 3.2.2. An indicator solution, such as N,N-diethyl-p-phenylenediamine (DPD) or DPD with potassium iodide, is added to ozonated water, resulting in a colour change [116]. The colour change depends on the ozone concentration, and different concentrations are shown in Fig. 3.5.

Fig. 3.5: Shows cuvettes with different ozone concentrations and indicator solutions. The darker purple colour of the solution indicates a higher ozone concentration.

The absorption of the indicator solution in ozonated water is measured using a specific absorption spectrum that depends on the indicator solution. Colourimetric measurement is selective for ozone compared to oxygen because of the different redox potentials. The response time for these sensors is about 2.5 min, but the recovery time is not reported [116].

Paolo et al. [32] proposed the use of markers to determine the ozone concentration in blood plasma. While only one of the markers can be determined directly with optical absorption methods, all of them, including total antioxidant status (TAS), protein thiol groups (PTG), and thiobarbituric acid reactants (TBAR), can be measured using colourimetric methods [32]. To measure the marker concentration using colourimetric methods, a detection reagent is added to the solution. After the reaction of ozone and blood plasma with the detection reagent, the marker concentration is quantitatively measured by observing the visible colour change with a photometer. With increasing ozone concentration, the concentration of TAS and PTG decreases, while the concentration of TBAR increases [32]. Paolo et al. [32] reported colourimetric measurement of PTG concentration at 412 nm, while Erel [117] investigated colourimetric measurement of TAS at 660 nm. Additionally, Kampa et al. [118] conducted colourimetric measurement of TAS concentration at 450 nm [32].

3.2.2 Optical absorption measurement

Optical absorption sensors, as illustrated in Fig. 3.6, are based on detecting the light absorption of a measurement substance that is sent out from a light source (for example, light-emitting diodes (LEDs)) and received by a detector (for example, photosensors). This enables the identification of specific absorption spectra for substances, such as ozone gas or dissolved ozone. By comparing the absorption of ozone in the measurement substance to the absorption without ozone, it is possible to calculate the ozone concentration in the measurement substance. The fundamental methods behind photometric ozone measurement include the Lambert-Beer law and the ozone absorption spectrum [119]. The Lambert-Beer law states the relationship between parameters, such as the initial

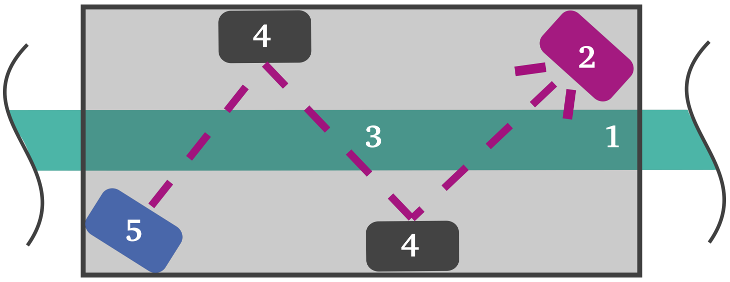

Fig. 3.6: Shows the structure of an optical absorption sensor. The measurement method involves detecting the light absorption of the gaseous or liquid measurement substance (1). This is achieved by emitting diodes (2) which send out light on a light path (3). The light may be reflected by mirrors (4), and then detected by a photosensor (5). (Modified according to [10])

intensity I_0, concentration c, attenuation coefficient α, wavelength λ, absorption path length d, and the resulting intensity $\mathrm{I(c)}$ and yields

$$\mathrm{I(c)} = \mathrm{I}_0 \cdot \exp(-\mathrm{c} \cdot \alpha(\lambda) \cdot \mathrm{d}). \tag{3.1}$$

Gengenbach and Sieber [120] provide guidelines and identify key factors for designing optical absorption sensors. To enhance sensitivity, the absorption cell can be heated or the path length increased [120]. Additionally, the optical path can be extended by using multiple reflections in the measuring chamber [120]. Most important for the optical absorption measurement of ozone are the absorption peaks. Ozone has four different absorption regions, such as the Hartley band (200 nm to 310 nm), the Huggins band (310 nm to 375 nm), the Chappius band (375 nm to 603 nm), and the Wulf band (beyond 700 nm) [119]. Thereby, the Hartley band, Huggins band, and Chappius band are shown in Fig. 3.7. The region with the highest absorption is around the Hartley band between 230 nm and 320 nm with an absorption peak at 253.7 nm [119]. Another advantage of using this wavelength range is its selectivity against oxygen. As there is always a mixture of oxygen and ozone in the measurement chamber during ozone measurement, the deep ultraviolet (UV) range (200 nm - 352 nm) provides a four orders of magnitude lower absorption cross-section of oxygen compared to ozone [122]. This is due to the fact that the oxygen absorption peaks are approximately at 150 nm, 688 nm, and 762 nm [123], [124]. Therefore, using the Hartley band for ozone absorption measurement ensures selectivity between ozone and oxygen without additional instrumentation effort. The oxygen and ozone absorption between 100 nm and 400 nm is shown in Fig. 3.8

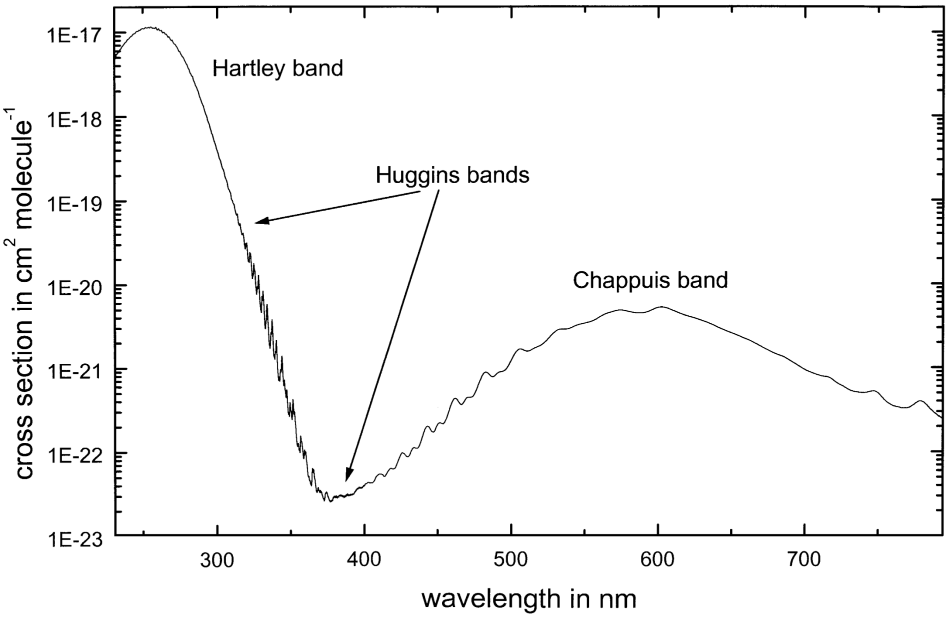

Fig. 3.7: Shows the absorption bands of ozone. (Reprinted from Publication Atmospheric Remote-Sensing Reference Data From GOME—2. Temperature-Dependent Absorption Cross Sections of O_3 in the 231–794 nm Range, 64 / 4, J. P. Burrows, A. Richter, A. Dehn, B. Deters, S. Himmelmann, S. Voigt, and J. Orphal, Journal of Quantitative Spectroscopy and Radiative Transfer, 509–517, CC-BY-NC-ND (1999), with permission from Elsevier) [121]

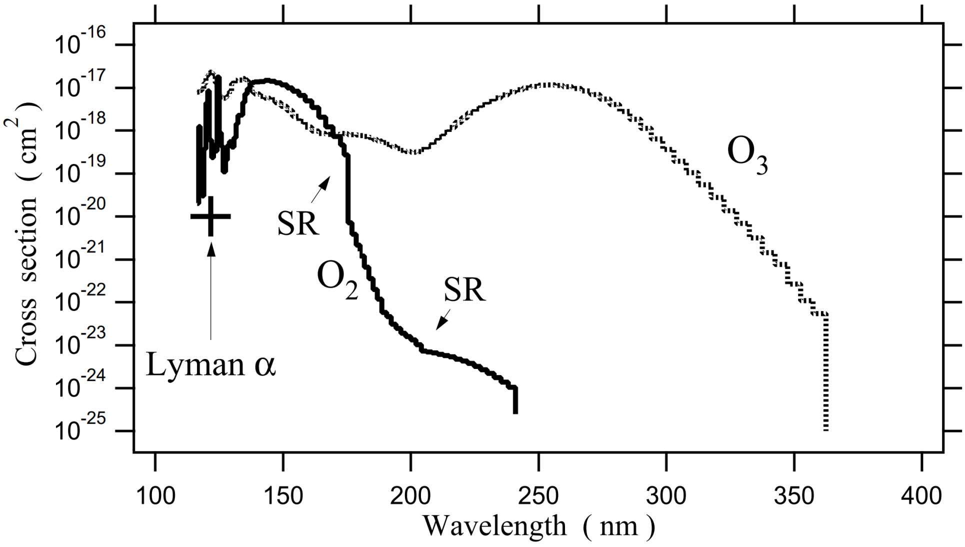

Fig. 3.8: Shows the absorption bands of oxygen and ozone between 100 nm and 400 nm. (Extracted from Publication Aeronomy, a 20th Century emergent science: the role of solar Lyman series, 20 / 5, G. Kockarts, Annales Geophysicae, 585–598, CC BY 3.0 (2002)) [125]

Absorption values below 1 absorbance units (AU) are desirable because the lowest relative error for absorption measurements is observed in the range of 0.1 AU to 0.8 AU [126]. Depending on the measurement of the optical absorption in gas or dissolved in water, the ozone absorption peak is slightly different. The peak absorption of ozone dissolved in water is approximately 260 nm [127] and for ozone gas approximately 254 nm [121].
As summarised in Tab. 3.3, optical absorption sensors for ozone gas utilise sensing materials such as ZnO or methylene blue applied to glass or quartz substrates. These sensors operate at RT, provide mostly real-time sensing, and the wavelength range is typically between 190 nm and 800 nm.
Optical absorption sensors for dissolved ozone measurements utilise photometers and fluorometers as sensing units. Photometers for these sensors use wavelengths between 190 nm and 900 nm while the excitation spectra for fluorometers range between 213 nm and 335 nm and the emission spectra range from 310 nm to 450 nm. Real-time measurements are mostly supported by optical absorption sensors.
In addition, markers can be used to measure the ozone concentration in blood plasma. Paolo et al. [32] suggested using TAS, PTG, or TBAR as markers. Among these, only the TAS marker can be measured directly using optical absorption methods and a photometer. The other two markers can be measured using colourimetric methods, as explained in Section 3.2.1. As the ozone concentration in blood plasma increases, the TAS concentration decreases. Paolo et al. [32] studied the optical absorption measurement of TAS at 600 nm.
Furthermore, optical absorption gas measurement of dissolved ozone is possible with gas stripping preprocessing. During this process, ozone gas is removed from a liquid stream, and its concentration is subsequently measured. A photometer is often used to measure the ozone gas concentration, but a heated metal-oxide sensor or other ozone gas sensor may also be used.

3.2.3 Photoluminescence

Moreover, there is the photoluminescence measurement method that uses optical measurement [78]. This method makes use of photoluminescence quantum dots, materials whose optical characteristics, particularly the strength of photoluminescence, alter irreversibly in the presence of ozone gas. To assess the ozone concentration, the approach includes forming thin films of core shell quantum dot particles on glass substrates and monitoring the quantum dots' photoluminescence intensity. Smaller quantum dots, which emit green light, respond to ozone better than larger quantum dots, which emit red light [78]. Thereby, selective measurement is enabled, as only the presence of ozone gas reduces the photoluminescence of quantum dots, not pure oxygen, nitrogen, argon, or carbon dioxide. It is possible to use cadmium selenide-based core-shell quantum dots as a sensing material for photoluminescence sensors on glass substrates [78]. The wavelengths range from 500 nm to 800 nm, the response time of the sensor is between 10 min to 20 min, and the recovery time is one day [78].

3.3 Volumetric measurement: titration

Furthermore, it is also possible to determine the ozone concentration with titration, as shown in Fig. 3.9. Titration is a volumetric measurement method. Thereby, the measurement substance is titrated with a titrant until neutralisation occurs, indicated by a visible colour change from clear to yellow-brown [81]. The concentration is determined by measuring the volume of the titrant, such as sodium thiosulfate, needed for neutralisation [81]. For example, sodium thiosulfate can be used as a suitable titrant for titration-based sensors as a sensing reagent [81].

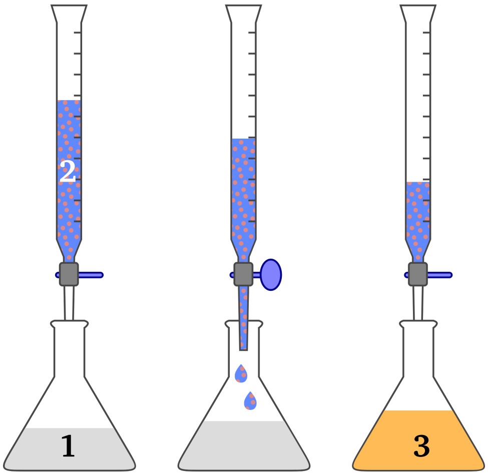

Fig. 3.9: Shows the procedure during a measurement based on titration, including measurement substance (1), titrant (2), and visible colour change from clear (1) to yellow-brown (3).

3.4 Ozone measurement methods in the context of medical therapy

Medical sensors must meet criteria such as sensitivity, selectivity, fast response and recovery, long-term stability, in-line measurement, aqueous or gaseous measurement environments, measurement range, measuring at RT, and the presence or absence of a light activation element, depending on the application. An average sensitivity is generally sufficient for medical applications where it is currently not possible to measure the concentration at the point of injection. Very small concentration changes, such as those that occur in an injection syringe's needle tip during ozone therapy, do not cause severe health problems, and it is still beneficial to measure with an average sensitivity compared to the current situation. When using electrochemical sensors, a membrane can improve the selectivity of the sensors. A membrane may also enable the use of a gas sensor in an aqueous environment. The membrane must be permeable to the analyte and less or ideally not permeable to interfering substances [128]. For some medical applications, the actual treatment lasts only 10 s to 15 s [7]. Thus, sensors with reaction times of several minutes have to be optimised in this regard. Because many devices, like injection syringes, are single-use items, long-term stability is a secondary property for the majority of the investigated medical applications. Ideally, a sensor capable of measuring both the gas phase (such as inside the injection needle before and during treatment) and the dissolved state in body liquids and tissues (such as outside the injection needle during treatment) is desirable for the described medical ozone therapy while also enabling in-line measurement. This allows for continuous and uninterrupted measurement before and during treatment without the need to stop or change the measuring sensor. As a result, measurement methods that can facilitate both types of measurements are preferred for this particular application. Regarding the measurement range, dissolved ozone measurements up to $70\,\mathrm{mg\,l^{-1}}$ have to be possible [14]. For sensors that come into contact with body liquid and tissue, a low measurement temperature and the avoidance of a UV light source as the light activation element for the sensing material are essential because high temperatures (higher than body core temperature) and UV light can harm biomolecules.

Colourimetric and titration measurement methods are not focused in the following because they do not enable in-line measurement and can only be used for dissolved ozone measurement. However, colourimetric and titration can still be used for sensor calibration or for referencing sensors. Also, for the focused application, photoluminescence and impedimetric CNTs sensors have reaction times that are too high. In the following, amperometric, impedimetric, and optical absorption sensors are further examined in relation to the application requirements of a dissolved ozone sensor during oxygen-ozone treatment. Optical absorption ozone sensors are most promising because of their fast response and recovery times. The major challenges for optical absorption ozone sensors are miniaturisation and the utilisation of UV light. The absence of a heating or light activation element and the ability to implement the measuring method in a compact design are the key benefits of amperometric sensors over other measuring methods. The major challenges for amperometric sensors are long response and recovery times and the further miniaturisation of these sensors. Due to the fast reaction time, metal oxide semiconductors (MOS)-based impedimetric sensors are also promising. However, the patient's health may be impacted by the heating (up to 350 °C) or light activation (UV light) elements that are frequently used in MOS in order to obtain fast reaction times. Compared to MOS-based impedimetric sensors, amperometric and optical absorption sensors can already be applied for dissolved and ozone gas sensing.

In summary, Tab. 3.2 gives an overview of the main advantages and main challenges of the reported ozone measurement methods in the context of medical therapy. In the following, amperometric and optical absorption sensors are the main focus, while impedimetric sensors are additionally considered for the biocompatibility investigation in Section 6. Currently, all of these measurement methods still pose major challenges. Nevertheless, fundamental research is necessary before newly designed sensors can be applied during medical treatment. First, the sensors have to be designed and subsequently optimised for the specific application. Tab. 3.3 lists notable publications on amperometric and optical absorption ozone gas sensors, while Tab. 3.4 focuses on impedimetric ozone gas sensors, and Tab. 3.5 considers dissolved ozone sensors that measure with the amperometric or optical absorption method. The measurement methods of the sensors are differentiated based on various criteria, such as the sensing unit or material, electrode material, measurement temperature, wavelength, measurement range, response time, recovery time, and commercial availability. For the here-focused application, an ozone sensor is necessary that fulfils the requirements listed in Tab. 2.3. Currently available ozone sensors, as shown in Tab. 3.3, Tab. 3.4, and Tab. 3.5 do not fulfil these requirements. Although some sensors from the current state of the art are capable of measuring below 40 °C and achieving a response and recovery time below 15 s, none of them simultaneously satisfy the conditions of operating without UV light and accurately detecting concentrations up to $70\,\mathrm{mg\,l^{-1}}$ (dissolved ozone) or $30\,\mathrm{mg\,l^{-1}}$ (ozone gas). While newly developed sensors may not fully meet all the specified requirements, further research is imperative to advance in the direction of meeting these criteria.

Tab. 3.2: Overview of the most important advantages and challenges of amperometric, impedimetric, colourimetric, optical absorption, photoluminescence, and titration ozone concentration measurement methods for medical therapy.

method	main advantage	main challenge
amperometric	compact design, no heating, no UV light, measurement of ozone gas and dissolved ozone	response time in the double-digit seconds range
impedimetric MOS	compact design, fast response time when heated or using UV light	either use of UV light or heating element, only ozone gas measurement
impedimetric CNTs	compact design, low measurement temperatures	response time in the double-digit minute range, only ozone gas measurement
colourimetric	no heating element	no in-line measurement, only dissolved ozone measurement
optical absorption	fast response time, no heating, measurement of ozone gas and dissolved ozone	miniaturisation, use of UV light
photoluminescence	no heating element, no UV light	response time is in the minute range, only ozone gas measurement
titration	no heating element	no in-line measurement, only dissolved ozone measurement

Tab. 3.3: Summary of amperometric and optical absorption ozone gas sensors. [10]

method	sensing material	T [°C]	λ [nm]	measurement range $[\mathrm{ppb}]^a$	$t_{Response}$ [s]	$t_{Recovery}$ [s]	com. av.	year [reference]
amperometric	WE; RE; CE: NR	20	-	20 - 250	<180	<180	yes	2016 [68], [69]
	WE; RE; CE: NR	12 - 26	-	5 - 1×10^4	NR	NR	yes	2017 [129]
	WE; RE; CE: NR	-30 - 50	-	20 - 2×10^4	15	NR	yes	2017 [65], [66]
	WE: Au; RE: Ag; CE: Pt	25, 35, 50	-	0.23 - 180	NR	NR	no	2017 [130]
	WE: Au, Ag, Pt; RE: Au, Ag, Pt; CE: Au, Ag, Pt	15 - 90	-	NR	NR	NR	no	2018 [131]
	WE: Au; RE: NR; CE: Ag	–5 - 45	-	0.6 - 5×10^4	30	NR	yes	2020 [67]
	WE; RE; CE: NR	–20 - 50	-	0 - 5×10^3	NR	NR	yes	2020 [132]
optical absorption	KI and α-CD	20 - 22	320 - 750	3 - 150	NR	NR	no	2017 [133]
	ZnO or $LiGaO_2$	NR	250 - 290	NR	NR	NR	no	2017 [84]
	rGO/ZnO	T_{Room}	190 - 500	300 - 700	real-time	real-time	no	2018 [76]
	methylene blue	23	400 - 800	10 - 200 ppbv	real-time	real-time	no	2019 [77]

α-CD: α-cyclodextrin; com. av.: commercially available; KI: potassium iodide; NR: not reported; rGO: reduced graphene oxide.

Tab. 3.4: Summary of impedimetric ozone gas sensors. The wavelength λ indicates that the sensor uses light activation, which enables a low measurement temperature while maintaining a fast response time. [10]

sensing material	T [°C]	λ [nm]	measurement range [ppb][a]	$t_{Response}$	$t_{Recovery}$	commercially available	year [reference]
ZnO	200	-	100 to 1×10^6	9.6 s	45.6 s	no	2016 [95]
$Co_xZn_{1-x}O$	150 to 350	-	42 to 560	40 s	6 min	no	2016 [107]
NR	12 to 32	-	1.5 to 110	10 min	NR	yes	2016 [75]
NR	12 to 32	-	0.5 to 110	5 min	NR	yes	2016 [75]
WO_3	12 to 32	-	1 to 110	10 min	NR	no	2016 [75]
NiAl-LDH	25	-	15 to 3580	4 s	4 s	no	2017 [74]
ZnO-SnO_2	26	325	20 to 300	13 s	90 s	no	2017 [72]
Ag (APTMS)	NR	-	15×10^4 to 1×10^6	50 s	NR	no	2017 [70]
Ag (PVA)	NR	-	18×10^4 to 1×10^6	15 s	NR	no	2017 [70]
Au (APTMS)	NR	-	15×10^4 to 1×10^6	70 s	NR	no	2017 [70]
Au (PVA)	NR	-	18×10^4 to 1×10^6	25 s	NR	no	2017 [70]
In_2O_3 dop. WO_3	75	-	200 to 500	60 s	60 to 120 s	no	2017 [105]
am.-IGZO	25	365	500 to 5000	775 s	2470 s	no	2018 [108]
$CuWO_4$	200 to 290	-	15 to 1400	7 s	5 to 10 s	no	2018 [100]
ZnO	300	-	NR to 100	NR	NR	no	2018 [102]
CNT func. ODA	75	-	200 to 500	15.5 min	28.7 min	no	2018 [85]
$CH_3NH_3Pbl_{3-x}Cl_x$	T_{Room}	-	5 to 2500	225 s	40 to 60 s	no	2018 [109]
TiO_2-In_2O_3	25	405	40 to 2000	40 s	280 s	no	2018 [134]
V_2O_5/TiO_2	300	-	90 to 1250	4.4 min	5 to 16 min	no	2019 [101]
ZnO mod. Au	26	370	30 to 570	13 s	29 s	no	2019 [93]
$Zn_{0.95}Co_{0.05}O$	250	-	20 to 1040	40 s	100 s	no	2019 [97]
$\beta - In_2S_3$	160	-	40 to 400	147	414	no	2022 [135]
InGaZnO	T_{Room}	-	1000 to 5000	80	120	no	2022 [136]

[a] unless otherwise stated; am.: amorphous; APTMS: aminopropyl trimethoxysilane; dec.: decorated; dop.: doped with; func.: functionalised by; ITO: tin-doped In_2O_3; IGZO: indium gallium ZnO; mod.: modified by; NiAl-LDH: nickel aluminide layered double hydroxide; NR: not reported; ODA: octadecylamine groups; PVA: polyvinyl alcohol; rGO: reduced graphene oxide.

Tab. 3.5: Summary of amperometric and optical absorption dissolved ozone sensors. [10]

method	sensing unit / material	T [°C]	λ [nm]	measurement range	t_{res} [s]	t_{rec} [s]	com. av.	year [reference]
amperometric	WE: BDD; RE: Pt; CE: Pt	25	-	0.185 - 740 µM	NR	NR	no	2017 [71], [92]
	WE: Au; RE: Au; CE: NR	26.4	-	0 - 5 $mg\,l^{-1}$	NR	1	yes	2020 [116], [137]
	WE: Au; RE: NR; CE: NR	26.4	-	0 - 3 $mg\,l^{-1}$	30	1	yes	2020 [116], [138]
	WE; RE; CE: NR	0 - 45	-	0.05 - 20 $mg\,l^{-1}$	15	NR	yes	2020 [139]
	WE: Au; RE: NR; CE: Ag	0 - 45	-	0 - 20 $mg\,l^{-1}$	50	NR	yes	2020 [140]
	WE; RE; CE: NR	0 - 50	-	0 - 200 ppb	60	NR	yes	2020 [141]
	WE: Au; RE: Ag; CE: Ag	-5 - 50	-	0 - 10 ppm	90	NR	yes	2020 [142]
	WE; RE; CE: NR	5 - 50	-	0 - 5 $mg\,l^{-1}$	30	NR	yes	2020 [82]
	WE; RE; CE: NR	0 - 40	-	0 - 5 $mg\,l^{-1}$	180	NR	yes	2020 [143]
optical absorption	photometer	25	190 - 900	0.05 - 9 $mg\,l^{-1}$	real-time		yes	2016 [127]
	fluorometer	15	ex.: 213 - 335 em.: 310 - 450	0 - 5 $mg\,l^{-1}$	real-time		yes	2017 [83]
	photometer	5 - 40	NR	0 - 150 $mg\,l^{-1}$	2	NR	yes	2020 [144]
	photometer[a]	NR	254	0 - 890 ppb	10	NR	no	2016 [87]
	photometer[a]	26.4	254	0 - 100 $mg\,l^{-1}$	20	10	yes	2020 [86], [116]

[a] preprocessing: gas stripping; com. av.: commercially available; em: emission; ex: excitation; NR: not reported; rec: recovery; res: response.

3.5 Conventional manufacturing of ozone sensors

The ozone sensors presented in Section 3.1 to Section 3.3 are fabricated with conventional fabrication methods. In the following, amperometric, impedimetric, and optical absorption sensors are the main focus. The schematics of these fabrication methods are depicted in Fig. 3.10. Hereafter, details about these conventional manufacturing methods are reported. Also, the maximum process temperature is provided, whenever reported by the cited publication, for the different manufacturing methods because the utilisation of flexible substrates is limited by high process temperatures, as they have the potential to cause damage to these substrates. Despite the challenges posed by high process temperatures, flexible substrates remain important due to their flexibility, light weight, and versatility, which enable their use in a wide range of applications with a compact design, such as biomedical devices. Amperometric ozone gas sensors in previous work were e.g. manufactured with WE, CE, and RE through screen-printing [65], [66] or with the sensing material potassium iodide polyaniline nanostructures through electropolymerisation at a maximum process temperature of 100 °C [130]. Amperometric dissolved ozone sensors are, e.g., made of BDD WE and Pt CE and RE, that are manufactured with the microwave plasma-assisted chemical vapour deposition process [71], [92]. For the fabrication of impedimetric ozone gas sensors, there is a wide range of different fabrication methods. For example, these sensors can be manufactured with hydrothermal synthesis with a maximum process temperature between 100 °C and 500 °C and sensing materials such as ZnO, $\mathrm{ZnOSnO_2}$, and V_2O_5/TiO_2 [72], [95], [101], [102]. Furthermore, these sensors can be manufactured with spin-coating using sensing materials such as $\mathrm{Co_xZn_{1-x}O}$, Au, ZnO, and $\mathrm{CH_3NH_3Pbl_{3-x}Cl_x}$ with maximum process temperatures between 80 °C and 500 °C [70], [98], [107], [109]. When using dip-coating to manufacture impedimetric ozone gas sensors, usually the sensing materials ZnO modified by nickel phthalocyanine, nickel aluminide layered double hydroxide, TiO_2-In_2O_3, and $\mathrm{rGo/WO_3}$ are applied with maximum process temperatures between 95 °C and 400 °C [74], [96], [103], [134]. For screen-printing these sensors, e.g., $\mathrm{In_2O_3}$ doped with $\mathrm{WO_3}$ and CNTs functionalised by octadecylamine groups are applied as sensing materials with maximum process temperatures of 100 °C [85] and 600 °C [105]. Furthermore, it is possible to manufacture impedimetric ozone gas sensors with spray-coating/spray pyrolysis and

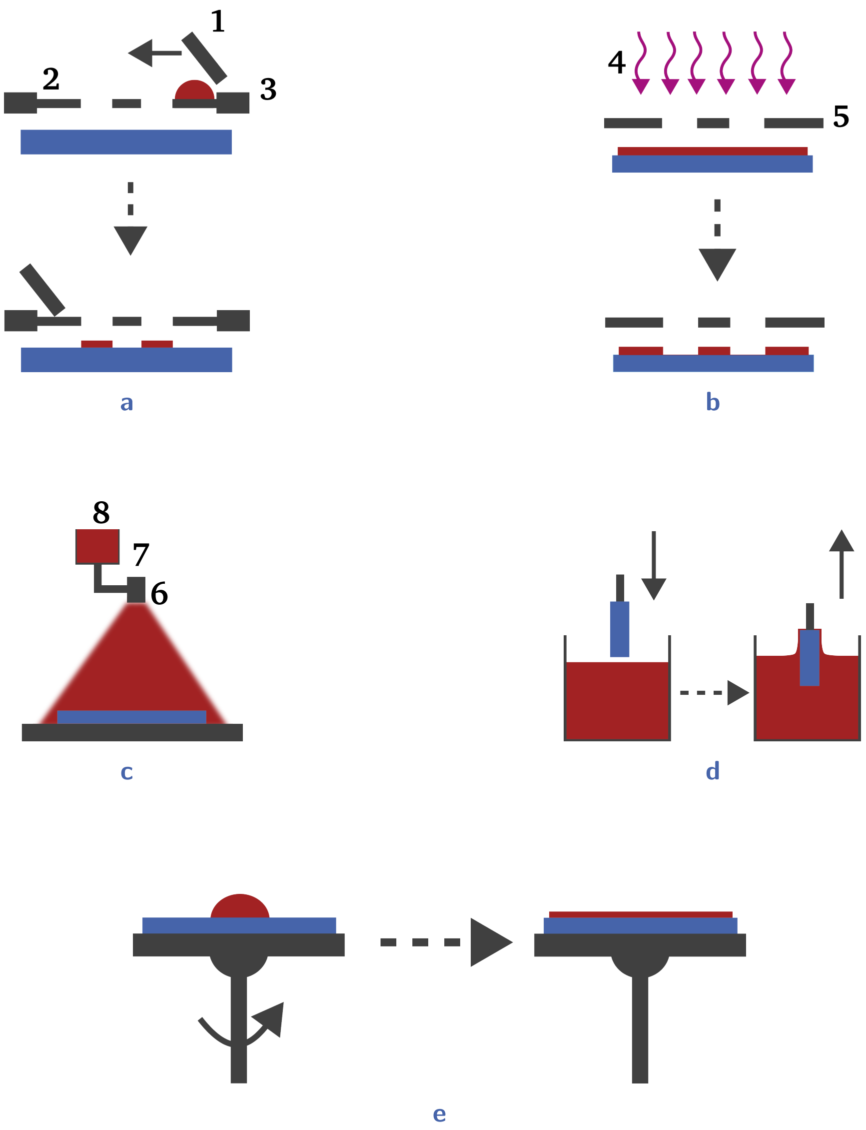

Fig. 3.10: Conventional fabrication methods for ozone sensors, whereby the ink or thin film material is depicted in red and the substrate in blue. (a) Shows the screen-printing process, including squeegee (1), mesh (2), and frame (3). (b) Depicts the UV photolithography process with UV light (4) and mask (5). (c) Explains the schematic of the spray-coating/spray pyrolysis process, including spray nozzle (6), gas input (7), and solution (8). (d) Shows the dip-coating/immersion process and (e) the spin-coating process. [10]

photolithography. For spray-coating/spray pyrolysis either CNTs (maximum process temperature is not reported) [104] or $Zn_{0.95}Co_{0.05}O$ (maximum process temperature of 300 °C) [97] are used as a sensing material. For the photolithography process, ZnO modified by Au (maximum process temperature of 95 °C) [93] or indium gallium ZnO decorated (processing at RT) [110] can be applied. Optical absorption ozone gas sensors can be manufactured, e.g., with dip-coating/immersion or radio frequency sputtering. During the dip-coating/immersion, sensing materials such as potassium iodide and α-cyclodextrin (maximum process temperature is not reported) [133], reduced graphene oxide/ZnO (maximum process temperature of 400 °C) [76], or methylene blue (maximum process temperature of 450 °C) [77] are applied. For the radio frequency sputtering process, the sensing material Ag-TiO_2 can be applied while having a maximum process temperature of 250 °C [111]. Photoluminescence ozone gas sensors with the sensing material cadmium selenide-based core-shell type quantum dots (CdSe/CdZnS, CdSe/ZnS, and CdSeTe/ZnS) can be manufactured via cast deposition (maximum process temperature is not reported) [78].

However, the presented conventional manufacturing methods are only suitable for rigid substrates that provide substrate planarity, such as Al_2O_3 or silicon wafers, rely on masks, stencils, or lithography processes for sensing structure definition, and require high process temperatures. The integration of a sensing element into medical or bioanalytical devices is an important requirement for the wider application of ozone therapy, but conformality to instrument shape may be necessary, rendering the aforementioned fabrication technologies unsuitable. Therefore, it is promising to investigate further manufacturing methods, such as inkjet-printing (IJP).

3.6 Inkjet-printed ozone sensors

Conventional fabrication methods for ozone sensors are spin-coating, dip-coating, screen-printing, UV photolithography, and spray-coating (see Section 3.5). Compared to the aforementioned fabrication methods, IJP is a digital printing process. Unlike screen-printing or UV photolithography, it does not require templates or masks, which reduces setup time and costs. The flexibility to print on flexible substrates and the ease with which the printing patterns can be modified make IJP superior to spin-coating, dip-coating, and spray-coating. Moreover, IJP may have the capability of printing ozone sensors directly onto syringe needles used in ozone therapy for herniated disks by attaching the print head or substrate, respectively, on a four-axis handling system. A further benefit of IJP over conventional methods is that it does not involve any direct contact. As a result, the substrate will experience less mechanical stress, and there will be fewer contamination sources, such as mask residue. There are two types of IJP: continuous IJP and drop-on-demand IJP [145]. Drops are only dispensed at the chosen target position in drop-on-demand IJP, as opposed to continuous IJP, where they are continually dispensed at a predetermined frequency [145]. In order to regulate the overall amount of material supplied to the target, drop-on-demand IJP, which is examined in the following, allows individual customisation of the drop size as well as the number of drops sent per trigger [145]. However, the ink and printer's initial expenses are high [146]. The schematics of the IJP process are depicted in Fig. 3.11. IJP is capable of depositing novel nanomaterials with a structural resolution of 50 µm or less on polymer substrates. However, to take advantage of these benefits, the printing process, ink and substrate materials, printing system, printed structure design, and post-processing need to be adapted to each other. For polymer substrates with low thermal stability, post-processing methods such as photonic sintering at low temperatures are recommended.

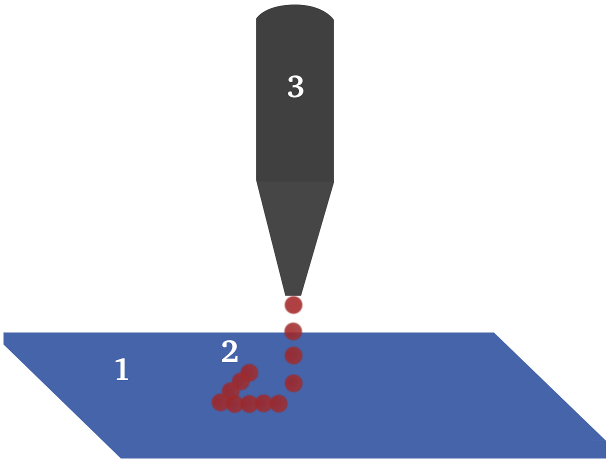

Fig. 3.11: Simplified schematics of the IJP process, including substrate (1), ink (2), and nozzle (3). [10]

Previous work [147] describes an approach for the methodical creation and validation of inkjet-printed electronic circuits with multiple layers, utilising a fully automated workflow from the design stage to the finished printed system. If the desired application requires flexibility of the printed structure, it is essential to optimise the adhesion between the printed layer and the substrate, as well as the morphology of the layers [148].

Currently, no inkjet-printed ozone sensors exist because flexible substrates and conformal sensors are not required for the applications of the ozone sensors reported in Section 3.1. Established thick film and thin film processes can be used to produce these sensors in large quantities. IJP shows potential for creating sensors for novel medical sensor applications that require conformal medical sensors on flexible substrates. The development of these sensors is essential for this purpose. Hereafter, inkjet-printed methods for electronic components that may potentially be applied to ozone sensors are presented. These methods can be adapted for developing an inkjet-printed ozone sensor.

The current approaches for creating inkjet-printed amperometric membrane-based sensors for oxygen or pH can be modified for use as ozone sensors by introducing a suitable membrane. These sensors typically involve inkjet-printed Au electrode arrays, or WE and CE made of AuNP ink, and RE made of AgNP ink. For instance, Hu et al. [73] developed an oxygen gas sensor using inkjet-printed Au electrode arrays on a cellulose membrane. Xu et al. [149] created a dissolved oxygen and pH sensor that is inkjet-printed using a three-electrode system on a Kapton film. Moya et al. [150], [151] explored different approaches, including printing electrodes on a paper substrate (thickness: 65 µm, porosity: 80%) or a polyethylene terephthalate (PET) substrate with different materials, such as SU-8, Ag, polyvinyl butyral, and sodium hypochlorite, to achieve a fully inkjet-printed solid-state Ag/AgCl RE. In the case of ozone sensors, PDMS is suggested as a suitable membrane material in Section 3.1.1. Wu et al. [152] proposed using inkjet-printed AgNPs as microelectrodes on PDMS for microfluidic sensing. Alternatively, membrane-free approaches for amperometric sensors can be implemented using BDD WEs [71], [92]. Laposa et al. [153] proposed an impedimetric gas sensor based on nanodiamond powder ink that combines IJP with the microwave chemical vapor deposition process, but further research is needed to enable boron-doping of the nanodiamond structure.

Several methods for IJP metal-oxide nanomaterials can be adapted as impedimetric ozone sensors. Rieu et al. [154] and Kassem et al. [155] explored tin dioxide-based inkjet-printed gas sensors. Rieu et al. [154] developed a nitrogen dioxide and carbon monoxide gas sensor that is fully inkjet-printed on a polymer substrate. Similarly, Kassem et al. [155] created a sensor on polyimide foil (sintered at 350 °C) that can measure carbon monoxide gas. Additionally, Spinella et al. [156] proposed a multilayer gas sensor that is based on ZnO. Other methods with inkjet-printed In_2O_3 semiconductor layers were described in previous work [157]–[159]. Leppäniemi et al. [157] optimised the IJP method of precursor solutions containing In_2O_3 for thin film transistors, which are annealed at low temperatures (150 °C to 200 °C) and with the use of UV exposure (160 nm). Moreover, Hassan et al. [158] proposed laser ablation and IJP to create a thin film transistor that is likewise based on In_2O_3 NP ink. The conductive ink channel resolution is increased using laser ablation, which leads to a decreased channel length [158]. Hong et al. [159] looked at how a field effect transistor performed at sensing humidity. CNTs are an additional choice for impedimetric ozone sensors. For thin film transistors, Kim et al. [160] reported inkjet-printed single-walled carbon nanotubes (SWCNT).

Photosensors and light activation are the foundation of optical absorption sensors. A wearable sensor with a response time of 0.3 s and an all-inkjet-printed ZnO photosensor on a Kapton substrate that measured at 370 nm was studied by Tran et al. [161]. An all-inkjet-printed photosensor that is based on Ag electrode material and ZnO semiconductor material was described by Kaufhold et al. [162]. The sensor is manufactured on a flexible polymer substrate and has a wavelength that is between 310 nm and 395 nm. Nahlik et al. [163] presented a photosensor based on inkjet-printed ZnO and diamond precursor ink with the highest photoresponsivity at 365 nm. According to the authors, the response time for the ZnO nanodiamond sensor is more than ten times higher than for a ZnO single-layered photosensor [163]. This finding is consistent with the results of Korotcenkov et al. [112], which suggest that optimising the sensing layer morphology can improve the sensor response. Figueira et al. [164] introduced another photosensor that is fully printed on a cork sheet and has a maximum sensitivity of 302 nm. The photosensor was printed using ZnO/ethylcellulose ink. Zhan et al. [165] provided a review of additional inkjet-printed photosensors and LEDs, which offer potential solutions for optical absorption sensors.

Han et al. [166] developed water-dispersible quantum dots for IJP of photoluminescence images that can be viewed under UV light. They optimised the printing process using these quantum dots. Additionally, Pan et al. [167] improved the process by using ethylene glycol with a high boiling point as a solvent to disperse the quantum dots, which prevented the coffee-ring effect.

The presented solutions can be transferred to the manufacturing of an IJP ozone sensor. Thus, the solutions have to be modified accordingly.

Part I

Referencing novel ozone sensors

Overview Part I

Reference systems or experimental setups are used to expose sensors to controlled environmental conditions and quickly ascertain their behaviour throughout a certain parameter range. By using reference systems as a standard against which to compare the performance of new sensors, researchers and developers can evaluate the accuracy, precision, and reproducibility of new sensors. Moreover, reference systems can be used to identify differences or anomalies in new sensor designs, leading to corrections and improvements in the new sensor's performance. Through advancements in reference systems, new and improved sensors can be established, leading to better ozone measurement and monitoring in various applications. Thus, the following part focuses on the investigation of the first research question (RQ) RQ1: How can novel dissolved and ozone gas sensors be references for their calibration, characterisation, and evaluation? While Chapter 4 focuses on ozone gas, Chapter 5 covers dissolved ozone. For each chapter, first the related work is provided, and then it is investigated whether a commercially available product already fulfils the requirements. Since there is not yet a commercially available product that meets all the requirements, novel reference systems have been developed. The used materials and methods, the final setup, and the evaluation are reported, and subsequently, the results are discussed.

4

Reference system for ozone gas sensors

Parts of this chapter are based on: L. Petani, D. Wickersheim, L. Koker, M. Reischl, U. Gengenbach, and C. Pylatiuk, “Experimental setup for evaluation of medical ozone gas sensors”, Sundsvall, Sweden: IEEE Sensors Applications Symposium (SAS), Aug. 1–3, 2022, pp. 1–6. DOI: `10.1109/SAS54819.2022.9881340`.

In the following, the state of the art is investigated regarding reference systems for ozone gas sensors. Currently, there is no reference system available that fulfils all essential requirements, which are shown in Tab. 4.1. It is important that the reference system be encapsulated in order to enable safe operation of the system. Thus, there should be no leakage of ozone into the surrounding air. Also, for the reference sensors, measurement of ozone gas up to $30\,\mathrm{mg\,l^{-1}}$ should be enabled. In-line measurement is necessary to allow continuous measurement. The response time of the sensors should be below 5 min. All sensors used should be suitable for an operating temperature of up to 37 °C. In order

Tab. 4.1: Overview of the most important requirements for a reference system for dissolved ozone sensors.

parameter	requirement
design	needs to be enclosed, no leakage of gaseous ozone into the air
range	ozone gas: up to $30\,\mathrm{mg\,l^{-1}}$
in-line	needs to be enabled for continuous measurement
response time	below 5 min
temperature	below 37 °C
selectivity	high selectivity against oxygen

to enable selective measurement of ozone, a high selectivity against oxygen is necessary. In the following, a reference system for ozone gas is developed. First, the used materials and methods are reported. Afterwards, the reference system, including its design, assembly, and calibration processes, is thoroughly described. An assessment of the reference system's performance, including its precision, accuracy, and repeatability, is also provided. The reference system is used to calibrate several kinds of ozone gas sensors and carry out ozone concentration measurements in various environmental scenarios to show the adaptability and usefulness of the reference system. Screen-printed sensors are evaluated as the initial application of this system. Moreover, a novel ozone-resistant adapter cable is presented that is designed for use with screen-printed amperometric sensors, which can be integrated into the reference system for the evaluation of novel sensors. Additionally, the performance of the adapter cable is evaluated, and its potential use in improving the sensitivity and stability of ozone gas sensors is demonstrated. Also, the results are discussed.

4.1 Related work regarding ozone gas reference systems

According to literature research, there is currently no reference system for ozone gas available that meets all the requirements listed in Tab. 4.1. However, there is still previous work available where ozone sensors have been evaluated. For example, Ghazaly et al. [77] tested ozone sensors at concentrations of up to 200 ppb ozone over a period of up to 200 min, using mass flow controllers to dilute the generated ozone mixture with purified air to obtain low concentrations of ozone. Pang et al. [129] utilise electrochemical ozone sensors that were calibrated with ultraviolet (UV) photometric sensors to monitor ozone concentrations between 10 ppb and 1000 ppb. Spinelle et al. [75] assess ozone sensors that monitor the gas at ppb levels. These sensors were commercially available and are based on metal oxide measurement. Furthermore, Klaus et al. [169] designed a measurement chamber with ozone sensors, measuring up to 220 ppb ozone. Nevertheless, ozone is present in higher concentrations during medical ozone therapy. This means that although the findings from previous work can be transferred to the presented reference system, the used sensors must encompass a substantially broader range of ozone concentrations.

4.2 Materials and methods

For the evaluation and realisation of the setup, the following materials, described in detail in previous work [168], are used: An ozone generator, supplied with medical oxygen, and an ozone destructor for the generation and reduction of ozone gas. Overall, the sensors utilised include two ozone sensors (one for detecting lower concentrations and one with a broader concentration range), an oxygen sensor, a nitrogen dioxide sensor, two sensors for measuring humidity and temperature, and two pressure sensors. The embedding of the reference system in the setup for the evaluation is shown in Fig. 4.1. The sensors are located inside a measurement chamber that is exposed to a gas mixture containing ozone. To maintain a consistent and adaptable temperature within the measurement chamber, it is submerged in a water bath.

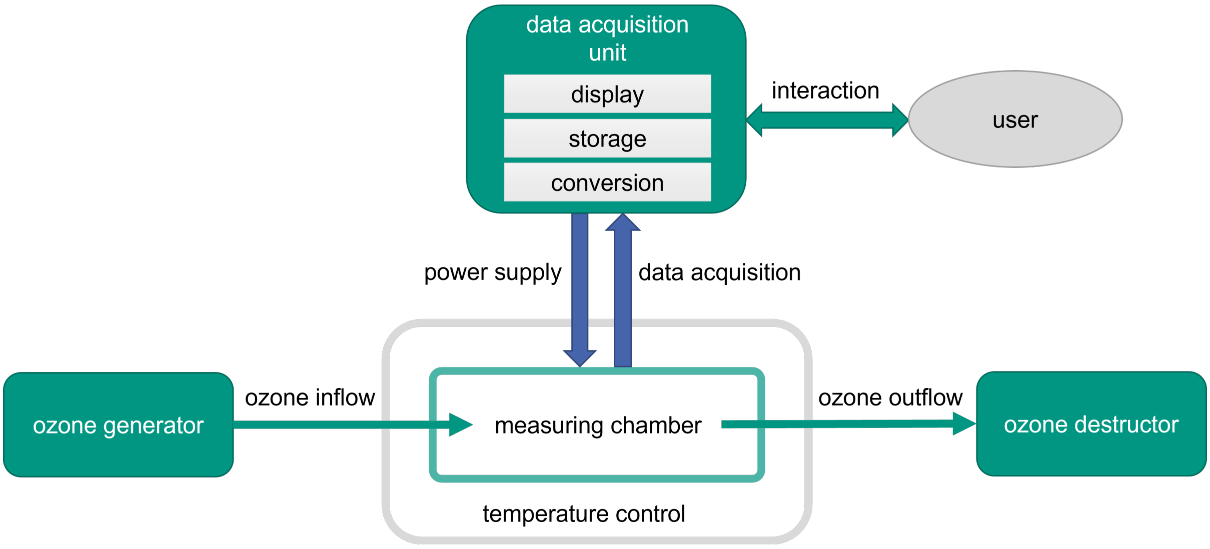

Fig. 4.1: Shows the reference system embedded within the setup for evaluation. The oxygen-ozone mixture is transferred from the ozone generator to the measuring chamber. The data acquisition unit is connected to the measurement chamber through a power supply. Users can operate the setup through a touch-screen interface. [168] © 2022 IEEE

The setup's data acquisition unit is important because it collects, processes, and transmits data from the sensors that are housed inside the measuring chamber. A power supply connects this device to the measurement chamber. Users interact with the system primarily through the touch-screen interface. Users can manage the experiment and monitor the measurements in real time. Overall, the setup is designed to efficiently and accurately assess the properties of the oxygen-ozone measurement substance, and the touch-screen interface offers a convenient way for users to control and monitor the experiment. Fig. 4.2 shows the measurement chain that connects the used sensors with the data acquisition unit and pre-processing steps.

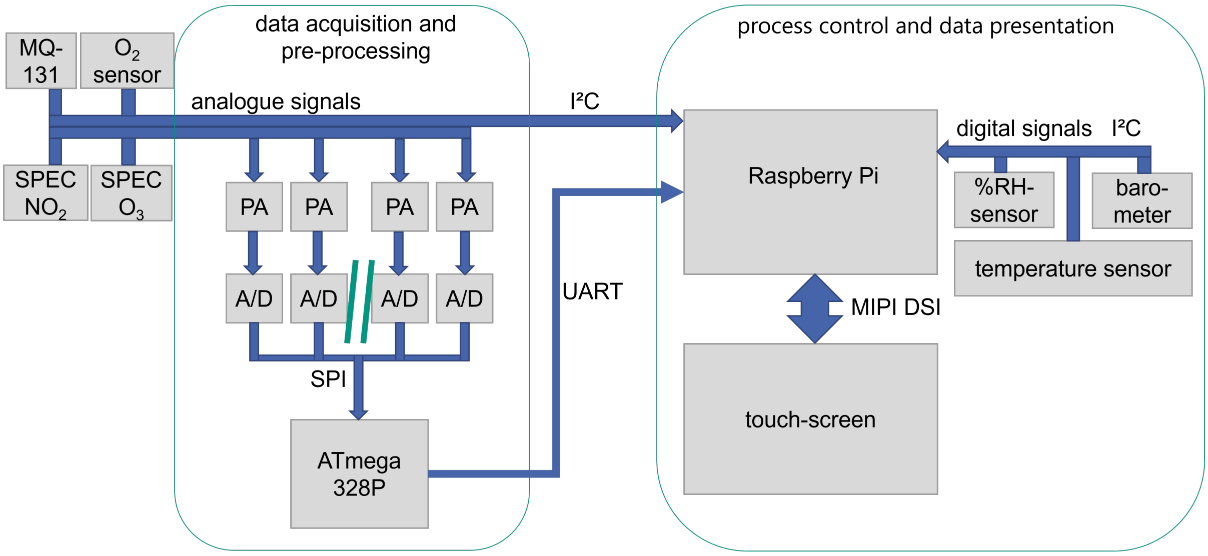

Fig. 4.2: Shows the measurement chain, which includes the process for obtaining, processing, and transmitting data from the used sensors to the Raspberry Pi. Thereby, data acquisition, pre-processing, process control, and data presentation are included. A/D stands for the analog digital converter (ADC), PA for pre-amplifiers, SPI for serial peripheral interface, I^2C for inter-integrated circuit, UART for universal asynchronous receiver-transmitter, and MIPI DSI for mobile industry processor interface display serial interface. The MQ-131 and the SPEC O3 represent the ozone sensors, and the ATmega 328P is the used micro-controller. [168] © 2022 IEEE

Furthermore, the measurement chain shows the connection between process control and the data presentation. The methods that are used for evaluating the reference system and the holder for the screen-printed electrodes are described in previous work [168]. In summary, the following methods are applied: Linear sweep voltammetry measurements are conducted to evaluate the holder for the screen-printed electrodes. Thereby, the designed holder is compared with commercial cables. Furthermore, for the evaluation of the reference system, the response time, temporal stability, and selectivity of the included sensors are calculated. In real-world situations, sensors often exhibit deviations from their ideal characteristic curve. To address this issue, calibration is performed by recording the characteristic curve at various points across the measuring range. A mapping function is then calculated based on the data obtained during calibration, which helps to compensate for any non-linearity exhibited by the sensor.

4.3 Setup of the proposed ozone gas reference system

The designed reference system, which may serve as a reference system for newly developed sensors, is shown in Fig. 4.3.

Fig. 4.3: Reference system for ozone gas measurement, including a glass gas chamber (1), holder (2) for screen-printed electrodes that can be evaluated with the setup, lid (3) with attached sensors and circulation fan that are used as reference, data acquisition unit with touch-screen (4), and connection between the screen-printed electrode holder and the potentiostat (5). [Image: Markus Breig, KIT]

4.4 Evaluation of the ozone gas reference system

The results for the evaluation are shown in Fig. 4.4 and Fig. 4.5. Fig. 4.4 shows the evaluation of the designed electrode holder. For the evaluation of the designed electrode holder, a voltammetric measurement is conducted. Thereby, a potential is applied, and the resulting current is measured. Three measurement series are conducted using both commercial and specially designed cables. Each series includes 410 measurement points for each cable, using a new screen-printed sensor for each measurement series. Although there are differences in the characteristic curves between the different screen-printed sensors, these discrepancies are attributed to variations in the sensors' condition rather than electromagnetic interference. For each of the 410 measurement points, the absolute difference between the current values of the designed and commercial cables is calculated, and the average difference is 0.17 µA. The standard deviation of the mean value is also calculated, with 1.16 µA for the designed cable and 1.31 µA for the commercial cable.

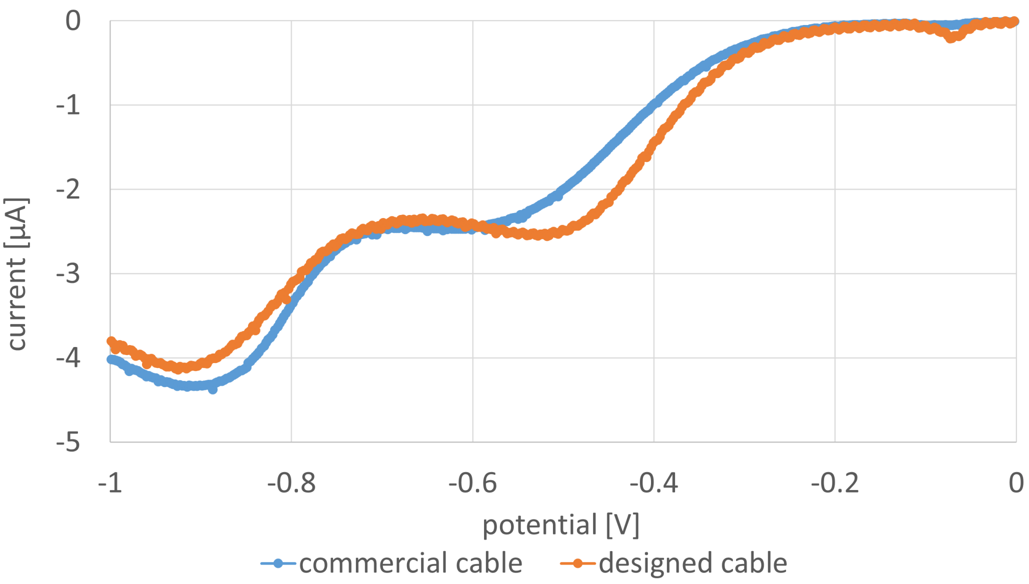

Fig. 4.4: A linear voltammetry sweep measurement was conducted using both commercial cables and cables specifically designed for ozone resistance. [168] © 2022 IEEE

Fig. 4.5 shows the results for the evaluation of the complete reference system. In the following, the results are described with regard to the measurement range, response time, temporal stability, and selectivity.

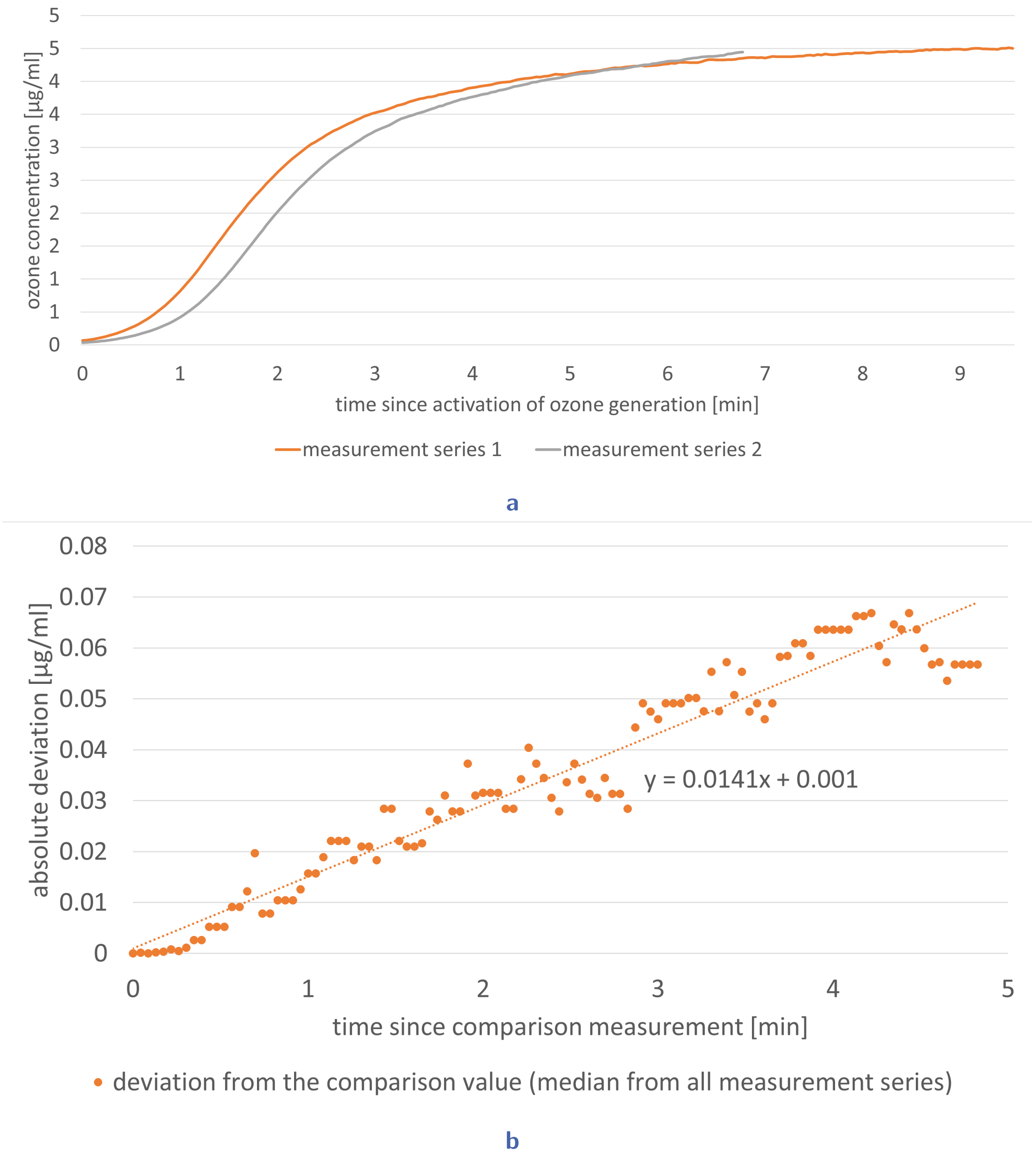

Fig. 4.5: **(a)** Assessment of the response time of the MQ-131 ozone sensor. [168] © 2022 IEEE **(b)** Evaluation of the temporal stability of the MQ-131 ozone sensor. [168] © 2022 IEEE

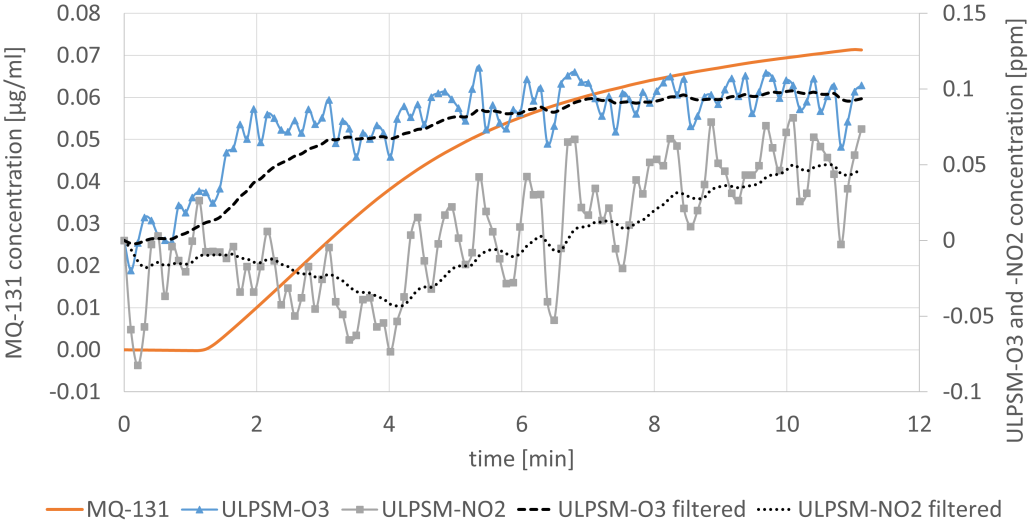

c

Fig. 4.5: **(c)** Examination of the response of different sensors to the introduction of pure oxygen into an air-filled measurement chamber, starting approximately 1 min after the start of the measurement series. All of these measurements provide data for the evaluation of the reference system. [168] © 2022 IEEE

The ULPSM-O_3 sensor saturates at its lowest configurable concentration, providing no information about concentrations outside the measuring range. The ULPSM-NO_2 has a membrane that reduces its sensitivity to ozone in order to measure NO_2 selectively but nevertheless saturates with the used ozone concentrations. The MQ-131 ozone sensor's linear correlation exceeds the manufacturer's specified range of up to $2.15\,\mathrm{mg\,l^{-1}}$ and reaches up to $5\,\mathrm{mg\,l^{-1}}$. Above $5\,\mathrm{mg\,l^{-1}}$, the correlation is no longer linear. A linear regression function yields a regression line with the following expression for the resistance y as a function of the ozone concentration x:

$$y = 3 \cdot 10^6 x - 6249.20. \tag{4.1}$$

As an estimate of the linearity of a characteristic curve, the coefficient of determination R^2 is determined, which is 0.98. The ME2-O_2 sensor saturates at low concentrations of pure oxygen gas and is unable to provide valid information. The MQ-131 ozone sensor is the only one suitable for detecting the targeted concentrations. Therefore, for the main evaluation, the MQ-131 ozone sensor is focused. The response time of the MQ-131 sensor is calculated using a total of 26 measurement points, resulting in 1.28 min±0.56 min. Deviations in response times may be caused by generator fluctuations, despite efforts to minimise their influence. Temporal stability is determined by measuring the ozone concentration during the past 5 min of a 15 min ozonation period. The MQ-131 sensor shows a drift of $1.41 \times 10^{-2}\,\mathrm{mg\,l^{-1}\,min^{-1}}$ over a period of 10 min. If a herniated disk is being treated with ozone, while the concentration is monitored with an ozone sensor, the oxygen-ozone injection time can be as short as 10 s to 15 s [7]. For injection times of 10 s to 15 s, the drift is negligible at $0.35 \times 10^{-2}\,\mathrm{mg\,l^{-1}}$. For the determination of selectivity, only oxygen is introduced. For this evaluation, the response of the following three sensors is compared: MQ-131, ULPSM-O_3, and ULPSM-NO_2. Low-pass filtering is applied to the ULPSM-O_3 and ULPSM-NO_2 sensors. The MQ-131 sensor shows less noise due to the lower resolution on the left y-axis. The two remaining curves on the graph are measured on the right y-axis. After one minute, oxygen flooding is initiated. The orange curve shows the immediate increase in oxygen, while the gray curve initially drops, likely due to the removal of nitrogen dioxide from the air, before increasing due to the initiated oxygen flooding. The blue curve follows the increase in oxygen and quickly reaches saturation. The ULPSM-O_3 sensor has a faster response time compared to the MQ-131 sensor. By the end of the experiment, the atmosphere is completely saturated with oxygen, which represents the worst-case scenario. In reality, oxygen values are much lower. After 10 min of oxygen introduction, the MQ-131 sensor measures a concentration of $0.07\,\mathrm{mg\,l^{-1}}$, the ULPSM-$O_3$ sensor measures 0.10 parts per million (ppm), and the ULPSM-NO_2 sensor measures 0.75 ppm. The MQ-131 sensor measures larger ozone signals compared to the ULPSM-O_3 sensor by a factor of 30.70, while the ULPSM-O_3 sensor measures larger ozone signals by a factor of 500 and the ULPSM-NO_2 sensor by a factor of 26.60. The cross-reactivity of the sensors with oxygen is minimal and can be disregarded, although the sensors are not entirely selective.

4.5 Discussion

A number of fundamental requirements are outlined in Tab. 4.1 in order to design a reference system for ozone gas sensors. The adequacy of the reference system is thoroughly evaluated against several criteria, and potential interferences, such as cross-selectivity, are investigated. Screen-printed sensors are used as an example to demonstrate the effectiveness of the setup. After examining the requirements, it is concluded that while some of these requirements have been effectively addressed, others need further focus and development. In the following, these results are summarised, compared to Tab 4.1, and discussed.

Enclosed design The enclosed design was implemented successfully. There is no leakage of gaseous ozone into the surrounding air, which otherwise may be inhaled by the operator.

Measurement range There is still further improvement necessary regarding the measurement range. The target is that ozone gas concentration measurements of up to $30\,\mathrm{mg\,l^{-1}}$ are possible. However, concentrations up to 1000 ppm ($\hat{=}10^6$ parts per billion (ppb) $\hat{\approx}$ $2.15\,\mathrm{mg\,l^{-1}}$) can be measured. Thus, the reference system expands previous research by allowing for measurements in the ppm range instead of the ppb range, which opens up possibilities for developing new micro-sensors in this previously unexplored measuring range.

In-line measurement The capability of in-line measurement for the reference system is realised. Thus, there is no need to take a sample, i.e., disruption of the continuous measurement process.

Response time The requirement for the response time is fulfilled because the used ozone sensor, MQ-131, provides a response time of 1.28 min±0.56 min.

Measurement temperature All included sensors are suitable for operating temperatures of up to 37 °C.

Selectivity against oxygen The requirement is met by the reference system, and there is a high selectivity of the reference sensors against oxygen.

In addition to the reference system, screen-printed electrode holders are presented. The evaluation shows that the electrochemical properties measured using the screen-printed electrode holder are not affected by increased noise or falsification compared to the adapter solutions provided by the manufacturer. The tests performed with the screen-printing electrodes show no increase in noise or distortion of the observed electrochemical properties compared to the proprietary adapter solutions of the manufacturer, Metrohm. The design of customised holders for electrodes on rigid substrates has the potential to speed up the development cycle of the inkjet-printed electrodes without complicating the acquisition of data due to electrical interference.

5

Reference system for dissolved ozone sensors

Parts of this chapter are based on: L. Petani, L. Wührl, L. Koker, M. Reischl, J. Renz, U. Gengenbach, and C. Pylatiuk, “Development of an experimental setup for real-time in-line dissolved ozone measurement for medical therapy”, *Ozone: Science & Engineering*, vol. 44, no. 5, pp. 499–509, 2022. DOI: `10.1080/01919512.2021.1932412`.

In the following, the state of the art is assessed regarding reference systems for dissolved ozone sensors. Since, after extensive literature research, there is currently no setup that meets all the important requirements presented in Tab. 5.1, a reference system is developed here. This reference system can be used for the calibration, evaluation, and characterisation of novel sensors. First, the used materials and methods are reported. Subsequently, the final setup is presented, evaluated, and the results discussed. Here, requirements for the reference system for dissolved ozone measurement are detailed. It is necessary to ensure the system is enclosed to prevent the operator from inhaling ozone gas. Additionally, any released ozone must be transformed into oxygen, which can be achieved, e.g., by using a catalytic reaction system. It is important to enclose the system to prevent ozone from reacting with the ambient air, which may speed up ozone decay. The reference sensor's measured concentration range must also include the range used in medical applications, which are explained in Chapter 2.1. Moreover, the reference system must enable in-line measurement. Thus, it is not necessary to take a sample and measure it in a different system while measuring in-line. This makes it possible to evaluate newly created sensors in the same sample that is used for the reference system. The second sample volume must either be removed or pumped into a second sample if the measurement is not in-line. These approaches result in more agitation, which accelerates the ozone's decomposition and alters the amounts in the two samples. The reference system needs to have a fast response and recovery time due to the short duration of the injection and ozone's half-life [7]. Optical sensors are a preferred choice for applications that require real-time monitoring. This is because they are not reliant on mass transport processes and reaction kinetics, unlike amperometric or impedimetric sensors. While optical ozone measurement is most suitable at the absorption peak of dissolved ozone at 260 nm [127], it is still advantageous to measure a broader spectrum instead of focusing on a single wavelength. Eliminating the need for flow is important because its presence can introduce additional agitation, accelerate ozone degradation, and lead to measurement inaccuracies. The reference system must be able to conduct measurements at 37 °C, which is the core body temperature. Furthermore, selectivity has to be provided. Also, the root-mean-square percentage error (RMSPE) should be below 10%.

Tab. 5.1: Overview of the most important requirements for a reference system for dissolved ozone sensors.

parameter	requirement
design	needs to be enclosed, no leakage of gaseous ozone into the ambient air
range	dissolved ozone: up to $70\,\mathrm{mg\,l^{-1}}$
in-line	needs to be enabled for continuous measurement
response time	real-time
recovery time	real-time
flow	should be avoided, otherwise ozone decay is accelerated
temperature	below 37 °C
selectivity	high selectivity against oxygen
RMSPE	below 10%

5.1 Related work regarding dissolved ozone reference systems

A system for referencing sensors for dissolved ozone should provide real-time, flow-free, and in-line ozone measurement. A literature and patent research revealed that either the sensors do not provide real-time measurement [116], [139]–[141], [143], [144], do require a flow [144], [170], or do require measurement with a sample in a separate system [81], [83], [116], [171]. Commercially available sensors provide the following accuracy values: For example, the Q46H/64 sensor (Analytical Technology, Collegeville, PA, USA) has an accuracy of 0.5% of the range or $0.02\,\mathrm{mg\,l^{-1}}$ (greater value) for a measurement range of $0\,\mathrm{mg\,l^{-1}}$ to $0.2\,\mathrm{mg\,l^{-1}}$, $0\,\mathrm{mg\,l^{-1}}$ to $200\,\mathrm{mg\,l^{-1}}$, or values in between [141]. The DO3 sensor (Eco Sensors, Santa Fe, NM, USA) has an accuracy of 20% for measurement values within the range of $0\,\mathrm{mg\,l^{-1}}$ to $2\,\mathrm{mg\,l^{-1}}$ [143], and the Model 470 (Teledyne API, San Diego, CA, USA) has a precision of $0.5\,\mathrm{mg\,l^{-1}}$ or 1% of the reading (greater value) for concentrations up to $150\,\mathrm{mg\,l^{-1}}$ [144]. The dissolved ozone sensor BMT 965 (BMT, Messtechnik, Stahnsdorf, Germany) has an accuracy of 0.4% of the measurement value plus an additional 0.1% of the range, within the range of $0\,\mathrm{mg\,l^{-1}}$ to $10\,\mathrm{mg\,l^{-1}}$, $0\,\mathrm{mg\,l^{-1}}$ to $150\,\mathrm{mg\,l^{-1}}$, or values in between [170]. At present, reference systems, including those examined in prior studies on dissolved oxygen measurement [172], [173] do not allow for ozone measurement. However, certain aspects of these previous reference systems, specifically those related to the mixture and delivery of the saturated solution, may be transferred. As a result, there is currently no reference system available for measuring ozone concentrations in-line, in real-time, and without requiring a flow, highlighting the need for further development in this area.

5.2 Materials and methods

To assess and realise the reference system, the materials outlined in previous work [14] are used. An ozone generator, medical oxygen, ultra-pure water, a disperser for ozonating water, and an ultraviolet (UV) spectroscopic sensor that measures between 200 nm and

360 nm and operates with a xenon lamp are applied. In the experiments, optical light path lengths of 5 mm and 10 mm are selected for the UV spectroscopic sensor. Furthermore, a colourimetric photometer with tube tests is applied to calibrate the UV spectroscopic sensor via N,N-diethyl-p-phenylenediamine (DPD) measurement. Therefore, a multi-point calibration is performed. The multi-point calibration involves both arithmetical dilution series and decay time calibration. For the arithmetical dilution, the sample is diluted in several steps until the ozone concentration is not detectable. For the decay time calibration, the sample is measured repeatedly until all the included ozone has decayed. To identify any outliers in the calculated data, obtained from both the arithmetical dilution series and calibration by decay time, the density-based spatial clustering of applications with noise (Dbscan) algorithm is utilised. This algorithm is applied using the scikit-learn Python module [174]. The Dbscan algorithm is applied with a maximum distance of $0.09\,\mathrm{mg\,l^{-1}}$ between any two samples in the same neighbourhood, and a minimum of two samples are required to form a neighbourhood. Once the outliers have been identified, a least-squares linear regression is used to establish the correlation between the spectroscopic sensor and colourimetric photometer. This involves optimising the following equation:

$$\mathrm{y_{fit,i}} = \mathrm{a} \cdot \mathrm{x_i} + \mathrm{b} \tag{5.1}$$

$$\min_{\mathrm{a,b}} \mathrm{Q(a,b)}, \quad \text{for } \mathrm{Q(a,b)} = \sum_{\mathrm{i=1}}^{\mathrm{N}} (\mathrm{y_i} - \mathrm{y_{fit,i}})^2 \tag{5.2}$$

Q represents the function to be optimised for the linear regression, with $\mathrm{x_i}$ denoting the data obtained from the colourimetric measurement and $\mathrm{y_i}$ representing the data obtained from the spectroscopic measurement. The total number of samples is represented by N, and the parameters a and b are adjusted to minimise the sum of squared errors. The calibration factor and slope for the linear regression function are determined by the values of a and b, which are equal to the intercept of the linear regression function. All plots generated in this process are created using the Python module Matplotlib [175]. To further confirm the accuracy of the measurement outcomes, the ozone decay curves with the UV spectroscopic sensor are compared to prior research conducted under the same conditions. The conditions for the decay curves involve using ultra-pure water with an unaltered pH value, maintaining a consistent temperature of either 20 °C or 30 °C, utilising an enclosed system without any agitation, and conducting pre-ozonation to break down easily oxidisable substances prior to the experiments, as detailed in [176].

Tab. 5.2 provides a summary of the experimental conditions. In the initial experiment, the colourimetric photometer is used to calibrate the UV spectroscopic sensor, and this process determines the final calibration factor that ensures precise measurements using the UV spectroscopic sensor. In the second experiment, measurements are taken by adjusting the water quality and temperature to match the conditions of a medical application as closely as possible. The third experiment focuses on the investigation of ozone decay curves to validate the results obtained from the colourimetric photometer calibration. Additionally, the relationship between the ozone concentration and the absorption at 254 nm and 258 nm is established for the ozone decay data, which can be used in future studies to convert absorption and concentration values. These wavelengths are chosen because, as shown in Fig. 3.7, there is the highest absorption peak in the absorption spectrum of ozone.

Tab. 5.2: Experimental conditions for the conducted experiments, such as the purpose of the experiment, the used water, the path length d, and the temperature T. [14]

purpose	water	d [mm]	T [°C]
calibration of the spectroscopic sensor	ultra pure	10	20
measurement with the parameters according to the medical application	bi-distilled	10	37
ozone decay curves	ultra pure	5, 10	20, 30

5.3 Setup of the proposed dissolved ozone reference system

Fig. 5.1a shows the complete reference system. The measurement module with the UV spectroscopic sensor mounted and the measurement chamber lid removed is presented in Fig. 5.1b. Polyvinyl chloride (PVC) is the material used to manufacture the measurement chamber due to its compatibility with ozone.

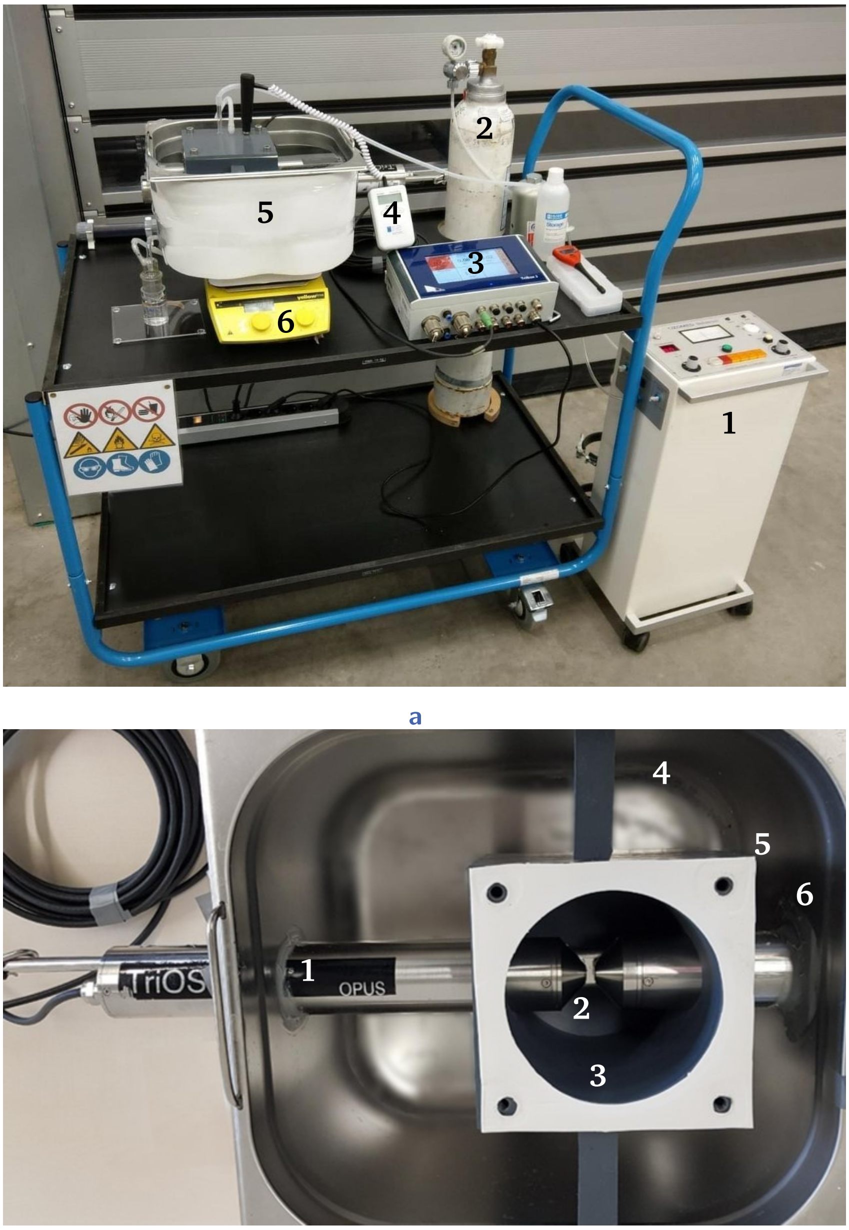

Fig. 5.1: **(a)** The configuration of the reference system comprises several components, such as an ozone generator (1), medical oxygen (2), sensor processing unit (3), temperature sensor (4), measurement module with a spectroscopic sensor and laboratory water bath (5), and a magnetic stirrer with heating plate (6). [14] **(b)** Top view of the measurement module, which consists of several components, such as the UV spectroscopic sensor (1), a measurement gap with adjustable light path length (2), the measurement chamber (3), a laboratory water bath (4), a silicone rubber sheet (5), and silicone sealant (6). [14]

5.4 Evaluation of the dissolved ozone reference system

The reference system can generate ozone concentrations up to 20.3 mg l^{-1} at 20 °C, while achieving higher concentrations requires an increased pressure or decreased temperature. Concentrations up to 21 mg l^{-1} can be measured with a light path length of 5 mm in the spectroscopic sensor. To measure higher concentrations, the light path length must be reduced to 2 mm, 1 mm, or 0.3 mm [177]. The presented spectroscopic sensor can, e.g., measure the theoretical concentrations of up to approximately 70 mg l^{-1} inside a herniated disk during ozone injection with a light path length of 2 mm and an absorbance at 258 nm below 1 absorbance units (AU) [177]. To calibrate the spectroscopic sensor, four measurement series are conducted, consisting of a total of 46 measurement points. Two series used arithmetical dilution (number one and two), and two used calibration by decay time (number three and four). Each measurement point included three consecutive values. The experiments showed that calibration by decay time was more effective than calibration by dilution because the additional motion during dilution accelerated the decay, leading to measurements being obtained at wider intervals. The average interval between two consecutive values of the colourimetric photometer for measurement series one to four was 0.184 mg l^{-1}, 0.196 mg l^{-1}, 0.15 mg l^{-1}, and 0.082 mg l^{-1}, respectively. A light path length of 10 mm was used for calibration. The mean value of the absorption signal at 360 nm was calculated with three values for each measurement point. Fig. 5.2 displays the linear regression used for calibration. The intercept is set to zero since both the colourimetric and spectroscopic sensors return zero for an ozone concentration of 0 mg l^{-1}. The slope of the linear regression is 6.486, which is also the final calibration factor. The standard error for the slope is 0.035, the correlation coefficient (R-value) is 0.998, and the two-sided p-value is smaller than 0.001 (null hypothesis: slope is zero, utilising the Wald test). The RMSPE between UV spectroscopic measurement and colourimetric photometer ground truth is 8.2% with the final calibration factor. The fifth measurement series is conducted to align the parameters with the medical application. The temperature is raised to 37 °C to match the core body temperature, and bi-distilled water is used instead of ultra-pure water, which has fewer reaction partners for ozone [45]. The light path length of 10 mm is used, and the series included eight measurement points, with each point consisting of three consecutive values. The final

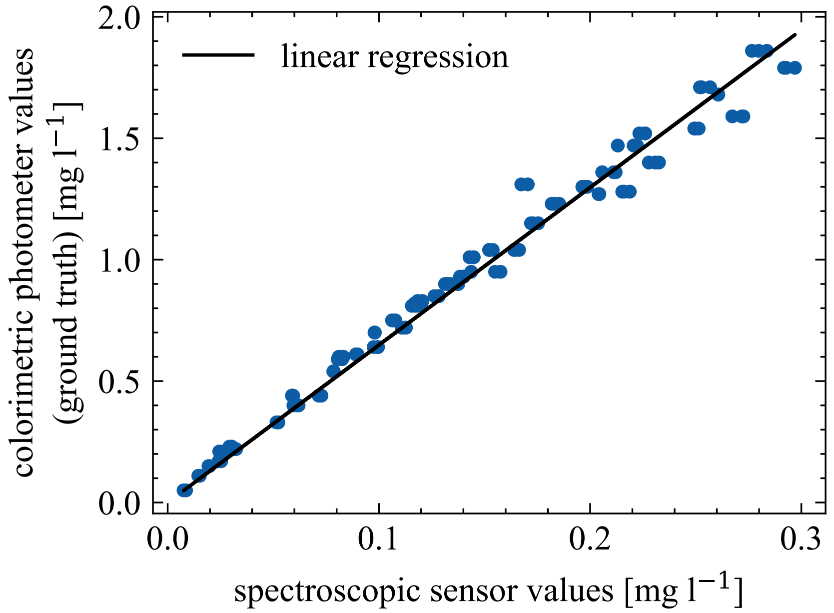

Fig. 5.2: A linear regression is performed to establish the correlation between the spectroscopic sensor and colourimetric photometer. The data used for this regression is obtained after outlier detection, carried out using the Dbscan algorithm. The resulting data is presented in the form of blue markers, while the linear regression with an intersection set to zero is illustrated by a black line. [14]

calibration factor is used to calculate the RMSPE, which is 6.054%, slightly lower than the RMSPE for the first four measurement series. To study ozone decay curves, the third experiment uses a calibrated spectroscopic sensor and is conducted under conditions similar to previous work [176]. The experiment uses ultra-pure, pre-ozonated water, the temperature is kept constant at either 20 °C or 30 °C, and the system is enclosed with no stirring. The first and second measurement series of the decay curves are performed at 10 mm for the light path length and at 20 °C. The third and fourth measurement series are performed with a light path length of 5 mm and at 20 °C. The last two measurement series, number five and six, are conducted with a light path length of 5 mm and at 30 °C. These decay curves are depicted in Fig. 5.3a. The relation between ozone concentration and absorption at wavelengths of 254 nm and 258 nm is established using the ozone decay curve data. The resulting relationship for absorption at 258 nm is presented in Fig. 5.3b.

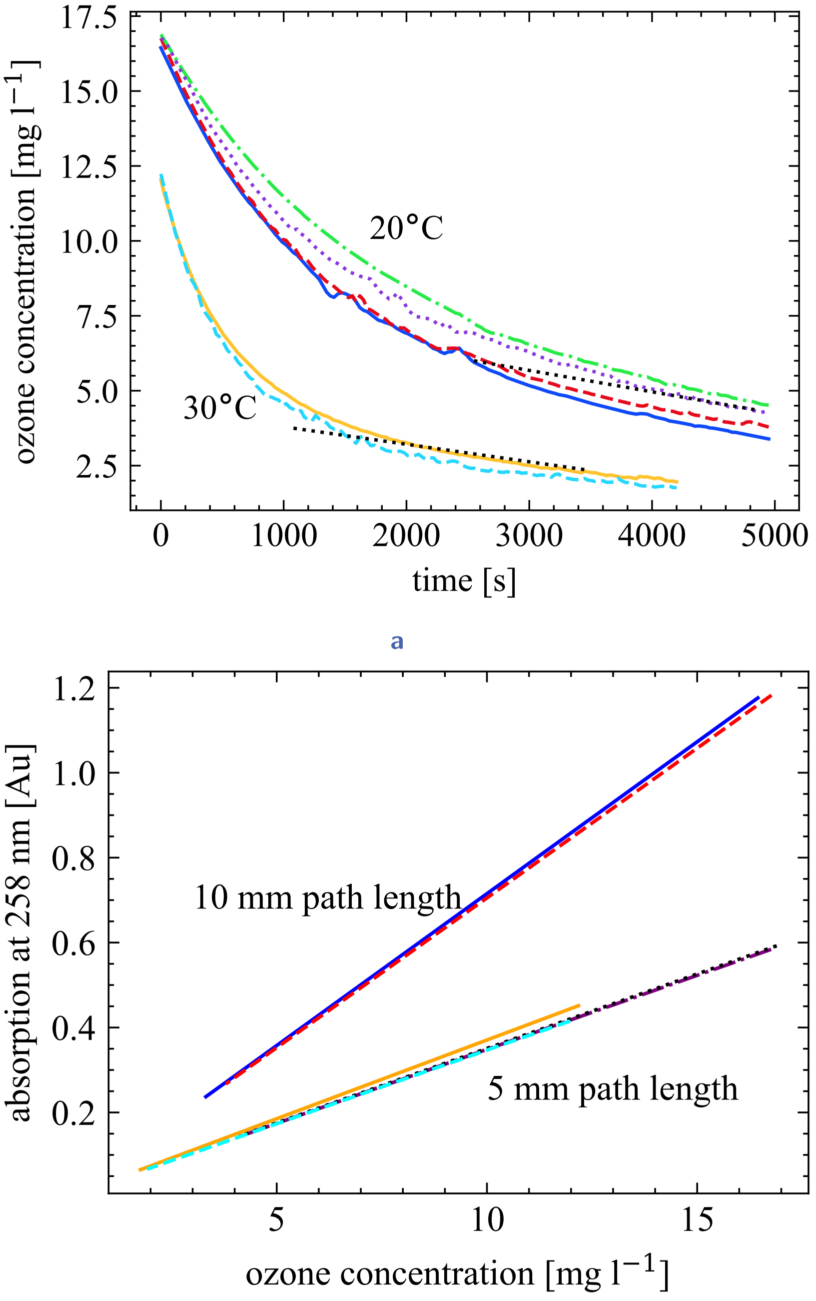

a

b

Fig. 5.3: **(a)** Shows the decay curves of ozone. The curves plotted in the upper part (blue solid, red dashed, purple dotted, and green dash-dotted) are obtained at 20 °C, while the two curves in the lower part (yellow solid and light blue dashed) are obtained at 30 °C. The black dotted lines show the curves obtained in previous research [176]. [14] **(b)** Displays the relation between ozone concentration and absorption at 258 nm. The upper curves (solid blue and dashed red) are obtained with a light path length of 10 mm, and the lower curves (dotted black, dash-dotted purple, dashed light blue, and solid orange) with 5 mm. [14]

All of the curves in Fig. 5.3b have an intercept set to zero, which leads to different slopes for the absorption at 258 nm. The first and second measurement series, conducted with a light path length of 10 mm and at 20 °C, have slopes of 0.072 (blue solid line) and 0.071 (red dashed line), respectively. For measurement series three and four, which are conducted with a light path length of 5 mm and at 20 °C, the slope is the same for both at 0.035 (black dotted and purple dash-dotted line). The last two measurement series, number five and six, conducted with a light path length of 5 mm and at 30 °C, have slopes of 0.035 (light blue dashed line) and 0.037 (orange solid line), respectively. For the absorption at 254 nm, the slopes for measurement series one to six are respectively 0.068, 0.067, 0.033, 0.033, 0.033, and 0.035.

5.5 Discussion

To develop a reference system for dissolved ozone sensors, various essential requirements are listed in Tab. 5.1. After reviewing the requirements, it is concluded that while some of them have been successfully met, others need further research. The results are summarised, compared to Tab. 5.1, and discussed hereafter.

Enclosed design The requirement to achieve an enclosed design is fulfilled since the measurement chamber provides a lid and is sealed with a silicone rubber sheet.

Measurement range The target is to enable measurements for ozone concentrations of up to 70 $\mathrm{mg\,l^{-1}}$. With the presented reference system, only ozone concentrations of up to 20.3 $\mathrm{mg\,l^{-1}}$ can be generated. To generate higher ozone concentrations, the ozonation process requires increased pressure or a decreased temperature. This can currently not be provided by the presented reference system. However, measurement of 70 $\mathrm{mg\,l^{-1}}$ should be possible theoretically with the reference sensor when using a path length of 2 mm while still achieving absorbance values below 1 AU.

In-line measurement In-line measurement is possible with the reported reference system. All sensors, reference sensors, and novel sensors measure continually in the same measurement substance.

Response and recovery time The reference sensor used is based on the optical absorption measurement principle, so real-time measurement is possible.

Flow For the applied reference sensor, no flow is necessary in order to ensure operation.

Measurement temperature This requirement is fulfilled because it is possible to conduct measurements at 37 °C.

Selectivity against oxygen Since the used reference sensor is based on the optical absorption principle and measures at wavelengths between 200 nm and 360 nm, selectivity against oxygen is ensured.

Root-mean-square percentage error The spectroscopic reference sensor and colourimetric photometer measurements have a low RMSPE of less than 8.2% when compared. Thus, the target of being below 10% for the RMSPE is fulfilled. The data also shows high linearity with a R-value of 0.998, and even with repeated measurements on the same sample, there is no significant scattering or change in colourimetric ozone concentration within the display and measuring accuracy of $\pm 0.01\,\mathrm{mg\,l^{-1}}$. The ozone decay curves obtained with the spectroscopic sensor calibrated with the colourimetric photometer are consistent with previous research [176]. The RMSPE between measurement series one to four and previous research at 20 °C is 11.001%, while for measurement series five and six at 30 °C the RMSPE is 10.995%. To further assess the system, calibration with iodometric titration or the indigo method may also be performed.

Part II

Biocompatibility of medical ozone sensors

Overview Part II

For medical sensors, biocompatibility is essential for their utilisation. This must be taken into account during the entire design process in order to prevent harm to the patient during the treatment. The term "biocompatible" refers to a sensor that does not cause an adverse reaction in the body, such as an allergic or toxic reaction. Several amperometric and impedimetric sensors, including acetone, glucose, sweat lactate, and ozone sensors, are made from the same or overlapping material sets. These sensors are often produced by screen printing [178], chemical gold plating [179], or metal evaporation. In general, such sensors can be made using additive process steps with organic and printed electronic (OPE) technologies. Inkjet-printing (IJP) is a substitute for conventional manufacturing. It provides a wide range of manufacturing process flexibility. Layouts are easily adaptable, and IJP is a cutting-edge technology that leads to low-waste and low-cost production [180]. Here, the biocompatibility of materials for exemplary IJP amperometric, impedimetric, and optical absorption ozone sensor structures is assessed. Thus, the following part focuses on the foundation of research question (RQ) RQ2: How can novel dissolved and ozone gas sensors be realised as electrochemical or optical sensors? Therefore, each material is assessed with regard to the international standard ISO 10993 [181]. According to the assessment, an amperometric sensor made of gold and silver nanoparticle (NP) inks, inkjet-printed on an polydimethylsiloxane (PDMS) membrane, and passivated with SU-8 ink gives the maximum biocompatibility. Moreover, biological characterisation studies are necessary to certify the biocompatibility for the specific medical application. From this investigation, the conclusions about biocompatibility can also be transferred to other sensors built of the same materials but intended for different purposes. This is applicable for sensors that measure glucose, oxygen, pH, sweat lactate, hydrogen peroxide, and acetone and use the same or an overlapping set of materials.

6

Biocompatibility of medical ozone sensors

Parts of this chapter are based on: L. Petani, V. Wehrheim, L. Koker, M. Reischl, M. Ungerer, U. Gengenbach, and C. Pylatiuk, "Systematic assessment of the biocompatibility of materials for inkjet-printed ozone sensors for medical therapy", *Flexible and Printed Electronics*, vol. 6, no. 4, p. 043 003, 2021. DOI: `10.1088/2058-8585/ac32ab`.

Medical devices can be grouped into three types based on their health risk, according to the European Commission of Health and Consumers for the European Union, the Health Risk Assessments of the Food and Drug Administration (FDA) for the United States of America, and the National Medical Product Administration for China. The groups range from low-risk (group I) equipment like bandages and wheelchairs to high-risk (group III) devices like pacemakers, cardiac catheters, and hip replacements [182]. According to the European Commission of Health and Consumers, group IIb, which includes brief contact with bodily fluids, is where ozone sensors for oxygen-ozone injection are classified.

There are various methods to achieve biocompatibility, including encapsulating the sensor, using only biocompatible materials, and coating the medical device with anti-inflammatory chemicals. Membranes (porous or non-porous) can be used for encapsulation; however, hydrogels are more frequently used in medical devices [183]. Anti-inflammatory drugs can be applied to the surface of a medical device to reduce inflammation in the body, or they can be injected into the encapsulation, such as acetylsalicylic acid (e.g. aspirin) or glucocorticoids (e.g. dexamethasone) [184], [185]. According to ISO 10993 [181], the properties shown in Fig. 6.1 for functionality and biocompatibility must be evaluated for the sensor and production process.

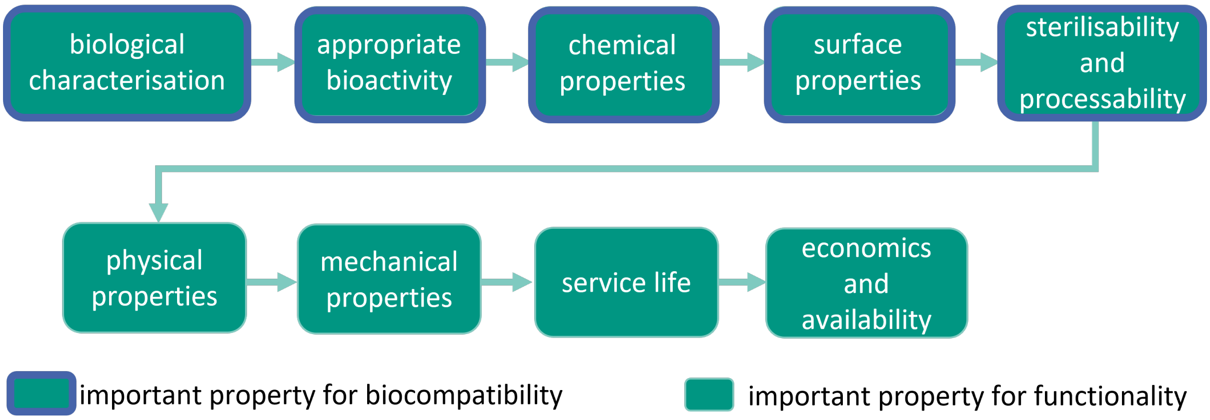

Fig. 6.1: According to the international standard ISO 10993 [181], the properties of materials are listed in descending order of relevance for biocompatibility. A blue frame denotes the key biocompatibility factors. The impact on biocompatibility of criteria that aren't in a blue frame is minor. [12]

The critical elements for biocompatibility are described in the following: To characterise a material biologically, it is researched how it behaves in a living biological environment [186]. As a result, biological characterisation tests must be carried out, with the tests varying depending on the type of interaction and duration of contact with the bodily tissue. In the here-focused application, the single-use sensor comes into brief contact with the intervertebral disk tissue but not with blood from the circulatory system [7]. This leads, in accordance with ISO 10993 [181], to group assignment 2A, from which the necessary tests are deduced. An extra hemocompatibility test is necessary if the sensor makes additional contact with the circulatory system's blood. For the focused application, the finished sensor must pass the following tests under ISO 10993 [181]: cytotoxicity, sensitisation, irritation and intracutaneous reactivity, pyrogenicity, and acute systemic toxicity.

Using cytotoxicity tests, researchers can determine how a substance affects nearby cells [181]. These can be carried out in-vitro and are the initial stage in determining a material's biocompatibility. To ascertain the likelihood of allergic reactions, sensitisation tests are used [181]. These tests must be carried out in-vivo. To assess the local response of tissue, irritancy and intracutaneous reactivity tests are required [187]. In order to conduct these tests, it is necessary to have information about the application method and the duration of contact [181]. Only pure compounds can be tested in-vitro; the finished sensor cannot. A medical device's irritability and intracutaneous reactivity are examined for the final sensor in-vivo [181]. Pyrogenicity tests determine whether substances cause inflammatory responses in the body [181]. In-vitro and in-vivo tests for the materials are therefore required. Investigations into acute systemic toxicity are also necessary. Systemic toxicity studies look at how a toxic chemical spreads from its source of entrance to different areas of the body where it can cause cell damage. Since a living organism must be used to simulate the system, in-vivo testing is the only way to determine a substance's systemic toxicity. All testing must be carried out on all utilised materials.

The appropriate bioactivity examines how the substance reacts with the host and can be categorised as toxic, biotolerable, bioinert, bioactive, and degradable [186], [188]. The sensor needs to be non-toxic and bioinert for the focused application. The sensor also needs to be biodegradable or at the very least recyclable, because it is a disposable product and thus has a major effect on the environment.

Chemical property characterisation is vital for determining biocompatibility and can be used in conjunction with biological testing. Further reducing the number of in-vivo tests is possible by applying the characterisation of the chemical characteristics to detect discrepancies between existing and newly developed devices [189]. Each manufacturing component, the material's composition and physical structure, and the interactions between the material and biological fluids or tissues must be identified in order to carry out the characterisation.

In order to determine the biocompatibility, it is also necessary to analyse the surface properties because surface alterations (surface oxidation or coating) affect how a material interacts with a biological system and, consequently, its biocompatibility [188], [190]. This comprises describing a material's surface tension, wettability, and surface roughness [186].

The sterilisability and processability of medical equipment are also fundamental. Because the material's surface and properties may change during sterilisation, its biocompatibility may be affected [191]. The sensor should ideally be created in a sterile environment to reduce any potential for pathogen interaction.

6.1 Structure and materials of ozone sensors

An overview of materials used for substrates, membranes, and the main components of amperometric, impedimetric, and optical sensors is shown in Tab. 6.1 and Tab. 6.2.

Tab. 6.1: Overview of the materials in previous work for the electrodes, light activation or heating element, and sensing material of ozone sensors. Thereby, amperometric, impedimetric, and optical absorption sensors are considered. (Modified according to [12])

amperometric	impedimetric		optical
Au [131], [192]	Au [93], [102]	Ti [98]	ZnO [76], [193]
Pt [131], [192]	Ag [93], [102]	Cu [85]	PEDOT:PSS [165]
Ag/AgCl [151]	Pt [93], [102]	SnO_2 [194]	
BDD [71], [92]	InGaN [195]	WO_3 [75]	
Ag [131], [192]	CNTs [196]–[198]	ZnO [95]	
	In_2O_3 [199]	ITO [110]	

Tab. 6.2: Overview of the materials in previous work for the substrate and membrane of ozone sensors based on the amperometric, impedimetric, and optical absorption measurement principles. (Modified according to [12])

substrates		membranes
Al [200]	PDMS [201], [202]	Al_2O_3 [74], [88]
Al_2O_3 [74], [88]	PVC [131]	ZrO_2 [88]
glass [70], [133], [200]	PVA [203]	PDMS [201], [202]
quartz [110], [204]	PTFE [150]	PTFE [150]
SiO_2/Si [95]	PMMA [205]	PVDF [89]
Si [206], PI [207]	PET [131]	

Suitable materials are required for the electrodes, substrate, membrane, passivation, and electrolyte in amperometric dissolved ozone sensors. Most electrodes are made of precious metals like gold, silver, and platinum or are made of metal and non-metal combinations like AgCl for reference electrodes (REs) or BDD for working electrodes (WEs) [71], [92], [131], [151], [192]. For the substrates, Al, glass [70], [133], [200], quartz [110], [204], Al_2O_3 [74], [88], Si [206], borosilicate wafers [173], SiO_2/Si [95], or fused silica [173] are used. Also, for the substrate, polymers like PET [131], PI [207], PVC [131], PMMA [205], PTFE [150], PVA [203], or PDMS [201], [202], [208] are applied. The here-focused application necessitates a flexible substrate since it allows the sensor to be integrated onto an injection syringe's needle. A membrane is required for amperometric sensors to ensure selective measurement. A substance that serves as both a substrate and a membrane is therefore recommended. For the membrane, a variety of materials, including ZrO_2 [88], Al_2O_3 [74], [88], PTFE [88], [89], [150], PDMS [209], or PVDF [89], are used. Here, PDMS is preferable because it can be processed with IJP [201] and has a gas permeability for ozone that is four times greater than that of oxygen [209]. For the passivation, SU-8 is a regularly used passivation ink [150], [210]. Moreover, the electrolytes potassium nitrate (KNO_3), potassium sulfate (K_2SO_4), and sodium chloride (NaCl) are widely used in amperometric sensors.

Impedimetric sensors require various components, including electrodes, made of Cu [85], Ti [98], ITO [110], or noble metals [93], [102], a sensing material, such as WO_3 [75], SnO_2 [194], ZnO [95], CNTs [196]–[198], or In_2O_3 [199], a substrate and membrane (similar to those used in amperometric sensors), and a heating or light activation element. The heating or light activation elements are made of materials with good thermal conductivity. Thus, the same materials as for the electrodes can be used. The light activation element can be made of aluminium gallium nitride (AlGaN) [211], InGaN/gallium nitride (GaN) [212], or InGaN [195]. The same materials that are used for optical ozone sensors can be selected for the light activation components of impedimetric sensors.

Optical sensors typically include a photosensor with a sensing component and a light source. The glass or quartz substrate that serves as the foundation for the photosensor with sensing material is covered by the sensing material. For sensing substances, methylene blue [77], ZnO [76], or PEDOT doped with PSS forming PEDOT:PSS [165], [213] are used.

In order to categorise currently used materials, a toxicity rating is necessary. Tab. 6.3 presents a toxicity rating for rats based on single oral doses using lethal doses (LDs) [214]. The individual biocompatibility of the materials in Tab. 6.4 is examined in the following. They are used for ozone sensors that measure with the amperometric, impedimetric, and optical absorption measurement methods.

Tab. 6.3: Overall rating of toxicity for rats following administration of single oral doses. Modified according to [214]. [12]

rating	description	LD_{50} [mg kg^{-1}]
1	extremely toxic	≤ 1
2	highly toxic	1-50
3	moderately toxic	50-500
4	slightly toxic	500-5000
5	practically non-toxic	5000-15000
6	relatively harmless	>15000

Tab. 6.4: Materials of assessed amperometric, impedimetric, and optical dissolved ozone sensors. [12]

component	amperometric	impedimetric	optical
electrodes	Au and Ag NP inks	Pt	NA
sensing material	NA	In_2O_3	ZnO
substrate	PDMS	Al_2O_3	ZnO
membrane	PDMS	PDMS	NA
passivation	SU-8	NA	NA
electrolyte	KNO_3, K_2SO_4, and NaCl	NA	NA
heating element	NA	Pt	NA
light activation	NA	InGaN	InGaN

NA: not applicable.

Amperometric sensor The examined sensor is based on a previously published oxygen sensor [215] and can be made using IJP. The sensor reacts to all oxidising substances, but selective measurement for ozone can be enabled by a suitable membrane. The selection of inks for the WE and counter electrode (CE) includes an gold nanoparticle (AuNP) ink (Au-LT-20 by Fraunhofer IKTS, Germany) and a silver nanoparticle (AgNP) ink (DGP 40LT-15C by ANP, Korea) for the RE. The SU-8 ink (XP PriElex SU-8 1.0 by MicroChem, USA) is chosen for passivating the electrodes. In addition, PDMS (Sylgard 184 Elastomer Kit by Dow Corning, USA) is utilised for the membrane and substrate. Also, the following electrolytes are investigated: KNO_3, K_2SO_4, and NaCl.

Impedimetric sensor The assessed sensor is an impedimetric dissolved ozone sensor that can be manufactured using IJP. It is based on a conventionally manufactured ozone sensor and consists of an Al_2O_3 substrate, an In_2O_3 sensing material, and Pt for the electrodes and the heating element [216]. The sensor includes a PDMS membrane, and InGaN is studied as a light activation element. A water-based platinum nanoparticle (PtNP) ink (PT-LT-20 by Fraunhofer IKTS, Germany) is assessed.

Optical absorption sensor The investigated optical absorption sensor is based on ZnO as the sensing material and InGaN as the material for the light-emitting diode (LED) [193], [217].

Tab. 6.5 displays a summary of the toxicity of the materials listed in Tab. 6.1 and Tab. 6.2. The amount of a chemical consumed that results in death of 50% of a sample set is known as LD_{50}. To assess toxicity in various species, such as mice, rats, or rabbits, various techniques, e.g. oral, inhalation, or skin contact (dermal), are applied. Rats were the main emphasis of the table, with oral being the only value accessible for practically all materials. The adjustments to the NPs size, shape, surface charge, and composition also impact how hazardous they are [218].

6.2 Biocompatibility in the context of inkjet-printing

Inks that are applied for IJP contain NPs that are included as functional solvents and components for enabling the printing process. After drying and curing, the solvent is removed, and the NPs agglomerate forms on the substrate surface. The resolution of IJP is just average at 10 µm to 50 µm, compared to gravure printing and photolithography. However, the waveform used during IJP can be used to alter the drop size [247]. Specialised inkjet-printers, such as electrohydrodynamic inkjet-printers or micro-plotters, are required when greater resolutions of 1 µm are required [248]–[251]. The substrates and inks used must be compatible with the IJP process. The sintering temperature is a variable that must be adjusted between the substrate and the ink. The substrate's glass transition or melting temperature may be exceeded by the high sintering temperatures needed to create a coherent porous NP layer, which may be necessary for some inks.

Tab. 6.5: Summary of the toxicity for the material listed in Tab. 6.1 and Tab. 6.2. [12]

material	LD$_{50}^{a}$ [mg kg^{-1}]^{a}	conditions	toxicity rating	ref.
Ag	280	rats, oral	3	[219]
	800	rabbits, oral	4	
AgCl	> 5000	rats, oral	5	[220]
Al	1000	oral	4	[221]
Al_2O_3	> 2000	rats, oral	4	[222]
Au	> 2000	rats, single dose, 10-50 nm NPs	4	[223]
BDD	NR	NR	NR	[92]
CNTs	> 5000	single-wall CNTs	5	[224]
Cu	30 (LD$_{100}$)	rats, copper sulphate	-	[225]
	10-20 g (LD)	humans, copper sulphate		[226]
glass	NR	NR	NR	[70]
InGaN	NR	NR	NR	[195]
In_2O_3	396	mice, oral	3	[227]
ITO	> 10000	rats, oral	5	[228]
PDMS	> 4800	rats, oral	4	[229]
PEDOT	650	oral	4	[230]
PSS	> 8000	rats, oral	5	[231]
PET	> 8000	rats, oral	5	[232]
PI	NR	NR	NR	[207]
PMMA	> 8400 - 9400	rats, oral	5	[233]
Pt	> 5000	rats, oral	5	[234]
PTFE	> 11280	rats, oral	5	[235]
PVA	5000	rats, oral	5	[236]
PVC	> 10000	rats, oral	5	[237]
PVDF	6000	rats, oral	5	[238]
quartz	> 2000	rats, oral	4	[239]
Si	3160	rats, oral	4	[240]
SiO_2	10000	rats, oral	5	[241]
SnO_2	> 20000	rats, oral	6	[242]
TiO_2	> 5000	no systemic toxicity, mice and rabbits, oral, 129.4 nm NPs	5	[243]
WO_3	> 5000	rats, oral	5	[244]
ZnO	> 5000	single dose, oral	5	[245]
ZrO_2	> 5000	rats, oral	5	[246]

[a] unless otherwise stated; NR: not reported; ref.: reference.

This reduces the substrate's functionality, stability, and biocompatibility. Piezoelectric drop-on-demand additive manufacturing offers a great prospect for the cost-effective fabrication of these sensors because it does not require a mask or template and can be digitally controlled. Moreover, printing on flexible surfaces is conceivable and ink may be applied without direct contact and at low temperatures [147], [158].

On the basis of IJP, sterilisation procedures can also be incorporated into production process chains. In general, the sensor can be sterilised using heat, ionising radiation, aqueous solution disinfection, or the low-temperature gas technique [252]. Medical equipment should ideally be produced immediately under sterile circumstances [252]. Thereby, pathogenic interaction can be reduced [252].

6.3 Biocompatibility assessment

First, literature references to bulk materials, inkjet-printed sensors, and the respective inks are evaluated. Then, the influence of the manufacturing process on the biocompatibility of the materials is considered. Finally, references on the transferability of the assessments are evaluated.

6.3.1 Biocompatibility of nanoparticle inks

For the electrodes or heating element, for example, metallic NP inks are frequently used. After being sintered, the NPs link to the substrate surface and create a cohesive porous layer. For the evaluation of biocompatibility, there are two risk variables. First, if not all NPs are sintered during the production process and afterwards detach, non-connected NPs may still be present on the printed structure. Moreover, when a flexible sensor is utilised, NPs have the potential to separate. Particularly, NPs that are not entirely or securely bound may separate. Only once the solvent and the coating on the NPs have been removed will the sintering process be working. The layer does not entirely sinter and the maximum conductivity is not obtained if there is still a sizable amount of residue. Post-processing, such as solvent expulsion, stabiliser removal, and actual sintering, can, in some circumstances, be accomplished in a single oven process step. However, the solvent may not have been entirely eliminated. The removal of stabilisers and other organic components is significantly more challenging. Moreover, there is a risk associated with inserting the sensor into the spinal disk due to shear forces. In strategies based on NPs, the NPs must be taken into account individually in terms of risk because of this. If most of the NPs are not bound, a conductive layer cannot exist. Conductivity tests on the printed structure can verify that the layer has not entirely broken down into individual NPs. When it comes to measurement, the target conductivity can be used for quality assurance to check for layer cracks. This implies that multiple printed structures are initially created and then examined under a microscope. The target conductivity is then compared to the conductivity of these printed objects. The target conductivity value can be used as a single measurement to perform quality control for subsequent testing. NPs can still detach in very small numbers, which doesn't affect conductivity but does affect biocompatibility. Because of this, additional testing is required. The size, shape, surface chemistry, and surface charge of NPs play a role in biocompatibility [253]. Whereas a smaller particle size results in a higher surface-to-volume ratio and a higher risk of cytotoxicity, a larger particle size increases surface reactivity, mass diffusivity, sedimentation velocity, and attachment efficiency [254]. In addition, particle size affects system toxicity, while it is unclear whether larger or smaller particles are more toxic [255], [256]. Moreover, the biocompatibility of the ink is significantly impacted by the aggregation of the NPs [257]. For instance, larger titanium dioxide (TiO_2) aggregates have a greater impact on cell viability compared to smaller ones [258]. Moreover, the shape of the NPs can affect their ability to penetrate a cell; for example, spherical NPs are less toxic and reactive than fiber-shaped ones [257], [259], [260]. A larger contact area results in lower penetration efficiency into a cell but also carries a higher risk of cytotoxicity [261], [262]. The molecular structure and bonding types at the surface of the NPs also have an impact on their cytotoxicity since these characteristics alter how the NPs are recognised by biomolecules like cells or proteins [263]. An immune response may happen if some particles are recognised by the body as foreign. Moreover, the biocompatibility may be impacted by the surface charge, depending on the density and polarity. In contrast to neutral or lightly charged surface charge densities, a higher surface charge density generally has a higher toxicity [264]. For instance, negatively charged NPs have an adverse effect on phagocytic cells, while positively charged NPs are more hazardous to non-phagocytic cells [257], [265]–[267]. The overall impact of a medical device's size, morphological characteristics, surface structure, and surface charge might be significant for the resulting biocompatibility. According to the particular material, there are other affects on biocompatibility as well. They are evaluated in the following section for the exemplary sensors.

6.3.2 Exemplary amperometric sensor

The biocompatibility of the individual materials of an exemplary amperometric sensor is evaluated in the paragraphs that follow. As a test that considers several materials, previous work cultured hepatocytes over a membrane that was placed on top of printed patterns to test the cytotoxicity of the gold, silver, and SU-8 inks [150]. The cells' viability was preserved, which suggests that these materials are not cytotoxic in the context of the setup described [150]. Here, it's essential that the processed ink be biocompatible. It is necessary to take into account the characteristics of NPs that are already bonded to a surface.

Gold nanoparticle ink as working and counter electrode material The optical properties and potential biocompatibility of AuNPs make them suitable for various biomedical applications, including medical imaging, drug delivery systems, and cancer treatment. The biocompatibility of these particles is determined by their size, shape, surface chemistry, and surface charge [253]. To create an amperometric sensor, the biological and printing properties of the gold ink from Tab. 6.4 are evaluated. The AuNP ink is used for the WE and CE of the sensor, after being dissolved in water and ethylene glycol. The manufacturer states that the NPs are non-toxic and biocompatible, and hepatocytes cultured on top of the printed ink show no signs of toxicity, as the cells remain viable [150]. However, the solvent ethylene glycol should be considered, as it is toxic to humans [268]. Since ethylene glycol has a boiling point of 196 °C [269], some residues may remain after curing or sintering below this temperature.

Silver nanoparticle ink as reference electrode material Due to their antibacterial qualities, AgNPs are used in medicine, such as in catheters and wound dressing [182], [270], [271]. Here, the RE of the amperometric sensor is made of AgNP ink. A higher quantity used in a medical ozone sensor may be hazardous to human cells [270]. A herniated disk's nucleus pulposus can be conceptualised as an aquatic habitat. AgNPs release silver ions that can attach to sulphur groups in biomolecules in an aqueous environment [270]. Cytoxicity, genotoxicity, or immunological reactions may ensue from this. Moreover, because AgNPs can cross the blood-brain barrier, they are categorised as neurotoxins [272]. The morphology of the AgNPs in the different inks has an impact on their biological characteristics. The silver ink according to Section 6.1 is examined for the exemplary amperometric sensor. The AgNPs are resolved in triethylene glycol monoethyl ether (TGME) and the ink adheres well to glass and polymer substrates. The AgNPs encapsulation is formed of polyvinylpyrrolidone (PVP) [273]. At the designated curing temperature, the PVP turns liquid and stays in the structure or on the substrate, meaning that it is not entirely evacuated [273]. According to regulation (EC) No. 1272/2008 [274], the ink is not classified as a hazardous product and does not include carcinogenic components in doses greater than 0.1% [274], [275]. Earlier studies utilising cultured hepatocytes on a membrane on top of the printed material indicated that this ink was well biocompatible [150]. No toxic components are present in the solvent TGME [276]. TGME residuals persist in the final sensor because its boiling temperature of 256 °C is higher than the ink's curing temperature. Prior to drying, the printed ink can be rinsed with polar solvents like ethyl alcohol or isopropyl alcohol (IPA) and then given a vacuum treatment to allow the solvent to completely evaporate. Hepatotoxicity, which can result in liver damage, occurs when large doses of ethyl alcohol are ingested or absorbed into the bloodstream [277]. The rinsing of the printed structure is intended to be safe because the two primary disinfectants used in the medical industry are ethyl alcohol and IPA. To ensure the product's biocompatibility, the amount used must be kept to a minimum.

Polydimethylsiloxane as substrate and membrane material The substrate and membrane are made of PDMS. As a result, the membrane has regulated permeation properties, and the substrate is made of strongly cross-linked PDMS. This allows for the membrane properties required for the specific application, such as high ozone and low oxygen permeability for an amperometric ozone sensor. It is beneficial to use photonic sintering to cure the gold and silver ink because of the PDMS substrate. Due to the fact that it does not heat up, photonic sintering is less harmful to the substrate. A membrane is required for the amperometric sensor in order to ensure selective ozone measurement. For this particular application, non-porous PDMS is seen as a promising membrane material. For instance, the porosity and the kind and number of functional groups on the surface affect the membrane's functionality. PDMS is described as non-flammable, hydrophobic, non-toxic, and bioinert [278]. It is used in medicine for things like contact lenses and the outer shell of breast implants [279]. Moreover, PDMS is printable; for instance, an elastomer matrix can be printed using Sylgard 184 ink [201], [208]. Sylgard 184 must be thinned out before printing, using extra solvents like octyl acetate (OA) [201], [208]. After printing and curing the PDMS layer, there was no evidence of OA residues [201], [208]. Although the biocompatibility of PDMS is documented, it also depends on the production and post-processing processes [280]. PDMS must undergo complete oligomerisation and be free of all short-chained molecules in order for its biocompatibility to be guaranteed. A PDMS (Sylgard 184)-coated device's in-vitro biocompatibility was also reported by Lee et al. [281].

SU-8 ink as passivation material SU-8 is used for the passivation of the electrodes. To prevent short-circuits, areas of the electrodes that aren't supposed to be exposed to the measurement substance must be passivated. Moreover, if the substrate is porous, the pores must be sealed with a passivation substance [150]. There are several different SU-8 types available, including the XP PriElex SU-8 1.0 and SU-8 2002. Whereas XP PriElex SU-8 1.0 is an ink that was especially created for IJP, SU-8 2002 was developed primarily for the spin coating process. It can, however, also be used for IJP. Earlier studies investigated SU-8 2002, a compound in which cyclopentanone serves as the solvent [150]. The biocompatibility of this ink has already been examined [150]. The epoxy-based photoresist jettable ink XP PriElex SU-8 1.0 is made up of resin, solvent, and a photosensitive element containing antimony. The printed layers undergo curing to generate stable isolation and dielectric layers that are also used as passivation layers for sensors [210]. The cross-linked polymer network, which is produced by ultraviolet (UV) light and heat, has good chemical resistance, thermal stability (up to 315 °C), and mechanical strength [282]. Previous work, however, disagrees on the issue of SU-8's biocompatibility. Several biological characterisation experiments in accordance with ISO 10993 [181] were performed, and the majority of them [282]–[284] concluded that SU-8 is non-toxic and non-irritating. Yet, according to other investigations [285], SU-8 is cytotoxic. According to [282], antimony's valency determines how poisonous it is. With more UV and heat exposure, the removable antimony content may be lowered.

To increase the biocompatibility of SU-8, a variety of surface treatments have been used, including chemical treatment with acid and base, surface grafting with polyethylene glycol, and oxygen plasma treatment [150], [282]. As a result of the oxygen plasma treatment, the surface's oxygen and carboxyl groups rise, increasing both the surface's wettability and surface energy [150]. When the ink has been applied, it is essential to treat SU-8 so that the solvents can be extracted as much as possible. To conclude, in-vivo testing is required to support or disprove the biocompatibility.

Potassium nitrate, potassium sulfate, and sodium chloride as electrolyte material To ensure optimal conductivity between the electrodes and hence the operation of the amperometric sensor, an electrolyte covering the active electrode area is required. If the sensor is used to measure bodily fluids and tissues, such as the nucleus pulposus, they may act naturally as an electrolyte, making the electrolyte superfluous. The biocompatibility of the electrolytes KNO_3, K_2SO_4, and NaCl is evaluated here. The human body naturally contains sodium and potassium. Potassium governs enzyme responses as well as the degrees of acidity, water balance, and blood pressure. Potassium and sodium are responsible for the transmission of signals in the body, including neurotransmission and muscular contradiction [286], [287]. Nitrates from meals enter the body and are converted to nitrites, which hinder haemoglobin from delivering oxygen and may result in an oxygen shortage in the cells [288]. Moreover, nitrate is converted into nitric oxide, which has a favourable impact on metabolism and blood flow rates [289]. Current research suggests that naturally existing quantities of nitrate do not raise the risk of tumours, contrary to previous studies that were highly disputed on nitrate and a correlating cancer risk [290]. Sulfates are necessary both inside the human body and in medicine, for example, during colonoscopies and cell growth processes [291], [292]. Nonetheless, sulphates can also cause skin or eye irritation [287]. KNO_3 is used in toothpaste and the food industry to boost product longevity [293]. There are no maximum addition limitations for the food additive K_2SO_4 (E515) in the European Union [294]. The primary human mineral NaCl can be administered intravenously as an isotonic saline solution by being greatly diluted [286].

The most promising electrolyte in terms of biocompatibility is NaCl, which can be administered intravenously as an isotonic saline solution without toxicity.

6.3.3 Exemplary impedimetric sensor

The biocompatibility of an exemplary impedimetric sensor is evaluated in the paragraphs that follow.

Platinum as electrode material Mostly, noble metals with excellent electrical conductivity are used as electrode materials [10]. In this case, Pt is evaluated due to its high biocompatibility, inertness to bodily fluids, low corrosivity, and strong mechanical strength [295], [296]. As a result, Pt is frequently used for medical devices, such as catheters, pacemakers, and stents [297]. PtNP or a Pt solution, such as chloroplatinic acid hydrate, are used to create inks that contain Pt [298]. In terms of biocompatibility, PtNPs are more promising because Pt solutions frequently contain hazardous materials. For the PT-LT-20 NP ink, Schubert et al. [299] found nearly 100% cell survival and the development of a highly biocompatible surface. They tested the cytotoxicity of the NP ink in in-vitro settings, in accordance with ISO 10993 [300]

Indium oxide as sensing material Frequently used as sensing materials for impedimetric sensors include ZnO, In_2O_3, WO_3, and SnO_2 [199]. Due to its high sensitivity, low cross-sensitivity, and quick response and recovery times, In_2O_3 was investigated here [301]. In_2O_3 is used as an impedimetric sensor's sensing material in a crystalline, water-insoluble form [302], and it performs best between 200 °C and 400 °C [301]. Commercially available In_2O_3 inks are not offered; however, they can be manufactured from oxide precursors based on sol-gel or NPs [303], [304]. Oxide precursors based on sol-gel require higher temperature treatments than NPs. Previous work [158] used a printed sodium alginate insulator layer on top of a printed In_2O_3 layer to test the lactate dehydrogenase (LDH) cytotoxicity of the combination. The test results in a non-cytotoxic finding. The applied In_2O_3 NP ink consists of deionised water and sodium polyacrylate. After the IJP procedure, the NP ink must be thermally treated at 150 °C. The diameter of the NPs is between 20 nm and 70 nm. More research is necessary regarding the interaction of In_2O_3 with bodily fluids and tissues. Numerous studies have focused on the effects of breathing in In_2O_3, which can be hazardous to the lungs [305], [306]. In addition, it is toxic for the kidneys when indium (III) ions are introduced into the bloodstream. Moreover, hydrated In_2O_3 is 40 times more hazardous than the equivalent ions [307]. Overall, there is not enough information in the literature to assess In_2O_3's biocompatibility reliably. More studies are required, particularly in relation to IJP and In_2O_3-based inks.

Alumina as substrate material The electrodes and the heat or light activation element are separated by a substrate for an impedimetric sensor. The substrate must be heat-conductive, heat-stable, and compatible with the ink that is used for the electrodes, heating element, and light activation element. Due to phonon resonance, Al_2O_3 is used as the substrate in the exemplary sensor, making it a good heat conductor and insulator [308]. If Al_2O_3 and NPs are disseminated in water or ethylene glycol, Al_2O_3 can be used via IJP [309]. Based on the biological characterisation tests [181], Denes et al. [310] reported satisfactory biocompatibility for Al_2O_3. Contrarily, Mestres et al. [311] found that macrophages release more reactive oxygen species (ROS) after being exposed to high concentrations of 20 nm Al_2O_3 NPs. This results in oxidative stress and may lead to cell death. The biocompatibility of the sensor may also be affected by additional chemicals needed for the manufacturing process, such as solvents to make the substances printable.

Polydimethylsiloxane as membrane material For the amperometric measuring principle, the biocompatibility of PDMS is already investigated in Section 6.3.2.

Platinum as heating or indium gallium nitride as light activation element
Section 6.3.3 already covered the biocompatibility of Pt. Histology investigations, in-vivo immunological response analyses, and in-vitro and in-vivo cytotoxicity testing were carried out for InGaN LEDs [312]. No cytotoxicity or immunological side effects were observed for the tested LEDs [312]. Gallium nitrate's immunosuppressive impact can generally reduce local inflammation [313], [314]. The LEDs material exhibits good biocompatibility. However, the usage of UV light may be a significant problem because UV light exposure increases the production of ROS, which can harm biomolecules [315]. Moreover, depending on the wavelength of the UV light, the deoxyribonucleic acid (DNA) may be harmed directly or indirectly [316].

6.3.4 Exemplary optical absorption sensor

The biocompatibility of an exemplary optical absorption sensor is investigated in the following paragraphs.

Zinc oxide as sensing material ZnO is frequently used in medicine, for example, in drug delivery systems, bioimaging, and biosensors, such as glucose sensors [317]. Moreover, it is a typical sensing component for impedimetric sensors [98], [318]. According to [319], [320], it is feasible to measure gas at room temperature (RT) with visible light enhancement. To analyse the dissolved ozone measurement under these circumstances, more research is required. Commercially available n-butanol dissolved ZnO NP ink is available under the trade name Helios'Ink H-SZ01034 from GenesInk, France. n-Butanol causes irritation when it comes into contact with the skin or eyes [321]. ZnO NPs, on the other hand, have anti-inflammatory, anti-bacterial, and biodegradable qualities. Moreover, the FDA has recognised ZnO NPs as safe substances [322].

Indium gallium nitride as light activation element For the impedimetric measuring principle, the biocompatibility of InGaN is already investigated in Section 6.3.3.

6.4 Potential alternatives with a higher biocompatibility

The likelihood of a biocompatible sensor is increased by the use of biocompatible materials, though the actual sensor still needs to be evaluated. Overall, the materials in Section 6.3 reveal PDMS for the membrane and substrate and Pt and AuNP inks for the electrodes as having the highest potential for biocompatibility. In contrast, the RE made of AgNP inks and the sensing material made of In_2O_3 have the lowest potential. The RE could be replaced by Ti, and the sensing material could be TiO_2 or ZnO. However, it is vital to remember that the size and shape of the NPs determine how poisonous TiO_2 and ZnO are [323].

Titanium as reference electrode material and titanium dioxide as sensing material Ti is frequently used in medical applications, including dental implants and prosthetics [188], [191], [324]. This is made feasible by Ti, which has exceptional biocompatibility, superior mechanical strength, and great corrosion resistance [325]. The primary cause of the high biocompatibility is that the surface of Ti oxidises to TiO_2, which exhibits non-toxic behaviour [325]. Although having a higher level of biocompatibility than silver, Ti has an electrical conductivity that is more than ten times lower [326]. However, using other noble metals, such as Pt, in conjunction with Ti can increase the electrical conductivity [98]. Earlier studies have demonstrated the usefulness of TiO_2 as a sensing material for impedimetric sensors with a heating element for the detection of oxygen, ozone, and other gases [327], [328]. The high temperatures required for the sensing material's performance limit the wide applicability of TiO_2, whose resistance is strongly correlated with temperature. In order to improve the electrical conductance of Ti, to lower the temperature required for the TiO_2 sensing material, and to examine the effects of the IJP process on the material's biocompatibility, more research is required.

Zinc oxide as sensing material For the optical absorption measuring principle, the biocompatibility of ZnO is already investigated in Section 6.3.4.

6.5 Transfer of the assessment to other sensors

Other sensors made from the same or overlapping material set as the exemplary amperometric, impedimetric, and optical absorption ozone sensors previously discussed include glucose, hydrogen peroxide, pH, sweat lactate, oxygen, and acetone sensors. The results can be transferred to hydrogen peroxide sensors, such as those described by [179], which are composed of a PDMS substrate, gold for the WE and CE, and silver for the RE. Transfer is also achievable for inkjet-printed electrochemical pH and glucose sensors, as demonstrated, for example, by [329]. WE and CE are made of gold, RE is made of silver, and PDMS is used for passivation [329]. Also, a polyaniline film is used on the WE for the pH sensor, and a poly(3,4-ethylenedioxythiophene) layer is used on the WE for the glucose sensor [329]. A transfer to sweat lactate measurement is conceivable using sensors made of a flexible silver electrode coated in Nafion with lactate oxidase as an enzyme [330]. A dissolved oxygen sensor made of AuNP ink for the WE and CE, AgNP ink for the RE, SU-8 ink for the passivation, and a polyethylene naphthalate (PEN) substrate are also similar [215]. It is also possible to create an oxygen sensor using Pt-doped In_2O_3, which is comparable to the evaluated impedimetric sensor and operates at RT [331]. Moreover, the electrolytes KNO_3, K_2SO_4, and NaCl are frequently used for amperometric sensors. Additionally, acetone sensors for biological applications incorporate Pt-decorated In_2O_3 NPs [178]. Other than for ozone measurement, In_2O_3 is frequently used for inkjet-printed transistors [157]–[159]. Transistors can be used in medical applications for skin and health surveillance [332]. In addition, refractometers in laboratory medicine use InGaN-based chips to measure the total plasma protein in blood and urine samples [333]. Overall, a wide range of medical applications make use of the same or overlapping materials used to measure dissolved ozone. The assessments made here can therefore be transferred to these overlapping materials.

6.6 Discussion

Using materials that are compatible with biological systems enhances the probability of developing a biocompatible sensor. In addition, the likelihood is further increased by the use of non-toxic additional chemicals and solvents. However, the IJP procedure and post-processing steps also affect the sensor's biocompatibility by altering the material's characteristics. After completing all production procedures, biocompatibility testing must be carried out on the finished sensor. A last heating step can increase the biocompatibility of sensors used in medical technologies. By removing the bound water, the electronics' ability to corrode may be prevented. Moreover, the solvents' volatile parts are removed. Since amperometric, impedimetric, and optical absorption sensors are now the most promising for an inkjet-printed sensor for the oxygen-ozone treatment of a disk herniation, they are the main focus of this research. However, other materials for impedimetric sensors, such as a combination of metal oxide semiconductors (MOS) materials and CNTs or polymers, may be preferable after more fundamental research is conducted. Polymers are frequently used as sensing components for sensors, but further study is needed before they can be used to measure ozone [334]. Here, the stability and miniaturisation of the sensor are not considered. Various cytotoxicity tests have already been published. However, the test findings depend on both the cells and the used material; thus, these tests must be repeated for the cells present during the specific application, in this example, the intervertebral disk tissue. Also, depending on the nation in which the medical device is made and sold, the biocompatibility of the sensor needs to conform to different regulations. Manufacturers must abide by the Medical Device Regulation in the European Union and the FDA in the United States. Here, the international standard ISO 10993 [181], which is a standard for determining whether a product is biocompatible and is fundamental for the technical documentation of a medical device, is taken into consideration.

Part III

Ozone sensing in medicine

Overview Part III

For medical therapy, measuring the dissolved and gas concentrations of ozone is important to enable reliable and safe patient care. The following chapters build upon Part II and further investigates research question (RQ) RQ2: How can novel dissolved and ozone gas sensors be realised as electrochemical or optical sensors? Optical absorption ozone gas sensing, optical absorption dissolved ozone sensing, and electrochemical dissolved ozone sensing are investigated. First, a photometer is presented for the measurement of ozone gas with optical absorption. Currently, the high cost of these instruments limits the application range of commercial photometers. Thus, a simplified photometer is presented here. The photometer can measure ozone gas with an accuracy of 2.5% compared to a reference sensor. Second, a photometer is reported for the measurement of dissolved ozone with optical absorption. The majority of the pieces are 3D-printed, with all other parts readily accessible in the marketplace. The proposed photometer's root-mean-square percentage error (RMSPE) is 14.7% compared to a commercially available reference sensor for dissolved ozone. The reference sensor has a RMSPE value of 8.2%, while at the same time it is 17 times more expensive than the photometer presented here. Thus, it is concluded that the photometer yields good measurement results, considering it's simplified design. Third, the measurement of dissolved ozone with an electrochemical sensor is investigated. As a preliminary assessment, the manufacturing of an exemplary oxygen sensor structure with inkjet-printing (IJP) is evaluated. This preliminary assessment is conducted because the conclusions can be transferred to an ozone sensor due to overlapping materials and production steps. In addition, a new dissolved ozone sensor that uses screen-printed electrodes from a commercial supplier together with various porous polytetrafluoroethene (PTFE) membranes and non-porous polydimethylsiloxane (PDMS) membranes is presented. With PTFE, it is possible to achieve a RMSPE of 30.41%. Also, using boron-doped diamond (BDD) electrodes without a membrane or an electrolyte, the detection of dissolved ozone in blood is investigated.

7

Optical ozone gas sensing in medicine

Parts of this chapter are based on: L. Petani, R. Barth, L. Wührl, I. Sieber, L. Koker, M. Reischl, U. Gengenbach, and C. Pylatiuk, “Investigation of a simplified photometer design for the measurement of ozone gas concentration”, Kuala Lumpur, Malaysia: IEEE-EMBS Conference on Biomedical Engineering and Sciences (IECBES), Dec. 7–9, 2022, pp. 1–6. DOI: `10.1109/IECBES54088.2022.10079356`.

First, the current state of the art in optical ozone gas sensing is investigated. A comprehensive literature review revealed that this is the first study to introduce a minimalist setup for measuring ozone gas without the use of lenses or mirrors, thus meeting the requirements detailed in Tab. 7.1.

Tab. 7.1: Overview of the most important requirements for a photometer for ozone gas.

parameter	requirement
design	needs to be enclosed, no leakage of gaseous ozone into the ambient air
range	ozone gas: between 0.4 vol% and 2 vol%
in-line	needs to be enabled for continuous measurement
response time	below 1 s
costs	below 1850 €
selectivity	high selectivity against oxygen
size	below 35 cm x 20 cm x 15 cm
parts	staple parts
manufacturing	no machining
RMSPE	below 5%

Subsequently, the used materials and methods for the photometer are presented. Overall, two photometer setups are introduced and assessed in the following. One setup is based on a minimal design, while the other uses collimating optics. Both setups are evaluated by comparing them to a commercial reference sensor. The photometer with collimating optics serves as an additional reference to the commercial reference sensor.

The following requirements are important for the developed photometer: The photometer needs to be enclosed, and there should be no gaseous ozone released into the ambient air. Also, the concentration range that can be measured should be between 0.4 vol% and 2 vol%. Continuous measurement should be enabled. The response time should be below 1 s. For the measurement, there should be a high selectivity against oxygen. The device should be portable and therefore not exceed the size of 35 cm x 20 cm x 15 cm. Only commercially available components should be used, and no mechanical processing should be necessary. For the RMSPE, the developed photometer should achieve values below 5%.

7.1 Current state of the art in optical ozone gas sensing

Previous work regarding photometric ozone measurement included relatively large absorption chambers in the visible light range (e.g., close to the Chappius band with an absorption chamber length of 70 cm [335] or of 50 mm [336]) to realise long path lengths, which leads to an overall larger design. Furthermore, for photometers in the ultraviolet (UV) range, optical components, such as lenses and mirrors, are used, which leads to an increase in the design size. Also, previous work often involved fibre-optics [119], [337] for light-emitting diodes (LEDs) in the Hartley band, which requires expensive peripherals and are not easily obtainable, or conventional UV lamps [119], which also yield an increase in the design size. In addition, there is also previous work where the authors manufactured their own UV LED [211], which is very interesting for the development of new light sources, but for the here presented application, it is not accessible enough due to their lack of commercial availability. In another approach, LEDs in the visible light range (i.e., the Chappius band) are applied [335]. Since the absorption in the Huggins, Chappius, and Wulf bands is significantly lower than in the Hartley band, longer path lengths are required to get a good signal, which results in a larger design. With an UV-LED, a high attenuation coefficient α is ensured.

7.2 Materials and methods

For the realisation and evaluation of the ozone gas photometer, the materials described in previous work [15] are used. The materials for the evaluation include an ozone generator, medical oxygen, an ozone destructor, and the ULTRA.sens AK25 reference ozone gas sensor. The error of the photometers presented here is determined by measuring the difference between their readings and those of the reference sensor. For connections between the ozone generator, photometer, and reference sensor, PTFE and silicone tubings and PTFE Luer lock connectors are selected. The final setups are shown in Fig. 7.4, while the schematic of all included parts is illustrated in Fig. 7.2. For the realisation of both photometer setups, the following components are used: an LED with a wavelength range between 270 nm and 286 nm, a Raspberry Pi (RPi) 4 model B, a heat sink attached to the LED, and an LED driver. Furthermore, an UV quartz glass cuvette with a path length of 5 mm, a photosensor, a temperature sensor, a pressure sensor, a 16-bit analog digital converter (ADC), a heatsink for the RPi, a real time clock for the RPi, and a touch-screen are used. The photometer that uses collimating optics includes several optical components that are not present in the minimal photometer. These components are a collimation lens, a spherical mirror, and a focusing lens. To accommodate the optical components as well as additional sensors, optical benches are created using additive manufacturing techniques with a Stratasys uPrint SE Plus 3D printer and acrylonitrile butadiene styrene (ABS) filament. A monolithic optical bench is designed for the minimal photometer, enabling passive alignment of the optical components against mechanical stops. For the photometer with collimating optics, an adjustable optical bench is designed, featuring a baseplate and adjustable submounts for the optical components.

To calibrate the photometers, three measurement series are conducted for each of the two photometers, covering the entire range of concentrations (0 vol% to 3.79 vol%) provided by the ozone generator. This resulted in a total of 94 measurement values. The concentration levels are predetermined by the ozone generator, and only specific values can be set. The reference sensor is placed between the cuvette and the ozone destructor. The resulting absorption measurements are adjusted for temperature, pressure, and LED reference beam photosensor measurements according to [338] and result in Equation 7.1.

$$\mathrm{A} = \frac{\mathrm{T}}{\mathrm{T_S}} \cdot \frac{\mathrm{P_S}}{\mathrm{P}} \cdot \log\left(\frac{\mathrm{S_{ref}} - \mathrm{S_{ref,d}}}{(\mathrm{S_{probe}} - \mathrm{S_{probe,d}}) \cdot \mathrm{Z}}\right) = \log\left(\frac{\mathrm{I_0}}{\mathrm{I(c)}}\right). \tag{7.1}$$

T and P are the measured temperature and pressure, while $\mathrm{T_S}$ and $\mathrm{P_S}$ represent the standard temperature (273.15 K) and standard pressure (1000 hPa). S refers to the photosensor signal, and Z represents the zero factor. The term ref refers to the LED reference beam photosensor, while probe represents the probe beam photosensor, and d corresponds to the dark photosensor signal. Both the LED reference beam and the probe beam photosensor are utilised in both photometers. During the measurement series, the LED is warmed up, the dark signal is measured, a second warm-up of the LED follows, and afterwards the zero factor is calculated. The purpose of the warm-up is to stabilise the signal of the LED. The LED is turned on for the entire measurement, except for the dark signal measurements. The zero factor is then determined to establish the correlation between the probe beam and LED reference beam photosensor signals when no ozone is present. The Lambert-Beer law is used to describe the relationship between the initial and measured intensity after absorption in the cuvette. The initial intensity, $\mathrm{I_0}$, corresponds to the LED reference beam signal, which is independent of the ozone concentration, and I represents the probe beam photosensor signal, which depends on the ozone concentration. The correlation is used to determine the zero factor. A linear regression is typically adequate for the lower concentration range, while a quadratic regression is appropriate for the full concentration range, and these are calculated using the least-squares method with NumPy [339].

The measurement method is shown in Fig. 7.1, which outlines the overall process. 10 measurement values are recorded for each output value, and their median value is calculated. Then, the ozone concentration is determined using the calibration function. The performance of the photometers is evaluated using different ozone concentrations according to Fig. 7.1. The ozone concentration measured by the photometers is compared to the reference sensor after the measurements. Five measurement series are conducted with concentrations ranging from 0 vol% to 3.79 vol%. A total of 143 measurement values are recorded to evaluate the photometers. The parameters used to evaluate the

DS: dark signal of photodiode, T: temperature signal, Ts: standard temperature, P: pressure signal, Ps: standard pressure, A: absorbance, S: signal of photodiode, Z: zero factor, ref: reference.

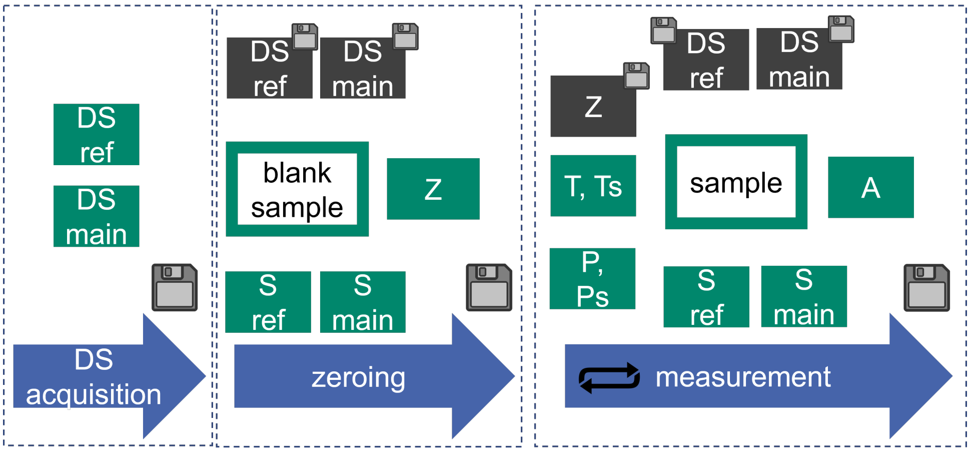

Fig. 7.1: Illustration of the process of the measurement method. Once the dark signal is acquired and zeroed, the measurement proceeds continuously until it is manually terminated or the timer expires. [15] © 2022 IEEE

instruments are relative error, accuracy, resolution, and response time. The empirical standard deviation is calculated [340]. Since the ozone generator produces varying output concentrations during measurements, the empirical standard deviation is determined using photosensor values obtained when there is no ozone in the cuvette. Additionally, the residual standard deviation is determined [341]. The measurement error and relative error between the photometers and the reference sensor are determined [342]. The resolution is determined by finding the smallest difference between two concentrations that can be identified [119]. To evaluate the response time, only the computation and sensor inquiry time are considered, while any delays caused by the connecting tubes and buffer flask length are not taken into account.

7.3 Setup of the novel photometers for ozone gas

The schematics of the minimal photometer and the photometer with collimating optics are illustrated in Fig. 7.2.

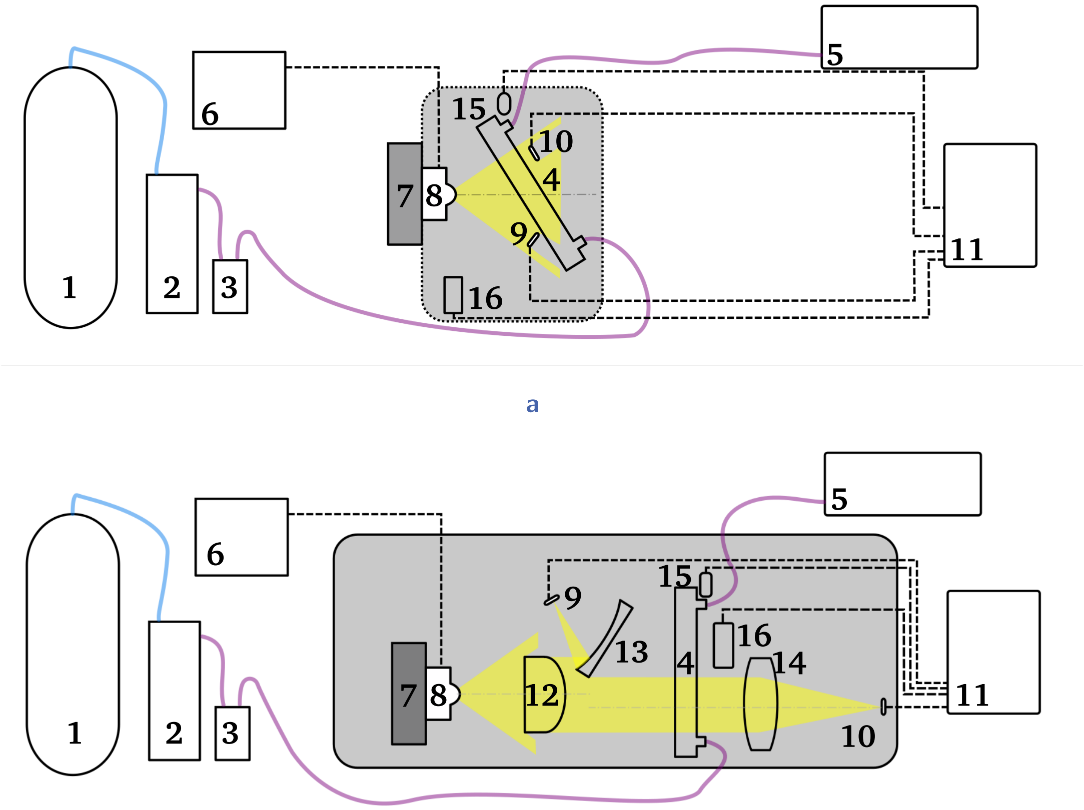

a

b

Fig. 7.2: (a) Minimal photometer. [15] © 2022 IEEE (b) Photometer with collimating optics. Oxygen connections are coloured blue, oxygen-ozone as purple, electrical as black dashed lines, and the UV light encapsulation as a grey box. Included are oxygen (1), ozone generator (2), buffer (3), cuvette (4), ozone destructor (5), LED driver (6), heat sink (7), LED (8), reference beam photosensor (9), probe beam photosensor (10), ADC (11), and temperature (15) and pressure sensor (16). For the collimating optics photometer, the following components are additionally included: aspheric lens (12), spherical mirror (13), and double convex lens (14). [15] © 2022 IEEE

The minimal photometer design is expanded with collimating optics to increase the light's interaction with the gas volume. An optical design for a photometer with collimating optics is created using off-the-shelf components. In the photometer with collimating optics, the light source emits light that is collimated by a planoconvex aspheric lens to pass through the gas cuvette as a parallel beam. However, due to the limited availability of components, the lens can only capture about $53°$, while the nominal radiance angle of the LED is $60°$. A concave mirror reflects a portion of the light and focuses it on the reference photosensor to create the reference beam path. The remaining light that passes through the cuvette is focused by a biconvex lens onto the photosensor. To achieve the minimal photometer design, there is no need for optical components, and instead, the LEDs wide beam angle and high intensity are used for direct irradiation of the photosensors. The minimal photometer is designed to use a minimal number of components mounted on a monolithic optical bench, eliminating the need for complex alignment. The use of a wide beam angle (60°) LED is beneficial because both photosensors can be placed in the beam, removing the need for a beam splitter or mirror for the LED reference beam path. For both designs, the components must be precisely aligned to obtain a high and stable signal. This is accomplished by designing tailored optical benches, where the components are either actively adjusted during instrument assembly or passively aligned against well-designed reference surfaces [343]. The complexity of the design, represented by the number of components, is directly proportional to the optical bench complexity and alignment effort required. The monolithic optical bench serves as the central component of the minimal photometer. At the back of the bench, the LED with heat sink is mounted, while at the front, the gas cuvette and two photosensors are mounted at an angle of 22° against mechanical stops. To protect the user, a cover with two holes for gas inlet and outlet is attached to the optical bench and encloses the UV light. The final version of the minimal photometer without a cover is depicted in Fig. 7.3a. The minimal photometer is connected via a cable to the same evaluation unit, which includes a touch-screen and an RPi as the photometer with collimating optics. The photometer with collimating optics is intended to optimise the utilisation of the light source and to allow for greater flexibility in the positioning of components, in contrast to the minimal photometer. The final version of the photometer with collimating optics is presented in Fig. 7.3b. Fig. 7.4 shows the realisation of the final minimal photometer setup and the photometer setup with collimating optics.

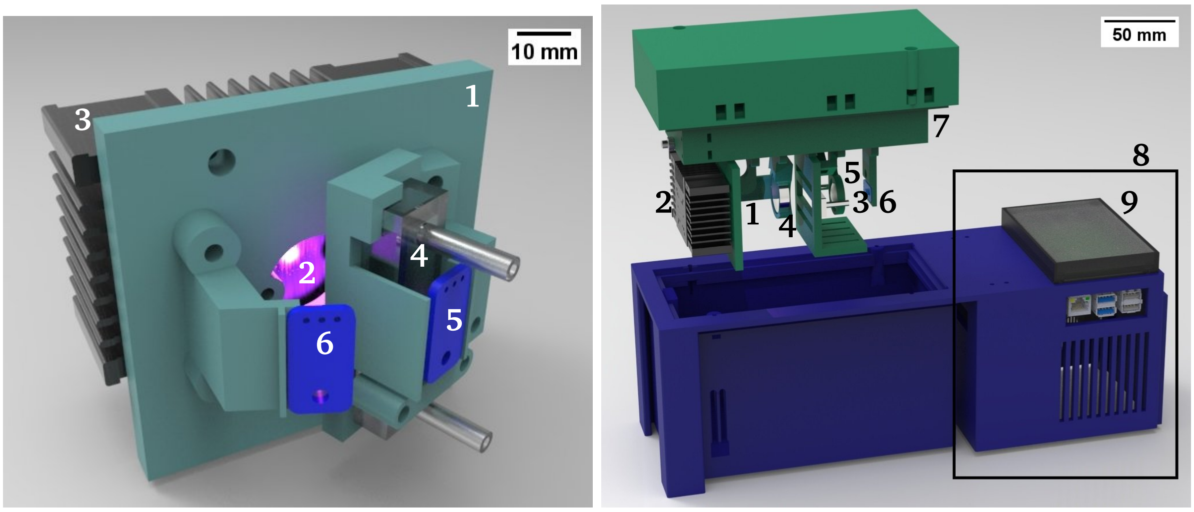

a

b

Fig. 7.3: **(a)** The final version of the minimal photometer includes the following components attached to the monolithic optical bench (1): the LED (2), heat sink (3), cuvette (4), probe beam photosensor (5), and LED reference beam photosensor (6). [15] © 2022 IEEE **(b)** Final version of the photometer with collimating optics, including LED (1), heat sink (2), cuvette (3), aspheric lens (4), double convex lens (5), probe beam photosensor (6), monolithical optical bench (7), external evaluation unit (8), and touch-screen with Raspberry Pi (9). The LED reference beam photosensor (not shown) and spherical mirror (not shown) are mounted on adjustable holders on the optical bench. [15] © 2022 IEEE

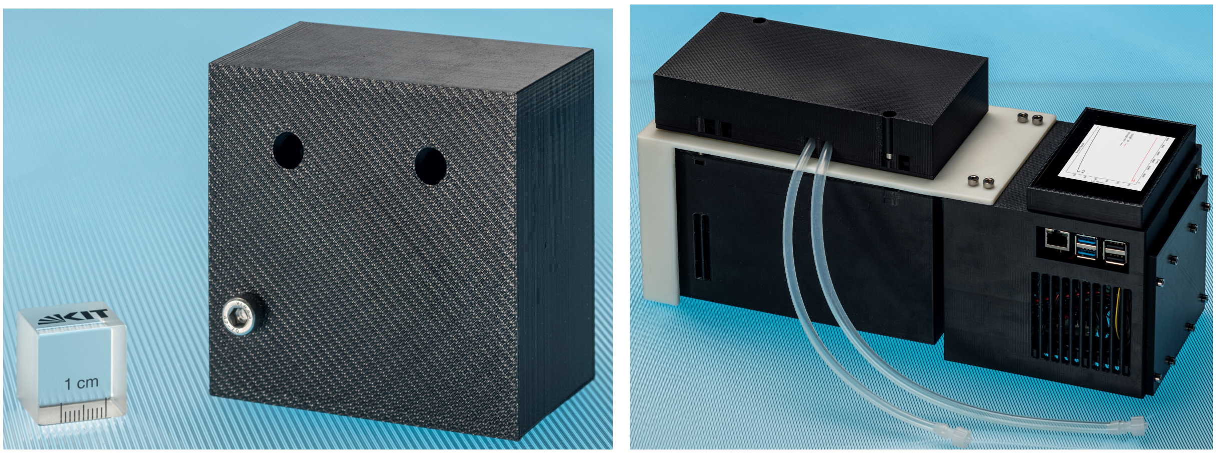

a

b

Fig. 7.4: **(a)** Shows the minimal photometer setup. **(b)** Depicts the photometer setup with collimating optics. [Images: Markus Breig, KIT]

7.4 Evaluation of the photometers for ozone gas

The photometer with collimating optics has 36% of the intensity in the probe beam path and 13% in the reference beam path, while the minimal photometer without any beam shaping optics only has 0.4% usable intensity in both paths [344]. However, despite the low amount of light being used for the measurement in the minimal design, the high power of the UVC-LED still allows for good measurement results.

The light absorption during calibration demonstrated an almost linear trend within the targeted concentration range of 0.3 vol% to 2.5 vol%, with a slight deviation outside of this range. As a result, quadratic regressions are calculated for the complete concentration range of 0 vol% to 3.79 vol%, with linear regressions being used for the lower concentration range of 0.3 vol% to 2.5 vol%. For the minimal photometer, the linear regression yields

$$c_{\mathrm{linear,minimal}} = 2.1760 \cdot A - 0.0950. \tag{7.2}$$

The quadratic regression for the minimal photometer results to

$$c_{\mathrm{quadratic,minimal}} = 0.3285 \cdot A^2 + 1.8003 \cdot A - 0.0089. \tag{7.3}$$

For the photometer with collimating optics, the linear regression results to

$$c_{\mathrm{linear,collimation}} = 2.4311 \cdot A - 0.1012. \tag{7.4}$$

The quadratic regression for the photometer with collimation optics yields

$$c_{\mathrm{quadratic,collimation}} = 0.5144 \cdot A^2 + 1.9140 \cdot A + 0.0008. \tag{7.5}$$

Here, c represents the concentration in vol%, and A represents the normalised absorbance value in absorbance units (AU), which ranges between 0 AU and approximately 1.6 AU. The regression's residual standard deviation for the collimation linear regression is 217.8 parts per million (ppm), for the collimation quadratic regression 182.8 ppm, for the minimal linear regression 486.9 ppm, and for the minimal quadratic regression 240.4 ppm. Fig. 7.5 displays the calibration measurements and both regressions for the minimal and collimation photometers. In general, quadratic regression is a more precise method of analysis than linear regression.

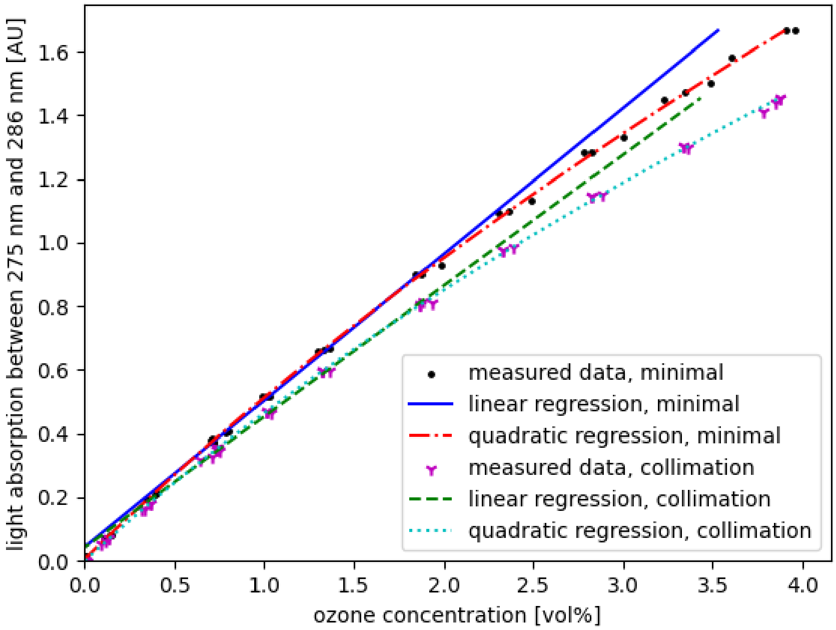

Fig. 7.5: The minimal photometer's calibration measurements are represented by black dots, while the blue solid line indicates the linear regression and the red dash-dotted line represents the quadratic regression. The collimation photometer's measurements are shown as purple crosses, with the green dashed line indicating the linear regression and the light blue dotted line representing the quadratic regression. The calibration process of both setups recorded 94 measurement values, and the absorption values are normalised. [15] © 2022 IEEE

However, within the specific measurement range being examined (up to 2.5 vol%), the linear regression still produces good results. Outside of this range, as demonstrated in Fig. 7.5, the quadratic regression is superior. The evaluation process involves performing five separate measurement series using both the minimal photometer and the collimating optics photometer. The results of this evaluation within the measurement range up to 2.5 vol% are displayed in Tab. 7.2. For the entire concentration range, the photometer with collimating optics and the minimal photometer both have a relative error below 15% and 11%, respectively. The relative error of these photometers is similar to that of other low-cost ozone sensors currently available on the market [345]. Fig. 7.6 displays the relative measurement errors for both photometers, indicating that the same pattern of behaviour for the linear regression versus the quadratic regression can be seen as in Fig. 7.5. According to the accuracy values presented in Tab. 7.2, the minimal photometer has better accuracy than the collimation photometer.

Tab. 7.2: The results of the assessment are presented, whereby reg. represents the type of regression used, s indicates the empirical standard deviation at zero concentration, s_{est} refers to the residual standard deviation, and a reflects the photometer's accuracy in relation to a reference sensor. [15] © 2022 IEEE

parameter	minimal photometer		collimation optics photometer	
	linear reg.	quadratic reg.	linear reg.	quadratic reg.
s	107.9 ppm	89.6 ppm	67.9 ppm	53.6 ppm
s_{est}	194.4 ppm	205.0 ppm	200.9 ppm	175.4 ppm
a	4.03%	2.50%	4.21%	2.64%

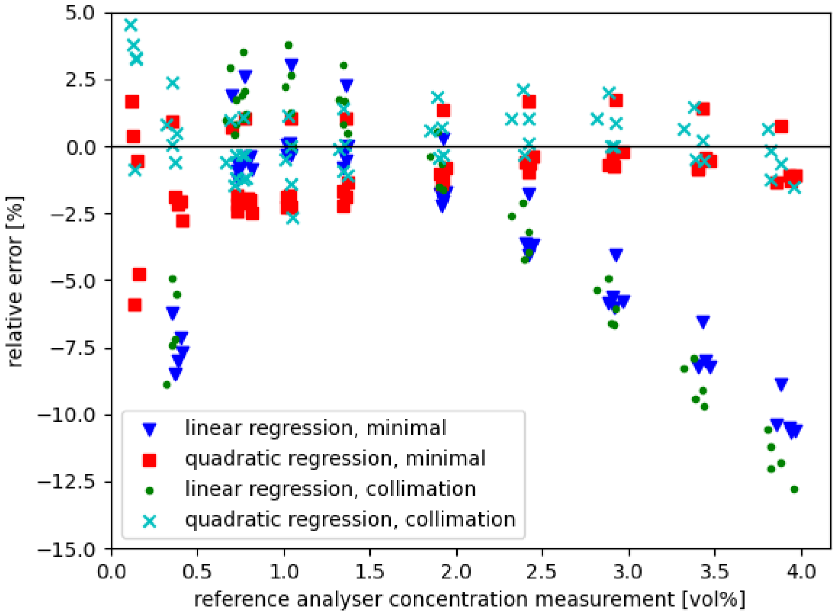

Fig. 7.6: The relative measurement errors of both photometers are determined by comparing their measurements to those of a reference sensor. A total of 143 measurement values are recorded to evaluate both photometers. [15] © 2022 IEEE

However, more data needs to be collected to make a significant comparison of accuracy between the two photometers. The resolution of the collimation photometer is less than 290 ppm, while the minimal photometer's resolution is less than 510 ppm, although the actual resolution is even smaller. An ozone generator that enables continuous adjustment of ozone concentration is necessary to determine the actual resolution. The quadratic regression for both photometers has an error of less than 5% for concentrations up to 4 vol%. The reaction time for one measurement for both photometers is 210 ms. This implies that the final concentration value is presented as measurement output to the user based on the average of 10 measurements.

To summarise, the cost of materials for the collimating optics photometer is approximately 1215 €, whereas the minimal photometer's cost is approximately 605 €. Additionally, assembly costs, including adjustment of optical components, are higher for the collimating optics photometer, while the minimal photometer can be easily assembled by appropriately designing the monolithic optical bench. The size advantage of the minimal photometer is also substantial, with dimensions of 7.5 cm x 7.5 cm x 7.5 cm compared to 20 cm x 12 cm x 16 cm for the collimating optics photometer (both excluding the external evaluation unit with touch-screen).

7.5 Discussion

Here, two different designs for an ozone gas photometer, one with a minimal number of optical components and the other with beam collimating optics, are investigated. In the following, the fulfilment of the requirements according to Tab. 7.1 is summarised and discussed.

Enclosed design The enclosed design is effectively implemented for both photometers. Gaseous ozone that may normally be released into the environment and inhaled by the operator is not present. The gaseous ozone measurement substance is enclosed by tubes and directed through an ozone destructor before being released into the surrounding air.

Measurement range The target for the photometers is to measure ozone gas concentrations up to 2 vol%. This requirement is fulfilled; measurements up to 2.5 vol% are possible with the photometers. Both photometers can detect ozone gas concentrations ranging from 0 vol% to 2.5 vol% ($\hat{=}$ 0 ppm to 25000 ppm) within a wavelength range of 275 nm to 286 nm.

In-line measurement In-line measurement is possible for both photometers. The measurement is conducted without the requirement of taking a sample, thus without a separation.

Response time The requirement for the response time is to be below 1 s. Both photometers provide a response time below that requirement. The response time for both photometers is 210 ms.

Costs The requirement regarding the costs is that the photometers cost each below 1850 €. This requirement is met; the photometer with the minimal number of optic components costs about 605 €, while the photometer with beam collimating optics costs about 1215 €.

Selectivity against oxygen The requirement of measuring selectively is fulfilled because both photometers are based on the optical absorption principle.

Size Regrading the overall design size of the photometers, the aim is to be below 35 cm x 20 cm x 15 cm. This requirement is fulfilled for both photometers. The minimal photometer has a size of 7.5 cm x 7.5 cm x 7.5 cm, while the collimating optics photometer has a size of 20 cm x 12 cm x 16 cm.

Staple parts, no machining necessary This requirement is fulfilled, and the presented ozone gas photometers can be developed using only standard components, 3D printing, and soldering.

Root-mean-square percentage error For the RMSPE the aim is to be below 5%. For the minimal photometer, the RMSPE is 2.5% and for the collimating optics photometer, the RMSPE is 2.64%.

Overall, the performance of the minimal design is as good as that of the more complicated design with collimating optics, which is a promising result for the development of compact and low-cost instruments.

8

Optical dissolved ozone sensing in medicine

Parts of this chapter are based on: L. Petani, D. Tils, L. Wührl, I. Sieber, and C. Pylatiuk, “Design, simulation, and evaluation of a low-cost photometer for dissolved ozone measurement”, (accepted), Tel Aviv, Israel: IEEE International Conference on Microwaves, Communications, Antennas, Biomedical Engineering & Electronic Systems (COMCAS), Jul. 9–11, 2024.

In the following, the state of the art in optical dissolved ozone sensing is assessed. Currently, there is no photometer available that meets the requirements listed in Tab 8.1. Here, a photometer for dissolved ozone sensing in medicine is developed. First, the used materials and methods are presented. Afterwards, the proposed photometer is reported, and the results are provided and discussed.

As reported in Tab. 8.1, the photometer needs to be encapsulated and to measure dissolved ozone up to $70\,\mathrm{mg\,l^{-1}}$. Furthermore, the photometer should measure with the direct optical absorption principle and thus not require the addition of supplementary chemicals. The response time should be below 10 s and the cost of the photometer below 1406 €. Additionally, a high selectivity against oxygen and a size below 35 cm x 20 cm x 15 cm are essential. Also, only commercially available staple parts should be used, and no machining should be used during the manufacturing process. The RMSPE should be below 15%.

Tab. 8.1: Overview of the most important requirements for a photometer for dissolved ozone

parameter	requirement
design	needs to be enclosed, no leakage of gaseous ozone into the ambient air
range	dissolved ozone: up to $70\,\mathrm{mg\,l^{-1}}$
measurement principle	direct optical absorption
response time	below 10 s
costs	below 1406 €
selectivity	high selectivity against oxygen
size	below 35 cm x 20 cm x 15 cm
parts	staple parts
manufacturing	no machining
RMSPE	below 15%

8.1 Current state of the art in optical dissolved ozone sensing

In comparison to electrochemical measurement, optical ozone measurement is generally promising due to the possibility of real-time observations and the resulting shorter reaction and recovery durations [10], [347]. According to Equation 3.1, which represents Lambert-Beer's law, the light absorption is directly proportional to the ozone concentration. There are two possible methods for measuring ozone optically: optical absorption or colourimetric methods. Ozone concentration is measured indirectly using colourimetric photometers such as the PF-3 photometer (Macherey-Nagel GmbH & Co. KG, Düren, Germany). This photometer costs approximately 445 € and measures at a wavelength of 530 nm. With colourimetric photometers, continuous measurement is not feasible, and additional chemicals are required. Hence, for use in medicine, direct optical absorption measurement is better suited. Devices for measuring direct optical ozone that are currently on the market are rather costly. For instance, the BMT 964 AQ (BMT Messtechnik GmbH, Stahnsdorf, Germany) and the OPUS sensor (TriOS Mess- und Datentechnik GmbH, Rastede, Germany) cost, respectively, more than 7032 €. The BMT 964 AQ has the following dimensions: 260 mm x 160 mm x 91 mm, and the OPUS sensor has a length of

470 mm and a diameter of 48 mm. As their size already indicates, they are not intended for integration in small bioanalytical devices.

8.2 Materials and methods

Materials The OPUS Sensor (TriOS Mess- und Datentechnik GmbH, Rastede, Germany) is used as a reference sensor during the evaluation. The RMSPE of the commercial optical sensor is less than 8.2% [14]. Also, the ozone production and dispersion in water are comparable to previous research [14]. During the tests, bi-distilled water is used. The following components, shown in Fig. 8.3, are used in the photometer: the quartz glass cuvette 100-QS with a 10 mm light path (Hellma GmbH & Co. KG, Müllheim, Germany), the 260 nm LED ILR-XN01-S260-LEDIL-SC201 (Intelligent Group Solutions Ltd, Thatcham, UK), an LED heat sink, and heat-conducting paste. To prevent rapid photosensor saturation, the power of the LED is decreased via pulse-width modulation to 35%. The GUVA-S12SD photosensor (Adafruit Industries, New York City, NY, USA) is additionally applied. Also, a voltage regulator (MF-6402402), an LED driver with an output current of 350 mA (RCD-24-0.35), a 22-bit analog digital converter (ADC) (MCP 3551) installed on a breakout board, a fan, and a safety switch are applied. The voltage regulator lowers the sensor voltage from 5.7 V to 3.3 V. A Raspberry Pi 3B+, a 4.3" touch-screen, and the ultraviolet (UV) plano-convex lens 48-814 (Edmund Optics Ltd, York, UK) are also used. The Stratasys uPrint SE Plus fused deposition modelling (FDM) 3D-printer is used to create the 3D-printed components, made of acrylonitrile butadiene styrene (ABS). Measurements are carried out using ozonised olive oil, which is used in medical therapy, in addition to ozonised water [40]. Commercially available olive oil purchased from a supermarket is compared with ozonised olive oil (Kastner-Praxisbedarf GmbH, Rastatt, Germany) for the purpose of measuring the ozone content in olive oil.

Lambert-Beer's law An optical absorption photometer, which is based on a direct measurement method, can measure the ozone concentration. Concentration and light absorption are inversely related. Equation 8.1 results by calculating the photometer's concentration using Lambert-Beer's law [126].

$$A = \log(\frac{I_0}{I}) = \varepsilon \cdot c \cdot d \tag{8.1}$$

The absorption is A, the light's intensity without the sample is I_0, the light's intensity with the sample is I, the molar absorption coefficient is ε, the concentration is c, and the path length is d. Lambert-law Beer's can only be applied if monochromatic light is present and the light's path length is known [126]. The molar absorption coefficient for ozone at 260 nm is $3000\,\mathrm{cm^{-1}M^{-1}}$ [348].

Simulation Ray Optics Simulation [349], an open-source online application that simulates light refraction and reflection, is used to replicate the photometer setup. Before assembly, the simulation is run to determine the initial configuration for the positions of the light-emitting diodes (LEDs), optical components, and photosensor.

Evaluation Preliminary tests are performed using a setup that allows easy movement of all included parts to identify the ideal positions for the strongest photometer signal. Then, using these positions, a second configuration is created. Two measurement series are conducted with a total of 66 measurement values for the evaluation of the photometer's second configuration. Measurements are done every 2 min to 4 min with gradually rising ozone concentrations during the first measurement series. A second series of measurements is conducted in a similar manner, but with decreasing ozone concentrations. The measurements are performed with increasing time intervals because the concentrations decline logarithmically rather than linearly. The ozone concentration is raised in the first measurement series during the course of 83 min, reaching a maximum of $19\,\mathrm{mg\,l^{-1}}$. Since ozone decay takes significantly longer than it does to ozonate water and hence raise the ozone concentration, additional measurements are made in the second measurement series with decreasing ozone concentrations. Thus, the second measurement series lasts 135 min. Non-ozonised and ozonised water are used for the measurements. Both the root mean squared error (RMSE) and the RMSPE are calculated after determining the linear regression.

The photometer is also used to measure the amount of ozone in both pure and ozonised olive oil, in addition to bi-distilled water. The utilised ozonised olive oil has a distinct look from pure olive oil. Instead of the pure olive oil's golden yellow colour, it looks more translucent and white. At room temperature (RT), the ozonised olive oil appears more viscous than the non-ozonated oil. For a comparison with Lambert-Beer's law, the viscosities of the various measuring substances (in this case, ozonised and pure olive oil) must be comparable [126]. In order to get a comparable viscosity for both samples, the oils are heated to 40 °C. Four measurements are taken for both oils. The average is then determined for both the pure and the ozonised olive oils.

Software Python 3 is used to create the software that controls all electronic components, conducts measurements with the photometer, communicates with the user through the graphical user interface (GUI), and displays the results on the GUI. A zero measurement, a single measurement, or a continuous measurement may all be performed using the GUI. Using the Lambert-Beer law, the concentration is determined by the observed intensity of the photosensor signal. The current readings, the moving average over the past 10 s, and the current ozone concentration are all shown for each measurement.

8.3 Setup of the novel photometer for dissolved ozone

The manufacturing technique for the photometer uses 3D-printing to enable low-cost production, and the device has a single-board microprocessor inside. The ideal positions for the LED, photosensor, and both lenses, according to simulation findings, are shown in Fig. 8.1. Moreover, Fig. 8.1 depicts the photometer's simulated light path. Fig. 8.2 shows a schematic overview of all electrical connections between the included components. The essential components for one photometer cost less than 843 € (for a quantity of 1 piece) and less than 496 € (for 100 pieces), making the photometer much less expensive than existing photometric ozone sensors. And this despite the fact that lenses and cuvettes constructed of borosilicate glass, which are expensive, high-quality optical components for UV light, are utilised. For manufacturing and assembly, only standardised or 3D-printed components that are easily available are selected.

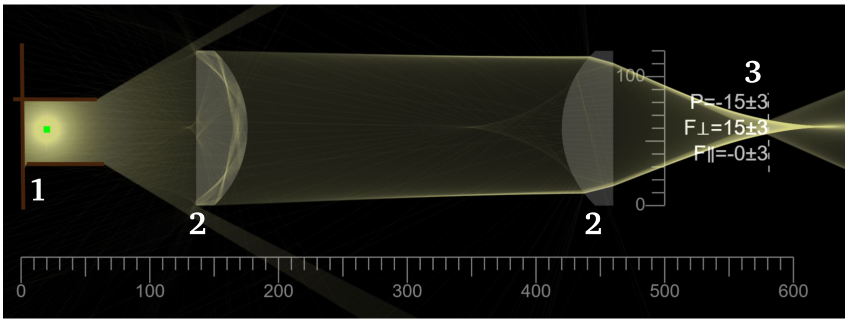

Fig. 8.1: Setup and initial positions of the LED (1), both lenses (2), and the photosensor (3). With the use of Ray Optics Simulation [349], the image is obtained. Both rulers display the scale in pixels. Calculated and presented for the photosensor are the rates of energy flow P, perpendicular momentum flow F⊥, and parallel momentum flow F‖ across the shown line segment. [346] © 2024 IEEE

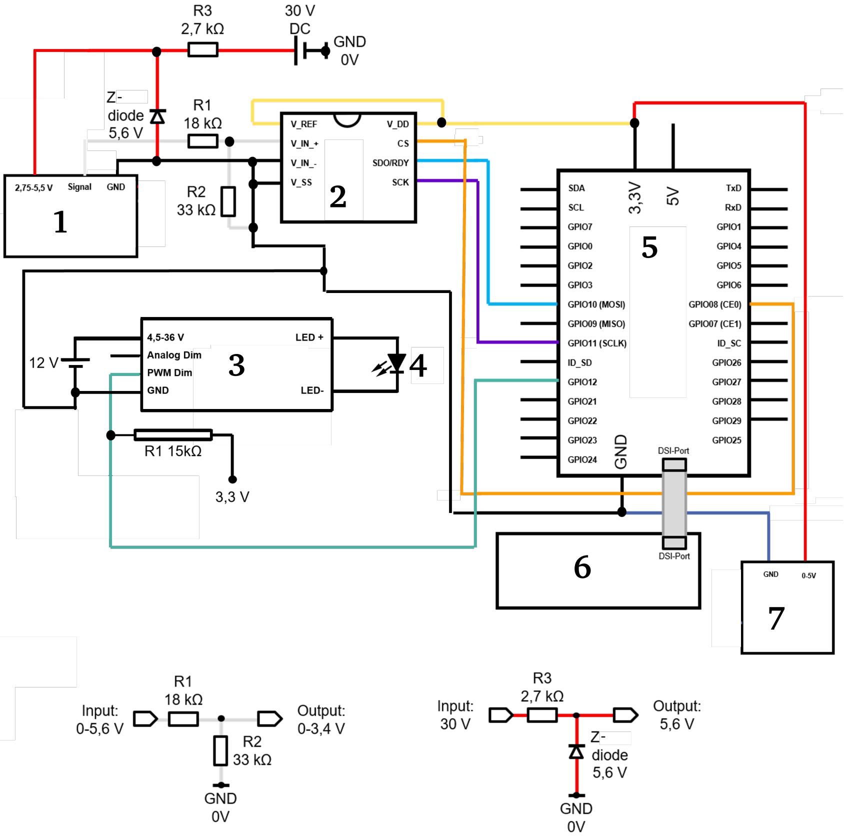

Fig. 8.2: Circuit of the final photometer setup for each of the following electrical components: photosensor (1), ADC (2), LED driver (3), LED (4), Raspberry Pi (5), touch-screen (6), and LED fan (7). [346] © 2024 IEEE

The photometer may therefore be easily rebuilt. An exploded view of all components, including the optical bench (depicted in green) and the housing (shown in blue) with touch-screen for the photometer setup, is shown in Fig. 8.3. The photometer's entire assembly size measures 11.5 cm x 16.1 cm x 9.8 cm.

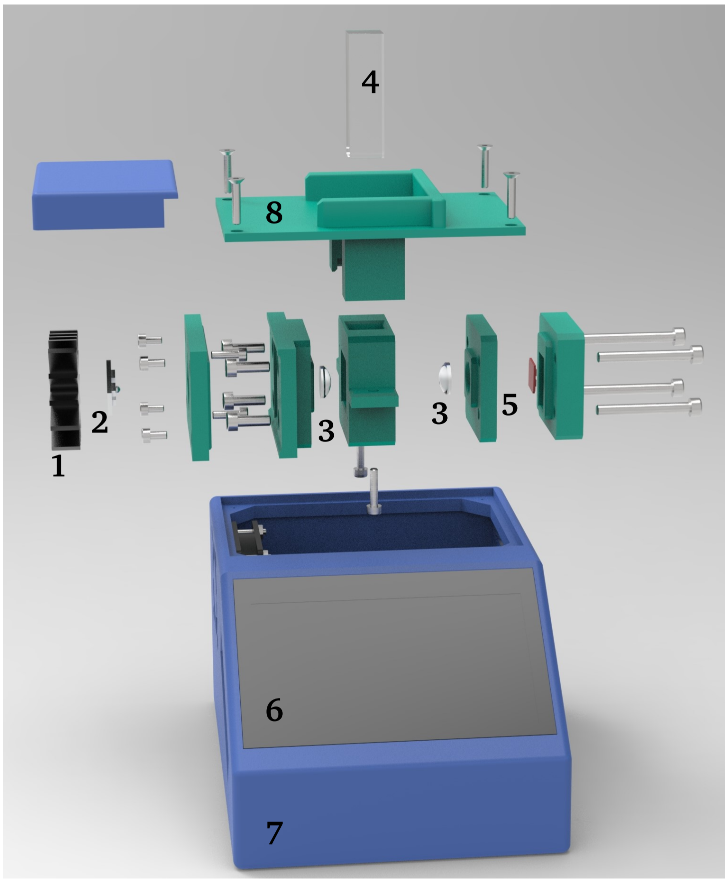

Fig. 8.3: LED heat sink (1), LED (2), lenses (3), cuvette (4), photosensor (5), and touch-screen (6) are shown in an exploded view of the photometer setup. The housing (7) is shown in blue, while the optical bench is depicted in green (8). [346] © 2024 IEEE

The final photometer that measures the dissolved ozone concentration through optical absorption is shown in Fig. 8.4.

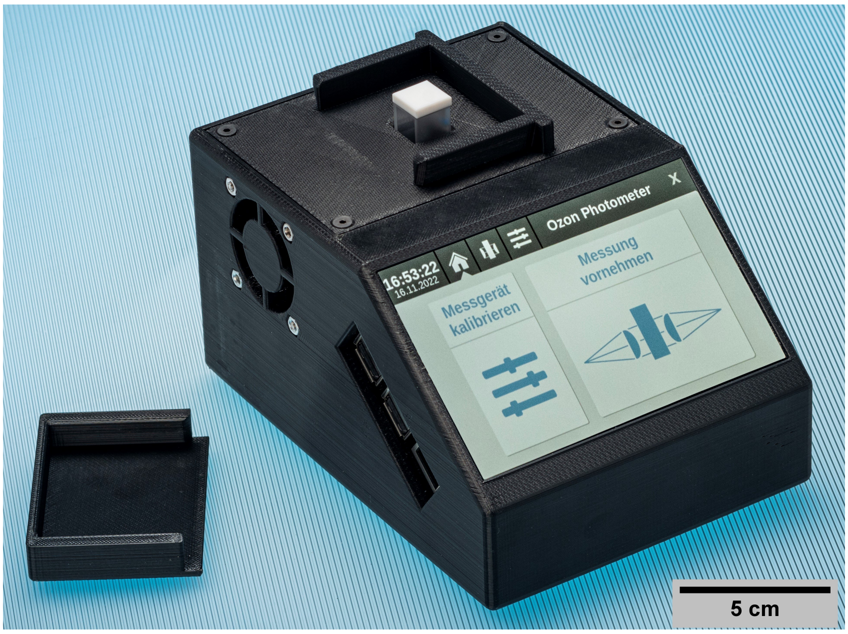

Fig. 8.4: Shows the final photometer configuration with touch-screen; the sliding cover is removed from the photometer's top side. [346] © 2024 IEEE [Image: Markus Breig, KIT]

8.4 Evaluation of the photometer for dissolved ozone

The developed photometer's measurement values in comparison to an optical reference sensor submerged in water are shown in Fig. 8.5. As a result, the linear regression is calculated, yielding

$$y = 1.1152 \cdot x. \tag{8.2}$$

The linear regression's R^2 value is 0.9977. The proposed photometer has a RMSPE of 14.68% and a RMSE of $1.04\,\mathrm{mg\,l^{-1}}$.

Moreover, studies are carried out to determine the concentrations of ozone in both pure and ozonised olive oil. Pure olive oil has an average photosensor output voltage of 2.2 mV, while ozonised olive oil has a value of 2.5 mV. Here, the intensity I from Equation 8.1 corresponds to the output voltage of the photosensor. Lambert-Beer's law predicts that when ozone is present, the output intensity I and consequently the photosensor's output voltage will be lower than they would be in the absence of ozone. The intensity in the absence of ozone yields I_0. The photosensor output voltage values indicate that there is a discernible difference between the two oils; however, the ozonated oil has a lower absorbance than pure olive oil. This demonstrates that Lambert-Beer's law does not apply here, making it impossible to determine the ozone concentration in ozonated oils with the presented photometer.

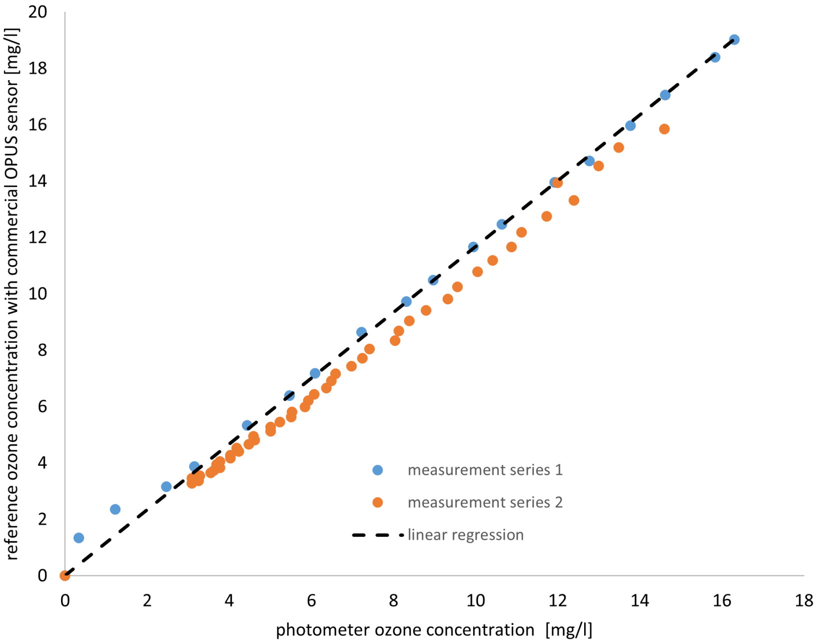

Fig. 8.5: Measurements for dissolved ozone and linear regression for the obtained photometer results in comparison to an optical reference sensor. The first measurement series with increasing ozone concentrations is displayed in blue, and the second measurement series with decreasing ozone concentrations is displayed in orange. For the combination of both measurement series, a linear regression is calculated. [346] © 2024 IEEE

8.5 Discussion

Here, a design for a dissolved ozone photometer is investigated. The following summarises and discusses the requirements that are fulfilled or need further research in accordance with Tab. 8.1.

Enclosed design The enclosed design was successfully implemented for the photometer. The dissolved ozone is separated from the operator by a lid.

Measurement range For the reported photometer, dissolved ozone concentrations of up to $20\,\mathrm{mg\,l^{-1}}$ are investigated. Further research is necessary to measure dissolved ozone up to $70\,\mathrm{mg\,l^{-1}}$. These ozone concentrations are currently not investigated because higher ozone concentrations could not be generated with the ozone generator. In general, measurement of higher ozone concentrations is possible with the photometer, but they need to be generated first. This is only possible if either the temperature during ozone generation is lower or an increased pressure is enabled during the ozonation process.

Measurement principle The measurement principle used for the photometer should be based on direct optical absorption. This requirement is fulfilled because this measurement principle is implemented for the photometer.

Response time The response time should be below 10 s. This is achieved because the current concentration is always calculated as an average over the last 10 s. Thus, every 10 s the ozone concentration value is calculated.

Costs The target regarding the costs of the photometer is a value below 1406 €. For a quantity of 1 piece, the photometer costs less than 843 €, and for a quantity of 100 pieces, the photometer costs less than 496 €.

Selectivity against oxygen The requirement of measuring ozone selectively is achieved because the photometer is based on the optical absorption measurement principle.

Size The photometer's dimensions should not exceed 35 cm x 20 cm x 15 cm. This target is reached, as the photometer has only a size of 11.5 cm x 16.1 cm x 9.8 cm.

Staple parts, no machining necessary Only commercially accessible or 3D-printed components are used in the proposed photometer, making it simple to build.

Root-mean-square percentage error The RMSPE for the photometer should be below 15%. The presented photometer has a RMSPE of 14.68% compared to 8.2% of the reference sensor. Thus, the presented photometer shows accurate measurement results while costing around 17 times less than the reference sensor.

Additionally to the presented photometer, the measurement of the ozone concentration in olive oil with the photometer is investigated. However, it is not possible to measure the ozone concentration in olive oil with the presented photometer. Probably, this is resulting from the oil's structure changing during the ozonation process.

9

Electrochemical dissolved ozone sensing in medicine

Parts of this chapter are based on: L. Petani, A. Schweizer, C. Pylatiuk, P. Stiller, U. Gengenbach, and M. Ungerer, “Optimised inkjet-printing parameters and processing techniques for an exemplary structure of an oxygen sensor on a polyimide substrate”, Boston, MA, USA: IEEE International Conference on Flexible, Printable Sensors and Systems (FLEPS), Jul. 9–12, 2023. DOI: `10.1109/FLEPS57599.2023.10220420`.

Parts of this chapter are based on: L. Petani, L. Llupa, Z. Peng, G. Ogata, L. Koker, U. Gengenbach, Y. Einaga, and C. Pylatiuk, “Dissolved ozone sensing in water and blood based on commercial screen-printed and BDD electrodes”, Toronto, Canada: IEEE Biomedical Circuits and Systems Conference (BIOCAS), Oct. 19–21, 2023. DOI: `10.1109/BioCAS58349.2023.10388985`.

As a preliminary assessment, the manufacturing of an exemplary oxygen sensor structure with inkjet-printing (IJP) is evaluated. Comparatively to traditional subtractive fabrication, additive manufacturing of sensors utilising printing methods minimises the consumption of functional materials and the generation of waste. It is also possible to meet new challenging criteria for healthcare, industrial, or environmental applications. Among these, electrochemical sensor-based healthcare monitoring applications are expanding rapidly [352]. Digital technologies, such as IJP [215] and aerosol jet printing [353], are reviewed in this context, with a focus on IJP as the most popular additive manufacturing technique for printed electronics [354]. There are two primary categories of IJP processes: raster- and vector-based IJP. Raster-based IJP includes moving a multi-nozzle printer across a substrate line-by-line and depositing droplets in accordance with an image of the target geometry that is represented as a bitmap. The quality of edges that are not parallel to the printing direction, however, may suffer from the staircase effect as a result of this line-by-line printing method unless particular steps, such as modifying droplet volume, are conducted. However, raster-based IJP is straightforward and yields uniform results when printing larger filled regions. In contrast, a single-nozzle printer is used in vector IJP to travel in every direction. As a result, high-quality printing may be achieved on edges that are not parallel to the main axis. Polygons are typically used to approximate non-straight lines. Parallel lines with an overlap are printed to fill up areas [355]. In conclusion, vector-based IJP provides greater flexibility in making high-quality prints with complicated forms and curves, whereas raster-based IJP is better suited for larger filled areas. Applications for printed sensors include biomolecule detection, pH measurement, ion detection, and gas sensing (for example, oxygen detection) [180]. For the performance of the final sensor, it is essential to investigate various IJP settings and sintering techniques [356]. As polyimide (PI) has exceptional thermal stability, it is frequently used as a substrate for flexible electronics, especially for high-temperature curing inks [207]. Pre-processing techniques, such as plasma treatment, may be considered since printing on a PI substrate presents difficulties with wetting [207]. The particular material combination must be taken into consideration while setting the pre-processing, post-processing, and IJP parameters. Here, the best pre-processing, IJP parameters, and sintering conditions are identified for the combination of a PI substrate with inkjet-printed commercial gold, silver, and SU-8 passivation inks. The processing conditions for this material combination have not yet been comprehensively examined, according to a survey of the literature.

In addition, novel electrochemical sensors for measuring dissolved ozone are investigated. While the metabolic processes that occur during ozone therapy are well understood, it is currently impossible to determine the amount of ozone present in tissues and blood [45]. Hence, a precise measurement of the ozone concentration is essential for the ongoing development and use of ozone treatment in order to prevent over- and under-dosing and to construct patient-specific therapies. Tab. 9.1 summarises the requirements for such an electrochemical ozone sensor. In the following, an electrochemical dissolved ozone sensor that is based on screen-printed electrodes from a commercial source is presented. Thereby, the modified commercial sensor with a polydimethylsiloxane (PDMS) or polytetrafluoroethene (PTFE) membrane costs in the low single-digit US dollar range.

Tab. 9.1: Overview of the most important requirements for an electrochemical ozone sensor

parameter	requirement
measurement temperature	below 40 °C
response time	below 15 s
wavelength	no UV light
size	integration in a 22-gauge spinal needle
measurement range	dissolved ozone: up to 70 $\mathrm{mg\,l^{-1}}$
costs	below 100 €
in-line measurement	enabled for continuous measurement
RMSPE	below 20%

The achieved accuracy for measuring ozone using various PTFE and PDMS membranes is examined, as both of the membranes are promising for an ozone sensor [138], [209]. Also, a proof-of-concept for the use of membrane-free and electrolyte-free boron-doped diamond (BDD) electrodes to monitor ozone in blood is presented. This establishes the basis for monitoring dissolved ozone concentrations with a compact design and low-cost sensors in a variety of applications.

9.1 Current state of the art in electrochemical dissolved ozone sensing

First, the manufacturing of an exemplary oxygen sensor structure with IJP is focused. In earlier research, the IJP parameters for a commercial silver nanoparticle (AgNP) ink on a paper substrate were examined [356]. Evaluation is also conducted for the ink ejection properties for commercial AgNP ink on a PI substrate, including drop spacing values, track widths, and gap sizes [357]. Also, it has been determined what the ideal printing layer number and sintering conditions are for a non-commercial gold ink when it is printed on paper or a silicon wafer [358]. In addition, the sintering procedures and IJP conditions for nano copper (Cu) ink on a polyethylene terephthalate (PET) substrate are investigated [359].

There are dissolved ozone sensors, as reported in Tab. 3.5, that are generally accessible on the market; however, they are often large and expensive [10]. For instance, the dissolved ozone monitor (Eco Sensors, Inc., Newark, CA, USA) measures ozone between $0\,\mathrm{mg\,l^{-1}}$ and $2\,\mathrm{mg\,l^{-1}}$ and has a size of 79.5 mm x 39.6 mm x 34.5 mm. The sensor costs 515 € and has an accuracy of 20%. For the measurement of the ozone concentration in blood, only indicators that change in response to ozone concentration, such as protein thiol groups, total antioxidant status, or thiobarbituric acid reactants, are presently used [32].

9.2 Material and methods

For the manufacturing of the exemplary oxygen sensor structure, the materials and methods are reported in the following. Afterwards, the materials and methods for the manufacturing of the novel ozone sensors are presented. Thereby, a novel sensor that uses either PTFE or PDMS membranes and commercial screen-printed electrodes is reported for measuring dissolved ozone in water. In addition, another novel sensor is presented that uses BDD electrodes and can measure dissolved ozone in blood. By using BDD electrodes, the use of an electrolyte and a membrane can be omitted.

Oxygen sensor layout The sensor layout is defined as a rectangular pad for the reference electrode (RE), a round pad for the working electrode (WE), and a circular arc pad for the counter electrode (CE), based on earlier work [215], and the commercial electrodes 8DS.C220AT (Metrohm GmbH & Co. KG, Filderstadt, Germany). Three conductor lines are added with rectangular pads at their ends to link the electrodes to the readout electronics. Fig. 9.1a shows the complete sensor layout, and Fig. 9.1b depicts the sensor layout without the passivation layer in order to visualise the conductor lines below. The commercial electrodes 8DS.C220AT use active sensor areas with the same dimensions as the electrodes, which are reported in the following. This causes the WE to be larger than in earlier studies [215], which results in a higher measured current of the amperometric sensor. It is important for repeatability that there is low fluctuation between the active electrode area's pads between multiple sensors on the same substrate or other substrates. Several filling techniques are examined for the vector IJP procedure used. The printed circuit board (PCB) design tool Altium Designer (Altium Europe GmbH, Karlsruhe, Germany) [147], [355] is used to design the sensor layout. This involves exporting the

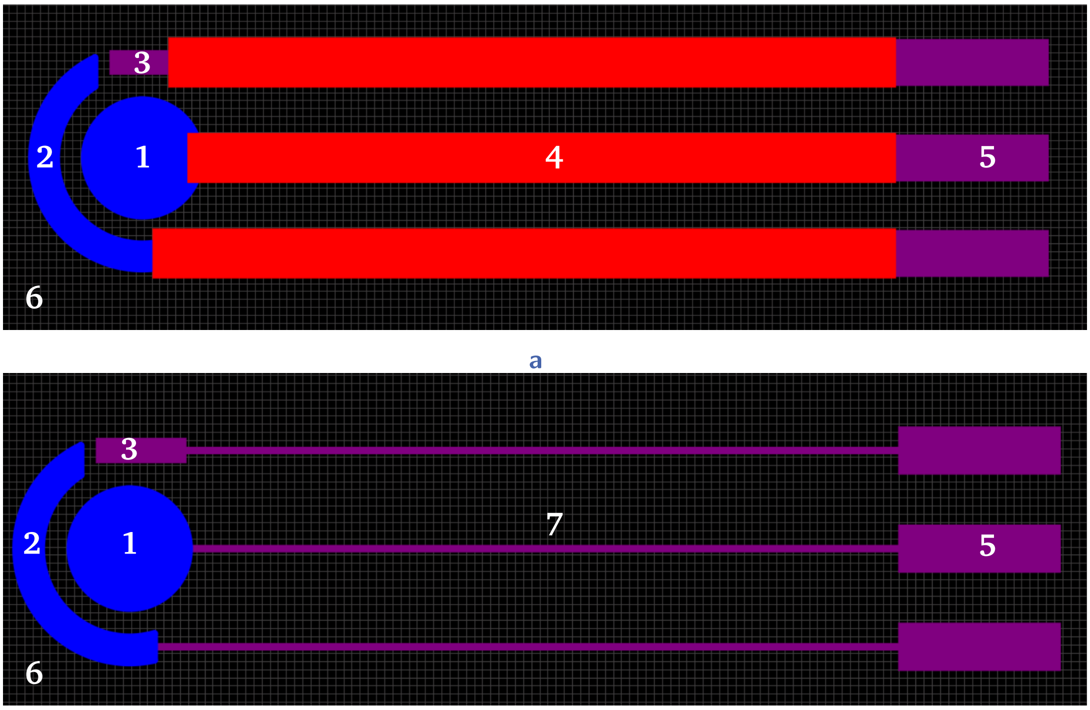

a

b

Fig. 9.1: (a) Oxygen sensor layout, including WE (1), CE (2), RE (3), passivation layer (4), rectangular pads for the readout electronics (5), and substrate (6). (b) Oxygen sensor layout without the passivation layer to show the conductor lines (7) below that layer.

layout file to the CAD-to-CAM data interchange format, known as odb++. A software application is used to post-process these files in order to build optimised machine paths, such as those for filling the pads. The files are then exported as job files for NC printing.

Materials used for the oxygen sensor structure For the manufacturing of the exemplary oxygen sensor structure, the following materials are used: the vector IJP printer MIBBS II [147], [355] with piezo jetters MJ-AL-01 (MicroFab Technologies, Inc., TX, USA), the plasma lab system Atto (Diener Electronic GmbH + Co. KG, Ebhausen, Germany), and ancillary laboratory equipment, such as ovens. The IJP system is shown in Fig. 9.2. The PI film Kapton® HN (DuPont de Nemours, Inc., DE, USA) is used as the substrate. It has a thickness of 125 µm and measures 152 mm by 214 mm. The AgNP ink S-CS01130 (GenesInk, Rousset, France), gold nanoparticle (NP) ink UTDAu40IJ

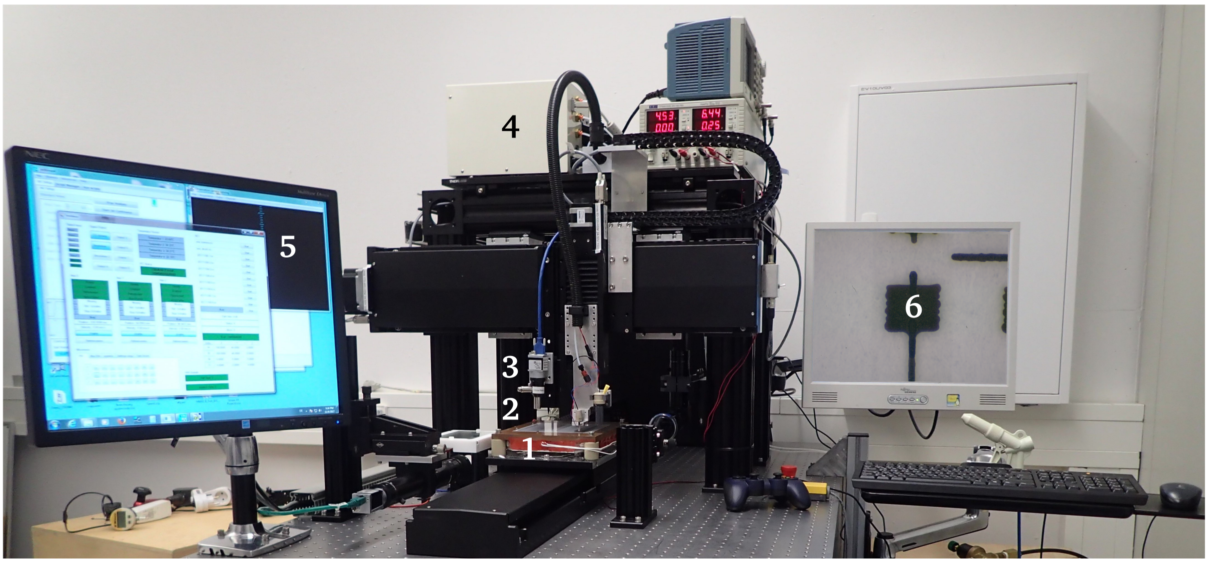

Fig. 9.2: The automated inkjet-printing system MIBBS II, reported by Gengenbach et al. [147], is shown. Included are the vacuum chuck where the substrate is printed (1), the print head (2), the printer reservoir (3), the controller for the printing head's vacuum pressure (4) the printer's user interface (5), where the settings are specified, and the inspection camera's detail view (6). (Modified according to [12])

(UT Dots, Inc., IL, USA), and passivation ink XP PriElex SU-8 1.0 (Kayaku Advanced Materials, Inc., MA, USA) are used for the IJP procedure. Prior to printing, all of the inks are filtered and degassed. Moreover, the UV curing system UJ35 (Panasonic Holdings Company, Osaka, Japan) is utilised. It has a hand-guided LED head (ANUJ6170) and lens (ANUJ6426). At a working distance of 20 mm and a spot diameter of 3 mm, it offers a peak intensity of 3010 $\mathrm{mW\,cm^{-2}}$. The VHX-7000 digital microscope (Keyence Cooperation, Osaka, Japan) is used to capture the microscope images. The probe station Cascade MPS150 (FormFactor Inc., Livermore, CA, USA), tungsten probe tips with a tip size of 150 µm, and the DC resistance measurement function of the LCR-Meter 981 (B&K Precision Corporation, CA, USA) are used to measure the electrical resistivity values. Cross-section measurements are performed using the S Neox 035 Optical Profiler (Sensorfar Group, Barcelona, Spain) in confocal measuring mode with a 50x bright field objective.

Selection of pre-processing, inkjet-printing, and post-processing process for the oxygen sensor Various pre-processing, vector IJP, and post-processing processes are investigated for gold, silver, and passivation inks. Moreover, several filling structures for the WE, CE, and RE are examined. The resulting structures are examined under a microscope for all variants and parameter changes, and the conductor tracks' resistivity is determined. The process with the best electrical resistivity values is then chosen. The electrical resistivity is always determined for three sensors of the same process, and the mean value is then calculated in order to compare various parameters and processing variants. For amperometric sensors, a higher conductivity and a lower electrical resistivity value are preferable [360].

Materials used for the novel ozone sensors An ozone generator and a reference sensor from an earlier published experiment [14] are used to produce and analyse dissolved ozone in water. The used reference sensor, the OPUS sensor (TriOS Mess- und Datentechnik GmbH, Rastede, Germany), has a RMSPE of less than 8.2%. Commercial electrodes 8DS.C220AT (Metrohm GmbH & Co. KG, Filderstadt, Germany), a potentiostat 8AUT204 Autolab PGStat 204 with multiplexer (Metrohm GmbH, Filderstadt, Germany), double-sided silicone tape 96042 with dimensions of 9 mm in width and 0.127 mm in thickness (3M Coperation, Maplewood, MN, USA), and an 8 mm stamping tool are also utilised. The commercial electrodes have the following size: 3.4 cm x 1 cm x 0.05 cm. Potassium nitrate 0.1 M is used as the electrolyte for the screen-printed electrodes, and bi-distilled water is applied as the measuring substance. 47 mm-diameter PTFE unlaminated hydrophilic membranes (Sterlitech Cooperation, WA, USA) are used. These membranes have the following pore sizes (thicknesses): 10 µm (thickness of 130 µm), 1 µm (thickness of 203 µm to 305 µm), 5 µm (thickness of 152 µm to 254 µm), 0.45 µm (thickness of 25 µm to 51 µm), and 0.2 µm (thickness of 25 µm to 51 µm). Also, 125 mm x 125 mm PDMS sheet membranes GASKET-UT-200PK, GASKET-UT-50PK, and GASKET-UT-20PK (SiMPore Inc., NY, USA) are applied. These membranes are non-porous and have the following thicknesses: 200 µm, 50 µm, and 20 µm. Fig. 9.3a shows all used materials for the application of the membranes on the commercial sensors.
BDD electrodes are used, which can measure ozone without utilising a membrane and electrolyte [71], to quantify the amount of ozone in blood. Shorter diffusion paths are achieved without a membrane. In addition, omitting an electrolyte makes the sensor design simpler. The Handlex ozone generator (Nikka Micron Co. Ltd., Waseda, Japan), as well as potentiostat 8AUT204 Autolab PGStat 204 (Metrohm GmbH, Filderstadt,

Germany), and 1% BDD as WE and CE are applied. The production of the 1% BDD electrodes follows the electrochemical methods described in earlier work [361]. For the RE, Ag/AgCl is connected with a salt bridge. Also, porcine blood (Tokyo Shibaura Zoki K.K., Tokyo, Japan) is purchased. The V-570 UV/VIS/NIR Spectrometer is used as the reference sensor for the blood ozone measurements (Jasco Cooperation, Tokyo, Japan).

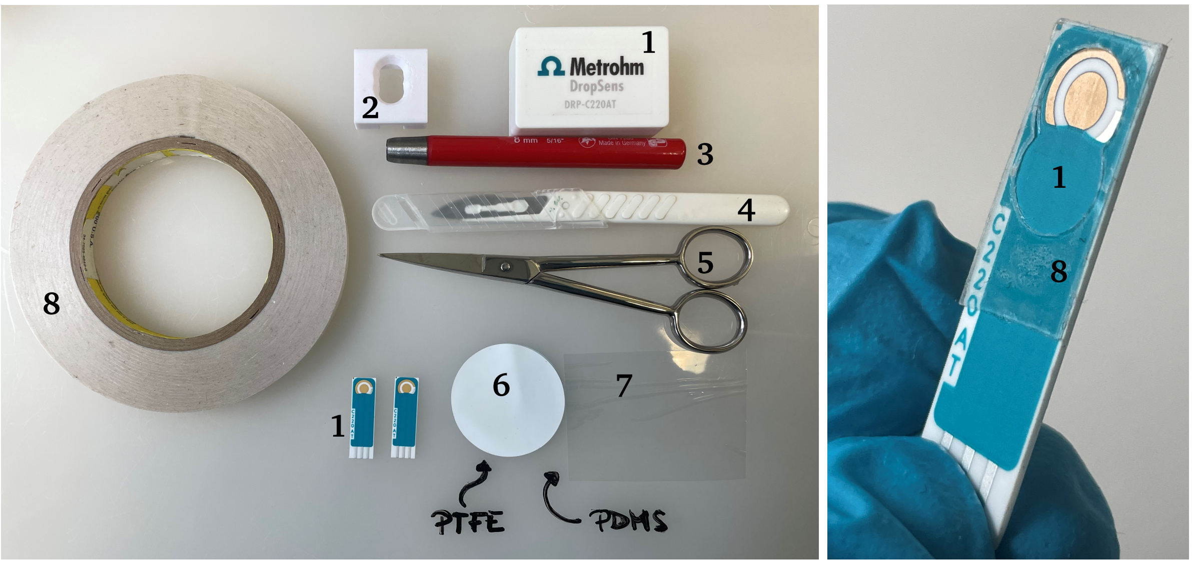

a

b

Fig. 9.3: **(a)** Materials that are used for the application of the membranes on the screen-printed commercial electrodes (1), including stamping mask (2), stamping tool (3), scalpel (4), sciccors (5), PTFE membrane (6), and PDMS membrane (7). **(b)** Applied double-sided silicone tape (8) on the screen-printed electrodes (1).

Preparation and modification of the ozone sensors An intermediate adhesive layer (shown in Fig. 9.3b), consisting of double-sided silicone tape, is created before the membrane is attached to the sensor. Three layers of double-sided adhesive tape make up the intermediate adhesive layer, creating a chamber above the sensor's active electrode area. Two circles with an overlapped diameter of 8 mm each make up the chamber. Afterwards, electrolyte is injected into a chamber between the membrane and the active electrode area of the commercially available screen-printed electrodes. The schematic of the overall preparation and modification process is shown in Fig. 9.4

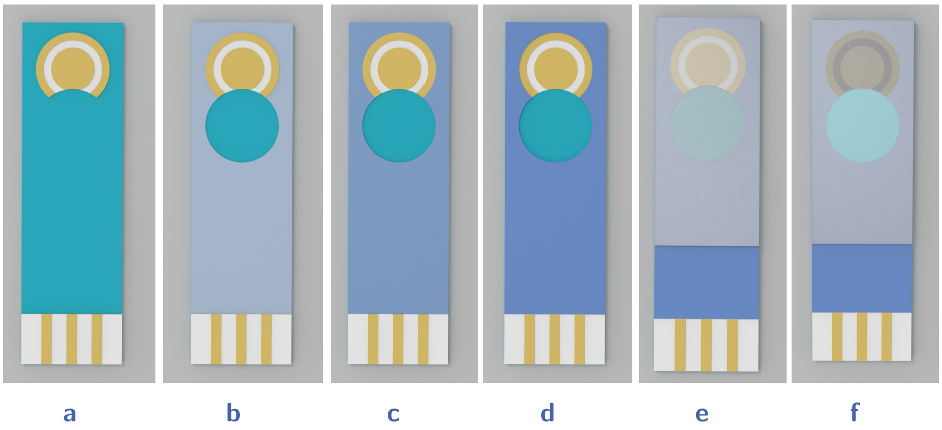

Fig. 9.4: (a) Original sensor. (b) Sensor with the first layer of double-sided adhesive tape. (c) Sensor with the second layer of tape. (d) Sensor with the third layer of tape. (e) Sensor with the attached membrane. (f) Final prepared ozone sensor with injected electrolyte.

Fig. 9.5a depicts the injection of the electrolyte into a sensor with a transparent PDMS membrane. Fig. 9.5b shows a sensor with a PTFE membrane and an injected electrolyte.

Fig. 9.5: (a) Injecting 0.1 M potassium nitrate electrolyte (1) into the space (2) between PDMS membrane (3) and the active electrode area (4). (Modified according to [351] © 2023 IEEE) (b) Ozone sensor based on commercial screen-printed electrodes (5) with a PTFE membrane (6). The o-ring sealing (7) and silicone sealing (8) are above the conductor paths (9) between the sensor and the potentiostat connection.

Furthermore, for the measurement of dissolved ozone in blood, BDD electrodes are used. The BDD electrodes are produced in accordance with prior work [362]. As a result, the electrodes are first pre-treated with cyclic voltammetry ($\mathrm{NaClO_4}$, start potential at 0 V, upper potential at 3.5 V, lower potential at -3.5 V, 20 scans, and a scan rate of $1\,\mathrm{V\,s^{-1}}$) and then hydrogen terminated using chronoamperometry ($\mathrm{NaClO_4}$, -3.5 V for 50 s).

Evaluation of the ozone sensors The experimental setup for measuring ozone in water to assess the performance of the screen-printed sensors is shown in Fig. 9.6a. Fig. 9.6b shows a detailed picture of the measuring chamber with all of the sensors it contains, including the novel ozone sensors. The measurement chamber with the reference sensor is filled with bi-distilled water prior to conducting the ozone concentration measurements in water using the modified commercial, screen-printed electrodes. The measurement chamber's dissolved ozone concentration is determined using the reference sensor. The chamber is entirely sealed off during the experiments by a lid with sealing. This lid has four apertures for the modified electrochemical sensors as well as additional apertures for an ozone disperser, oxygen sensor, and temperature sensor. The water is ozonised using an ozone generator until the target ozone concentration is obtained.

Every membrane type is subjected to three to four measurement series, each of which has between 15 and 18 measurement points with an ozone concentration range of $0\,\mathrm{mg\,l^{-1}}$ to $15\,\mathrm{mg\,l^{-1}}$. The measuring chamber is refilled with fresh bi-distilled water for each measurement series, and new ozone sensors are selected. Using a potentiostat and the NOVA software (Metrohm GmbH & Co. KG, Filderstadt, Germany), linear voltammetric measurements are conducted. With the start potential at 0 V, the stop potential at 1 V, the scan rate at $0.1\,\mathrm{V\,s^{-1}}$, and the step at 2.44 mV, the NOVA process includes a linear sweep voltammogram with a staircase profile. A multiplexer is used to record the four channels' findings directly, one after the other. Following that, the peak current of the linear voltammetric readings is calculated using Python. The reference sensor's measurements of the dissolved ozone concentration levels are plotted against the peak currents of each measurement series. The ozone concentration is determined using the modified screen-printed electrodes and the obtained linear regression. Outliers are then located using the Z-score approach. When a measurement's Z-score is either -1 or 1, it qualifies as an outlier.

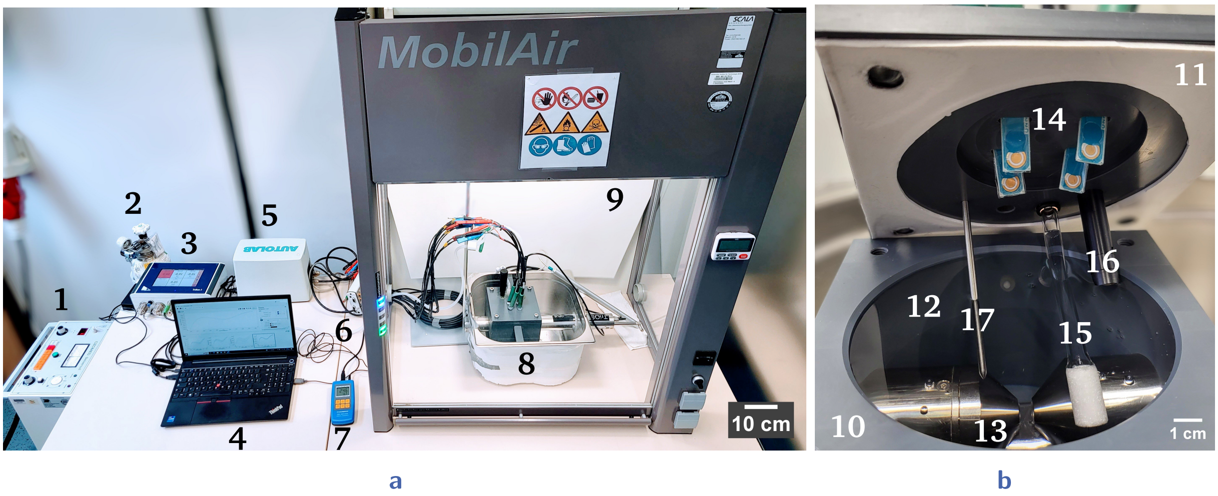

Fig. 9.6: **(a)** Ozone generator (1), medical oxygen (2), reference sensor processing unit (3), laptop (4), potentiostat (5), multiplexer (6), reference oxygen sensor processing unit (7), measurement chamber (8), and mobile filtration cupboard (9) are all parts of the experimental setup used for the evaluation. [351] © 2023 IEEE **(b)** Measurement chamber (10), lid with sealing (11), bi-distilled water (12), reference sensor for dissolved ozone (13), novel ozone sensors (14), ozone-oxygen disperser (15), dissolved oxygen sensor (16), and temperature sensor (17). [351] © 2023 IEEE

The number of outliers varies from measurement series to measurement series, between six and twenty-four outliers per membrane type.

The experimental setup for evaluating the BDD electrodes for the detection of the dissolved ozone concentration in blood is shown in Fig. 9.7. When using BDD electrodes to measure dissolved ozone in blood, cyclic voltammetry is used. Thereby, a start potential at 0.7 V, an upper potential at 0.7 V, a lower potential at -0.1 V, a stop potential at 0.69 V, one scan, and a scan rate of 0.1 $\mathrm{V\,s^{-1}}$ are applied. Between each measurement, hydrogen termination is carried out. Using the reference sensor, the concentration is calculated for each measurement value. Also, a calibration curve is carried out, in which the reference sensor and BDD electrodes are used to detect the amount of dissolved ozone in water.

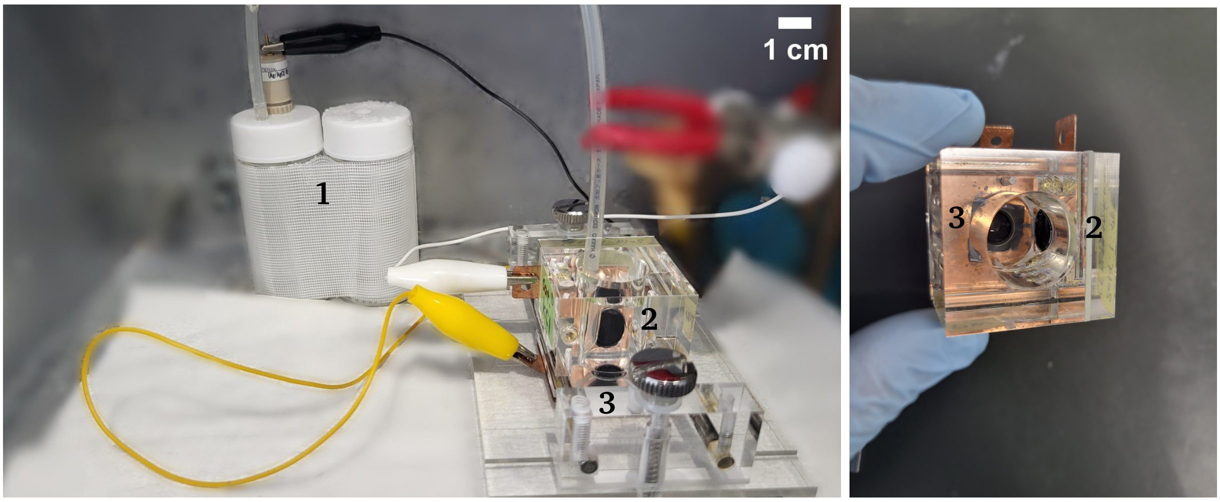

a

b

Fig. 9.7: **(a)** RE (1), CE (2), and WE (3) are part of the experimental setup for the assessment of the BDD electrodes for measuring ozone in blood. [351] © 2023 IEEE **(b)** Shows a close-up view of the measurement chamber, including CE (2) and WE (3).

Summary of the preparation process for the ozone sensors Fig. 9.8 shows an overview of the preparation, modification, and evaluation process for the screen-printed ozone sensors.

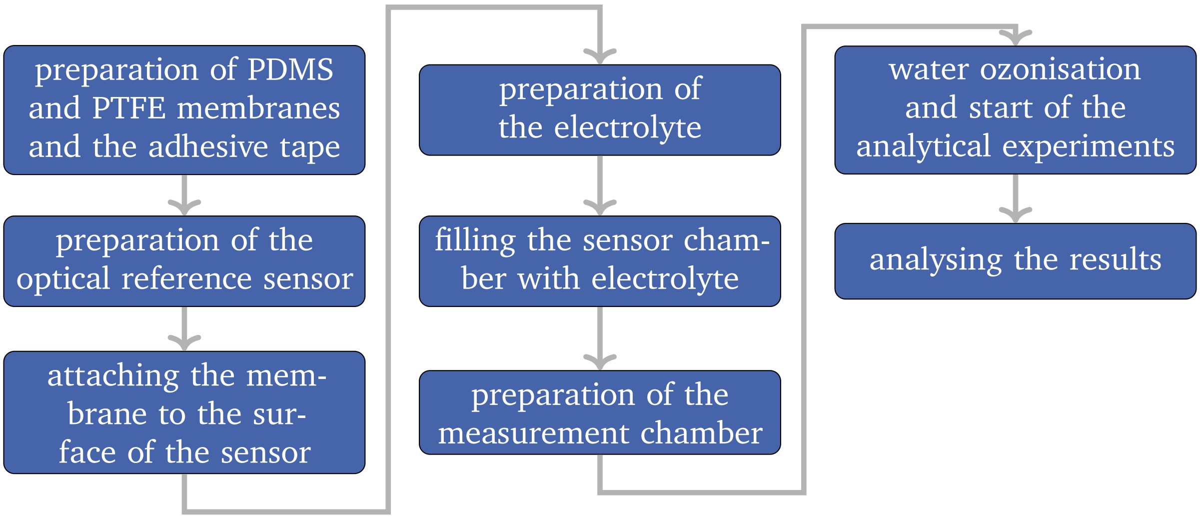

Fig. 9.8: Overview of the process for preparing, modifying, and evaluating the screen-printed ozone sensors.

9.3 Evaluation and results of the oxygen and ozone sensors

First, the evaluation and results of the exemplary oxygen sensor structure are reported.

Filling strategy for the vector inkjet-printing process Several electrode boundaries, filling procedures, and directions for each ink and electrode shape are examined in order to produce electrode surfaces with consistent morphology. All active gold electrode pads have polygonal boundary lines printed around them for good sensor repeatability with regard to electrode edge quality. Sufficient edge quality is attained for the active electrode region formed of silver ink without the use of an additional boundary line. Lines parallel to the long pad axis produce the best results as a filling approach for the vector IJP procedure of the rectangular pads. For the circular arc pad, optimal results are attained with parallel lines printed perpendicular to the conductor tracks. For the circular pad, optimal results are achieved when filled with parallel lines.

Final process chain for manufacturing the sensors Here, the whole workflow is outlined that enabled the best possible electrode surface morphology and electrical resistivity measurements for the exemplary oxygen sensor structure. First, the silver ink is printed, then the gold ink, and subsequently the passivation ink. The schematics of the final process chain is shown in Fig. 9.9.

The PI substrate is first thermally pre-processed for 60 min at 300 °C in a preheated oven. Then, using a MJ-AL-01-050 piezo jetter, the silver ink is printed at a substrate temperature T_S of 50 °C. For this IJP process, the following parameters are selected: a backpressure p of -5.17 mbar, a single-pulse waveform (44.0 V for 25 µs), an axis acceleration a of 1500 $\mathrm{mm\,s^{-2}}$, and a printing velocity v of 12.5 $\mathrm{mm\,s^{-1}}$. The drop distance (centre to centre) is 50 µm for both printed conductor tracks p_L and pad filling lines p_P. The distance between two consecutive pad filling lines l_L is 80 µm. The conductor tracks and pads' overlap D measures 0.5 mm. The ink droplets have a mean velocity of 2.91 $\mathrm{m\,s^{-1}}$ and a mean volume of 153 pl at a frequency of 2 kHz. The vacuum chamber drying process is followed by oven sintering in the post-processing of the printed silver structures. Drying is conducted with the plasma lab system. The substrate is held in the

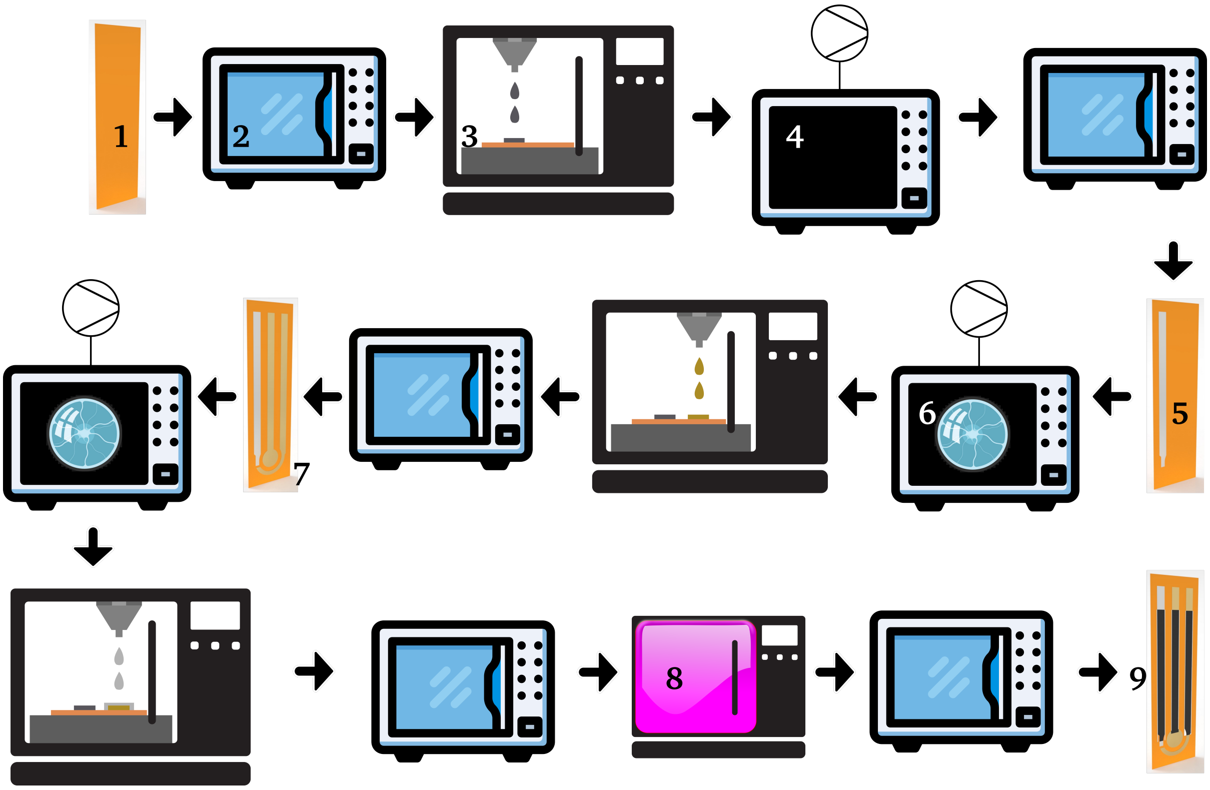

Fig. 9.9: Shows an overview of the final process chain, including initial PI substrate (1), oven (2), IJP (3), vacuum chamber (4), post-processed silver ink (5), vacuum plasma chamber (6), and post-processed silver and gold ink (7), UV radiation step (8), and post-processed silver and gold ink passivated with SU-8 ink (9).

vacuum chamber until a 0.24 mbar chamber pressure is attained. The oven sintering is carried out for 10 min at 150 °C.

Following the post-processing steps for the silver ink, plasma pre-processing for the gold ink is carried out. In the vacuum plasma lab system, the substrate with the printed silver structures is placed. The chamber is then evacuated to 0.26 mbar, argon is injected at 0.22 l min^{-1}, and plasma is ignited at 0.3 mbar and maintained for 3 min at 50 W. The gold ink is then printed using a MJ-AL-01-050 piezo jetter with the following settings: a backpressure p of -5.17 mbar and an adjusted double-pulse waveform (50.0 V for 15 µs followed by an idle time of 12 µs and then again 50.0 V for 9 µs). Additionally, the parameters p_L=30 µm, p_P=40 µm, l_P=90 µm, D=0.5 mm, v=50 mm s^{-1}, a=1500 mm s^{-2}, and T_S=75 °C are determined with preliminary experiments for the selected ink and substrate combination. The ink droplets have a mean velocity of 1.69 m s^{-1} and a mean

volume of 91 pl at a frequency of 2 kHz. The substrate is sintered in the oven for post-processing following printing with the gold ink, using a heating curve that consists of three heating ramps, each followed by a dwell period. The initial ramp begins at room temperature (RT) and rises to 100 °C in 30 min, followed by the same amount of dwell time. A dwell duration of 60 min follows the second ramp to 250 °C in 30 min. Following the third ramp, which takes place within 20 min and gets the temperature to 300 °C, there is a 30 min dwell period. The oven is then cooled down to 50 °C in 6 h. When RT is once more attained after 6 h, the substrate is taken out of the oven.
The pre-processing for the SU-8 ink is carried out using an additional argon plasma treatment, using the same plasma process settings that were used prior to printing the gold ink. Following that, the SU-8 ink is jetted using a MJ-AL-01-025 piezo jetter with the following settings: backpressure p of 3.79 mbar, a modified double-pulse waveform (35.0 V for 29 µs, followed by 5 µs of idle time, and then 40.0 V for 5 µs), p_P=8 µm, l_P=65 µm, D=0.5 mm, v=25 mm s^{-1}, a=1500 mm s^{-2}, and T_S=50 °C. The ink droplets have a mean velocity of 5.67 m s^{-1} and a mean volume of 69 pl at a frequency of 2 kHz. The four processes that follow are post-processing procedures that adhere to the criteria set out by ink manufacturer Kayaku. The substrate is first heated for 5 min at 110 °C. The SU-8 structures are exposed to UV radiation in the next step. At maximum power, the UV curing is carried out at a distance of about 30 mm at a speed of 4.5 mm s^{-1}. The substrate is then post-processed in the oven for 5 min at 110 °C. The substrate is placed in an oven for the last phase of the process, during which the oven is heated from RT to 160 °C in 45 min. For 30 min, the temperature is maintained at 160 °C. After that, the oven is turned off, and the substrate is left inside the enclosed oven for the rest of the night to slowly cool down.

Results for the exemplary oxygen sensor layout The finished exemplary structure of the oxygen sensor, obtained with the final process chain, is depicted in Fig. 9.10a, and Fig. 9.10b displays a close-up of the inkjet-printed structure. These images demonstrate the very consistent surface morphology of the electrodes made possible by the vector IJP process chain optimisation. The RE is created of silver ink, while the WE and CE are made of gold ink. The three conductor tracks are all SU-8-passivated. Measurements of resistance and profile with the final process chain are used to determine the electrical resistivity values (ρ). An overview of these results is shown in Tab. 9.2.

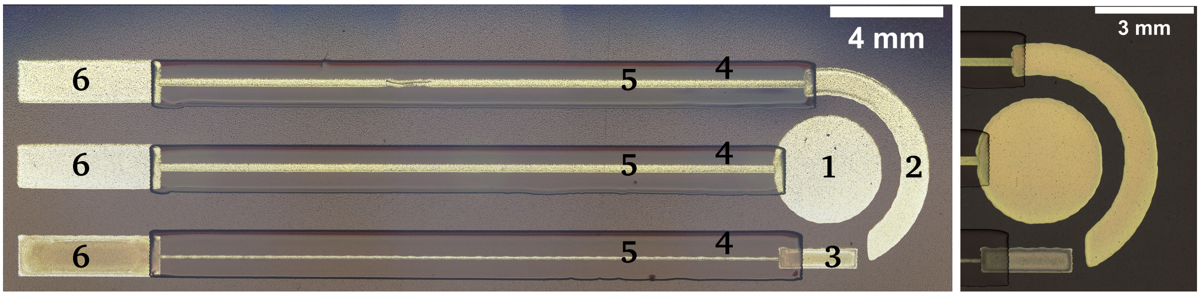

a b

Fig. 9.10: **(a)** Shows the sensor obtained with the final process chain, including WE (1), CE (2), RE (3), passivation layer (4), conductor tracks (5), and connection pads to readout electronics (6). **(b)** Depicts a detailed view of the active electrode area of the final sensor. Silver is the first printed layer, gold the second, and SU-8 passivation the third. [350]

Tab. 9.2: Electrical resistivity values ρ (average, maximum, and minimum) for gold and silver ink for the exemplary oxygen sensor structure and maximum temperature during the final process chain. The maximum process temperature is determined by the gold ink because it is printed after the silver ink. Therefore, the silver ink is also exposed to the sintering temperature of the gold ink. Also, the resistivity of the bulk material is provided.

ink	maximum process temperature	ρ_{average} [µΩ cm]	ρ_{maximum} [µΩ cm]	ρ_{minimum} [µΩ cm]	ρ_{bulk} [µΩ cm]	$\frac{\rho_{\text{average}}}{\rho_{\text{bulk}}}$
gold	300 °C	5.25	6.00	4.16	2.214 [363]	2.37
silver	300 °C	2.56	2.78	2.33	1.587 [363]	1.61

Thereby, ρ yields for silver 2.56 µΩ cm with a maximum value of 2.78 µΩ cm and a minimum value of 2.33 µΩ cm. For gold, ρ results in 5.25 µΩ cm with a maximum value of 6.00 µΩ cm and a minimum value of 4.16 µΩ cm. This is equivalent to about 1.61 times the specific bulk resistivity of silver (1.587 µΩ cm) and approximately 2.37 times the specific bulk resistivity of gold (2.214 µΩ cm), respectively at 293 K [363]. Additionally, after being post-processed in a tunnel furnace for 5 min at 200 °C, the obtained resistivity of the silver lines is even lower than the lowest resistivity recommended by the manufacturer, GenesInk (2.8 µΩ cm). The producer UT Dots states that the resistivity of the gold ink is 2 to 7 times that of bulk gold after curing at 200 °C to 400 °C. The achieved resistivity of 2.37 times the bulk gold is close to the minimum specified by the ink producer, even though the ink was never heated above 300 °C.

Results for the novel ozone sensors The findings (root mean squared error (RMSE) and RMSPE) for the various membranes for the novel sensors measuring ozone in water, either composed of PDMS or PTFE, are shown in Tab. 9.3. Because PDMS is a non-porous material, the pore size is not specified for any of the membranes and is not listed in the table. No measurements are conducted for the PDMS membrane, which has a thickness of 20 µm, because it was impossible to fill the chamber with electrolyte because of the thin thickness. The PTFE membranes with 0.2 µm pore sizes and thicknesses between 25 µm and 51 µm yield the lowest error and, thus, the lowest difference between the novel sensor and the reference sensor. The RMSE and RMSPE values for this membrane are 3.62 $\mathrm{mg\,l^{-1}}$ and 30.41%, respectively.

Tab. 9.3: RMSE and RMSPE values for several membranes with diverse materials, pore sizes, and thicknesses.[351] © 2023 IEEE

material	pore size [µm]	thickness [µm]	RMSE [$\mathrm{mg\,l^{-1}}$]	RMSPE [%]
PDMS	-	200	6.34	62.60
PDMS	-	50	5.14	106.47
PDMS	-	20	-	-
PTFE	10	130	5.38	49.02
PTFE	5	152-254	3.12	38.87
PTFE	1	203-305	3.06	37.30
PTFE	0.45	25-51	3.57	35.51
PTFE	0.2	25-51	3.62	30.41

In order to determine the concentration of dissolved ozone in water, several series of measurements are conducted. In the following, the results for a PTFE membrane with a pore size of 0.2 µm are reported. The results of the linear voltammetric measurement with a staircase profile between 0 V and -0.5 V, the reference sensor values for the peak absorption value, and the resulting linear regression are shown in Fig. 9.11. For the linear voltammetric measurement, the start potential is at 0 V, the stop potential is at

-0.5 V, the scan rate is $0.1\,\mathrm{V\,s^{-1}}$, and the step is 0.00244 V. As a result, the R^2 of the linear regression is 0.94 and the linear regression for this measurement series yields

$$\mathrm{y} = (-2.5 \cdot 10^{-7}) \cdot \mathrm{x} + (-5.4 \cdot 10^{-7}). \tag{9.1}$$

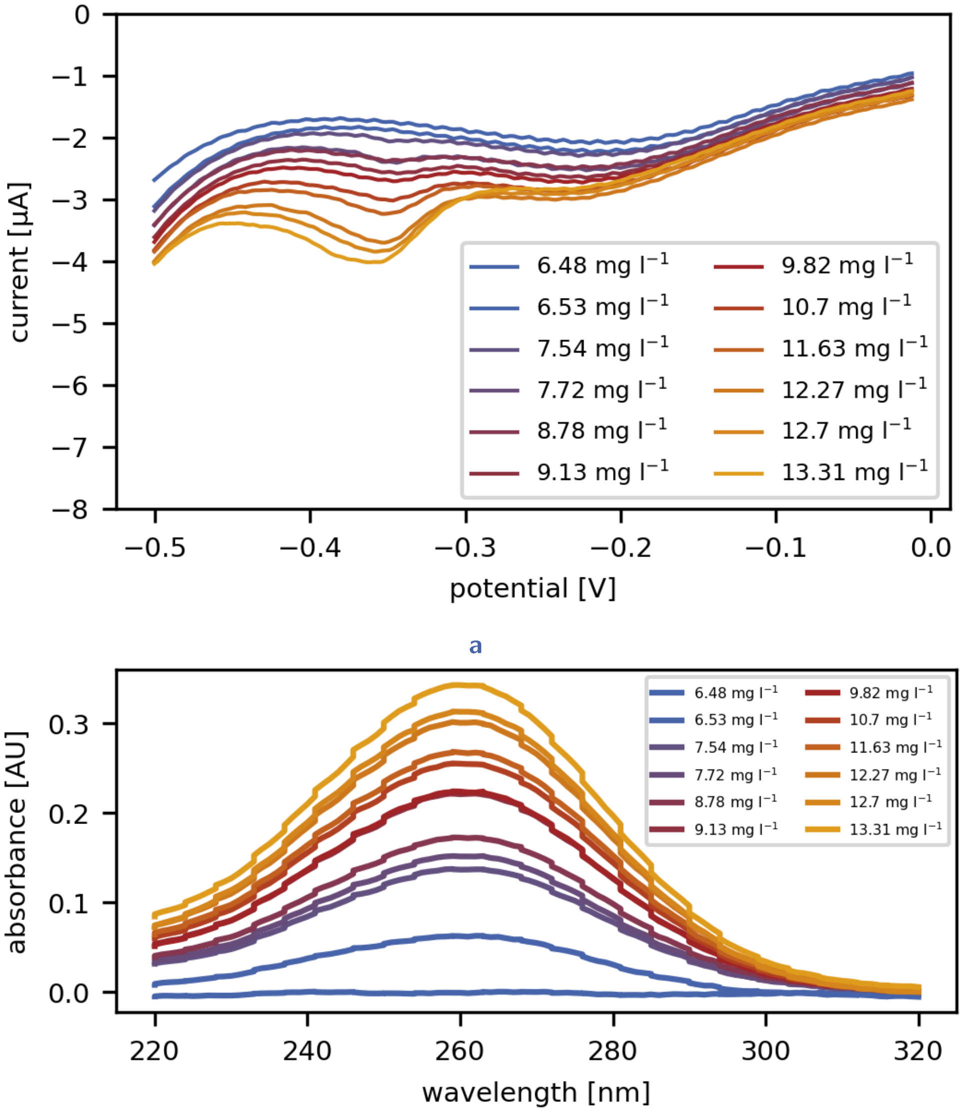

a

b

Fig. 9.11: **(a)** Measurement of the dissolved ozone concentration in water using a linear voltammetric procedure. [351] © 2023 IEEE **(b)** Resulting reference sensor values for the peak absorption.

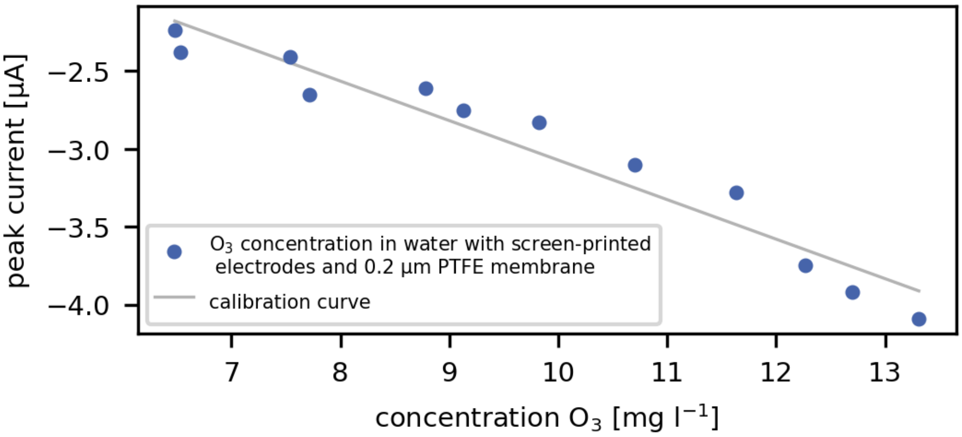

c

Fig. 9.11: **(c)** Displays the calibration curve (shown in grey) and the difference between the novel ozone sensors (represented in blue) and the reference sensor's ozone concentration. [351] © 2023 IEEE

The calibration curve for measurements of the dissolved ozone concentration in water (shown in blue) using BDD electrodes is presented in Fig. 9.12a. The R^2 is 0.95 and the linear regression yields

$$\mathrm{y} = -1.31 \cdot \mathrm{x} + 0.268. \tag{9.2}$$

Also, the results of the measurement of the dissolved ozone concentration in blood are displayed in red, and the peak current values are mapped with the linear regression to the concentration values. A proof-of-concept for the detection of dissolved ozone in blood using BDD electrodes is shown in Fig. 9.12b. The different ozone concentrations can be differentiated with discernible peak currents. When different materials are applied for the electrodes in the two sensor designs, the position of the peak current changes [71], which can be observed in Fig. 9.11a and Fig. 9.12b. Only the electrochemical sensor with the BDD electrodes can distinguish between the changing concentrations of ozone in blood; the UV sensor cannot measure its concentration. Due to the strong reactivity of blood and ozone, it is feasible to quantify residual ozone levels in blood using the BDD electrodes even at low residual ozone concentrations of around $0.2\,\mathrm{mg\,l^{-1}}$.

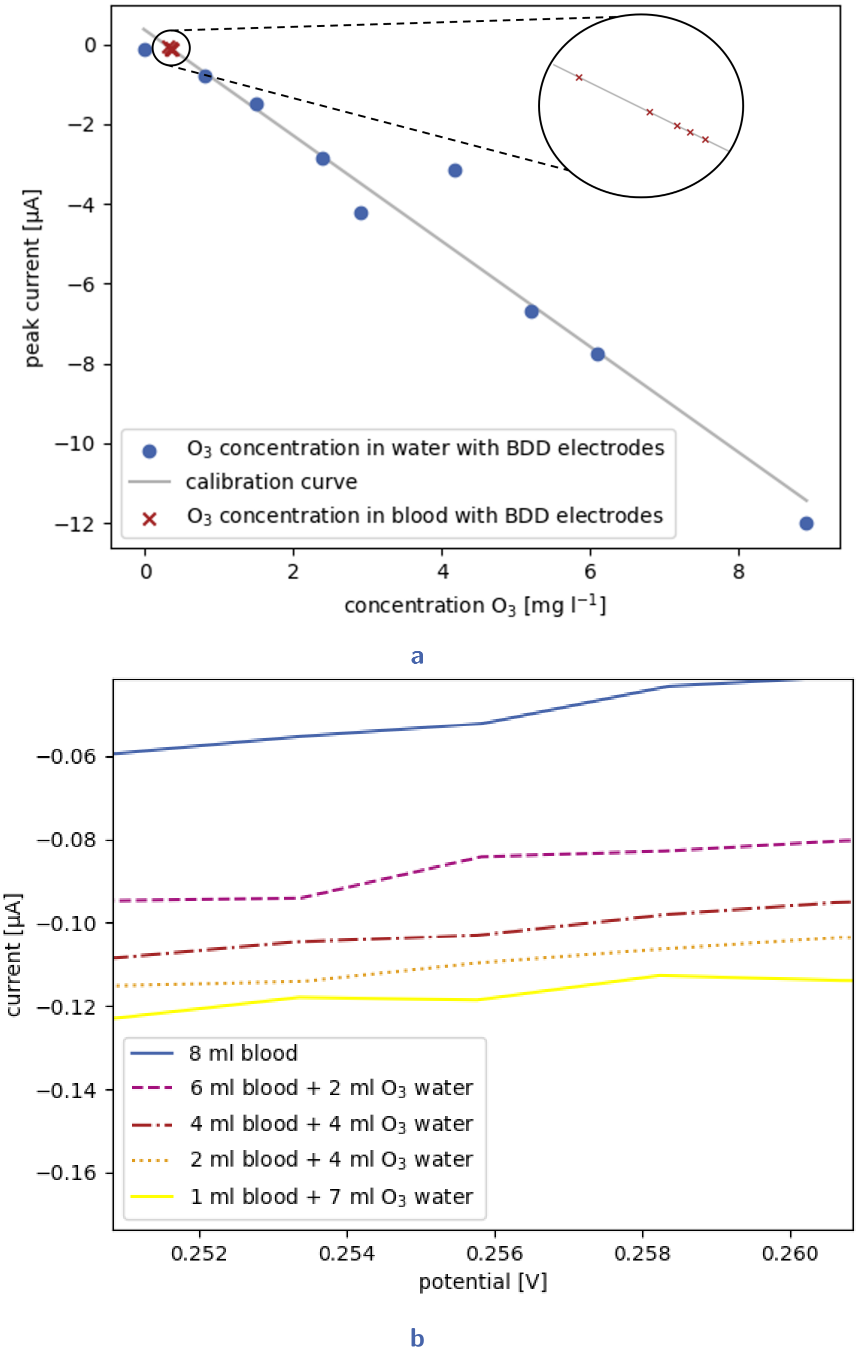

Fig. 9.12: **(a)** Dissolved ozone measured with BDD electrodes in blood (shown in red) are mapped with the calibration curve for dissolved ozone in water (shown in blue) compared to the reference sensor. The resulting regression is displayed in grey. [351] © 2023 IEEE **(b)** Detail view of the cyclic voltammetry used to measure ozone in blood with BDD electrodes. [351] © 2023 IEEE

9.4 Discussion

First, several inks, pre-processing variants, sintering methods, and post-processing variants are examined to determine the best parameters for an exemplary oxygen sensor structure to be printed using IJP. This preliminary experiment builds the foundation for printing an ozone sensor. Here, the workflow that produces the highest conductivity results is outlined. Gold conductors with an electrical resistance of 5.25 µΩ cm and silver conductors with 2.56 µΩ cm are produced using these optimal processing settings. This creates a foundation for the repeatable manufacturing of electrochemical sensors using vector IJP and electrodes made of gold and silver.
Secondly, a sensor is presented for the detection of ozone in water based on either non-porous PDMS or porous PTFE membranes and commercial screen-printed electrodes. The following summarises and discusses the requirements that are fulfilled or need further research in accordance with Tab. 9.1.

Measurement temperature The presented sensors do not need a heated substrate, thus this requirement is fulfilled.

Response time The response time should be below 15 s. Currently, the measurements are conducted with a linear voltammetric measurement. Thereby, the scan rate is $0.1\,\mathrm{V\,s^{-1}}$ and the range between 0 V and -0.5 V is measured. Thus, the duration for one measurement is 5 s.

Wavelength For the electrochemical measurement principle, there is no need for a light activation. Thus, no UV light is present during the measurement.

Size The requirement for the developed sensor is that it needs to be integrated in a 22-gauge spinal needle. The current size of the presented sensor is 3.4 cm x 1 cm x 0.05 cm. Thus, additional work is necessary to further improve the miniaturisation.

Measurement range The aim for the sensor is to be able to measure dissolved ozone concentrations up to 70 $\mathrm{mg\,l^{-1}}$. With the reported sensors, measurements up to 15 $\mathrm{mg\,l^{-1}}$ are conducted. Currently, higher ozone concentrations are not investigated because of the ozonation process with the ozone generator.

Costs The target for the presented sensor are costs below 100 €. This requirement is fulfilled. The cost of the sensor is below 5 €. Thereby, the commercial sensor costs about 3.5 € per sensor. The PDMS membrane costs about 0.36 € and the PTFE membrane 1.13 € per sensor.

In-line measurement The requirement to measure in-line with the sensor is enabled. The sensor measures in the same measurement substance as the reference sensor. Thus, continuous measurement is possible.

Root-mean-square percentage error The RMSPE for the reported sensor should be below 20%. A RMSE of 6.34 $\mathrm{mg\,l^{-1}}$ and a RMSPE of 62.60% is achieved for the PDMS membrane. Also, a 3.62 $\mathrm{mg\,l^{-1}}$ RMSE and a 30.41% RMSPE is attained for the PTFE membrane. However, additional work is important to further reduce the RMSPE of the sensor.

The reported dissolved ozone sensor, which has a compact size, provides an effective substitute for low-cost monitoring of dissolved ozone concentrations in a range of applications. A proof-of-concept for the use of BDD electrodes is also provided to assess blood's dissolved ozone content. Ozone measurements can be performed without a membrane and without electrolyte by utilising BDD electrodes.

Part IV

Antibacterial effects of ozone

Overview Part IV

In the following part, the focus is on investigating research question (RQ) RQ3: Can ozone be further used in medicine as an antibacterial agent for the treatment of, e.g., chronic wounds? First, the outcomes of earlier investigations into the antibacterial properties of ozonated oils are compared. Subsequently, the aim is here to investigate the antibacterial activity against *Escherichia coli* (*E. coli*) for two distinct ozonated oils in relation to the exposure amount and time. The minimal inhibitory concentration of the oils is investigated using agar dilution. Bacterial growth is seen at all of the doses that are tested using the agar dilution method. To assess the inhibitory zone with and without an emulsifier, spread-plating combined with agar dilution is also used. Here, ozonated oils do not prevent bacterial growth in the emulsifier-free and emulsifier-containing experiments with agar dilution combined with spread plating. In order to ascertain the ozonated oil's time-dependent antibacterial activities, the bacteria are also exposed to the oils for varying lengths of time before being cultivated on either a solid or liquid medium. The outcomes for each medium are compared with non-ozonated oil and NaCl solution as a negative control. After 5 min of exposure to the ozonated oil, the bacteria on solid medium are already fully inactivated. Shorter exposure periods are also investigated for the liquid medium. After 1 min, the ozonated oils in the liquid medium show no inhibition. The bacterial growth in the ozonated oils in the liquid medium is significantly reduced after 5 min.

10

Investigation of antibacterial effects of ozone in medicine

Parts of this chapter are based on: L. Petani, A.-M. Jung, R.-R. Frietsch Musulin, G. Sturm, A.-K. Kaster, and C. Pylatiuk, “Exploring the antibacterial effects of ozonated oils in medicine: A study on Escherichia coli inhibition”, *Ozone: Science & Engineering*, pp. 1–8, 2023. DOI: `10.1080/01919512.2023.2233746`.

In the following, the focus is on exploring the antibacterial effects of different ozonated oils. First, the related work in this area is summarised. Second, the materials and methods of the present investigation are described. Afterwards, the results of the conducted experiments are reported and discussed.

10.1 Related work regarding antibacterial effects of ozone

Many studies using various methods, different strains, and yielding conflicting results investigated the antibacterial properties of ozonated oils. The Gram-negative strain *E. coli* [364]–[372] is used in the majority of studies, whereas *Staphylococcus aureus* (*S. aureus*) [8], [364]–[367], [369]–[373] is primarily used to represent Gram-positive species. Just a small number of research focused other strains, such as *Staphylococcus epidermidis* (*S. epidermidis*) [364], [365] and methicillin-resistant *Staphylococcus aureus* (MRSA) [8]. Table 10.1 and Table 10.2 provide systematic summaries of the findings of previous research.

Tab. 10.1: A summary of the techniques currently being utilised, together with experimental data, such as measurement parameter, oil type, peroxide value, culture medium, additive, and bacterial species. [16]

ref.	method	measurement parameter	oil type	peroxide value [meq kg^{-1}]	culture medium	additive	bacterial species
[364]	agar dilution	MIC	sunflower	1300	MH	Tween-80	*E. coli*
[364]	makrodilution	MBC	sunflower	1300	MH	NR	*S. aureus*, *S. epidermidis*
[364]	kinetic analysis	LCC	sunflower	1300	MH	Tween-80	*S. aureus*, *S. epidermidis*
[365]	agar dilution	MIC	sunflower	1300	MH	Tween-80	*S. aureus*, *E. coli*, *S. epidermidis*
[366]	agar diffusion	Hemmhof diameter	sunflower	1400	BHB	NR	*S. aureus*, *E. coli*
[366]	makrodilution	MIC	sunflower	1400	BHB	-	*S. aureus*, *E. coli*
[367]	agar dilution	MIC	sunflower, olive	735-2506	NR	NR	*S. aureus*, *E. coli*
[367]	makrodilution	MBC	sunflower, olive	735-2507	NR	NR	*S. aureus*, *E. coli*
[368]	PP	peroxide value	sunflower	204-1187	NR	NR	*E. coli*
[369]	agar dilution	MIC	sunflower	361-675	NR	NR	*S. aureus*, *E. coli*
[369]	makrodilution	MBC	sunflower	361-675	NR	NR	*S. aureus*, *E. coli*
[373]	agar diffusion	Hemmhof diameter	olive	560-590	MH	NR	*S. aureus*
[370]	agar dilution	MIC	sunflower, linseed, baru	1617-2619	MH	Tween-80	*S. aureus*, *E. coli*
[371]	mikrodilution	MIC	sunflower	150-1800	MH	Tween-80	*S. aureus*, *E. coli*
[372]	modified agar diffusion	Hemmhof diameter	sunflower	335	LB	NR	*S. aureus*, *E. coli*
[8]	agar diffusion	Hemmhof diameter	camellia	2000-2200	NR	NR	*S. aureus*, MRSA
[8]	kinetic analysis	inactivation rate	camellia	2000-2200	NR	DMSO	*S. aureus*, MRSA

LCC: live cell count depending on the time; MBC: minimum bactericidal concentration; NR: not reported; PP: pour-plating and moisted with oil; ref.: reference

Tab. 10.2: Results of the techniques from Tab. 10.1 for various oils with different peroxide values and in relation to *E. coli*, *S. aureus*, and *S. epidermidis*. The number of hours represents the length of time that the particular oil was ozonated. The text "H_2O", "air", or "O_2" adds information on how the oil is ozonated. [16]

reference	oil	PV [$\mathrm{meq\,kg^{-1}}$]	*E. coli*	*S. aureus*	*S. epidermidis*
agar dilution method - MIC for the bacterial species in [$\mathrm{mg\,ml^{-1}}$]					
[370]	SO_{12h}	1761	NA	NA	-
	SO_{24h}	2065	NA	NA	-
	SO_{36h}	2151	7	7	-
	LO_{12h}	1617	10	10	-
	LO_{24h}	2016	10	5	-
	BO_{12h}	2324	NA	NA	-
	BO_{24h}	2619	7	NA	-
	BO_{36h}	1988	10	10	-
	gel_{24h}	1933	≤ 3	≤ 3	-
[367]	SO_{H_2O}	862	9.5	4.5	-
	SO_{H_2O}	2506	0.95	0.95	-
	OO_{H_2O}	735	9.5	4.5	-
	OO_{H_2O}	2439	0.95	0.95	-
[369]	$SO_{\text{with air}}$	361	28.5	19	-
	SO_{air}	675	19	9.5	-
	SO_{O_2}	376	19	9.5	-
	SO_{O_2}	658	8.5	4.75	-
[364]	Oleozón	1300	-	9.5	9.5
[365]	Oleozón	1300	4.75	9.5	2.37
agar diffusion method - Hemmhof diameter in [mm]					
[366]	Bioperoxoil	1400	35.6	42.2	-
[8]	CO	2200	-	17	-

Continued on next page

Tab. 10.2 – *Continued from previous page*

reference	oil	PV [meq kg^{-1}]	*E. coli*	*S. aureus*	*S. epidermidis*
[373]	Novox	590	-	30	-
[372]	Oz.Or.Oil30	335	22.5	23	-
mikrodilution method - MIC in [mg ml^{-1}]					
[371]	$SO_{H_2O, 2h}$	1250	5-10	2.5	-
	$SO_{H_2O, 5h}$	1800	5	1.25	-
mikrodilution method - MIC in [mg ml^{-1}]					
[371]	SO_{2h}	150	NA	40	-
	SO_{5h}	250	20-40	10-20	-
mikrodulution method - MIC in [mg ml^{-1}]					
[366]	Bioperoxoil	1400	2-3.5	2-3.5	-
makrodilution method - MBC in [mg ml^{-1}]					
[364]	Oleozón	1300	-	356	356
[369]	SO_{air}	361	285	128	-
	SO_{air}	675	178	22.5	-
	SO_{O_2}	376	285	178	-
	SO_{O_2}	658	89	22.5	-
[367]	SO_{H_2O}	862	22.5	22.25	-
	SO_{H_2O}	2506	11.12	11.12	-
	OO_{H_2O}	735	22.5	22.25	-
	OO_{H_2O}	2439	11.12	11.12	-
kinetic analysis					
[364]	Oleozón	1300	-	linear correlation between cell count and contact time	
[8]	CO	2200	-	100% after 5 min	
pour plating and wetting with oil - minimum peroxide value in [meq kg^{-1}]					
[368]	SO	204-1187	864	-	-

BO: baru oil; CO: camellia oil; LO: linseed oil; MBC: minimum bactericidal concentration; MIC: minimum inhibitory concentration; NA: not active; OO: olive oil; PV: peroxide value; SO: sunflower oil.

Mueller-Hinton (MH), Brain Heart Blood (BHB), or lysogeny broth (LB) were the three major culture media applied (e.g. [364], [372], [374]). Emulsifying agents, such as Tween-80 [364], [365], [370], [371] or dimethyl sulfoxide (DMSO) [8], were added to enable improved dispersion of oil in water-based media. Numerous research, including [8], [366]–[369], [372], [373], do not specify the media or emulsifiers that were utilised. The oil type containing the antimicrobial agent (here ozone) applied in earlier investigations was primarily ozonated sunflower oil [364]–[372]. Moreover, ozonated olive oil [367], [373], ozonated linseed oil [370], ozonated baru oil [370], and ozonated camellia oil [8], were used. The minimum inhibitory concentration (MIC) was primarily determined by agar dilution [364], [365], [367], [369], [370] and microdilution [371]. Also, agar diffusion experiments were used to identify the inhibitory zone (see [8], [366], [372], [373]). Moreover, the minimal bactericidal concentration was utilised as the primary measuring parameter for the makrodilution approach (see [364], [367], [369]). While minimal peroxide value was the main factor in the study conducted by [368], [364] determined the relation of contact time (ozonated oil with bacteria) and live cell count.

The following investigation is conducted to evaluate the time-dependent effects of exposing *E. coli* cells to ozonated oils in a kinetic analysis due to the conflicting information and lack of systematic assessments of the antimicrobial action of ozonated oils. In the following, the experimental design and the outcomes of an investigation into the antibacterial effects of ozonated oils on *E. coli* K-12 are described.

10.2 Materials and methods

Materials As test strain, *E. coli* K-12 MG1655 is utilised. Growth is conducted on plates with 2% agar-agar or in LB broth (10 g l-1 tryptone, 5 g l-1 yeast extract, 10 g l-1 NaCl). If necessary, Tween-80 (2%, v/v) is applied as an emulsifying agent. Ozonated oils are purchased from ACTIVOZONE (Pontevedra, Spain, Ozone Oil 1200) and Ozolife® (Valencia, Spain, Ozone Oil 600). The peroxide values of the oils are 600 $\mathrm{meq\,kg^{-1}}$ and 1200 $\mathrm{meq\,kg^{-1}}$ ± 10%, respectively, as stated by the manufacturers. Ozone Oil 600 consists of sunflower oil that has been ozonated, olive oil, tea tree oil, ascorbyl palmitate, and tocopherol acetate, while Ozone Oil 1200 contains ozonated sunflower oil and ozonated olive oil. All experiments utilised sunflower oil (Brölio, Hamm, Germany) as a negative control. For both ozonated oils, a test in a third-party laboratory is requested to ascertain the peroxide value's real concentration (my-lab International GmbH, Berlin, Germany). According to the test results, Ozone Oil 1200 has a peroxide value of $428.4\,\mathrm{meq\,kg^{-1}}$, while Ozone Oil 600 has a peroxide value of $92.1\,\mathrm{meq\,kg^{-1}}$.

Preliminary experiments To ensure that the used oils contain ozone and that it has not decomposed due to incorrect storage or transport conditions, or that the oils are falsely declared, qualitative experiments are carried out using potassium iodide starch paper (Macherey-Nagel, Düren, Germany) [375]. Depending on the concentration, the iodide paper turns between brown to blue-violet. The first experiment is for the qualitative detection of ozone. Since the ozonated oil is heated by melted agar during some experiments, it is examined whether ozone outgasses from the oil at increased temperatures. The experiments are carried out with both ozonated oils and, as a negative control, with non-ozonated oil and distilled water. The iodide papers are dipped into the respective oil and the discolouration is recorded with images after 15 min, 45 min, 2 h, and one day, respectively.

Plating and CFU counts *E. coli* cultures are cultivated over night and diluted to an optical density at a wavelength of 600 nm (OD_{600}) of 0.1, i.e. 1.5 x 10^8 $\mathrm{CFU\,ml^{-1}}$ [376]. The lowest temperature achievable (55 °C) is used for plate casting in order to reduce heat-based ozone degradation. Oil is added to the medium at the following concentrations: $1\,\mathrm{mg\,ml^{-1}}$, $15\,\mathrm{mg\,ml^{-1}}$, and $30\,\mathrm{mg\,ml^{-1}}$. The mixture is then vortexed for 60 s. Each plate received 100 µl of a standard bacterium dilution, and each plate is then incubated at 37 °C for 18 h. Manual counting and various automatic cell counters are used to assess the colony forming unit (CFU) count (Promega Colony Counter by Promega Cooperation, APD Colony Counter by APD Lab, and Microbial Colony Counter by MLTool Technologies)

Minimum inhibitory concentration determination The agar dilution procedure without an emulsifier in accordance with the Clinical and Laboratory Standard Institute (CLSI) is used to determine the MIC [364], [365], [367], [369], [370]. Ozone Oil 1200 is used in all experiments in triplicates at concentrations of 30 mg ml^{-1} and 45 mg ml^{-1}. A bacterial suspension with an OD_{600} of 0.01 is created. On agar plates, a spot of 2 µl of the suspension is placed. The inoculated plates are incubated until the spots are absorbed at room temperature (RT). Then, they are incubated for 18 h at 37 °C.

Inhibition zone determination Spread-plating CFU counts are also performed in addition to the CLSI method, where bacteria are distributed evenly across the plate rather than in spots. Plates are incubated at 37 °C for 18 h with oil concentrations of 1 mg ml^{-1}, 15 mg ml^{-1}, and 30 mg ml^{-1} (Ozone Oil 600). The experiments are performed in triplicates. For CFU counts without an emulsifier, oil and medium are combined by vortexing. In 2 ml eppis, a bacterial suspension is made using LB medium as the diluent and an OD_{600} of 0.1. They are diluted by a total of 3^{-1} x 10^{-4} using LB medium. 2% Tween-80 is added to plates that included emulsifiers [365], [370]. 100 µl are used for the inoculation. For combining the medium and emulsifier, two potential scenarios are examined since they can affect how well the oil disperses in the agar medium. Before adding oil, 500 µl of Tween-80 and 25 ml of agar are first combined in a flacon tube and stirred for 10 s. Plates are cast after a second 10 s vortexing period. For the second scenario, 500 µl of Tween-80 and oil are combined in a falcon tube, vortexed for 10 s, and then 25 ml of the agar medium is added and vortexed. Three alternative mixing times of 20 s, 40 s, and 60 s are evaluated here.

Kinetic analysis with liquid and solid medium With a few minor adjustments, kinetic studies in a liquid medium are carried out in accordance with [8]. 900 µl of ozonated oils are combined with 100 µl of oil/bacteria suspension (cell count ml^{-1} in 0.9% NaCl), vortexed for 10 s, and then incubated for 5 min, 10 min, 20 min, or 60 min in Eppendorf tubes, respectively. 10 ml of liquid LB is added to 50 µl of the oil/bacteria solution in culture tubes. At 37 °C, incubation is done for 20 min, 60 min, and 120 min while being shaken (at 180 rpm). The ozone exposure times ranged from 1 min to 60 min, and the OD_{600} is measured at 0 min, 20 min, 60 min, and 90 min. OD_{600} is calculated after 18 h of growth.

Kinetic evaluations are carried out using both a solid medium and a liquid medium. For the solid medium, 50 µl of the same mixture are placed onto agar plates and distributed equally, using the same process as is outlined for the liquid medium. Before counting CFUs, plates are incubated for 18 h at 37 °C.

10.3 Results of conducted experiments

Preliminary experiment - potassium iodide starch paper for the detection of ozone In the following, the results of dipping the iodide paper into the respective oil and the yielding discoloration are reported. After 15 min, no colour change is visible in any of the iodide papers. Since ozone is not present directly in the oil, but binds to the double bonds of the fatty acids during ozonisation and forms stable ozonides there, it may be that the iodide paper does not react to it in the first few minutes. After 2 h, the iodide paper dipped in non-ozonated oil shows no significant discolouration apart from the oily stain. The iodide paper immersed in Ozone Oil 600 shows a slight yellowish discolouration over the entire iodide paper and a yellowish-brown discolouration of the tip. The iodide paper dipped in Ozone Oil 1200 shows a light brown discolouration of the tip. The slightly brownish colour after 2 h indicates that some of the ozonides have decomposed to ozone due to external influences. After one day, a large part of the control iodide paper as well as the ozone oil iodide paper with the Ozone Oil 600 is discoloured light brown with a yellowish discolouration of the ends. The iodide paper treated with Ozone Oil 1200 is completely dark brown.

In the second experiment, the ozone outgassing is examined as a function of temperature. A slightly moistened piece of the iodide paper is clamped in the lid of a 1.5 ml eppi. Two eppis are filled with 10 drops of the respective oil and incubated with the lid closed at 55 °C or 65 °C for 10 min. After 2 min and after 10 min, images of the iodide paper pieces are recorded. To determine how the ozonated oil behaves when mixed with heated aqueous medium, 1 ml of distilled water together with 3 drops of the respective oil is placed in two eppis each, homogenised with the vortexer, and the iodide paper pieces are clamped in the lids. The eppis are incubated at 55 °C and 65 °C, respectively, for 10 min and images are recorded after 2 min and 10 min. In the control experiments, there is no significant discolouration at 55 °C after 2 min. The Ozone Oil 600 discolours the paper yellowish, while the Ozone Oil 1200 turns it yellowish and slightly purple at the edges. After 10 min the negative control still shows no changes. The paper treated with Ozone Oil 600 becomes slightly more yellowish, while the paper treated with Ozone Oil 1200 becomes mostly purple. The experiments at 65 °C show that both ozonated oils turn the paper partially purple after 2 min and almost completely purple after 10 min. The negative controls show no significant discolouration.

From the observations of the experiments, it can be concluded that both tested oils contain ozone. The Ozone Oil 1200, as stated by the manufacturers, has a higher peroxide value than the Ozone Oil 600. The peroxide value serves, among other factors, as an indicator of the amount of ozone present in the oil.

Minimum inhibitory concentration determination This experiment tests the ozonated oil's MIC against *E. coli* using agar dilution without an emulsifier. Bacterial growth is seen at all chosen concentrations, despite very high ozonated oil concentrations. As a result, no MIC can be established. The development of a stable emulsion of oil and nutrient medium is more difficult to achieve at greater concentrations, hence testing at even higher concentrations is not conducted.

Inhibition zone determination The emulsifier-containing and the emulsifier-free experiment are both conducted. In contrast to the control plates with non-ozonated oil, the results for the emulsifier-free experiment reveal no inhibition of bacterial growth by ozonated oil. The findings of the manual counting of the CFUs on each plate are displayed in Tab. 10.3. In summary, no correlation between CFUs and ozone quantity is apparent, and all values, including those of the control groups, are in the same order of magnitude. Because just one sample can be achieved for some groups due to colonies that can not be individually identified, no statistical analysis is done.

Furthermore, the emulsifier-containing experiment is an additional focus. Two methods are used to conduct the Tween-80 emulsifier experiment, and they differ in the sequence in which Tween-80, oil, and culture medium are mixed. To prepare the plates for the first mixing option, Tween-80 and LB medium are mixed together first. Then, the oil is added in the following step at the appropriate concentrations, and the entire mixture is homogenised. The non-ozonated oil is used to make the control plates at concentrations of $1\,\mathrm{mg\,ml^{-1}}$, $15\,\mathrm{mg\,ml^{-1}}$, and $30\,\mathrm{mg\,ml^{-1}}$, respectively. The same concentrations of Ozone Oil 600 are used to create the experimental plates. Both for the experimental plates treated with ozonated oil and for the control plates, the size and quantity of

Tab. 10.3: Counting the CFUs in the experiments to determine the inhibition zone for the emulsifier-free experiment using the test strain *E. coli* and the culture medium LB. Ozone Oil 600 is used as an antibacterial agent, while pure LB medium and non-ozonated oil are used as negative control agents. The oils (ozonated and non-ozonated) are used in each experiment in triplicates (n=3) at three different concentrations (c1, c15, and c30). [16]

LB	oil_{c1}	oil_{c15}	oil_{c30}	ozon. oil_{c1}	ozon. oil_{c15}	ozon. oil_{c30}
1.8×10^7	4.5×10^7	8×10^7	3.4×10^7	4.8×10^7	3×10^7	3.15×10^7
2.4×10^7	NA	NA	4×10^7	7.2×10^7	7.26×10^7	3.45×10^7
3.4×10^7	NA	NA	NA	9.24×10^7	NA	4.7×10^7

c1: 1 mg ml^{-1}; c15: 15 mg ml^{-1}; c30: 30 mg ml^{-1}; NA: not analysable because of too many cells in non-distinct colonies; ozon.: ozonated.

individual colonies do not significantly vary depending on the concentration. Tween-80 aggregates can be detected in the medium of most plates. A quantitative analysis in the form of CFUs counts is omitted due to anomalies, such as partially uncountable cell clusters and air bubbles obstructing quantitative counts.

A second mixing option is used when doing the emulsifier-containing experiment. The LB medium is added, and then the entire medium is mixed to prepare the experimental plates for the second mixing alternative. The amount of time needed to thoroughly merge the LB medium and Tween-80 oil mixture is tested between 20 s, 40 s, and 60 s. Ozone Oil 600 is used to make all plates at concentrations between 15 mg ml^{-1} and 30 mg ml^{-1}. The quantity, shape, and size of colonies on the plates with concentrations of 30 mg ml^{-1} are comparable. Due to some cell clusters, the plates with a concentration of 15 mg ml^{-1} are challenging to evaluate. Comparable to those of the emulsifier-free mixing experiment are the control plates made with agar medium and Tween-80 as well as with agar medium alone. The CFUs are also not counted here for the same reasons as described above.

The first mixing alternative results in plates that have substantially more foam, air bubbles, and Tween-80 clumps in the medium. Because of this, the second mixing alternative is more promising than the first. When compared to the control plates with non-ozonated oil, the results for the emulsifier-free and emulsifier-containing experiments both demonstrate no inhibition of bacterial growth by ozonated oil.

Kinetic analysis with liquid and solid medium OD_{600} measurements are carried out for the kinetic analysis in a liquid medium. Compared to the non-ozonated oil and NaCl treated tubes, the ozonated oils' initial OD_{600} values at 0 min are noticeably greater. For the majority of the examined groups, the OD_{600} decreases when incubator time is increased. The experimental groups using ozonated oil have a higher decrease. The results for the Ozone Oil 1200 are shown in Fig. 10.1a, while those for the Ozone Oil 600 are shown in Fig. 10.1b. The ozone oil exposure times are 1 min, 5 min, 20 min, and 60 min, from left to right. After 1 min, the liquid is extremely turbid for both oils. It starts to get considerably clearer at 5 min and stays that way for longer exposure times after that. The Ozone Oil 1200 exhibits little and huge clumps after 5 min and 20 min, respectively. In the last tube, there are only tiny particles. The control groups are shown in Fig. 10.1c. The left tubes are made with an oil or NaCl suspension and incubated for 1 min, while the right tubes are incubated for 60 min. Liquids that are turbid and include a few tiny particles are visible.

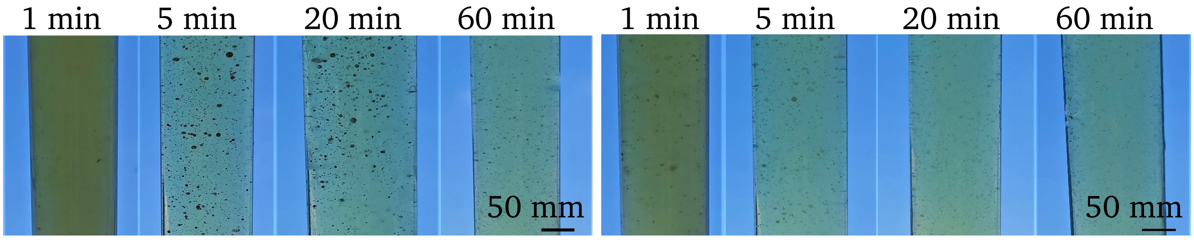

a Ozone Oil 1200 **b** Ozone Oil 600

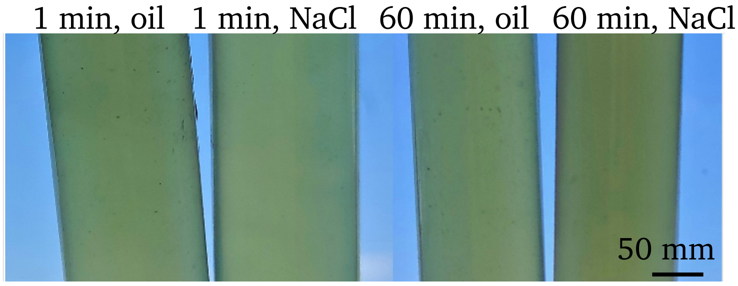

c Control (NaCl and oil)

Fig. 10.1: Tubes filled with the test strain *E. coli* for liquid medium kinetic analysis. The antimicrobial agents utilised are Ozone Oil 1200 (a) and Ozone Oil 600 (b). The used negative control agents (c) are non-ozoanted oil and NaCl and the used culture medium is LB. All agents have exposure periods ranging from 1 min to 60 min. Cloudy patches are seen in the Ozone Oil 1200 analysis, just like in the solid medium kinetic analysis. [16]

There are not many visual differences between the four tubes. The Ozone Oil 1200 and the non-ozonated oil appear quite similar when exposed for 1 min, with the exception that the liquid in the experimental group is clearer than that in the control group. Generally speaking, there are a lot more particles in the experimental group than in the control group. After 18 h of incubation, the OD_{600} is not calculated because the particles and clumps affect the readings and bias the results. After 1 min, the brief exposure duration is insufficient to significantly affect growth because there is no difference between the experimental group and the control group. Both ozonated oils have less bacterial growth after a 5-min exposure period. The results support the finding from solid medium experiments that, for both oils, bacterial growth is significantly to entirely reduced even after a 5-min exposure period. In the experiments, an emulsifier is not required.
Fig. 10.2 displays the results of the kinetic analysis with solid medium. Ozone Oil 600 is used to treat the plates in the top row, and Ozone Oil 1200 is used to treat the plates in the second row. The two bottom rows show the control plates on which non-ozonated oil or NaCl solution is distributed. The results from all of the replicate plates are similar. From left to right, the exposure times are 5 min, 10 min, 20 min, 60 min, and 90 min. Colonies have grown significantly in the two lower rows (control groups). Even after only 5 min of exposure, the Ozone Oil 600 stopped bacterial growth. Individual circular colonies are not visible on any of the Ozone Oil 1200 plates, but tiny areas are seen on each plate, which appear milky and foggy in daylight. A microscope is also used to examine the plates. Using a microscope, a sizable number of rod-shaped *E. coli* bacteria are visible on the control plates. Cloudy patches are seen under the microscope on the experimental plates that are exposed for 90 min to the Ozone Oil 1200. The foggy spots on the experimental plates are not *E. coli*, according to the microscope investigations, but rather another substance that may have been brought on by additives or impurities in the oil. After incubating with ozone for 5 min, no growth is apparent. The CFUs count of the control plates with NaCl solution or non-ozonated oil is therefore skipped. With the exception of leaving out the additive, the kinetic analysis with solid medium is carried out in accordance with [8]. With respect to the different cell types, the results can be compared to the current study. The inactivation rate of *S. aureus* and *S. epidermidis* with camellia oil is 100% after 5 min [8]. The outcomes are thus equivalent to the current work.

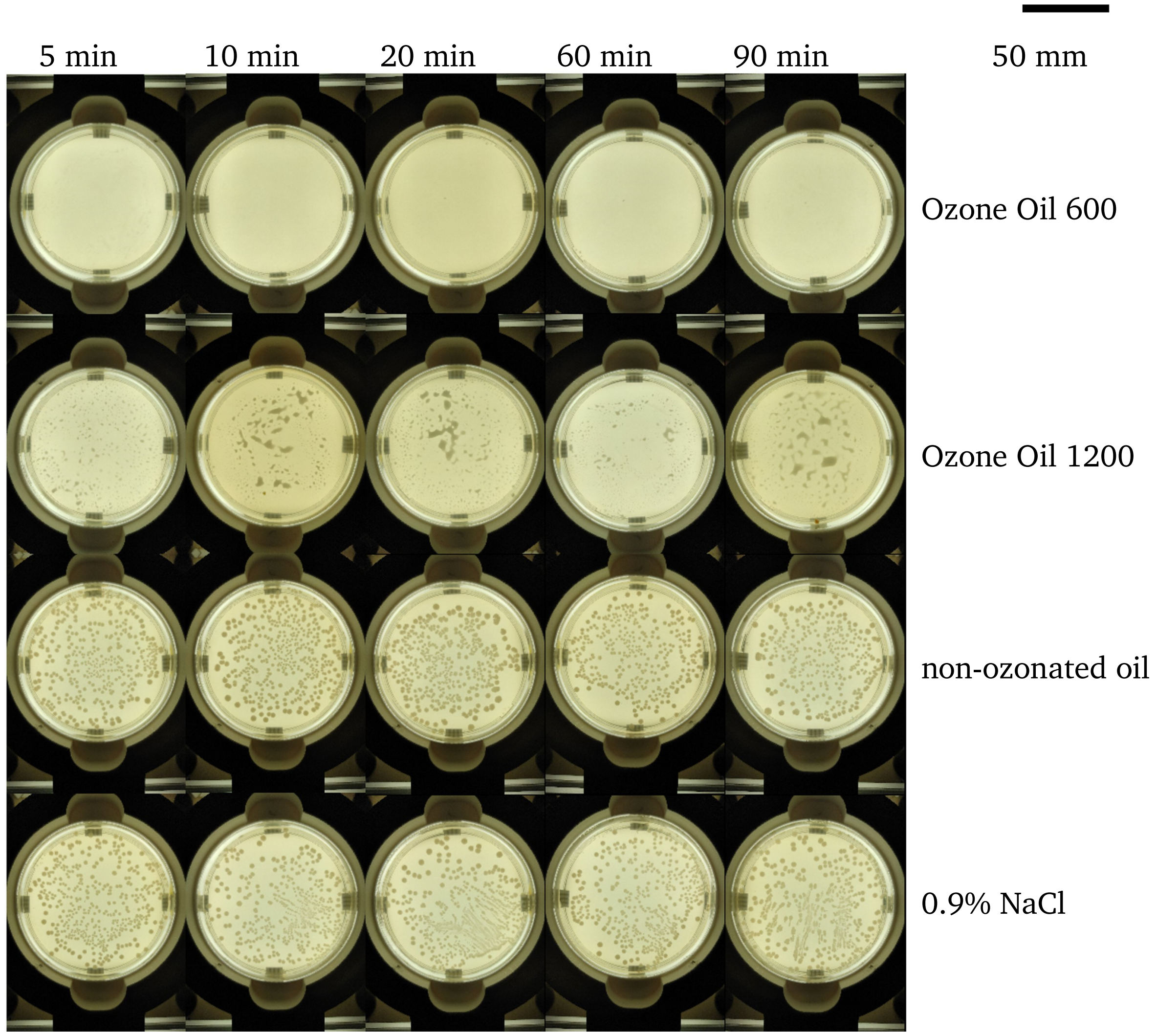

Fig. 10.2: Petri dishes containing the test strain *E. coli* for solid medium kinetic analysis, along with various exposure durations, antimicrobial agents, and negative control agents. At exposure times of 5 min, 10 min, 20 min, 60 min, and 90 min, respectively, non-ozonated oil and NaCl are used as negative control agents, while Ozone Oil 600 and 1200 are compared as antimicrobial agents. 0.9% NaCl is used as the culture medium. [16]

10.4 Discussion

The tested Ozone Oil 1200 causes a decrease in the growth of the *E. coli* bacteria in the agar dilution used to determine the MIC. However, a comparison with the literature reveals that the oil under test has a significantly lower antimicrobial effect despite having relatively high peroxide numbers, according the manufacturer. There is not much information supplied in prior studies about the mixing and casting of the plates, which may be the reason for this. Most of the time, the guideline is mentioned and not the specific instructions on how to perform the experiment. Particularly, there is no description of how to mix the different components. The guideline can not be followed here either, as it is created for research of antibiotics, which behave differently compared to oil. No emulsifier is applied, in contrast to the studies described in earlier works. Based on the findings of preliminary experiments, an emulsifier is not used; instead, a vortexer is used to combine the ozonated oil with the LB medium. Despite the fact that emulsifiers like Tween-80 adversely affect the oils' antibacterial effect [377], [378], the oils outperformed the controls in the studies. Even for oils with comparable peroxide values, a significant deviation from the MICs found in earlier studies is seen. This is also true when comparing the most recent research findings to those from earlier studies. An oil's antibacterial activity can also differ among different bacterial species [365]. The MIC values of two different *E. coli* strains are $4.75\,\mathrm{mg\,ml^{-1}}$ and $1.18\,\mathrm{mg\,ml^{-1}}$, respectively. Therefore, only research using the same bacterial strain can be compared. The contrast between the findings of this study's results and between and within those of earlier studies confirms the need for standardised norms for the production and assessment of ozonated oils. Additionally, a more detailed record of the mixing procedure and the casting of the plates is essential.

The inhibition zone is also determined through experiments using the agar dilution and spread-plating method. Here, it is impossible to determine whether the examined oils have antibacterial properties. Information on the mixing procedure is lacking for comparison with earlier studies [364], [365], [370], which used Tween-80 as an emulsifier. The exception is the experiment by [364], in which the mixing procedure is supported by ultrasonic. Nevertheless, the precise experimental conditions are also unknown, making replication difficult. Tween-80 may have had only modest success as an emulsifier in the current studies because it is administered differently. Tween-80, according to [377],

[379], decreases the antibacterial activity of oils. This assertion can not be evaluated since no antibacterial impact of the oil is detected for both the emulsifier-free and emulsifier-containing experiments. The plates prepared with the emulsifier-containing experiment responded similarly to those made with the emulsifier-free experiment, while spreading the bacterial solution. It is likely not the ozone in the oil that causes the variations in bacterial growth when compared to the other control groups, but rather other elements like the oil itself and the addition of an emulsifier. The medium's high temperatures of approximately 55 °C may be a contributing factor in the absence of an antibacterial effect. At the temperatures required to cast the agar plates, ozone escapes from the oil, as is seen in the preliminary experiments using potassium iodide starch paper. So, even before the plates are cast and solidified, a significant amount of ozone may be lost. Spread-plating in combination with diluted agar turned out to be less practical because the oil on the agar surface prevented the bacteria from spreading effectively.

Due to no discernible growth, the inhibition rate for both ozonated oils is recorded to be 100% for the kinetic study in solid medium. Although completely inhibiting *E. coli* bacterial growth, the Ozone Oil 1200 left cloudy areas on the plates that can not be attributed to a usual bacterial culture. Except for the cloudy areas, the oils exhibit comparable activity in the liquid medium.

The efficacy of ozonated oil in medical therapy is significantly influenced by its quality. Effectiveness of the ozone generator, ozonation settings, species concentrations, and reaction kinetics all affect the quality of ozonated oil. The iodine value, acid value, and peroxide value are three critical criteria that serve as indications of the quality of ozonated oil. While the iodine value and the acid value are unavailable on the manufacturer's website, the peroxide value is here included because ozonated oil from a commercially available source is utilised. It is significant to note that the European Chemical Agency (ECHA) has authorised OZONIA 3000 sunflower oil (Innovares Srl, Sant'Ilario d'Enza, Italy) in conformity with Registration, Evaluation, Authorisation, and Restriction of Chemicals (REACH) regulation. With its certification, more research into this oil's antimicrobial activity in medical therapy is important.

The findings support the therapeutically use of ozonated oils to treat wounds infected with *E. coli* bacteria because they have an antibacterial impact. Nevertheless, further research is still necessary.

11

Conclusion and future work

Herniated disk pain is a significant and common health problem [380]. There are several therapeutic options, including ozone therapy, pharmacological steroid injections, surgery, and physical therapy [26]. Clinical investigations indicate that ozone therapy, which includes injecting an oxygen-ozone mixture into the nucleus pulposus of the intervertebral disk, is effective in treating herniated disks [6], [7]. Despite awareness of the metabolic processes involved, it is presently not possible to measure the concentration of ozone in body fluids, tissues, and blood during ozone therapy [10], [45], [92]. It is essential to develop sensors and conduct more research for enabling ozone monitoring at the point of injection, which prevents over- or under-dosing and enables patient-specific treatments, in order to assure the secure and broad use of ozone therapy.

The first part of this thesis focuses on the investigation of the first research question (RQ) RQ1: How can novel dissolved and ozone gas sensors be references for their calibration, characterisation, and evaluation? Accurate and reliable measurement of ozone gas and dissolved ozone concentrations is critical in various fields, including environmental monitoring, water treatment, and medical therapy. The development of novel ozone sensors is necessary, and to achieve this, an accurate and reliable ozone reference system that comprises ozone generation and measurement is important. Reference systems with sensors that serve as references for calibration, characterisation, and evaluation of new ozone sensors are essential to advance and ensure the accuracy, precision, and reproducibility of new sensors. By using reference systems as a standard against which to compare the performance of new sensors, researchers and developers can evaluate their new sensors' accuracy, precision, and reproducibility. In this way, new and improved sensors can be developed, leading to better ozone measurement and monitoring in various applications. A reference system for ozone gas and a second reference system for dissolved ozone are presented. A comprehensive description and evaluation of the reference systems is provided, designed explicitly for the development, characterisation, and evaluation of novel ozone gas and dissolved ozone sensors. The reference systems offer researchers and practitioners a reliable and accurate tool for the advancement of ozone sensing technology, with potential applications in various fields. This provides a basis for the widespread and secure implementation and further investigation of ozone therapy. Further research regarding the ozone gas reference system is important to further increase the measurement range of the reference sensors. In comparison to earlier studies, the ozone gas reference system described here already increases the measurement range from the ppb into the ppm range. There are several ways to further increase this measurement range. It is possible to utilise sensors with a larger measurement range as soon as they are available. Presently, this can only be achieved with optical sensors, which are, e.g., connected to the inlet and outlet of the measurement chamber. However, these sensors are relatively expensive. For this, it is necessary to take into account how the gas tubes affect the ozone's chemical stability. Alternatively, the gas supplied by the ozone generator may be diluted in a given ratio before the concentration is measured. The installation of a flow controller that enables accurate continuous gas mixing is necessary for the execution of this option. The concentration range of up to $100\,\mathrm{mg\,l^{-1}}$, which is the range found in literature, may be mapped, for instance, by mixing one part oxygen-ozone mixture with 99 parts oxygen. Ensuring that all of the elements contained in the flow ratio are ozone-compatible is a major challenge here, in addition to the correct setting of the flow ratio. A calibrated ozone gas sensor can be used to experimentally confirm the fulfilment of these challenges. For the reference system for the measurement of the dissolved ozone concentration, further research may be beneficial that considers other liquids, such as drinking water, waste water, ozonated oil, blood, and body liquids. In addition to referencing novel sensors for calibration, characterisation, and evaluation, the biocompatibility, which is essential for a medical sensor, is also highly significant.

Thus, the second part of this thesis focuses on the foundation of RQ2: How can novel dissolved and ozone gas sensors be realised as electrochemical or optical sensors? In general, impedimetric, amperometric, and optical absorption sensors are frequently made of the same materials. Here, the focus is on developing a dissolved ozone sensor when treating a disk herniation with oxygen-ozone. Monitoring the ozone concentration is essential, both during this therapy and generally during ozone-related therapies [9]. Throughout the design and manufacturing process, the biocompatibility of sensors for use in medicine needs to be considered. Here, an exemplary amperometric, impedimetric, and optical absorption sensor are assessed in accordance with ISO 10993 [181]. The following materials are chosen for the amperometric sensor: gold nanoparticle (AuNP) ink for the working electrode (WE) and counter electrode (CE), silver nanoparticle (AgNP) ink for the reference electrode (RE), SU-8 for the passivation of the electrodes, polydimethylsiloxane (PDMS) for the substrate and membrane, and potassium sulfate (K_2SO_4), sodium chloride (NaCl), or potassium nitrate (KNO_3) for the electrolyte. The following materials are selected for the impedimetric sensor: aluminium oxide (Al_2O_3) for the substrate, platinum (Pt) for the electrodes, indium oxide (In_2O_3) for the sensing material, PDMS for the membrane, and Pt or indium gallium nitride (InGaN) for the heating element or light activation element. The materials chosen for the optical sensor are the following: zinc oxide (ZnO) for the sensing material of the photosensor and InGaN for the light activation element. The materials of the investigated sensors are also used in medicine to monitor acetone, glucose, hydrogen peroxide, sweat lactate, oxygen, and pH. The biocompatibility evaluations can therefore be transferred to these sensors. All of the materials under investigation are promising for use in biocompatible sensors. The biological and chemical characterisation, bioactivity, cytotoxicity, sterilisation, and packaging processes for the sensors need to be tested further because a literature review cannot replace them. Further research may also investigate the feasibility of using ions in the nucleus pulposus for the sensor's operation instead of the electrolyte. To reduce the negative environmental effects of single-use products, the biodegradability and recycling process of the final sensor need to be taken into account. Using biocompatible or non-toxic materials increases the likelihood of creating a biocompatible device. However, it also needs to be considered that during the production process, the characteristics and consequently the biocompatibility may change. Moreover, materials that are only required during production may impact how biocompatible a device is. The sensors need to be sterile in order to come into contact with body fluids and tissues. This can be accomplished by establishing a sterile inkjet-printing (IJP) production process or by performing a final sterilisation step. However, because of high sintering and curing temperatures, which may sufficiently destroy microorganisms, sterilisation measures may not be required. Overall, the biocompatibility of the device is influenced by the materials used, the surface properties, the manufacturing process, and the level of pathogen contamination. Further research regarding biocompatibility is important to examine the final sensor after production through biological characterisation tests.

After presenting reference systems for sensor development and investigating the biocompatibility of sensor materials, prototypes of various sensors are reported. The third part builds upon the second part and further investigates RQ2: How can novel dissolved and ozone gas sensors be realised as electrochemical or optical sensors? A simplified optical photometer for measuring ozone gas is presented as a step towards sensors that measure ozone concentrations for medical purposes. Two designs of an ozone gas photometer setup are focused. The first has a low number of optical components, and the second is a more conventional setup with beam collimating optics. Prototypes of the two designs are produced using just standard components, 3D-printing, and soldering. The photometers have a fast response time of 210 ms and measure ozone concentrations up to 2.5 vol% through a photosensor that operates between 275 nm and 286 nm. The performance of the simplified design is almost as excellent as the more complex design with collimation optics, according to the first characterisation of both setups. Thereby, the simplified photometer yields a root-mean-square percentage error (RMSPE) of 2.5% compared to a reference analyser. This serves as a proof-of-concept for a straightforward, inexpensive photometer and illustrates the possibility of optical absorption measurement as a method for determining ozone concentrations. Additional research may be conducted to further reduce the size and cost of the photometer. Also, investigations are carried out to assess dissolved ozone concentrations optically using comparable methodologies. A low-cost photometer setup that makes it possible to quantify the concentration of dissolved ozone is presented. By absorbing UV light (260 nm), the dissolved ozone content is measured optically. With a RMSPE of 14.68% compared to 8.2% of the reference sensor, the presented photometer provides accurate measurement results, considering the provided photometer costs around 17 times less than the reference sensor. Only commercially accessible or 3D-printed components are used in the proposed photometer, making it simple to reassemble. The photometer forms the basis for future research and advancements in the detection of dissolved ozone in medicine. Also, an exemplary inkjet-printed oxygen sensor structure is presented in order to get towards the objective of a miniaturised ozone sensor on flexible substrates for medical purposes. This investigation has advanced the development of compact, flexible sensors that may be included in medical equipment. Therefore, several inks, pre-processing methods, sintering variants, and post-processing options are examined to determine the optimal settings for the exemplary sensor structure produced with vector IJP. Here, the workflow that produces the highest conductivity results is outlined. Silver and gold conductors with electrical resistivity values of 2.56 µΩ cm and 5.25 µΩ cm, respectively, are produced by using the optimised workflow. This creates a foundation for the reproducible manufacturing of electrochemical sensors using vector IJP and electrodes made of gold and silver. In addition, commercial low-cost electrodes are modified to serve as ozone sensors, whereby they are manufactured with alternative methods, such as screen-printing. Thereby, a novel dissolved ozone sensor made of commercial electrodes that are modified with a variety of non-porous PDMS and polytetrafluoroethene (PTFE) membranes is demonstrated. A root mean squared error (RMSE) of $6.34\,\mathrm{mg\,l^{-1}}$ and a RMSPE of 62.60% is obtained for the PDMS membrane. In contrast, a $3.62\,\mathrm{mg\,l^{-1}}$ RMSE and a 30.41% RMSPE are attained for the PTFE membrane. The suggested dissolved ozone sensor provides a substitute for low-cost monitoring of dissolved ozone concentrations in a number of applications with a compact size. Additionally, a proof-of-concept that shows how to assess the dissolved ozone concentration in blood using boron-doped diamond (BDD) electrodes is provided, whereby the peak currents of the different dissolved ozone concentrations are well discernible.

Further research is important to reduce the response time of the amperometric sensors. For the optical sensors, the main challenges are a further reduction in size and the presence of ultraviolet (UV) light, which may be toxic for human body liquids and tissues. For impedimetric sensors, the main challenge are the necessary measurement temperatures. The optical absorption ozone measurement in the visible spectrum light range has previously been investigated [77], [381], but thereby long optical path lengths are needed, which result in a large sensor size, which is challenging for the application during medical therapy. Additional previous work [382] also examined the measurement with visible light. The ability to use blue light with gold (Au)/titanium dioxide (TiO_2)–tungsten trioxide (WO_3) sensing material is reported, although the response time over 200 s needs to be improved for the here-focused application [382]. In order to use optical absorption sensors with UV light or reduce the response time for light activation with visible light during medical treatments, more research is required. Additionally, a hybrid combination of impedimetric metal oxide semiconductors (MOS) and carbon nanotubes (CNTs) sensors offers a chance to get beyond the shortcomings of both sensor types, such as high measuring temperatures for MOS and long response times for CNTs [383]. Positive findings at room temperature (RT) are reported; however, further research is required to further decrease the response time for the here-focused application [383]. The main remaining challenge in measuring dissolved ozone during oxygen-ozone therapy is the current assumption that body liquids and tissues within the herniated disk are water-based. The interaction of the sensor with body fluids and tissues may make it less effective. Because of the body's high ion concentration, the liquid may function as an electrolyte, making the sensor's electrolyte unnecessary. Due to fewer chemicals coming into contact with the human body when the sensor is manufactured without an additional electrolyte, there is a greater probability of a final biocompatible sensor.

In the fourth part, the focus is on investigating RQ3: Can ozone be further used in medicine as an antibacterial agent for the treatment of, e.g., chronic wounds? Experiments are carried out to examine the impact of ozone on bacterial cultures, such as *Escherichia coli* (*E. coli*), in order to identify other applications of the usage of ozone in medical therapy. Numerous studies have demonstrated the effectiveness of ozonated oils for the treatment of chronic wounds when antibiotic therapy is unavailable or ineffective due to resistance. However, very different detection methods have been used, and the methods are often incompletely described. Two ozonated oils are investigated regarding their antibacterial effect on *E. coli* and, thus, for their suitability for treating infected wounds. For evaluation, both agar dilution and agar dilution combined with spread-plating are applied. Unlike previous studies, no complete growth inhibition of *E. coli* for either of the two ozonated oils is found in both agar dilution methods despite high concentrations. In contrast, control experiments conducted without oil but with Tween-80 as an emulsifier showed inhibition of the formation of bacterial colonies. A comparison of the literature of the agar dilution method revealed that high peroxide levels of ozonated oils are more inhibiting to bacterial growth than low levels. Furthermore, the influence of the ozone exposure time on the bacteria is investigated in a kinetic analysis for solid and liquid media. On both media and for both oils, the experiments showed complete inactivation of the bacteria after an exposure time of 5 min. In the liquid nutrient medium, the oils showed comparable activity in inhibiting bacterial growth. A comparison of the findings with previous research is difficult due to the fact that many different methods and different parameters have been used in previous studies. Ozonated oils in previous experiments have been produced in different ways. The peroxide number can differ greatly from what the manufacturer has stated, as experiments on the purchased oils have shown, which affects their effectiveness. Additionally, there is a lack of standardised procedures or guidelines for accurately testing the antibacterial effect of ozonated oils. Also, there is still no standardised process for the production of ozonated oils or which oil with which peroxide number should preferably be used. Thus, further studies on ozone concentrations, exposure times, and the effect of ozone on different bacteria, as well as the manufacturing of standardised oils and test procedures, are required to further investigate the effectiveness and safety of using ozonated oils as a reliable and safe therapy for the treatment of chronic wounds.

Overall, this establishes a basis for the assessment of ozone concentration during medical therapy, which may expand the application of ozone in medicine and enhance patient outcomes.

List of own publications

Main publications

[10] L. Petani, L. Koker, J. Herrmann, V. Hagenmeyer, U. Gengenbach, and C. Pylatiuk, “Recent developments in ozone sensor technology for medical applications”, *Micromachines*, vol. 11, no. 6, 2020. DOI: `10.3390/mi11060624`.

[12] L. Petani, V. Wehrheim, L. Koker, M. Reischl, M. Ungerer, U. Gengenbach, and C. Pylatiuk, “Systematic assessment of the biocompatibility of materials for inkjet-printed ozone sensors for medical therapy”, *Flexible and Printed Electronics*, vol. 6, no. 4, p. 043 003, 2021. DOI: `10.1088/2058-8585/ac32ab`.

[14] L. Petani, L. Wührl, L. Koker, M. Reischl, J. Renz, U. Gengenbach, and C. Pylatiuk, “Development of an experimental setup for real-time in-line dissolved ozone measurement for medical therapy”, *Ozone: Science & Engineering*, vol. 44, no. 5, pp. 499–509, 2022. DOI: `10.1080/01919512.2021.1932412`.

[15] L. Petani, R. Barth, L. Wührl, I. Sieber, L. Koker, M. Reischl, U. Gengenbach, and C. Pylatiuk, “Investigation of a simplified photometer design for the measurement of ozone gas concentration”, Kuala Lumpur, Malaysia: IEEE-EMBS Conference on Biomedical Engineering and Sciences (IECBES), Dec. 7–9, 2022, pp. 1–6. DOI: `10.1109/IECBES54088.2022.10079356`.

[16] L. Petani, A.-M. Jung, R.-R. Frietsch Musulin, G. Sturm, A.-K. Kaster, and C. Pylatiuk, “Exploring the antibacterial effects of ozonated oils in medicine: A study on Escherichia coli inhibition”, *Ozone: Science & Engineering*, pp. 1–8, 2023. DOI: `10.1080/01919512.2023.2233746`.

[168] L. Petani, D. Wickersheim, L. Koker, M. Reischl, U. Gengenbach, and C. Pylatiuk, “Experimental setup for evaluation of medical ozone gas sensors”, Sundsvall, Sweden: IEEE Sensors Applications Symposium (SAS), Aug. 1–3, 2022, pp. 1–6. DOI: 10.1109/SAS54819.2022.9881340.

[346] L. Petani, D. Tils, L. Wührl, I. Sieber, and C. Pylatiuk, “Design, simulation, and evaluation of a low-cost photometer for dissolved ozone measurement”, (accepted), Tel Aviv, Israel: IEEE International Conference on Microwaves, Communications, Antennas, Biomedical Engineering & Electronic Systems (COMCAS), Jul. 9–11, 2024.

[350] L. Petani, A. Schweizer, C. Pylatiuk, P. Stiller, U. Gengenbach, and M. Ungerer, “Optimised inkjet-printing parameters and processing techniques for an exemplary structure of an oxygen sensor on a polyimide substrate”, Boston, MA, USA: IEEE International Conference on Flexible, Printable Sensors and Systems (FLEPS), Jul. 9–12, 2023. DOI: 10.1109/FLEPS57599.2023.10220420.

[351] L. Petani, L. Llupa, Z. Peng, G. Ogata, L. Koker, U. Gengenbach, Y. Einaga, and C. Pylatiuk, “Dissolved ozone sensing in water and blood based on commercial screen-printed and BDD electrodes”, Toronto, Canada: IEEE Biomedical Circuits and Systems Conference (BIOCAS), Oct. 19–21, 2023. DOI: 10.1109/BioCAS58349.2023.10388985.

Further publications

L. Petani, S. Essig, J. Zeilfelder, M. Kortenhaus, and C. Pylatiuk. "Simulation and evaluation of a body energy harvesting device for arm and leg swing motions", *AIP Advances*, vol. 11, no. 6, pp. 065201, 2021. DOI: 10.1063/5.0050424 .

L. Petani, M. Lorenz, and C. Pylatiuk. "Continuous measurement of individual formaldehyde exposure with a DIY photometer", Vienna, Austria: IEEE Sensors Conference, Oct. 29 - Nov. 1, 2023. DOI: 10.1109/SENSORS56945.2023.10325275.

Bibliography

[1] E. Fitzpatrick, O. J. Holland, and J. J. Vanderlelie, “Ozone therapy for the treatment of chronic wounds: A systematic review”, *International Wound Journal*, vol. 15, no. 4, pp. 633–644, 2018. DOI: `10.1111/iwj.12907`.

[2] E. Borrelli, A. Alexandre, E. Iliakis, A. Alexandre, and V. Bocci, “Disc herniation and knee arthritis as chronic oxidative stress diseases: The therapeutic role of oxygen ozone therapy”, *Journal of Arthritis*, vol. 4, no. 3, p. 161, 2015. DOI: `10.4172/2167-7921.1000161`.

[3] M. Hashemi, P. Jalili, S. Mennati, *et al.*, “The effects of prolotherapy with hypertonic dextrose versus prolozone (intraarticular ozone) in patients with knee osteoarthritis”, *Anesthesiology and Pain Medicine*, vol. 5, no. 5, 2015. DOI: `10.5812/aapm.27585`.

[4] A. Azarpazhooh and H. Limeback, “The application of ozone in dentistry: A systematic review of literature”, *Journal of Dentistry*, vol. 36, no. 2, pp. 104–116, 2008. DOI: `10.1016/j.jdent.2007.11.008`.

[5] D. Zimmermann, T. Waltimo, and A. Filippi, “Ozonized water in dental traumatology – a preliminary study on the treatment of avulsed teeth, in vitro”, *Ozone: Science & Engineering*, vol. 34, no. 6, pp. 484–488, 2012. DOI: `10.1080/01919512.2012.718223`.

[6] V. Bocci, E. Borrelli, I. Zanardi, and V. Travagli, “The usefulness of ozone treatment in spinal pain”, *Drug Design, Development and Therapy*, vol. 9, pp. 2677–2685, 2015. DOI: `10.2147/DDDT.S74518`.

[7] T. Lehnert, N. N. Naguib, S. Wutzler, *et al.*, “Analysis of disk volume before and after CT-guided intradiscal and periganglionic ozone-oxygen injection for the treatment of lumbar disk herniation”, *Journal of Vascular and Interventional Radiology*, vol. 23, no. 11, pp. 1430–1436, 2012. DOI: `10.1016/j.jvir.2012.07.029`.

[8] M. Song, Q. Zeng, Y. Xiang, *et al.*, "The antibacterial effect of topical ozone on the treatment of MRSA skin infection", *Molecular Medicine Reports*, vol. 17, no. 2, pp. 2449–2455, 2018. DOI: `10.3892/mmr.2017.8148`.

[9] N. L. Smith, A. L. Wilson, J. Gandhi, S. Vatsia, and S. A. Khan, "Ozone therapy: An overview of pharmacodynamics, current research, and clinical utility", *Medical Gas Research*, vol. 7, no. 3, pp. 212–219, 2017. DOI: `10.4103/2045-9912.215752`.

[10] L. Petani, L. Koker, J. Herrmann, V. Hagenmeyer, U. Gengenbach, and C. Pylatiuk, "Recent developments in ozone sensor technology for medical applications", *Micromachines*, vol. 11, no. 6, 2020. DOI: `10.3390/mi11060624`.

[11] T. Han, S. Kundu, A. Nag, and Y. Xu, "3D printed sensors for biomedical applications: A review", *Sensors (Basel, Switzerland)*, vol. 19, no. 7, 2019. DOI: `10.3390/s19071706`.

[12] L. Petani, V. Wehrheim, L. Koker, *et al.*, "Systematic assessment of the biocompatibility of materials for inkjet-printed ozone sensors for medical therapy", *Flexible and Printed Electronics*, vol. 6, no. 4, p. 043 003, 2021. DOI: `10.1088/2058-8585/ac32ab`.

[13] S. Gupta, S. Sagar, G. Maheshwari, T. Kisaka, and S. Tripathi, "Chronic wounds: Magnitude, socioeconomic burden and consequences", *Wounds Asia*, vol. 4, no. 1, pp. 8–14, 2021.

[14] L. Petani, L. Wührl, L. Koker, *et al.*, "Development of an experimental setup for real-time in-line dissolved ozone measurement for medical therapy", *Ozone: Science & Engineering*, vol. 44, no. 5, pp. 499–509, 2022. DOI: `10.1080/01919512.2021.1932412`.

[15] L. Petani, R. Barth, L. Wührl, *et al.*, "Investigation of a simplified photometer design for the measurement of ozone gas concentration", Kuala Lumpur, Malaysia: IEEE-EMBS Conference on Biomedical Engineering and Sciences (IECBES), Dec. 7–9, 2022, pp. 1–6. DOI: `10.1109/IECBES54088.2022.10079356`.

[16] L. Petani, A.-M. Jung, R.-R. Frietsch Musulin, G. Sturm, A.-K. Kaster, and C. Pylatiuk, "Exploring the antibacterial effects of ozonated oils in medicine: A study on Escherichia coli inhibition", *Ozone: Science & Engineering*, pp. 1–8, 2023. DOI: `10.1080/01919512.2023.2233746`.

[17] G. Stoker, “The surgical uses of ozone”, *The Lancet*, vol. 188, no. 4860, p. 712, 1916. DOI: `10.1016/S0140-6736(01)49000-3`.

[18] N. Owen, G. N. Healy, C. E. Matthews, and D. W. Dunstan, “Too much sitting: The population health science of sedentary behavior”, *Exercise and Sport Sciences Reviews*, vol. 38, no. 3, pp. 105–113, 2010. DOI: `10.1097/JES.0b013e3181e373a2`.

[19] H. Ihira, N. Sawada, T. Yamaji, *et al.*, “Occupational sitting time and subsequent risk of cancer: The Japan public health center-based prospective study”, *Cancer Science*, vol. 111, no. 3, pp. 974–984, 2020. DOI: `10.1111/cas.14304`.

[20] J. G. Van Uffelen, J. Wong, J. Y. Chau, *et al.*, “Occupational sitting and health risks: A systematic review”, *American Journal of Preventive Medicine*, vol. 39, no. 4, pp. 379–388, 2010. DOI: `10.1016/j.amepre.2010.05.024`.

[21] D. J. Gaskin and P. Richard, “The economic costs of pain in the United States”, *The Journal of Pain*, vol. 13, no. 8, pp. 715–724, 2012. DOI: `10.1016/j.jpain.2012.03.009`.

[22] C. B. Groenewald, B. S. Essner, D. Wright, M. D. Fesinmeyer, and T. M. Palermo, “The economic costs of chronic pain among a cohort of treatment-seeking adolescents in the United States”, *The Journal of Pain*, vol. 15, no. 9, pp. 925–933, 2014. DOI: `10.1016/j.jpain.2014.06.002`.

[23] E. Ambrósio, K. Bloor, and H. MacPherson, “Costs and consequences of acupuncture as a treatment for chronic pain: A systematic review of economic evaluations conducted alongside randomised controlled trials”, *Complementary Therapies in Medicine*, vol. 20, no. 5, pp. 364–374, 2012. DOI: `10.1016/j.ctim.2012.05.002`.

[24] J. Margolis, J. J. Barron, and W. D. Grochulski, “Health care resources and costs for treating peripheral artery disease in a managed care population: Results from analysis of administrative claims data”, *Journal of Managed Care Pharmacy*, vol. 11, no. 9, pp. 727–734, 2005. DOI: `10.18553/jmcp.2005.11.9.727`.

[25] G. M. Estadt, “Chiropractic/rehabilitative management of post-surgical disc herniation: A retrospective case report”, *Journal of Chiropractic Medicine*, vol. 3, no. 3, pp. 108–115, 2004. DOI: `10.1016/S0899-3467(07)60095-0`.

[26] R. R. de Andrade, O. B. de Oliveira-Neto, L. T. Barbosa, I. O. Santos, C. F. de Sousa-Rodrigues, and F. T. Barbosa, "Effectiveness of ozone therapy compared to other therapies for low back pain: A systematic review with meta-analysis of randomized clinical trials", *Brazilian Journal of Anesthesiology (English Edition)*, vol. 69, no. 5, pp. 493–501, 2019. DOI: `10.1016/j.bjane.2019.06.007`.

[27] R. Klocke, K. Levasseur, G. D. Kitas, J. P. Smith, and G. Hirsch, "Cartilage turnover and intra-articular corticosteroid injections in knee osteoarthritis", *Rheumatology International*, vol. 38, no. 3, pp. 455–459, 2018. DOI: `10.1007/s00296-018-3988-2`.

[28] F. Glocker, *Lumbale radikulopathie*, `www.awmf.org/uploads/tx_szleitlinien/030-058l_S2k_Lumbale_Radikulopathie_2018-04.pdf`, Accessed: 2 Oct. 2019.

[29] M. E. Schoenherr, M. W. Hollmann, and B. Graf, "Lachgas", *Der Anaesthesist*, vol. 53, no. 9, pp. 796–812, 2004. DOI: `10.1007/s00101-004-0742-9`.

[30] T. Brockow, T. Heissner, A. Franke, and K.-L. Resch, "Evaluation of the efficacy of subcutaneous carbon dioxide insufflations for treating acute non specific neck pain in general practice: A sham controlled randomized trial", *European Journal of Pain*, vol. 12, no. 1, pp. 9–16, 2008. DOI: `10.1016/j.ejpain.2007.01.002`.

[31] N. Di Paolo, V. Bocci, D. Salvo, *et al.*, "Extracorporeal blood oxygenation and ozonation (EBOO): A controlled trial in patients with peripheral artery disease", *The International Journal of Artificial Organs*, vol. 28, no. 10, pp. 1039–1050, 2005. DOI: `10.1177/039139880502801012`.

[32] N. Di Paolo, E. Gaggiotti, and F. Galli, "Extracorporeal blood oxygenation and ozonation: Clinical and biological implications of ozone therapy", *Redox Report*, vol. 10, no. 3, pp. 121–130, 2005. DOI: `10.1179/135100005X38888`.

[33] M. Roostan and W. H. Frishman, "Xenon: An emerging neuroprotectant with potential application for cardiac arrest care", *Cardiology in Review*, vol. 26, no. 4, pp. 207–212, 2018. DOI: `10.1097/CRD.0000000000000198`.

[34] H. Karaca and Y. S. Velioglu, "Ozone applications in fruit and vegetable processing", *Food Reviews International*, vol. 23, no. 1, pp. 91–106, 2007. DOI: `10.1080/87559120600998221`.

[35] T. Batakliev, V. Georgiev, M. Anachkov, S. Rakovsky, and G. E. Zaikov, "Ozone decomposition", *Interdisciplinary Toxicology*, vol. 7, no. 2, pp. 47–59, 2014. DOI: `10.2478/intox-2014-0008`.

[36] C. Wu, Y. Zhou, X. Sun, and L. Fu, "The recent development of advanced wastewater treatment by ozone and biological aerated filter", *Environmental Science and Pollution Research*, vol. 25, no. 9, pp. 8315–8329, 2018. DOI: `10.1007/s11356-018-1393-8`.

[37] E. Ortenberg, L. Groisman, and C. Rav-Acha, "Taste and odour removal from an urban groundwater establishment - a case study", *Water Science and Technology*, vol. 42, no. 1-2, pp. 123–128, 2000. DOI: `10.2166/wst.2000.0302`.

[38] A. Schwartz, G. M. Sánchez, F. Sabah, *et al.*, *Madrid Declaration on Ozone Therapy*. Madrid, Spain: International Scientific Committee of Ozone (ISCO3), 2010, ISBN: 978-8409199327.

[39] M. Hashemi, M. Poorfarokh, S. A. Mohajerani, *et al.*, "Injection of intradiscal O_2-O_3 to reduce pain and disability of patients with low back pain due to prolapsed lumbar disk", *Anesthesiology and Pain Medicine*, vol. 4, no. 5, e19206, 2014. DOI: `10.5812/aapm.19206`.

[40] G. Valacchi, V. Fortino, and V. Bocci, "The dual action of ozone on the skin", *British Journal of Dermatology*, vol. 153, no. 6, pp. 1096–1100, 2005. DOI: `10.1111/j.1365-2133.2005.06939.x`.

[41] A. M. Fathi, M. N. Mawsouf, and R. Viebahn-Hänsler, "Ozone therapy in diabetic foot and chronic, nonhealing wounds", *Ozone: Science & Engineering*, vol. 34, no. 6, pp. 438–450, 2012. DOI: `10.1080/01919512.2012.718700`.

[42] R. Viebahn-Hänsler, O. S. León Fernández, and Z. Fahmy, "Ozone in medicine: Clinical evaluation and evidence classification of the systemic ozone applications, major autohemotherapy and rectal insufflation, according to the requirements for evidence-based medicine", *Ozone: Science & Engineering*, vol. 38, no. 5, pp. 322–345, 2016. DOI: `10.1080/01919512.2016.1191992`.

[43] P. P. Raj, "Intervertebral disc: Anatomy-physiology-pathophysiology-treatment", *Pain Practice*, vol. 8, no. 1, pp. 18–44, 2008. DOI: `10.1111/j.1533-2500.2007.00171.x`.

[44] O. Airaksinen, J. I. Brox, C. Cedraschi, *et al.*, "Chapter 4. European guidelines for the management of chronic nonspecific low back pain", *European Spine Journal*, vol. 15, no. 2, S192–300, 2006. DOI: `10.1007/s00586-006-1072-1`.

[45] V. Bocci, *Ozone. A New Medical Drug.* Dordrecht, Netherlands: Springer, 2011, ISBN: 978-9048192335. DOI: `10.1007/978-90-481-9234-2`.

[46] G. Pizzino, N. Irrera, M. Cucinotta, *et al.*, "Oxidative stress: Harms and benefits for human health", *Oxidative Medicine and Cellular Longevity*, vol. 2017, 2017. DOI: `10.1155/2017/8416763`.

[47] Y. Zhang, Y. Ma, J. Jiang, T. Ding, and J. Wang, "Treatment of the lumbar disc herniation with intradiscal and intraforaminal injection of oxygen-ozone", *Journal of Back and Musculoskeletal Rehabilitation*, vol. 26, no. 3, pp. 317–322, 2013. DOI: `10.3233/BMR-130386`.

[48] M. Nagayoshi, T. Fukuizumi, C. Kitamura, J. Yano, M. Terashita, and T. Nishihara, "Efficacy of ozone on survival and permeability of oral microorganisms", *Oral Microbiology and Immunology*, vol. 19, no. 4, pp. 240–246, 2004. DOI: `10.1111/j.1399-302X.2004.00146.x`.

[49] C. F. Andreula, L. Simonetti, F. de Santis, R. Agati, R. Ricci, and M. Leonardi, "Minimally invasive oxygen-ozone therapy for lumbar disk herniation", *American Journal of Neuroradiology*, no. 24, pp. 996–1000, 2003.

[50] M. Muto, C. Andreula, and M. Leonardi, "Treatment of herniated lumbar disc by intradiscal and intraforaminal oxygen-ozone (O_2-O_3) injection", *Journal of Neuroradiology*, vol. 31, no. 3, pp. 183–189, 2004. DOI: `10.1016/S0150-9861(04)96989-1`.

[51] M. Gallucci, N. Limbucci, L. Zugaro, *et al.*, "Sciatica: Treatment with intradiscal and intraforaminal injections of steroid and oxygen-ozone versus steroid only", *Radiology*, vol. 242, no. 3, pp. 907–913, 2007. DOI: `10.1148/radiol.2423051934`.

[52] D. J. Botsford, S. I. Esses, and D. J. Ogilvie-Harris, "In vivo diurnal variation in intervertebral disc volume and morphology", *Spine*, vol. 19, no. 8, pp. 935–940, 1994. DOI: `10.1097/00007632-199404150-00012`.

[53] N. Roberts, D. Hogg, G. H. Whitehouse, and P. Dangerfield, "Quantitative analysis of diurnal variation in volume and water content of lumbar intervertebral discs", *Clinical Anatomy: The Official Journal of the American Association of Clinical Anatomists and the British Association of Clinical Anatomists*, vol. 11, no. 1, pp. 1–8, 1998. DOI: `10.1002/(SICI)1098-2353(1998)11:1<1::AID-CA1>3.0.CO;2-Z`.

[54] J. A. Malko, W. C. Hutton, and W. A. Fajman, "An in vivo MRI study of the changes in volume (and fluid content) of the lumbar intervertebral disc after overnight bed rest and during an 8-hour walking protocol", *Journal of Spinal Disorders & Techniques*, vol. 15, no. 2, pp. 157–163, 2002. DOI: `10.1097/00024720-200204000-00012`.

[55] M. Özdikici, "The estimation of lumbar intervertebral disc volumes before and after exercise using the cavalieri method", *MOJ Anatomy & Physiology*, vol. 5, no. 2, pp. 106–08, 2018. DOI: `10.15406/mojap.2018.05.00172`.

[56] K. H. Luepke, K. J. Suda, H. Boucher, *et al.*, "Past, present, and future of antibacterial economics: Increasing bacterial resistance, limited antibiotic pipeline, and societal implications", *Pharmacotherapy: The Journal of Human Pharmacology and Drug Therapy*, vol. 37, no. 1, pp. 71–84, 2017. DOI: `10.1002/phar.1868`.

[57] R. J. Fair and Y. Tor, "Antibiotics and bacterial resistance in the 21st century", *Perspectives in Medicinal Chemistry*, vol. 6, pp. 25–64, 2014. DOI: `10.4137/PMC.S14459`.

[58] J. Derco and M. Koman, *Ozone in nature and practice*. London, United Kingdom: IntechOpen, 2018, ISBN: 978-1838813628. DOI: `10.5772/intechopen.68925`.

[59] A. P. Anzolin, N. L. da Silveira-Kaross, and C. D. Bertol, "Ozonated oil in wound healing: What has already been proven?", *Medical Gas Research*, vol. 10, no. 1, pp. 54–59, 2020. DOI: `10.4103/2045-9912.279985`.

[60] J. L. Sotelo, F. J. Beltran, F. J. Benitez, and J. Beltran-Heredia, "Ozone decomposition in water: Kinetic study", *Industrial & Engineering Chemistry Research*, vol. 26, no. 1, pp. 39–43, 1987. DOI: `10.1021/ie00061a008`.

[61] V. Bocci, I. Zanardi, D. Michaeli, and V. Travagli, "Mechanisms of action and chemical-biological interactions between ozone and body compartments: A critical appraisal of the different administration routes", *Current Drug Therapy*, vol. 4, no. 3, pp. 159–173, 2009. DOI: `10.2174/157488509789055045`.

[62] E. Bakker and M. Telting-Diaz, “Electrochemical sensors”, *Analytical Chemistry*, vol. 74, no. 12, pp. 2781–2800, 2002. DOI: `10.1021/ac0202278`.

[63] D. W. Kimmel, G. LeBlanc, M. E. Meschievitz, and D. E. Cliffel, “Electrochemical sensors and biosensors”, *Analytical Chemistry*, vol. 84, no. 2, pp. 685–707, 2012. DOI: `10.1021/ac202878q`.

[64] C. McDonagh, C. S. Burke, and B. D. MacCraith, “Optical chemical sensors”, *Chemical Reviews*, vol. 108, no. 2, pp. 400–422, 2008. DOI: `10.1021/cr068102g`.

[65] J. R. Stetter, V. Patel, M. W. Findlay, and M. T. Carter, “Printed gas sensor”, U.S. Patent 9,784,708, Oct. 2017.

[66] SPEC Sensors, *Technical document: Ozone sensor*, `www.spec-sensors.com/product/ozone-gas-sensor-developer-kit/`, Accessed: 10 Mar. 2020.

[67] Hach, *User manual: Orbisphere C1100 ozone sensor*, `www.uk.hach.com/orbisphere-c1100-ozone-sensor-stainless-steel-up-to-40-bar/product-downloads?id=26369768223`, Accessed: 7 Apr. 2020.

[68] R. M. Duvall, R. W. Long, M. R. Beaver, K. G. Kronmiller, M. L. Wheeler, and J. J. Szykman, “Performance evaluation and community application of low-cost sensors for ozone and nitrogen dioxide”, *Sensors*, vol. 16, no. 10, p. 1698, 2016. DOI: `10.3390/s16101698`.

[69] ENVEA Cairpol, *Technical document: Cairsens O_3/NO_2 sensor*, `http://www.cairpol.com/wp-content/uploads/2017/05/Cairsens-O3NO2-0-250ppb-Technical-specifications.pdf`, Accessed: 31 Mar. 2020.

[70] S. Addanki and D. Nedumaran, “Fabrication of ozone sensors on porous glass substrates using gold and silver thin films nanoislands”, *Optik*, vol. 150, pp. 11–21, 2017. DOI: `10.1016/j.ijleo.2017.09.080`.

[71] Y. Ishii, T. A. Ivandini, K. Murata, and Y. Einaga, “Development of electrolyte-free ozone sensors using boron-doped diamond electrodes”, *Analytical Chemistry*, vol. 85, no. 9, pp. 4284–4288, 2013. DOI: `10.1021/ac400043b`.

[72] L. F. da Silva, J.-C. M’peko, A. C. Catto, *et al.*, “UV-enhanced ozone gas sensing response of ZnO-SnO_2 heterojunctions at room temperature”, *Sensors and Actuators B: Chemical*, vol. 240, pp. 573–579, 2017. DOI: `10.1016/j.snb.2016.08.158`.

[73] C. Hu, X. Bai, Y. Wang, W. Jin, X. Zhang, and S. Hu, “Inkjet printing of nanoporous gold electrode arrays on cellulose membranes for high-sensitive paper-like electrochemical oxygen sensors using ionic liquid electrolytes”, *Analytical Chemistry*, vol. 84, no. 8, pp. 3745–3750, 2012. DOI: `10.1021/ac3003243`.

[74] G. Kang, Z. Zhu, B.-H. Tang, C.-H. Wu, and R.-J. Wu, “Rapid detection of ozone in the parts per billion range using a novel Ni–Al layered double hydroxide”, *Sensors and Actuators B: Chemical*, vol. 241, pp. 1203–1209, 2017. DOI: `10.1016/j.snb.2016.10.012`.

[75] L. Spinelle, M. Gerboles, M. Aleixandre, and F. Bonavitacola, “Evaluation of metal oxide sensors for the monitoring of O_3 in ambient air at pbp level”, *Chemical Engineering Transactions*, vol. 54, pp. 319–324, 2016. DOI: `10.3303/CET1654054`.

[76] J. Jayachandiran, A. Raja, M. Arivanandhan, R. Jayavel, and D. Nedumaran, “A facile synthesis of hybrid nanocomposites of reduced graphene oxide/ZnO and its surface modification characteristics for ozone sensing”, *Journal of Materials Science: Materials in Electronics*, vol. 29, no. 4, pp. 3074–3086, 2018. DOI: `10.1007/s10854-017-8239-x`.

[77] C. Ghazaly, M. Guillemot, B. Castel, E. Langlois, M. Etienne, and M. Hebrant, “Real-time optical ozone sensor for occupational exposure assessment”, Berlin, Germany: International Conference on Solid-State Sensors, Actuators and Microsystems & Eurosensors XXXIII, Jun. 23–27, 2019, pp. 1403–1406. DOI: `10.1109/TRANSDUCERS.2019.8808516`.

[78] M. Ando, T. Kamimura, K. Uegaki, V. Biju, and Y. Shigeri, “Sensing of ozone based on its quenching effect on the photoluminescence of CdSe-based core-shell quantum dots”, *Microchimica Acta*, vol. 183, no. 11, pp. 3019–3024, 2016. DOI: `10.1007/s00604-016-1938-9`.

[79] C. Gottschalk, J. A. Libra, and A. Saupe, *Ozonation of water and waste water: A practical guide to understanding ozone and its applications*. Weinheim, Germany: John Wiley & Sons, 2009, ISBN: 978-3527319626. DOI: `10.1002/9783527628926`.

[80] C. Von Sonntag and U. V. Gunten, *Chemistry of ozone in water and wastewater treatment*. London, United Kingdom: IWA Publishing, 2012, ISBN: 978-1780400839. DOI: `10.2166/9781780400839`.

[81] U. Chasanah, E. Yulianto, A. Zain, *et al.*, "Evaluation of titration method on determination of ozone concentration produced by dielectric barrier discharge plasma (DBDP) technology", *Journal of Physics: Conference Series*, vol. 1153, no. 1, p. 012 086, 2019. DOI: `10.1088/1742-6596/1153/1/012086`.

[82] METTLER TOLEDO, *Sensor pure* O_3, `www.mt.com/de/de/home/products/Process-Analytics/DO-CO2-ozone-sensor/dissolved-O3-meter/pureO3-ISM.html#documents`, Accessed: 17 Mar. 2020.

[83] A. Spiliotopoulou, R. Martin, L.-F. Pedersen, and H. R. Andersen, "Use of fluorescence spectroscopy to control ozone dosage in recirculating aquaculture systems", *Water Research*, vol. 111, pp. 357–365, 2017. DOI: `10.1016/j.watres.2016.12.036`.

[84] Y. Bilenko, A. Dobrinsky, M. Shur, and R. Gaska, "Ultraviolet-based ozone sensor", U.S. Patent 9,625,372, Apr. 2017.

[85] D. Ziegler, E. Bekyarova, A. Marchisio, J.-M. Tulliani, and K. Naishadham, "Highly selective ozone sensors based on functionalized carbon nanotubes", New Dehli, India: IEEE SENSORS Conference, Oct. 28–31, 2018, pp. 1–4. DOI: `10.1109/ICSENS.2018.8589868`.

[86] 2B Technologies, *Model UV-106-W aqueous ozone monitor*, `www.twobtech.com/model-uv-106-w-aqueous-ozone-monitor.html`, Accessed: 5 Apr. 2020, 2020.

[87] J. W. Birks, B. Xiong, C. M. Ford, P. C. Andersen, and C. J. Williford, "Aqueous ozone monitor utilizing gas stripping", U.S. Patent 9,423,340, Aug. 2016.

[88] P. Janknecht, C. Picard, A. Larbot, and P. A. Wilderer, "Membrane ozonation in wastewater treatment", *Acta Hydrochimica et Hydrobiologica*, vol. 32, no. 1, pp. 33–39, 2004. DOI: `10.1002/aheh.200300521`.

[89] G. A. Zoumpouli, R. Baker, C. M. Taylor, *et al.*, "A single tube contactor for testing membrane ozonation", *Water*, vol. 10, no. 10, p. 1416, 2018. DOI: `10.3390/w10101416`.

[90] P. V. Shanbhag and K. K. Sirkar, "Ozone and oxygen permeation behavior of silicone capillary membranes employed in membrane ozonators", *Journal of Applied Polymer Science*, vol. 69, no. 7, pp. 1263–1273, 1998. DOI: `10.1002/(SICI)1097-4628(19980815)69:7<1263::AID-APP1>3.0.CO;2-C`.

[91] H. Zhang and A. Cloud, “The permeability characteristics of silicone rubber”, Dallas, TX, USA: Society for the Advancement of Material and Process Engineering (SAMPE) Fall Technical Conference, Nov. 6–9, 2006.

[92] Y. Einaga, I. Tribidasarianggraningrum, Y. Ishii, S. Sekiguchi, and K. Murata, “Ozone water concentration measurement apparatus and ozone water concentration measurement method”, U.S. Patent 9,625,405, Apr. 2017.

[93] N. Joshi, L. F. da Silva, F. M. Shimizu, *et al.*, “UV-assisted chemiresistors made with gold-modified ZnO nanorods to detect ozone gas at room temperature”, *Mikrochimica Acta*, vol. 186, no. 7, p. 418, 2019. DOI: `10.1007/s00604-019-3532-4`.

[94] X. Liu, S. Cheng, H. Liu, S. Hu, D. Zhang, and H. Ning, “A survey on gas sensing technology”, *Sensors (Basel, Switzerland)*, vol. 12, no. 7, pp. 9635–9665, 2012. DOI: `10.3390/s120709635`.

[95] L. S. R. Rocha, C. R. Foschini, C. C. Silva, E. Longo, and A. Z. Simões, “Novel ozone gas sensor based on ZnO nanostructures grown by the microwave-assisted hydrothermal route”, *Ceramics International*, vol. 42, no. 3, pp. 4539–4545, 2016. DOI: `10.1016/j.ceramint.2015.11.145`.

[96] J. Jayachandiran, M. Arivanandhan, O. Padmaraj, R. Jayavel, and D. Nedumaran, “Investigation on ozone-sensing characteristics of surface sensitive hybrid rgo/$\mathrm{WO_3}$ nanocomposite films at ambient temperature”, *Advanced Composites and Hybrid Materials*, vol. 3, no. 1, pp. 16–30, 2020. DOI: `10.1007/s42114-020-00134-8`.

[97] Y. J. Onofre, A. C. Catto, S. Bernardini, *et al.*, “Highly selective ozone gas sensor based on nanocrystalline $\mathrm{Zn_{0.95}Co_{0.05}O}$ thin film obtained via spray pyrolysis technique”, *Applied Surface Science*, vol. 478, pp. 347–354, 2019. DOI: `10.1016/j.apsusc.2019.01.197`.

[98] S. Bernardini, M. H. Benchekroun, T. Fiorido, *et al.*, “Ozone sensors working at room temperature using zinc oxide nanocrystals annealed at low temperature”, 4, vol. 1, Paris, France: Eurosensors Conference, Sep. 3–6, 2017, p. 423. DOI: `10.3390/proceedings1040423`.

[99] J. Huang, X. Wang, Y. Gong, *et al.*, “Construction of $\mathrm{WO_3}$ coatings with micro-nano hybrid structures by liquid precursor flame spray for enhanced sensing performances to sub-ppm ozone”, *Materials Letters*, vol. 205, pp. 106–109, 2017. DOI: `10.1016/j.matlet.2017.06.076`.

[100] A. C. Catto, T. Fiorido, É. L. Souza, *et al.*, “Improving the ozone gas-sensing properties of $\mathrm{CuWO_4}$ nanoparticles”, *Journal of Alloys and Compounds*, vol. 748, pp. 411–417, 2018. DOI: `10.1016/j.jallcom.2018.03.104`.

[101] W. Avansi Jr, A. C. Catto, L. F. da Silva, *et al.*, “One-dimensional $\mathrm{V_2O_5/TiO_2}$ heterostructures for chemiresistive ozone sensors”, *ACS Applied Nano Materials*, vol. 2, no. 8, pp. 4756–4764, 2019. DOI: `10.1021/acsanm.9b00578`.

[102] Y.-T. Tsai, S.-J. Chang, I.-T. Tang, Y.-J. Hsiao, and L.-W. Ji, “High density novel porous ZnO nanosheets based on a microheater chip for ozone sensors”, *IEEE Sensors Journal*, vol. 18, no. 13, pp. 5559–5565, 2018. DOI: `10.1109/JSEN.2018.2830508`.

[103] N. Joshi, F. M. Shimizu, I. T. Awan, *et al.*, “Ozone sensing properties of nickel phthalocyanine: ZnO nanorod heterostructures”, Orlando, FL, USA: IEEE SENSORS Conference, Oct. 30–Nov. 3, 2016, pp. 1–3. DOI: `10.1109/ICSENS.2016.7808407`.

[104] D. Ziegler, E. Bekyarova, G. Naishadham, *et al.*, “Nanotechnology-based ozone sensors exploiting low-frequency impedance changes for detection”, Vienna, Italy: International Meeting on Chemical Sensors, Jul. 15–19, 2018, pp. 740–741. DOI: `10.5162/IMCS2018/P2EC.22`.

[105] D. Ziegler, A. Marchisio, P. Palmero, and J.-M. Tulliani, “$\mathrm{WO_3}$-doped indium oxide thick films for ozone detection at low temperature”, Paris, France: Eurosensors Conference, Sep. 3–6, 2017, p. 428. DOI: `10.3390/proceedings1040428`.

[106] N. Joshi, L. F. da Silva, H. Jadhav, *et al.*, “One-step approach for preparing ozone gas sensors based on hierarchical $\mathrm{NiCo_2O_4}$ structures”, *The Royal Society of Chemistry*, vol. 6, no. 95, pp. 92 655–92 662, 2016. DOI: `10.1039/C6RA18384K`.

[107] A. C. Catto, L. F. d. Silva, M. I. B. Bernardi, *et al.*, “Local structure and surface properties of $\mathrm{Co_xZn_{1-x}O}$ thin films for ozone gas sensing”, *ACS Applied Materials & Interfaces*, vol. 8, no. 39, pp. 26 066–26 072, 2016. DOI: `10.1021/acsami.6b08589`.

[108] C.-H. Wu, G.-J. Jiang, K.-W. Chang, *et al.*, “Analysis of the sensing properties of a highly stable and reproducible ozone gas sensor based on amorphous InGaZnO thin film”, *Sensors*, vol. 18, no. 1, p. 163, 2018. DOI: `10.3390/s18010163`.

[109] G. Kakavelakis, E. Gagaoudakis, K. Petridis, *et al.*, “Solution processed $CH_3NH_3PbI_{3-x}Cl_x$ perovskite based self-powered ozone sensing element operated at room temperature”, *ACS Sensors*, vol. 3, no. 1, pp. 135–142, 2018. DOI: `10.1021/acssensors.7b00761`.

[110] Y. Sui, H. Liang, Q. Chen, W. Huo, X. Du, and Z. Mei, “Room-temperature ozone sensing capability of IGZO-decorated amorphous Ga_2O_3 films”, *ACS Applied Materials & Interfaces*, vol. 12, no. 7, pp. 8929–8934, 2020. DOI: `10.1021/acsami.9b22400`.

[111] T.-H. Lo, P.-Y. Shih, and C.-H. Wu, “The response of UV/blue light and ozone sensing using $Ag\text{-}TiO_2$ planar nanocomposite thin film”, *Sensors*, vol. 19, no. 23, p. 5061, 2019. DOI: `10.3390/s19235061`.

[112] G. Korotcenkov, V. Brinzari, and B. K. Cho, “In_2O_3- and SnO_2-based ozone sensors: Design and characterization”, *Critical Reviews in Solid State and Materials Sciences*, vol. 43, no. 2, pp. 83–132, 2018. DOI: `10.1080/10408436.2017.1287661`.

[113] D. Sauter, U. Weimar, G. Noetzel, J. Mitrovics, and W. Göpel, “Development of modular ozone sensor system for application in practical use”, *Sensors and Actuators B: Chemical*, vol. 69, no. 1-2, pp. 1–9, 2000. DOI: `10.1016/S0925-4005(00)00295-1`.

[114] M. Penza, G. Cassano, and F. Tortorella, “Gas recognition by activated WO_3 thin-film sensors array”, *Sensors and Actuators B: Chemical*, vol. 81, no. 1, pp. 115–121, 2001. DOI: `10.1016/S0925-4005(01)00941-8`.

[115] T. Belysheva, L. Bogovtseva, and E. Gutman, “Application of semiconductor metal oxide heterosystems for gas analysis”, *International Scientific Journal for Alternative Energy and Ecology*, vol. 122, p. 122, 2003.

[116] E. C. Chen, A. N. Pisarenko, A. Kolakovsky, E. W. Howe, R. S. Trussell, and R. R. Trussell, “Evaluation of four dissolved ozone residual meters performance and disinfection credits in potable reuse applications”, *Ozone: Science & Engineering*, vol. 42, no. 3, pp. 213–229, 2020. DOI: `10.1080/01919512.2020.1712187`.

[117] O. Erel, “A novel automated direct measurement method for total antioxidant capacity using a new generation, more stable ABTS radical cation”, *Clinical Biochemistry*, vol. 37, no. 4, pp. 277–285, 2004. DOI: `10.1016/j.clinbiochem.2003.11.015`.

[118] M. Kampa, A. Nistikaki, V. Tsaousis, N. Maliaraki, G. Notas, and E. Castanas, “A new automated method for the determination of the total antioxidant capacity (TAC) of human plasma, based on the crocin bleaching assay”, *BMC Clinical Pathology*, vol. 2, no. 1, p. 3, 2002. DOI: `10.1186/1472-6890-2-3`.

[119] S. O’Keeffe, C. Fitzpatrick, and E. Lewis, “An optical fibre based ultra violet and visible absorption spectroscopy system for ozone concentration monitoring”, *Sensors and Actuators B: Chemical*, vol. 125, no. 2, pp. 372–378, 2007. DOI: `10.1016/j.snb.2007.02.023`.

[120] I. Sieber and U. Gengenbach, “Design and optimization of optical gas sensor systems”, in *Chemical Sensors - Simulation and Modelling Volume 4: Optical Senosrs*, G. Korotcenkov and J. Watson, Eds., ISBN: 978-1606503188, New York, NY, USA: Momentum Press, 2013, ch. 11, pp. 405–453. DOI: `10.5643/9781606503201/ch11`.

[121] J. P. Burrows, A. Richter, A. Dehn, *et al.*, “Atmospheric remote-sensing reference data from GOME—2. Temperature-dependent absorption cross sections of O_3 in the 231–794 nm range”, *Journal of Quantitative Spectroscopy and Radiative Transfer*, vol. 61, no. 4, pp. 509–517, 1999. DOI: `10.1016/S0022-4073(98)00037-5`.

[122] I. M. Campbell, *Energy and the atmosphere: A physical-chemical approach*. London, UK: Wiley, 1977, ISBN: 978-0471994817.

[123] D. A. Newnham and J. Ballard, “Visible absorption cross sections and integrated absorption intensities of molecular oxygen (O_2 and O_4)”, *Journal of Geophysical Research: Atmospheres*, vol. 103, no. D22, pp. 28 801–28 815, 1998. DOI: `10.1029/98JD02799`.

[124] C. Wang, “Metal organic chemical vapor deposition of indium oxide for ozone sensing”, Ph.D. dissertation, Albert Ludwig University, Freiburg, Germany, 2009.

[125] G. Kockarts, “Aeronomy, a 20th century emergent science: The role of solar lyman series”, *Annales Geophysicae*, vol. 20, no. 5, pp. 585–598, 2002. DOI: `10.5194/angeo-20-585-2002`.

[126] W. Mäntele and E. Deniz, "UV–VIS absorption spectroscopy: Lambert-beer reloaded", *Spectrochimica Acta Part A: Molecular and Biomolecular Spectroscopy*, vol. 173, pp. 965–968, 2017. DOI: `10.1016/j.saa.2016.09.037`.

[127] J.-S. Oh, H. Yajima, K. Hashida, *et al.*, "In-situ UV absorption spectroscopy for observing dissolved ozone in water", *Journal of Photopolymer Science and Technology*, vol. 29, no. 3, pp. 427–432, 2016. DOI: `10.2494/photopolymer.29.427`.

[128] G. Reach, J. Feijen, and S. Alcock, "BIOMED concerted action chemical sensors for in vivo monitoring. the biocompatibility issue: First workshop held in Fontainebleau, France, 7–9 June 1993", *Biosensors & Bioelectronics*, vol. 9, no. 6, pp. xxi–xxviii, 1994. DOI: `doi.org/10.1016/0956-5663(94)90023-X`.

[129] X. Pang, M. D. Shaw, A. C. Lewis, L. J. Carpenter, and T. Batchellier, "Electrochemical ozone sensors: A miniaturised alternative for ozone measurements in laboratory experiments and air-quality monitoring", *Sensors and Actuators B: Chemical*, vol. 240, pp. 829–837, 2017. DOI: `10.1016/j.snb.2016.09.020`.

[130] S. Srinives, T. Sarkar, R. Hernandez, and A. Mulchandani, "Potassium iodide-functionalized polyaniline nanothin film chemiresistor for ultrasensitive ozone gas sensing", *Polymers*, vol. 9, no. 3, p. 80, 2017. DOI: `10.3390/polym9030080`.

[131] E. H. Schenk, P. A. Burke, and M. A. Centanni, "Amperometric gas sensor", U.S. Patent 10,001,455, Jun. 2018.

[132] Kuntze Instruments GmbH, O_3*/M-5*, `www.kuntze.com/de/gas-sensor-fuer-ozon`, Accessed: 17 Mar. 2020.

[133] K. Izumi, M. Utiyama, and Y. Y. Maruo, "A porous glass-based ozone sensing chip impregnated with potassium iodide and α-cyclodextrin", *Sensors and Actuators B: Chemical*, vol. 241, pp. 116–122, 2017. DOI: `10.1016/j.snb.2016.10.026`.

[134] C.-H. Wu, T.-L. Chou, and R.-J. Wu, "Rapid detection of trace ozone in $TiO_2–In_2O_3$ materials by using the differential method", *Sensors and Actuators B: Chemical*, vol. 255, pp. 117–124, 2018. DOI: `10.1016/j.snb.2017.08.055`.

[135] R. Souissi, N. Bouguila, M. Bendahan, *et al.*, "Ozone sensing study of sprayed β-In_2S_3 thin films", *Journal of Alloys and Compounds*, vol. 900, p. 163 513, 2022. DOI: `10.1016/j.jallcom.2021.163513`.

[136] P.-T. Lin and C.-Y. Huang, “Increasing the gas response of ozone sensors based on solution-processed InGaZnO by tuning the size of the nanostructure”, *ECS Journal of Solid State Science and Technology*, vol. 11, no. 6, p. 067 001, 2022. DOI: `10.1149/2162-8777/ac7255`.

[137] Kuntze Instruments GmbH, *Kuntze Krypton Dis*, `www.kuntze.com/de/download`, Accessed: 5 Apr. 2020.

[138] Emerson Electric Co., *Rosemount 499AOZ amperometric ozone sensor*, `www.emerson.com/de-de/catalog/rosemount-sku-499aoz-amperometric-ozone-sensor-de-de`, Accessed: 5 Apr. 2020.

[139] JUMO GmbH & Co. KG, *Jumo TecLine* ClO_2 *and* O_3, `www.jumo.de/web/products/apps/productdetailpage?pdpId=202634`, Accessed: 17 Mar. 2020.

[140] Process Instruments Pi, *Ozosense residual ozone analyser - data sheet*, https://www.processinstruments.net/wp-content/uploads/pdf/ISB134-Residual-Ozone-OzoSense.pdf, Accessed: 26 Jan. 2021.

[141] Analytical Technology Inc., *Dissolved ozone monitor model Q46H/64 - data sheet*, `www.analyticaltechnology.com/sys/docs/2096/ATI_Q46-64%20Dissolved%20Ozone%20Monitor.pdf`, Accessed: 26 Jan. 2021.

[142] Thermo Fisher Scientific, AquaSensors$^{\text{TM}}$ *AnalogPlus*$^{\text{TM}}$ *sensor*, `www.thermofisher.com/order/catalog/product/ASAPOZNE#/ASAPOZNE`, Accessed: 17 Mar. 2020, 2020.

[143] Eco Sensors, *DO3 - data sheet*, `www.spectrex.com/html_files2/pdf/Pocket%20Ozone%20DO3%20r1%200%20Manual%201-3-09.pdf`, Accessed: 26 Jan. 2021.

[144] Teledyne API, *Model 470*, `www.teledyne-api.com/products/dissolved-ozone-instruments/470`, Accessed: 17 Mar. 2020.

[145] A. Famili, S. A. Palkar, and W. J. Baldy Jr, “First drop dissimilarity in drop-on-demand inkjet devices”, *Physics of Fluids*, vol. 23, no. 1, p. 012 109, 2011. DOI: `10.1063/1.3543758`.

[146] B. Andò, S. Baglio, A. R. Bulsara, T. Emery, V. Marletta, and A. Pistorio, “Low-cost inkjet printing technology for the rapid prototyping of transducers”, *Sensors (Basel, Switzerland)*, vol. 17, no. 4, 2017. DOI: `10.3390/s17040748`.

[147] U. Gengenbach, M. Ungerer, L. Koker, *et al.*, “Automated fabrication of multi-layer printed electronic circuits using a novel vector ink-jet printing process control and surface mounting of discrete components”, *IFAC-PapersOnLine*, vol. 52, no. 15, pp. 609–614, 2019. DOI: `10.1016/j.ifacol.2019.11.743`.

[148] S. Kim, S. Won, G.-D. Sim, I. Park, and S.-B. Lee, “Tensile characteristics of metal nanoparticle films on flexible polymer substrates for printed electronics applications”, *Nanotechnology*, vol. 24, no. 8, p. 085 701, 2013. DOI: `10.1088/0957-4484/24/8/085701`.

[149] Z. Xu, Q. Dong, B. Otieno, *et al.*, “Real-time in situ sensing of multiple water quality related parameters using micro-electrode array (MEA) fabricated by inkjet-printing technology (IPT)”, *Sensors and Actuators B: Chemical*, vol. 237, pp. 1108–1119, 2016. DOI: `10.1016/j.snb.2016.09.040`.

[150] A. Moya, M. Ortega-Ribera, X. Guimerà, *et al.*, “Online oxygen monitoring using integrated inkjet-printed sensors in a liver-on-a-chip system”, *Lab Chip*, vol. 18, no. 14, pp. 2023–2035, 2018. DOI: `10.1039/c8lc00456k`.

[151] A. Moya, R. Pol, A. Martínez-Cuadrado, R. Villa, G. Gabriel, and M. Baeza, “Stable full-inkjet-printed solid-state Ag/AgCl reference electrode”, *Analytical Chemistry*, vol. 91, no. 24, pp. 15 539–15 546, 2019. DOI: `10.1021/acs.analchem.9b03441`.

[152] J. Wu, R. C. Roberts, N. C. Tien, and D. Li, “Inkjet printed silver patterning on PDMS to fabricate microelectrodes for microfluidic sensing”, Valencia, Spain: IEEE SENSROS Conference, Nov. 2–5, 2014, pp. 1100–1103. DOI: `10.1109/ICSENS.2014.6985197`.

[153] A. Laposa, J. Kroutil, M. Davydova, *et al.*, “Inkjet seeded CVD-grown hydrogenated diamond gas sensor under UV-LED illumination”, *IEEE Sensors Journal*, vol. 20, no. 3, p. 1, 2019. DOI: `10.1109/JSEN.2019.2946947`.

[154] M. Rieu, M. Camara, G. Tournier, *et al.*, “Fully inkjet printed $\mathrm{SnO_2}$ gas sensor on plastic substrate”, *Sensors and Actuators B: Chemical*, vol. 236, pp. 1091–1097, 2016. DOI: `10.1016/j.snb.2016.06.042`.

[155] O. Kassem, M. Saadaoui, M. Rieu, S. Sao-Joao, and J. P. Viricelle, “Synthesis and inkjet printing of sol-gel derived tin oxide ink for flexible gas sensing application”, *Journal of Materials Science*, vol. 53, no. 18, pp. 12 750–12 761, 2018. DOI: `10.1007/s10853-018-2577-9`.

[156] N. Spinella, C. Galati, and L. Renna, “Inkjet printing of controlled ZnO nanoparticles layering”, *Journal of Materials and Applications*, vol. 8, no. 1, pp. 34–40, 2019. DOI: `10.32732/jma.2019.8.1.34`.

[157] J. Leppäniemi, K. Eiroma, H. Majumdar, and A. Alastalo, “Far-UV annealed inkjet-printed In_2O_3 semiconductor layers for thin-film transistors on a flexible polyethylene naphthalate substrate”, *ACS Applied Materials & Interfaces*, vol. 9, no. 10, pp. 8774–8782, 2017. DOI: `10.1021/acsami.6b14654`.

[158] B. Hassan, Y. Liang, J. Yong, *et al.*, “Facile fabrication of an electrolyte-gated In_2O_3 nanoparticle-based thin-film transistor uniting laser ablation and inkjet printing”, *Flexible Printed Electronics*, vol. 3, no. 4, p. 042 001, 2018. DOI: `10.1088/2058-8585/aaed19`.

[159] S. Hong, J. Shin, Y. Hong, *et al.*, “Humidity-sensitive field effect transistor with In_2O_3 nanoparticles as a sensing layer”, *Journal of Nanoscience and Nanotechnology*, vol. 19, no. 10, pp. 6656–6662, 2019. DOI: `10.1166/jnn.2019.17092`.

[160] B. Kim, M. L. Geier, M. C. Hersam, and A. Dodabalapur, “Inkjet printed circuits based on ambipolar and p-type carbon nanotube thin-film transistors”, *Scientific Reports*, vol. 7, p. 39 627, 2017. DOI: `10.1038/srep39627`.

[161] V.-T. Tran, Y. Wei, H. Yang, Z. Zhan, and H. Du, “All-inkjet-printed flexible ZnO micro photodetector for a wearable UV monitoring device”, *Nanotechnology*, vol. 28, no. 9, p. 095 204, 2017. DOI: `10.1088/1361-6528/aa57ae`.

[162] R. Kaufhold, M. Baeuscher, B. Wang, *et al.*, “An all-inkjet printed photosensor on flexible plastic substrate for the detection of ultraviolet radiation”, Barcelona, Spain: International Conference and Exhibition on Integration Issues of Miniaturized Systems, Apr. 10–11, 2019, pp. 126–133.

[163] J. Nahlik, A. Laposa, J. Voves, J. Kroutil, J. Drahokoupil, and M. Davydova, “A high sensitivity UV photodetector with inkjet printed ZnO/nanodiamond active layers”, *IEEE Sensors Journal*, vol. 19, no. 14, pp. 5587–5593, 2019. DOI: `10.1109/JSEN.2019.2893572`.

[164] J. Figueira, C. Gaspar, J. T. Carvalho, *et al.*, “Sustainable fully printed UV sensors on cork using zinc oxide/ethylcellulose inks”, *Micromachines*, vol. 10, no. 9, 2019. DOI: `10.3390/mi10090601`.

[165] Z. Zhan, J. An, Y. Wei, T. van Tran, and H. Du, "Inkjet-printed optoelectronics", *Nanoscale*, vol. 9, no. 3, pp. 965–993, 2017. DOI: `10.1039/c6nr08220c`.

[166] T. Han, Y. Yuan, X. Liang, Y. Zhang, C. Xiong, and L. Dong, "Colloidal stable quantum dots modified by dual functional group polymers for inkjet printing", *Journal of Materials Chemistry C*, vol. 5, no. 19, pp. 4629–4635, 2017. DOI: `10.1039/c7tc00452d`.

[167] Y. Pan, W. Zhang, S. Zhang, *et al.*, "Inkjet printing of water-soluble quantum dots", in *Advanced Graphic Communication, Printing and Packaging Technology*, P. Zhao, Z. Ye, M. Xu, and L. Yang, Eds., ISBN: 978-9811518645, Singapore: Springer Nature, 2020, pp. 296–303. DOI: `10.1007/978-981-15-1864-5_41`.

[168] L. Petani, D. Wickersheim, L. Koker, M. Reischl, U. Gengenbach, and C. Pylatiuk, "Experimental setup for evaluation of medical ozone gas sensors", Sundsvall, Sweden: IEEE Sensors Applications Symposium (SAS), Aug. 1–3, 2022, pp. 1–6. DOI: `10.1109/SAS54819.2022.9881340`.

[169] D. Klaus, D. Klawinski, S. Amrehn, M. Tiemann, and T. Wagner, "Light-activated resistive ozone sensing at room temperature utilizing nanoporous In_2O_3 particles: Influence of particle size", *Sensors and Actuators B: Chemical*, vol. 217, pp. 181–185, 2015. DOI: `10.1016/j.snb.2014.09.021`.

[170] BMT Messtechnik GmbH, *Datasheet: BMT 965*, `www.bmt-berlin.de/wp-content/uploads/965aq-datasheet.pdf`, Accessed: 26 Jan. 2021.

[171] Macherey-Nagel, *Technical data: PF-3*, `https://www.mn-net.com/media/pdf/80/fb/f9/Instruction-compact-photometer-PF-3.pdf`, Accessed: 26 Jan. 2021.

[172] M. Sosna, G. Denuault, R. W. Pascal, R. D. Prien, and M. Mowlem, "Development of a reliable microelectrode dissolved oxygen sensor", *Sensors and Actuators B: Chemical*, vol. 123, no. 1, pp. 344–351, 2007. DOI: `10.1016/j.snb.2006.08.033`.

[173] A. Moya, "Integrated sensors for overcoming organ-on-a-chip monitoring challenges", PhD dissertation, Universitat Autonoma de Barcelona, Barcelona, Spain, 2017.

[174] F. Pedregosa, G. Varoquaux, A. Gramfort, *et al.*, "Scikit-learn: Machine learning in python", *The Journal of Machine Learning Research*, vol. 12, pp. 2825–2830, 2011.

[175] J. D. Hunter, “Matplotlib: A 2D graphics environment”, *IEEE Annals of the History of Computing*, vol. 9, no. 03, pp. 90–95, 2007. DOI: `10.1109/MCSE.2007.55`.

[176] T. Mizuno, H. Tsuno, and H. Yamada, “Development of ozone self-decomposition model for engineering design”, *Ozone: Science & Engineering*, vol. 29, no. 1, pp. 55–63, 2007. DOI: `10.1080/01919510601115849`.

[177] TriOS Mess- und Datentechnik GmbH, *Datasheet: Opus*, `https://www.trios.de/en/files/D02-049en202009-Brochure-OPUS.pdf`, Accessed: 19 Aug. 2020.

[178] M. Karmaoui, S. G. Leonardi, M. Latino, *et al.*, “Pt-decorated $\mathrm{In_2O_3}$ nanoparticles and their ability as a highly sensitive ($<$ 10 ppb) acetone sensor for biomedical applications”, *Sensors and Actuators B: Chemical*, vol. 230, pp. 697–705, 2016. DOI: `10.1016/j.snb.2016.02.100`.

[179] W.-Y. Wu, X. Zhong, W. Wang, Q. Miao, and J.-J. Zhu, “Flexible PDMS-based three-electrode sensor”, *Electrochemistry Communications*, vol. 12, no. 11, pp. 1600–1604, 2010. DOI: `10.1016/j.elecom.2010.09.005`.

[180] Y. Sui and C. A. Zorman, “Inkjet printing of metal structures for electrochemical sensor applications”, *Journal of The Electrochemical Society*, vol. 167, no. 3, p. 037 571, 2020. DOI: `10.1149/1945-7111/ab721f`.

[181] DIN Deutsches Institut für Normung e. V., *DIN EN ISO 10993-1: Biologische Beurteilung von Medizinprodukten – Teil 1: Beurteilung und Prüfungen im Rahmen eines Risikomanagementsystems*, 2017.

[182] Q. Chen and G. A. Thouas, “Metallic implant biomaterials”, *Materials Science and Engineering: R: Reports*, vol. 87, pp. 1–57, 2015. DOI: `10.1016/j.mser.2014.10.001`.

[183] E. H. Nafea, A. Marson, L. A. Poole-Warren, and P. J. Martens, “Immunoisolating semi-permeable membranes for cell encapsulation: Focus on hydrogels”, *Journal of Controlled Release: Official Journal of the Controlled Release Society*, vol. 154, no. 2, pp. 110–122, 2011. DOI: `10.1016/j.jconrel.2011.04.022`.

[184] Y. Onuki, U. Bhardwaj, F. Papadimitrakopoulos, and D. J. Burgess, “A review of the biocompatibility of implantable devices: Current challenges to overcome foreign body response”, *Journal of Diabetes Science and Technology*, vol. 2, no. 6, 2008. DOI: `10.1177/193229680800200610`.

[185] C. A. Dinarello, “Anti-inflammatory agents: Present and future”, *Cell*, vol. 140, no. 6, pp. 935–950, 2010. DOI: `10.1016/j.cell.2010.02.043`.

[186] Y. Dahman, *Biomaterials science and technology: Fundamentals and developments*. Boca Raton, FL, USA: CRC Press, 2019, ISBN: 978-0429878350.

[187] R. Simeonova and N. Danchev, “Assessment of surgical sutures polymed by intracutaneous irritation test in rabbits”, *Interdisciplinary Toxicology*, vol. 6, no. 2, pp. 99–102, 2013. DOI: `10.2478/intox-2013-0017`.

[188] V. dos Santos, R. N. Brandalise, and M. Savaris, *Engineering of biomaterials*. Cham, Germany: Springer International Publishing, 2017, ISBN: 978-3319586069. DOI: `10.1007/978-3-319-58607-6`.

[189] DIN Deutsches Institut für Normung e. V., *DIN EN ISO 10993-18: Biologische Beurteilung von Medizinprodukten – Teil 18: Chemische Charakterisierung von Werkstoffen für Medizinprodukte im Rahmen eines Risikomanagementsystems*, 2021.

[190] J. M. Anderson, A. Rodriguez, and D. T. Chang, “Foreign body reaction to biomaterials”, *Seminars in Immunology*, vol. 20, no. 2, pp. 86–100, 2008. DOI: `10.1016/j.smim.2007.11.004`.

[191] V. Hasirci and N. Hasirci, *Fundamentals of Biomaterials*. New York, NY, USA: Springer New York, 2018, ISBN: 978-1493988549. DOI: `10.1007/978-1-4939-8856-3`.

[192] U. Guth, F. Gerlach, M. Decker, W. Oelßner, and W. Vonau, “Solid-state reference electrodes for potentiometric sensors”, *Journal of Solid State Electrochemistry*, vol. 13, no. 1, pp. 27–39, 2009. DOI: `10.1007/s10008-008-0574-7`.

[193] D. Lee, M.-L. Seol, G. Motilal, *et al.*, “All 3D-printed flexible ZnO UV photodetector on an ultraflat substrate”, *ACS Sensors*, vol. 5, no. 4, pp. 1028–1032, 2020. DOI: `10.1021/acssensors.9b02544`.

[194] M. Batzill and U. Diebold, “The surface and materials science of tin oxide”, *Progress in Surface Science*, vol. 79, no. 2-4, pp. 47–154, 2005. DOI: `10.1016/j.progsurf.2005.09.002`.

[195] C. Y. Wang, R. Becker, T. Passow, *et al.*, “Photon stimulated sensor based on indium oxide nanoparticles I: Wide-concentration-range ozone monitoring in air”, *Sensors and Actuators B: Chemical*, vol. 152, no. 2, pp. 235–240, 2011. DOI: `10.1016/j.snb.2010.12.014`.

[196] Y. Park, K.-Y. Dong, J. Lee, J. Choi, G.-N. Bae, and B.-K. Ju, “Development of an ozone gas sensor using single-walled carbon nanotubes”, *Sensors and Actuators B: Chemical*, vol. 140, no. 2, pp. 407–411, 2009. DOI: `10.1016/j.snb.2009.04.055`.

[197] S. C. Colindres, K. Aguir, F. Cervantes Sodi, L. V. Vargas, J. M. Salazar, and V. G. Febles, “Ozone sensing based on palladium decorated carbon nanotubes”, *Sensors (Basel, Switzerland)*, vol. 14, no. 4, pp. 6806–6818, 2014. DOI: `10.3390/s140406806`.

[198] B. Ghaddab, J.-B. Sanchez, C. Mavon, *et al.*, “Detection of O_3 and NH_3 using hybrid tin dioxide/carbon nanotubes sensors: Influence of materials and processing on sensor’s sensitivity”, *Sensors and Actuators B: Chemical*, vol. 170, pp. 67–74, 2012. DOI: `10.1016/j.snb.2011.01.044`.

[199] G. Korotcenkov, V. Brinzari, and B. K. Cho, “In_2O_3- and SnO_2-based thin film ozone sensors: Fundamentals”, *Journal of Sensors*, vol. 2016, no. 5, pp. 1–31, 2016. DOI: `10.1155/2016/3816094`.

[200] C.-H. Wu, T.-L. Chou, and R.-J. Wu, “Rapid detection of trace ozone in TiO_2-In_2O_3 materials by using the differential method”, *Sensors and Actuators B: Chemical*, vol. 255, pp. 117–124, 2018. DOI: `10.1016/j.snb.2017.08.055`.

[201] R. Mikkonen, P. Puistola, I. Jönkkäri, and M. Mäntysalo, “Inkjet printable polydimethylsiloxane for all-inkjet-printed multilayered soft electrical applications”, *ACS Applied Materials & Interfaces*, vol. 12, no. 10, pp. 11 990–11 997, 2020. DOI: `10.1021/acsami.9b19632`.

[202] H. Becker and L. E. Locascio, “Polymer microfluidic devices”, *Talanta*, vol. 56, no. 2, pp. 267–287, 2002. DOI: `10.1016/S0039-9140(01)00594-X`.

[203] Y. Htwe, W. S. Chow, G. Suriati, A. A. Thant, and M. Mariatti, “Properties enhancement of graphene and chemical reduction silver nanoparticles conductive inks printed on polyvinyl alcohol (PVA) substrate”, *Synthetic Metals*, vol. 256, p. 116 120, 2019. DOI: `10.1016/j.synthmet.2019.116120`.

[204] J. Jayachandiran, M. Arivanandhan, O. Padmaraj, R. Jayavel, and D. Nedumaran, “Investigation on ozone-sensing characteristics of surface sensitive hybrid rGO/WO_3 nanocomposite films at ambient temperature”, *Advanced Composites and Hybrid Materials*, vol. 3, no. 1, pp. 16–30, 2020. DOI: `10.1007/s42114-020-00134-8`.

[205] S. Kim, A. Shamim, A. Georgiadis, H. Aubert, and M. M. Tentzeris, “Fabrication of fully inkjet-printed Vias and SIW structures on thick polymer substrates”, *IEEE Transactions on Components, Packaging and Manufacturing Technology*, vol. 6, no. 3, pp. 486–496, 2016. DOI: `10.1109/TCPMT.2016.2522461`.

[206] K. E. Petersen, “Silicon as a mechanical material”, *Proceedings of the IEEE*, vol. 70, no. 5, pp. 420–457, 1982. DOI: `10.1109/PROC.1982.12331`.

[207] Y. Fang and M. M. Tentzeris, “Surface modification of polyimide films for inkjet-printing of flexible electronic devices”, in *Flexible electronics*, S. Rackauskas, Ed., ISBN: 978-1789234565, London, UK: IntechOpen, 2018. DOI: `10.5772/intechopen.76450`.

[208] C. Sturgess, C. J. Tuck, I. A. Ashcroft, and R. D. Wildman, “3D reactive inkjet printing of polydimethylsiloxane”, *Journal of Materials Chemistry C*, vol. 5, no. 37, pp. 9733–9743, 2017. DOI: `10.1039/C7TC02412F`.

[209] P. V. Shanbhag and K. K. Sirkar, “Ozone and oxygen permeation behavior of silicone capillary membranes employed in membrane ozonators”, *Journal of Applied Polymer Science*, vol. 69, no. 7, pp. 1263–1273, 1998. DOI: `10.1002/(SICI)1097-4628(19980815)69:7<1263::AID-APP1>3.0.CO;2-C`.

[210] Z. Cui, *Printed electronics: Materials, technologies and applications*. Hoboken, NJ, USA: Solaris South Tower Singapore and Wiley/Higher Education Press, 2016, ISBN: 978-1118920923.

[211] A. Yoshinobu, T. Misaichi, Y. Kaoru, *et al.*, “High-sensitivity ozone sensing using 280 nm deep ultraviolet light-emitting diode for detection of natural hazard ozone”, *Journal of Environmental Protection*, vol. 3, no. 8, pp. 695–699, 2012. DOI: `10.4236/jep.2012.38082`.

[212] C. Y. Wang, V. Cimalla, T. Kups, *et al.*, “Integration of $\mathrm{In_2O_3}$ nanoparticle based ozone sensors with gainn/ gan light emitting diodes”, *Applied Physics Letters*, vol. 91, no. 10, p. 103 509, 2007. DOI: `10.1063/1.2779971`.

[213] Y. Yang, Y. Jiang, J. Xu, and J. Yu, “Conducting PEDOT–PSS composite films assembled by LB technique”, *Colloids and Surfaces A: Physicochemical and Engineering Aspects*, vol. 302, no. 1-3, pp. 157–161, 2007. DOI: `10.1016/j.colsurfa.2007.02.013`.

[214] C. P and M. C, *Hazardous Chemicals Handbook*. Woburn, MA, USA: Butterworth-Heinemann, 2002, ISBN: 978-0-7506-4888-2. DOI: `10.1016/B978-0-7506-4888-2.X5000-2`.

[215] A. Moya, E. Sowade, F. J. del Campo, *et al.*, "All-inkjet-printed dissolved oxygen sensors on flexible plastic substrates", *Organic Electronics*, vol. 39, pp. 168–176, 2016. DOI: `10.1016/j.orgel.2016.10.002`.

[216] T. Takada, K. Suzuki, and M. Nakane, "Highly sensitive ozone sensor", *Sensors and Actuators B: Chemical*, pp. 404–407, 1993. DOI: `10.1016/0925-4005(93)85412-4`.

[217] K. Tadatomo, H. Okagawa, Y. Ohuchi, *et al.*, "High output power ingan ultraviolet light-emitting diodes fabricated on patterned substrates using metalorganic vapor phase epitaxy", *Japanese Journal of Applied Physics*, vol. 40, no. 6B, p. L583, 2001. DOI: `10.1143/JJAP.40.L583`.

[218] Y.-P. Jia, B.-Y. Ma, X.-W. Wei, and Z.-Y. Qian, "The in vitro and in vivo toxicity of gold nanoparticles", *Chinese Chemical Letters*, vol. 28, no. 4, pp. 691–702, 2017. DOI: `10.1016/j.cclet.2017.01.021`.

[219] N. Hadrup and H. R. Lam, "Oral toxicity of silver ions, silver nanoparticles and colloidal silver–a review", *Regulatory Toxicology and Pharmacology*, vol. 68, no. 1, pp. 1–7, 2014. DOI: `10.1016/j.yrtph.2013.11.002`.

[220] Carl Roth, *Data sheet AgCl*, `www.carlroth.com/en/en/a-to-z/silver-chloride/p/6877.1`, Accessed: 4 Oct. 2021.

[221] RÖMPP, *Data sheet Al*, `www.roempp.thieme.de/lexicon/RD-01-01786?searchterm=ld50+al2o3;content_type=lexicon&context=search`, Accessed: 30 Sept. 2021.

[222] ECHA, *Data sheet* Al_2O_3 *1344-28-1*, `www.echa.europa.eu/de/registration-dossier/-/registered-dossier/16039/7/3/1`, Accessed: 30 Sept. 2021.

[223] V. Pokharkar, S. Dhar, D. Bhumkar, V. Mali, S. Bodhankar, and B. Prasad, "Acute and subacute toxicity studies of chitosan reduced gold nanoparticles: A novel carrier for therapeutic agents", *Journal of Biomedical Nanotechnology*, vol. 5, no. 3, pp. 233–239, 2009. DOI: `10.1166/jbn.2009.1027`.

[224] Z. Zhao, M. Liu, X. Jia, *et al.*, "Toxicity effect of carbon nanotubes", *Nano Life*, vol. 4, no. 03, p. 1 441 009, 2014. DOI: `10.1142/S1793984414410098`.

[225] M. Araya, M. Olivares, and F. Pizarro, “Copper in human health”, *International Journal of Environment and Health*, vol. 1, no. 4, pp. 608–620, 2007. DOI: `10.1504/IJENVH.2007.018578`.

[226] T. G. Rosano, “Ellenhorn’s medical toxicology: Diagnosis and treatment of human poisoning”, *Clinical Chemistry*, vol. 44, no. 2, p. 366, 1998. DOI: `10.1093/clinchem/44.2.366`.

[227] I. C. Smith and B. L. Carson, *Trace metals in the environment*. Ann Arbor, MI, USA: Ann Arbor Science Publishers, 1977, ISBN: 978-0250402328.

[228] DryWired, *Data sheet ITO*, `www.drywired.com/drywired-defense-liquid-nanotint-clear-msds/`, Acessed: 30 Sept. 2021.

[229] S. Saeidifard, F. Sohrabi, and S. M. Hamidi, “Polydimethylsiloxane (PDMS): A promising material for biological applications”, in *Polydimethylsiloxane: Structure and Applications*, P. N. Carlsen, Ed., ISBN: 978-1536175905, New York, NY, USA: Nova Science Publishers Inc., 2020, p. 145.

[230] R. A. Green, N. H. Lovell, G. G. Wallace, and L. A. Poole-Warren, “Conducting polymers for neural interfaces: Challenges in developing an effective long-term implant”, *Biomaterials*, vol. 29, no. 24-25, pp. 3393–3399, 2008. DOI: `10.1016/j.biomaterials.2008.04.047`.

[231] S. P. Products, *Data sheet PSS 25704-18-1*, `www.scipoly.com/wp-content/uploads/2020/09/Sodium%20polystyrene%20sulfonate-sds.pdf`, Accessed: 30 Sept. 2021.

[232] INEOS, *Data sheet PET 9002-88-4*, `www.ineos.com/show-document/?grade=G50-100&bu=INEOS+O+%26+P+USA&documentType=SDS&docLanguage=CA-EN&version=e84c7003ec56c432cae3f968bf14c69b`, Accessed: 30 Sept. 2021.

[233] REACH, *Data sheet PMMA*, `www.sumitomo-chem.com.sg/wp-content/uploads/2019/09/SDS-09-0041_PMMA_PRIME_EX_EXN_MH_20190108.pdf`, Accessed: 30 Sept. 2021.

[234] Heraeus, *Data sheet Platin 7440-06-4*, `www.heraeus.com/media/media/hpm/doc_hpm/safety_data_sheets/de_1/Platin.pdf`, Accessed: 29 Sept. 2021.

[235] DuPont, *Data sheet PTFE 9002-84-0*, `http://www1.mscdirect.com/MSDS/MSDS00014/48703219-20110702.PDF`, Accessed: 30 Sept. 2021.

[236] C. DeMerlis and D. Schoneker, “Review of the oral toxicity of polyvinyl alcohol (PVA)”, *Food and Chemical Toxicology*, vol. 41, no. 3, pp. 319–326, 2003. DOI: `10.1016/s0278-6915(02)00258-2`.

[237] A & C Plastics, *Data sheet PVC 9002-86-2*, `www.acplasticsinc.com/media/documents/MSDS_Type1PVC.pdf`, Accessed: 30 Sept. 2021.

[238] MTI Japan, *Data sheet PVDF*, `www.mti-japan.com/wp/wp-content/uploads/2014/08/MSDS_PVDF.pdf`, Accessed: 30 Sept. 2021.

[239] Safe Silica, *Data sheet quartz*, `www.safesilica.eu/wp-content/uploads/2018/05/Quartz-SDS-template.pdf`, Accessed: 30 Sept. 2021.

[240] Sciencelab, *Data sheet Si 7440-21-3*, `www.louisville.edu/micronano/files/documents/safety-data-sheets-sds/silicon/`, Accessed: 4 Oct. 2021.

[241] W. Mills, *Data sheet* $\mathrm{SiO_2}$*/Si 7631-86-9*, `www.washingtonmills.com/sites/default/files/2019-02/sds_silicon_dioxide_fused_silica_june_2018_0.pdf`, Accessed: 30 Sept. 2021.

[242] Ionic Liquids Technologies, *Data sheet* $\mathrm{SnO_2}$ *18282-10-5*, `www.nanomaterials.iolitec.de/sites/nanomaterials.iolitec.de/files/sds/SDS%20NO-0009%20SnO2.pdf`, Accessed: 4 Oct. 2021.

[243] H. Shi, R. Magaye, V. Castranova, and J. Zhao, “Titanium dioxide nanoparticles: A review of current toxicological data”, *Particle and Fibre Toxicology*, vol. 10, pp. 1–33, 2013. DOI: `10.1186/1743-8977-10-15`.

[244] Optron, *Data sheet Tungsten Trioxide 215-231-4*, `www.optron.canon/ja/support/img/pdf/en_18/optical_en/214_WO3_d_en.pdf`, Accessed: 30 Sept. 2021.

[245] ECHA, *Data sheet ZnO 1314-13-2*, `www.echa.europa.eu/de/registration-dossier/-/registered-dossier/16139/7/3/1`, Accessed: 30 Sept. 2021.

[246] Saint-Gobain, *Data sheet Zirconium dioxide 1314-23-4*, `www.dawson-macdonald.com/wp-content/uploads/sds-alumina-zirconia.pdf`, Accessed: 30 Sept. 2021.

[247] O. Oktavianty, Y. Ishii, S. Haruyama, T. Kyoutani, Z. Darmawan, and S. E. Swara, "Controlling droplet behaviour and quality of dod inkjet printer by designing actuation waveform for multi-drop method", *IOP Conference Series: Materials Science and Engineering*, vol. 1034, no. 1, p. 012 091, 2021.

[248] T. Sekitani, Y. Noguchi, U. Zschieschang, H. Klauk, and T. Someya, "Organic transistors manufactured using inkjet technology with subfemtoliter accuracy", *Proceedings of the National Academy of Sciences*, vol. 105, no. 13, pp. 4976–4980, 2008. DOI: `10.1073/pnas.0708340105`.

[249] K.-S. Kwon, M. K. Rahman, T. H. Phung, S. D. Hoath, S. Jeong, and J. S. Kim, "Review of digital printing technologies for electronic materials", *Flexible and Printed Electronics*, vol. 5, no. 4, p. 043 003, 2020. DOI: `10.1088/2058-8585/abc8ca`.

[250] SIJ Technology, *Product line-up*, `www.sijtechnology.com/en/products/#pro1`, Accessed: 5 Oct. 2021.

[251] K. Fukuda and T. Someya, "Recent progress in the development of printed thin-film transistors and circuits with high-resolution printing technology", *Advanced Materials*, vol. 29, no. 25, p. 1 602 736, 2017. DOI: `10.1002/adma.201602736`.

[252] E. Wintermantel and S.-W. Ha, *Medizintechnik*. Berlin, Germany: Springer Berlin Heidelberg, 2009, ISBN: 978-3540939351. DOI: `10.1007/978-3-540-93936-8`.

[253] P. M. Favi, M. Gao, L. Johana Sepúlveda Arango, *et al.*, "Shape and surface effects on the cytotoxicity of nanoparticles: Gold nanospheres versus gold nanostars", *Journal of Biomedical Materials Research Part A*, vol. 103, no. 11, pp. 3449–3462, 2015. DOI: `10.1002/jbm.a.35491`.

[254] M. Akter, M. T. Sikder, M. M. Rahman, *et al.*, "A systematic review on silver nanoparticles-induced cytotoxicity: Physicochemical properties and perspectives", *Journal of Advanced Research*, vol. 9, 2018. DOI: `10.1016/j.jare.2017.10.008`.

[255] B. A. Katsnelson, T. D. Degtyareva, I. I. Minigalieva, *et al.*, "Subchronic systemic toxicity and bioaccumulation of $\mathrm{Fe_3O_4}$ nano- and microparticles following repeated intraperitoneal administration to rats", *International Journal of Toxicology*, vol. 30, no. 1, pp. 59–68, 2011. DOI: `10.1177/1091581810385149`.

[256] H. B. Raju, Y. Hu, A. Vedula, S. R. Dubovy, and J. L. Goldberg, “Evaluation of magnetic micro- and nanoparticle toxicity to ocular tissues”, *PlOS One*, vol. 6, no. 5, e17452, 2011. DOI: `10.1371/journal.pone.0017452`.

[257] E. Fröhlich, “The role of surface charge in cellular uptake and cytotoxicity of medical nanoparticles”, *International Journal of Nanomedicine*, vol. 7, pp. 5577–5591, 2012. DOI: `10.2147/IJN.S36111`.

[258] J. Okuda-Shimazaki, S. Takaku, K. Kanehira, S. Sonezaki, and A. Taniguchi, “Effects of titanium dioxide nanoparticle aggregate size on gene expression”, *International Journal of Molecular Sciences*, vol. 11, no. 6, pp. 2383–2392, 2010. DOI: `10.3390/ijms11062383`.

[259] C. A. Poland, R. Duffin, I. Kinloch, *et al.*, “Carbon nanotubes introduced into the abdominal cavity of mice show asbestos-like pathogenicity in a pilot study”, *Nature Nanotechnology*, vol. 3, no. 7, pp. 423–428, 2008. DOI: `10.1038/nnano.2008.111`.

[260] A. Takagi, A. Hirose, T. Nishimura, *et al.*, “Induction of mesothelioma in p53+/- mouse by intraperitoneal application of multi-wall carbon nanotube”, *The Journal of Toxicological Sciences*, vol. 33, no. 1, pp. 105–116, 2008. DOI: `10.2131/jts.33.105`.

[261] K. Yang and Y.-Q. Ma, “Computer simulation of the translocation of nanoparticles with different shapes across a lipid bilayer”, *Nature Nanotechnology*, vol. 5, no. 8, pp. 579–583, 2010. DOI: `10.1038/nnano.2010.141`.

[262] Z. Chu, S. Zhang, B. Zhang, *et al.*, “Unambiguous observation of shape effects on cellular fate of nanoparticles”, *Scientific Reports*, vol. 4, p. 4495, 2014. DOI: `10.1038/srep04495`.

[263] I. Nasir, M. Lundqvist, and C. Cabaleiro-Lago, “Size and surface chemistry of nanoparticles lead to a variant behavior in the unfolding dynamics of human carbonic anhydrase”, *Nanoscale*, vol. 7, no. 41, pp. 17 504–17 515, 2015. DOI: `10.1039/C5NR05360A`.

[264] N. M. Schaeublin, L. K. Braydich-Stolle, A. M. Schrand, *et al.*, “Surface charge of gold nanoparticles mediates mechanism of toxicity”, *Nanoscale*, vol. 3, no. 2, pp. 410–420, 2011. DOI: `10.1039/c0nr00478b`.

[265] C. M. Goodman, C. D. McCusker, T. Yilmaz, and V. M. Rotello, “Toxicity of gold nanoparticles functionalized with cationic and anionic side chains”, *Bioconjugate Chemistry*, vol. 15, no. 4, pp. 897–900, 2004. DOI: `10.1021/bc049951i`.

[266] M. Baek, I.-S. Kim, J. Yu, H. E. Chung, J.-H. Choy, and S.-J. Choi, “Effect of different forms of anionic nanoclays on cytotoxicity”, *Journal of Nanoscience and Nanotechnology*, vol. 11, no. 2, pp. 1803–1806, 2011. DOI: `10.1166/jnn.2011.3408`.

[267] S. Bhattacharjee, L. H. de Haan, N. M. Evers, *et al.*, “Role of surface charge and oxidative stress in cytotoxicity of organic monolayer-coated silicon nanoparticles towards macrophage NR8383 cells”, *Particle and Fibre Toxicology*, vol. 7, p. 25, 2010. DOI: `10.1186/1743-8977-7-25`.

[268] R. D. Cox and W. J. Phillips, “Ethylene glycol toxicity”, *Military Medicine*, vol. 169, no. 8, pp. 660–663, 2004. DOI: `10.7205/MILMED.169.8.660`.

[269] Sigma-Aldrich, *Safety data sheet ethyleneglycol*, `www.sigmaaldrich.com/catalog/product/sial/324558?lang=de&region=DE`, Accessed: 7 Aug. 2020.

[270] C. Greulich, S. Kittler, M. Epple, G. Muhr, and M. Köller, “Studies on the biocompatibility and the interaction of silver nanoparticles with human mesenchymal stem cells (hMSCs)”, *Langenbeck’s Archives of Surgery*, vol. 394, no. 3, pp. 495–502, 2009. DOI: `10.1007/s00423-009-0472-1`.

[271] I. Khan, K. Saeed, and I. Khan, “Nanoparticles: Properties, applications and toxicities”, *Arabian Journal of Chemistry*, vol. 12, no. 7, pp. 908–931, 2019. DOI: `10.1016/j.arabjc.2017.05.011`.

[272] J. Tang, L. Xiong, G. Zhou, *et al.*, “Silver nanoparticles crossing through and distribution in the blood-brain barrier in vitro”, *Journal of Nanoscience and Nanotechnology*, vol. 10, no. 10, pp. 6313–6317, 2010. DOI: `10.1166/jnn.2010.2625`.

[273] I. Lee, S. Kim, J. Yun, I. Park, and T.-S. Kim, “Interfacial toughening of solution processed ag nanoparticle thin films by organic residuals”, *Nanotechnology*, vol. 23, no. 48, p. 485 704, 2012. DOI: `10.1088/0957-4484/23/48/485704`.

[274] Sigma-Aldrich, *Safety data sheet silver dispersion*, `www.sigmaaldrich.com/catalog/product/aldrich/736465?lang=de&region=DE`, Accessed: 30 May 2020.

[275] ANP Co. Ltd, *Silver jet ink - nano-silver ink for inkjet printing*, `http://anapro.com/eng/product/silver_inkjet_ink.html#`, Accessed: 03 Aug. 2020.

[276] Sigma-Aldrich, *Safety data sheet TGME*, `www.sigmaaldrich.com/catalog/product/aldrich/568554?lang=de&region=DE`, Accessed: 26 Jul. 2020.

[277] C. S. Lieber, “Biochemical and molecular basis of alcohol-induced injury to liver and other tissues”, *New England Journal of Medicine*, vol. 319, no. 25, pp. 1639–1650, 1988. DOI: `10.1056/NEJM198812223192505`.

[278] D. Wang, D. Ba, Z. Hao, *et al.*, “A novel approach for PDMS thin films production towards application as substrate for flexible biosensors”, *Materials Letters*, vol. 221, pp. 228–231, 2018. DOI: `10.1016/j.matlet.2018.03.114`.

[279] F. J. Schoen, J. E. Lemons, B. D. Ratner, and A. S. Hoffman, *Biomaterials science: An introduction to materials in medicine*. Burlington, NJ, USA: Academic Press, 2013, vol. 3rd ed, ISBN: 978-0080877808. DOI: `10.1016/C2009-0-02433-7`.

[280] M.-C. Bélanger and Y. Marois, “Hemocompatibility, biocompatibility, inflammatory and in vivo studies of primary reference materials low-density polyethylene and polydimethylsiloxane: A review”, *Journal of Biomedical Materials Research*, 2001. DOI: `10.1002/jbm.1043`.

[281] D. S. Lee, S. J. Kim, J. H. Sohn, *et al.*, “Biocompatibility of a PDMS-coated micro-device: Bladder volume monitoring sensor”, *Chinese Journal of Polymer Science*, vol. 30, no. 2, pp. 242–249, 2012. DOI: `10.1007/s10118-012-1119-1`.

[282] K. V. Nemani, K. L. Moodie, J. B. Brennick, A. Su, and B. Gimi, “In vitro and in vivo evaluation of su-8 biocompatibility”, *Materials Science & Engineering. C, Materials for Biological Applications*, vol. 33, no. 7, pp. 4453–4459, 2013. DOI: `10.1016/j.msec.2013.07.001`.

[283] E. S. Ereifej, S. Khan, G. Newaz, J. Zhang, G. W. Auner, and P. J. VandeVord, “Characterization of astrocyte reactivity and gene expression on biomaterials for neural electrodes”, *Journal of Biomedical Materials Research*, 2010. DOI: `10.1002/jbm.a.33170`.

[284] G. Kotzar, M. Freas, P. Abel, *et al.*, “Evaluation of mems materials of construction for implantable medical devices”, *Biomaterials*, vol. 23, 2002. DOI: `10.1016/S0142-9612(02)00007-8`.

[285] V. N. Vernekar, D. K. Cullen, N. Fogleman, *et al.*, “SU-8 2000 rendered cytocompatible for neuronal bioMEMS applications”, *Journal of Biomedical Materials Research Part A*, vol. 89, no. 1, pp. 138–151, 2009. DOI: `10.1002/jbm.a.31839`.

[286] N. A. Campbell, J. B. Reece, A. Kratochwil, and T. Lazar, *Biologie* (Pearson Studium - Biologie). Munich, Germany: Pearson Studium, 2012, ISBN: 978-3827372871.

[287] PubChem, *Potassium sulfate*, `www.pubchem.ncbi.nlm.nih.gov/compound/Potassium-sulfate#section=Absorption-Distribution-and-Excretion`, Accessed: 7 Aug. 2020.

[288] W. Bedale, J. J. Sindelar, and A. L. Milkowski, “Dietary nitrate and nitrite: Benefits, risks, and evolving perceptions”, *Meat Science*, vol. 120, pp. 85–92, 2016. DOI: `10.1016/j.meatsci.2016.03.009`.

[289] L. Ma, L. Hu, X. Feng, and S. Wang, “Nitrate and nitrite in health and disease”, *Aging and Disease*, vol. 9, no. 5, pp. 938–945, 2018. DOI: `10.14336/AD.2017.1207`.

[290] N. S. Bryan, D. D. Alexander, J. R. Coughlin, A. L. Milkowski, and P. Boffetta, “Ingested nitrate and nitrite and stomach cancer risk: An updated review”, *Food and Chemical Toxicology: An International Journal Published for the British Industrial Biological Research Association*, vol. 50, no. 10, pp. 3646–3665, 2012. DOI: `10.1016/j.fct.2012.07.062`.

[291] S. Priyamvada, S. Saksena, W. A. Alrefai, and P. K. Dudeja, “Intestinal anion absorption”, in *Physiology of the Gastrointestinal Tract*, F. K. Ghishan and H. M. Said, Eds., ISBN: 978-0128099544, London, UK: Academic Press, 2018, pp. 1317–1362. DOI: `10.1016/B978-0-12-809954-4.00057-8`.

[292] D. K. Rex, J. A. Di Palma, R. Rodriguez, J. McGowan, and M. Cleveland, “A randomized clinical study comparing reduced-volume oral sulfate solution with standard 4-liter sulfate-free electrolyte lavage solution as preparation for colonoscopy”, *Gastrointestinal Endoscopy*, vol. 72, no. 2, pp. 328–336, 2010. DOI: `10.1016/j.gie.2010.03.1054`.

[293] V. B. Haywood, R. Cordero, K. Wright, *et al.*, “Brushing with a potassium nitrate dentifrice to reduce bleaching sensitivity”, *The Journal of Clinical Dentistry*, vol. 16, no. 1, pp. 17–22, 2005.

[294] European Parliament and Council, *Regulation (EC) no 1333/2008 on food additives*, `www.eur-lex.europa.eu/legal-content/EN/TXT/?uri=celex%3A32008R1333`, Accessed: 31 Mar. 2021.

[295] S. B. Brummer and M. J. Turner, “Electrical stimulation with Pt electrodes: II-estimation of maximum surface redox (theoretical non-gassing) limits”, *IEEE Transactions on Bio-Medical Engineering*, vol. 24, no. 5, pp. 440–443, 1977. DOI: `10.1109/tbme.1977.326179`.

[296] W. F. Agnew, T. Yuen, D. B. McCreery, and L. A. Bullara, “Histopathologic evaluation of prolonged intracortical electrical stimulation”, *Experimental Neurology*, vol. 92, no. 1, pp. 162–185, 1986. DOI: `10.1016/0014-4886(86)90132-9`.

[297] A. Cowley and B. Woodward*, “A healthy future: Platinum in medical applications”, *Platinum Metals Review*, vol. 55, no. 2, pp. 98–107, 2011. DOI: `10.1595/147106711X566816`.

[298] M. Özkan, S. G. Hashmi, J. Halme, *et al.*, “Inkjet-printed platinum counter electrodes for dye-sensitized solar cells”, *Organic Electronics*, vol. 44, pp. 159–167, 2017. DOI: `10.1016/j.orgel.2017.02.015`.

[299] M. Schubert, L. Rebohle, Y. Wang, *et al.*, “Evaluation of nanoparticle inks on flexible and stretchable substrates for biocompatible application”, Dresden, Germany: 7th Electronic System-Integration Technology Conference (ESTC), Sep. 18–21, 2018, pp. 1–6. DOI: `10.1109/ESTC.2018.8546494`.

[300] DIN Deutsches Institut für Normung e. V., *DIN EN ISO 10993-5: Biologische Beurteilung von Medizinprodukten – Teil 5: Prüfungen auf In-vitro-Zytotoxizität*, 2009.

[301] G. Korotcenkov, “Metal oxides for solid-state gas sensors: What determines our choice?”, *Materials Science and Engineering B*, vol. 139, 2007. DOI: `10.1016/j.mseb.2007.01.044`.

[302] M. Marezio, “Refinement of the crystal structure of $\mathrm{In_2O_3}$ at two wavelengths”, *Acta Crystallographica*, vol. 20, no. 6, pp. 723–728, 1966. DOI: `10.1107/S0365110X66001749`.

[303] S. K. Garlapati, N. Mishra, S. Dehm, *et al.*, “Electrolyte-gated, high mobility inorganic oxide transistors from printed metal halides”, *ACS Applied Materials & Interfaces*, vol. 5, no. 22, pp. 11 498–11 502, 2013. DOI: `10.1021/am403131j`.

[304] S. Dasgupta, R. Kruk, N. Mechau, and H. Hahn, “Inkjet printed, high mobility inorganic-oxide field effect transistors processed at room temperature”, *ACS Nano*, vol. 5, no. 12, pp. 9628–9638, 2011. DOI: `10.1021/nn202992v`.

[305] E. M. Bomhard, “The toxicology of indium oxide”, *Environmental Toxicology and Pharmacology*, vol. 58, pp. 250–258, 2018. DOI: `10.1016/j.etap.2018.02.003`.

[306] S.-H. Kim, S. Jeon, D.-K. Lee, *et al.*, “The early onset and persistent worsening pulmonary alveolar proteinosis in rats by indium oxide nanoparticles”, *Nanotoxicology*, vol. 14, no. 4, pp. 468–478, 2020. DOI: `10.1080/17435390.2019.1694184`.

[307] F. P. Castronovo and H. N. Wagner, “Factors affecting the toxicity of the element indium”, *British Journal of Experimental Pathology*, vol. 52, no. 5, pp. 543–559, 1971.

[308] S. Guo, R. Zheng, J. Jiang, J. Yu, K. Dai, and C. Yan, “Enhanced thermal conductivity and retained electrical insulation of heat spreader by incorporating alumina-deposited graphene filler in nano-fibrillated cellulose”, *Composites Part B: Engineering*, vol. 178, p. 107 489, 2019. DOI: `10.1016/j.compositesb.2019.107489`.

[309] E. V. Timofeeva, A. N. Gavrilov, J. M. McCloskey, *et al.*, “Thermal conductivity and particle agglomeration in alumina nanofluids: Experiment and theory”, *Physical Review. E, Statistical, Nonlinear, and Soft Matter Physics*, vol. 76, no. 6, p. 061 203, 2007. DOI: `10.1103/PhysRevE.76.061203`.

[310] E. Denes, G. Barrière, E. Poli, and G. Lévêque, “Alumina biocompatibility”, *Journal of Long-Term Effects of Medical Implants*, vol. 28, no. 1, pp. 9–13, 2018. DOI: `10.1615/JLongTermEffMedImplants.2018025635`.

[311] G. Mestres, M. Espanol, W. Xia, M. Tenje, and M. Ott, “Evaluation of biocompatibility and release of reactive oxygen species of aluminum oxide-coated materials”, *ACS Omega*, vol. 1, no. 4, pp. 706–713, 2016. DOI: `10.1021/acsomega.6b00198`.

[312] G. Park, H.-J. Chung, K. Kim, *et al.*, “Immunologic and tissue biocompatibility of flexible/stretchable electronics and optoelectronics”, *Advanced Healthcare Materials*, vol. 3, no. 4, pp. 515–525, 2014. DOI: `10.1002/adhm.201300220`.

[313] E. H. Huang, D. M. Gabler, M. E. Krecic, N. Gerber, R. M. Ferguson, and C. G. Orosz, “Differential effects of gallium nitrate on t lymphocyte and endothelial cell activation”, *Transplantation*, vol. 58, no. 11, pp. 1216–1222, 1994.

[314] L. A. Burns and A. E. Munson, “Gallium arsenide selectively inhibits T cell proliferation and alters expression of CD25 (IL-2R/p55)”, *The Journal of Pharmacology and Experimental Therapeutics*, 1992.

[315] T. L. de Jager, A. E. Cockrell, and S. S. Du Plessis, “Ultraviolet light induced generation of reactive oxygen species”, in *Ultraviolet Light in Human Health, Diseases and Environment*, ser. Advances in Experimental Medicine and Biology Ser, S. I. Ahmad, Ed., ISBN: 978-3319560175, Cham, Germany: Springer, 2017, pp. 15–23. DOI: `10.1007/978-3-319-56017-5_2`.

[316] R. P. Rastogi, Richa, A. Kumar, M. B. Tyagi, and R. P. Sinha, “Molecular mechanisms of ultraviolet radiation-induced dna damage and repair”, *Journal of Nucleic Acids*, vol. 2010, p. 592 980, 2010. DOI: `10.4061/2010/592980`.

[317] Y. Zhang, T. R. Nayak, H. Hong, and W. Cai, “Biomedical applications of zinc oxide nanomaterials”, *Current Molecular Medicine*, vol. 13, no. 10, pp. 1633–1645, 2013. DOI: `10.2174/1566524013666131111130058`.

[318] M. Bender, E. Gagaoudakis, E. Douloufakis, *et al.*, “Production and characterization of zinc oxide thin films for room temperature ozone sensing”, *Thin Solid Films*, vol. 418, no. 1, pp. 45–50, 2002. DOI: `10.1016/S0040-6090(02)00588-6`.

[319] Q. Geng, Z. He, X. Chen, W. Dai, and X. Wang, “Gas sensing property of ZnO under visible light irradiation at room temperature”, *Sensors and Actuators B: Chemical*, vol. 188, pp. 293–297, 2013. DOI: `10.1016/j.snb.2013.07.001`.

[320] W. Xu, W. Wang, Z. Guo, and Z. Liu, “Fabrication of submillimeter-sized single-crystalline graphene arrays by a commercial printing-assisted CVD method”, *RSC Advances*, vol. 7, no. 29, pp. 17 800–17 805, 2017. DOI: `10.1039/C7RA01947E`.

[321] Sigma-Aldrich, *Safety data sheet zinc oxide ink*, `www.sigmaaldrich.com/catalog/product/aldrich/901091?lang=de&region=DE`, Accessed: 22 Aug. 2020.

[322] J. Jiang, J. Pi, and J. Cai, “The advancing of zinc oxide nanoparticles for biomedical applications”, *Bioinorganic Chemistry and Applications*, vol. 2018, p. 1 062 562, 2018. DOI: `10.1155/2018/1062562`.

[323] I.-L. Hsiao and Y.-J. Huang, “Effects of various physicochemical characteristics on the toxicities of ZnO and $\mathrm{TiO_2}$ nanoparticles toward human lung epithelial cells”, *Science of the Total Environment*, vol. 409, no. 7, pp. 1219–1228, 2011. DOI: `10.1016/j.scitotenv.2010.12.033`.

[324] J. J. Ramsden, “Introduction to medical materials and devices”, in *Joining and Assembly of Medical Materials and Devices*, ISBN: 9781845695774, Amsterdam, Netherlands: Elsevier, 2013, pp. 3–27. DOI: `10.1533/9780857096425.1.3`.

[325] D. M. Brunette, P. Tengvall, M. Textor, and P. Thomsen, *Titanium in medicine: material science, surface science, engineering, biological responses and medical applications*. Berlin, Germany: Springer, 2001, ISBN: 978-3642564864. DOI: `10.1007/978-3-642-56486-4`.

[326] W. Winter, *Webelements periodic table electrical resistivity periodicity*, `www.webelements.com/periodicity/electrical_resistivity/`, Accessed: 19 Aug. 2020.

[327] J. Bai and B. Zhou, “Titanium dioxide nanomaterials for sensor applications”, *Chemical Reviews*, vol. 114, no. 19, pp. 10 131–10 176, 2014. DOI: `10.1021/cr400625j`.

[328] A. Abbasi and J. J. Sardroodi, “Investigation of the adsorption of ozone molecules on TiO_2/WSe_2 nanocomposites by DFT computations: Applications to gas sensor devices”, *Applied Surface Science*, vol. 436, pp. 27–41, 2018. DOI: `10.1016/j.apsusc.2017.12.010`.

[329] A. Määttänen, U. Vanamo, P. Ihalainen, *et al.*, “A low-cost paper-based inkjet-printed platform for electrochemical analyses”, *Sensors and Actuators B: Chemical*, vol. 177, pp. 153–162, 2013. DOI: `10.1016/j.snb.2012.10.113`.

[330] M. A. Abrar, Y. Dong, P. K. Lee, and W. S. Kim, “Bendable electro-chemical lactate sensor printed with silver nano-particles”, *Scientific Reports*, vol. 6, no. 1, p. 30 565, 2016. DOI: `10.1038/srep30565`.

[331] G. Neri, A. Bonavita, G. Micali, *et al.*, “A highly sensitive oxygen sensor operating at room temperature based on platinum-doped In_2O_3 nanocrystals”, *Chemical Communications*, no. 48, pp. 6032–6034, 2005. DOI: `10.1039/b510832b`.

[332] G. Schwartz, B. C.-K. Tee, J. Mei, *et al.*, “Flexible polymer transistors with high pressure sensitivity for application in electronic skin and health monitoring”, *Nature Communications*, vol. 4, no. 1, p. 1859, 2013. DOI: `10.1038/ncomms2832`.

[333] L. Chen, X. An, J. Jing, H. Jin, Z. Chu, and K. H. Li, “Ultracompact chip-scale refractometer based on an ingan-based monolithic photonic chip”, *ACS Applied Materials & Interfaces*, vol. 12, no. 44, pp. 49 748–49 754, 2020. DOI: `10.1021/acsami.0c13144`.

[334] Y. C. Wong, B. C. Ang, A. Haseeb, A. A. Baharuddin, and Y. H. Wong, “Conducting polymers as chemiresistive gas sensing materials: A review”, *Journal of The Electrochemical Society*, vol. 167, no. 3, p. 037 503, 2020. DOI: `10.1149/2.0032003JES`.

[335] S. Jodpimai, S. Boonduang, and P. Limsuwan, “Inline ozone concentration measurement by a visible absorption method at wavelength 605 nm”, *Sensors and Actuators B: Chemical*, vol. 222, pp. 8–14, 2016. DOI: `10.1016/j.snb.2015.08.028`.

[336] S. O’Keeffe, C. Fitzpatrick, and E. Lewis, “An optical fibre based ultra violet and visible absorption spectroscopy system for ozone concentration monitoring”, *Sensors and Actuators B: Chemical*, vol. 125, no. 2, pp. 372–378, 2007. DOI: `10.1016/j.snb.2007.02.023`.

[337] M. Degner, N. Damaschke, H. Ewald, S. O’Keeffe, and E. Lewis, “UV LED-based fiber coupled optical sensor for detection of ozone in the ppm and ppb range”, Christchurch, New Zealand: IEEE Sensors Conference, Oct. 25–28, 2009. DOI: `10.1109/ICSENS.2009.5398230`.

[338] K. Teranishi, Y. Shimada, N. Shimomura, and H. Itoh, “Investigation of ozone concentration measurement by visible photo absorption method”, *Ozone: Science & Engineering*, vol. 35, no. 3, pp. 229–239, 2013. DOI: `10.1080/01919512.2013.780544`.

[339] C. R. Harris, K. J. Millman, S. J. Van Der Walt, *et al.*, “Array programming with NumPy”, *Nature*, vol. 585, no. 7825, pp. 357–362, Sep. 2020. DOI: `10.1038/s41586-020-2649-2`.

[340] M. P. Barde and P. J. Barde, “What to use to express the variability of data: Standard deviation or standard error of mean?”, *Perspectives in Clinical Research*, vol. 3, no. 3, p. 113, 2012. DOI: `10.4103/2229-3485.100662`.

[341] L. Rieger, M. Thomann, W. Gujer, and H. Siegrist, “Quantifying the uncertainty of on-line sensors at WWTPs during field operation”, *Water Research*, vol. 39, no. 20, pp. 5162–5174, 2005. DOI: `10.1016/j.watres.2005.09.040`.

[342] H. Bernstein, *Measuring Electronics and Sensors*. Wiesbaden, Germany: Springer, 2022, vol. 1st ed, ISBN: 978-3658350673. DOI: 10.1007/978-3-658-35067-3.

[343] J. W. Birks, P. C. Andersen, C. J. Williford, *et al.*, "Folded tubular photometer for atmospheric measurements of NO_2 and no", *Atmospheric Measurement Techniques*, vol. 11, no. 5, pp. 2821–2835, 2018. DOI: 10.5194/amt-11-2821-2018.

[344] R. Barth, "Design and evaluation of a low-cost photometer for measuring ozone gas concentrations", Master's Thesis, Karlsruhe Institiue of Technology, Karlsruhe, Germany, 2022.

[345] N. Afshar-Mohajer et al., "Evaluation of low-cost electro-chemical sensors for environmental monitoring of ozone, nitrogen dioxide, and carbon monoxide", *Journal of Occupational and Environmental Hygiene*, vol. 15, no. 2, pp. 87–98, 2018. DOI: 10.1080/15459624.2017.1388918.

[346] L. Petani, D. Tils, L. Wührl, I. Sieber, and C. Pylatiuk, "Design, simulation, and evaluation of a low-cost photometer for dissolved ozone measurement", (accepted), Tel Aviv, Israel: IEEE International Conference on Microwaves, Communications, Antennas, Biomedical Engineering & Electronic Systems (COMCAS), Jul. 9–11, 2024.

[347] J. Hodgkinson and R. P. Tatam, "Optical gas sensing: A review", *Measurement Science and Technology*, vol. 24, no. 1, p. 012 004, 2013. DOI: 10.1088/0957-0233/24/1/012004.

[348] A. Levanov, O. Y. Isaikina, A. Tyutyunnik, E. Antipenko, and V. Lunin, "Molar absorption coefficient of ozone in aqueous solutions", *Journal of Analytical Chemistry*, vol. 71, no. 6, pp. 549–553, 2016. DOI: 10.1134/S1061934816060083.

[349] Y.-T. Tu and W.-F. Sun, *Ray Optics Simulation*, Feb. 2016. DOI: 10.5281/zenodo.6386611.

[350] L. Petani, A. Schweizer, C. Pylatiuk, P. Stiller, U. Gengenbach, and M. Ungerer, "Optimised inkjet-printing parameters and processing techniques for an exemplary structure of an oxygen sensor on a polyimide substrate", Boston, MA, USA: IEEE International Conference on Flexible, Printable Sensors and Systems (FLEPS), Jul. 9–12, 2023. DOI: 10.1109/FLEPS57599.2023.10220420.

[351] L. Petani, L. Llupa, Z. Peng, *et al.*, “Dissolved ozone sensing in water and blood based on commercial screen-printed and BDD electrodes”, Toronto, Canada: IEEE Biomedical Circuits and Systems Conference (BIOCAS), Oct. 19–21, 2023. DOI: `10.1109/BioCAS58349.2023.10388985`.

[352] M. Dyson, “Printed and flexible sensors 2022-2032: Technologies, players, markets: Market for printed sensors including biosensors, organic photodetectors, skin patch and medical electrodes, force and piezoresistive sensors, piezoelectric, temperature, capacitive touch sensors, stretchable strain sensors: Sample pages”, *IDTechEx Ltd.*, 2021.

[353] T. Fapanni, E. Sardini, M. Serpelloni, and S. Tonello, “3D electrochemical sensor and microstructuration using aerosol jet printing”, *Sensors*, vol. 21, no. 23, 2021.

[354] I. Sieber, D. Zeltner, M. Ungerer, A. Wenka, T. Walter, and U. Gengenbach, “Design and experimental setup of a new concept of an aerosol-on-demand print head”, *Aerosol Science and Technology*, vol. 56, no. 4, pp. 355–366, 2022. DOI: `10.1080/02786826.2021.2022094`.

[355] M. Ungerer, “Neue methodik zur optimierung von druckverfahren für die herstellung funktionaler mikrostrukturen und hybrider elektronischer schaltungen”, Ph.D. dissertation, Karlsruhe Institute of Technology, Karlsruhe, Germany, 2020.

[356] T. K. Saha, T. N. Knaus, A. Khosla, and P. K. Sekhar, “Investigation of printing properties on paper substrate”, *Journal of The Electrochemical Society*, vol. 165, no. 8, B3163, 2018. DOI: `10.1149/2.0211808jes`.

[357] H. Al-Mohsin, S. Ali, and A. Bermak, “Design and fabrication process optimization of silver-based inkjet-printed microheater”, *Processes*, vol. 10, no. 9, p. 1677, 2022. DOI: `10.3390/pr10091677`.

[358] W. Cui, W. Lu, Y. Zhang, G. Lin, T. Wei, and L. Jiang, “Gold nanoparticle ink suitable for electric-conductive pattern fabrication using in ink-jet printing technology”, *Colloids and Surfaces A: Physicochemical and Engineering Aspects*, vol. 358, no. 1-3, pp. 35–41, 2010. DOI: `10.1016/j.colsurfa.2010.01.023`.

[359] S. Lim, M. Joyce, P. D. Fleming, A. T. Aijazi, and M. Atashbar, “Inkjet printing and sintering of nano-copper ink”, *Journal of Imaging Science and Technology*, vol. 57, no. 5, pp. 50 506–1, 2013. DOI: `10.2352/J.ImagingSci.Technol.2013.57.5.050506`.

[360] Y. Yang and C.-C. Liu, "Development of a nasicon-based amperometric carbon dioxide sensor", *Sensors and Actuators B: Chemical*, vol. 62, no. 1, pp. 30–34, 2000. DOI: `10.1016/S0925-4005(99)00370-6`.

[361] Z. Peng, J. Xu, K. Kurihara, M. Tomisaki, and Y. Einaga, "Electrochemical CO_2 reduction on sub-microcrystalline boron-doped diamond electrodes", *Diamond and Related Materials*, vol. 120, p. 108 608, 2021. DOI: `10.1016/j.diamond.2021.108608`.

[362] Z. Peng, K. Akai, M. Murata, M. Tomisaki, and Y. Einaga, "Simultaneous electrochemical detection of ozone and free chlorine with a boron-doped diamond electrode", *Analyst*, vol. 147, no. 8, pp. 1655–1662, 2022. DOI: `10.1039/D1AN02347K`.

[363] D. R. Lide, Ed., *CRC Handbook of Chemistry and Physics, Internet Version 2005*. Boca Raton, FL, USA: CRC Press, 2005, ISBN: 978-0849304866.

[364] I. Lezcano, N. Nuñez, M. Espino, and M. Gómez, "Antibacterial activity of ozonized sunflower oil, oleozón, against *Staphylococcus Aureus* and *Staphylococcus Epidermidis*", *Ozone: Science & Engineering*, vol. 22, no. 2, pp. 207–214, 2000. DOI: `10.1080/01919510008547221`.

[365] L. A. Sechi, I. Lezcano, N. Nunez, *et al.*, "Antibacterial activity of ozonized sunflower oil (oleozon)", *Journal of Applied Microbiology*, vol. 90, no. 2, pp. 279–284, 2001. DOI: `10.1046/j.1365-2672.2001.01235.x`.

[366] K. L. Rodrigues, C. C. Cardoso, L. R. Caputo, J. C. T. Carvalho, J. E. Fiorini, and J. M. Schneedorf, "Cicatrizing and antimicrobial properties of an ozonised oil from sunflower seeds", *Inflammopharmacology*, vol. 12, no. 3, pp. 261–270, 2004. DOI: `10.1163/1568560042342275`.

[367] M. F. Díaz, R. Hernández, G. Martínez, *et al.*, "Comparative study of ozonized olive oil and ozonized sunflower oil", *Journal of the Brazilian Chemical Society*, vol. 17, no. 2, pp. 403–407, 2006. DOI: `10.1590/S0103-50532006000200026`.

[368] K. Skalska, S. Ledakowicz, J. Perkowski, and B. Sencio, "Germicidal properties of ozonated sunflower oil", *Ozone: Science & Engineering*, vol. 31, no. 3, pp. 232–237, 2009. DOI: `10.1080/01919510902838669`.

[369] M. F. Díaz, Y. Sánchez, M. Gómez, F. Hernández, and M. C. d. C. Veloso, "Physicochemical characteristics of ozonated sunflower oils obtained by different procedures", *Grasas y Aceites*, vol. 63, pp. 466–474, 2012. DOI: `10.3989/gya.073212`.

[370] N. R. de Almeida Kogawa, E. J. de Arruda, A. C. Micheletti, *et al.*, "Synthesis, characterization, thermal behavior, and biological activity of ozonides from vegetable oils", *RSC Advances*, vol. 5, no. 80, pp. 65 427–65 436, 2015. DOI: `10.1039/C5RA02798E`.

[371] S. Moureu, F. Violleau, D. A. Haimoud-Lekhal, and A. Calmon, "Ozonation of sunflower oils: Impact of experimental conditions on the composition and the antibacterial activity of ozonized oils", *Chemistry and Physics of Lipids*, vol. 186, pp. 79–85, 2015. DOI: `10.1016/j.chemphyslip.2015.01.004`.

[372] F. Serio, G. Pizzolante, G. Cozzolino, *et al.*, "A new formulation based on ozonated sunflower seed oil: In vitro antibacterial and safety evaluation", *Ozone: Science & Engineering*, vol. 39, no. 3, pp. 139–147, 2017. DOI: `10.1080/01919512.2016.1272405`.

[373] M. Montevecchi, A. Dorigo, M. Cricca, and L. Checchi, "Comparison of the antibacterial activity of an ozonated oil with chlorhexidine digluconate and povidone-iodine. A disk diffusion test", *New Microbiologica*, vol. 36, no. 3, pp. 289–302, 2013.

[374] M. Grootveld, A. Baysan, N. Sidiiqui, J. Sim, C. Silwood, and E. Lynch, "History of the clinical applications of ozone", in *Ozone: the revolution in dentistry*, ISBN: 1850970882, London, UK: Quintessence Publishing Company, 2004, pp. 23–30. DOI: `10.1038/sj.bdj.4812728`.

[375] J. Strähle and E. Schweda, *Lehrbuch der analytischen und präparativen anorganischen Chemie*. Stuttgart, Germany: S. Hirzel Verlag, 1995, ISBN: 3-7776-0612-X. DOI: `10.1002/pauz.19960250420`.

[376] Y. Trau, *Direct E.coli cell count at OD600*, `www.tipbiosystems.com/wp-content/uploads/2020/05/AN102-E.coli-Cell-Count_2019_04_25.pdf`, Accessed: 1 Jun. 2022, 2019.

[377] F. Iten, "In-vitro vergleiche der antimikrobiellen wirkung von pflanzlichen vielstoffgemischen, artifiziellen stoffkombinationen und phytogenen monosubstanzen am beispiel des ätherischen öls von thymus vulgaris", Ph.D. dissertation, University of Zürich, Zürich, Switzerland, 2010.

[378] A. Remmal, T. Bouchikhi, K. Rhayour, M. Ettayebi, and A. Tantaoui-Elaraki, "Improved method for the determination of antimicrobial activity of essential oils in agar medium", *Journal of Essential Oil Research*, vol. 5, no. 2, pp. 179–184, 1993. DOI: `10.1080/10412905.1993.9698197`.

[379] J. R. Donaldson, S. L. Warner, R. G. Cates, and D. Gary Young, "Assessment of antimicrobial activity of fourteen essential oils when using dilution and diffusion methods", *Pharmaceutical Biology*, vol. 43, no. 8, pp. 687–695, 2005. DOI: `10.1080/13880200500384932`.

[380] S. Noori, S. Diwan, and N. Mehta, "Lumbar diskogenic back pain", *Symptom Oriented Pain Management*, vol. 187, 2017.

[381] V. Gorshelev, A. Serdyuchenko, M. Weber, W. Chehade, and J. P. Burrows, "High spectral resolution ozone absorption cross-sections – part 1: Measurements, data analysis and comparison with previous measurements around 293 K", *Atmospheric Measurement Techniques*, vol. 7, no. 2, pp. 609–624, 2014. DOI: `10.5194/amt-7-609-2014`.

[382] R.-J. Wu, Y.-C. Chiu, C.-H. Wu, and Y.-J. Su, "Application of $\mathrm{Au}/\ \mathrm{TiO_2}$–$\mathrm{WO_3}$ material in visible light photoreductive ozone sensors", *Thin Solid Films*, vol. 574, pp. 156–161, 2015. DOI: `10.1016/j.tsf.2014.12.009`.

[383] B.-Y. Wei, M.-C. Hsu, P.-G. Su, H.-M. Lin, R.-J. Wu, and H.-J. Lai, "A novel $\mathrm{SnO_2}$ gas sensor doped with carbon nanotubes operating at room temperature", *Sensors and Actuators B: Chemical*, vol. 101, no. 1-2, pp. 81–89, 2004. DOI: `10.1016/j.snb.2004.02.028`.

List of figures

List of tables

Abbreviations

ABS	acrylonitrile butadiene styrene.
ADC	analog digital converter.
Ag	silver.
AgCl	silver chloride.
AgNP	silver nanoparticle.
Al	aluminium.
Al_2O_3	aluminium oxide.
AlGaN	aluminium gallium nitride.
AU	absorbance units.
Au	gold.
AuNP	gold nanoparticle.

BDD	boron-doped diamond.
BHB	Brain Heart Blood.

CAD	computer-aided design.
CE	counter electrode.
CFU	colony forming unit.
CLSI	Clinical and Laboratory Standard Institute.
CNTs	carbon nanotubes.
CT	computer tomography.
Cu	copper.

Dbscan	density-based spatial clustering of applications with noise.
DMSO	dimethyl sulfoxide.
DNA	deoxyribonucleic acid.
DPD	N,N-diethyl-p-phenylenediamine.

EBOO	extracorporeal blood oxygenation and ozonation.
ECHA	European Chemical Agency.
E. coli	*Escherichia coli*.
FDA	Food and Drug Administration.
FDM	fused deposition modelling.
GaN	gallium nitride.
GUI	graphical user interface.
IJP	inkjet-printing.
In_2O_3	indium oxide.
InGaN	indium gallium nitride.
IPA	isopropyl alcohol.
ITO	tin-doped indium oxide.
K_2SO_4	potassium sulfate.
KNO_3	potassium nitrate.
LB	lysogeny broth.
LD	lethal dose.
LDH	lactate dehydrogenase.
LED	light-emitting diode.
MH	Mueller-Hinton.
MIC	minimum inhibitory concentration.
MOS	metal oxide semiconductors.
MRSA	methicillin-resistant *Staphylococcus aureus*.
NaCl	sodium chloride.
NP	nanoparticle.
OA	octyl acetate.
OD_{600}	optical density at a wavelength of 600 nm.

OPE	organic and printed electronic.
PCB	printed circuit board.
PDMS	polydimethylsiloxane.
PE	polyethylene.
PEDOT	poly(3,4-ethylenedioxythiophene).
PEI	polyetherimide.
PEN	polyethylene naphthalate.
PES	polyethersulfone.
PET	polyethylene terephthalate.
PI	polyimide.
PMMA	polymethyl methacrylate.
PP	polypropylene.
ppb	parts per billion.
ppm	parts per million.
PSS	polystyrene-sulfonate.
Pt	platinum.
PTFE	polytetrafluoroethene.
PTG	protein thiol groups.
PtNP	platinum nanoparticle.
PVA	polyvinyl alcohol.
PVC	polyvinyl chloride.
PVDF	polyvinylidene difluoride.
PVP	polyvinylpyrrolidone.
RE	reference electrode.
REACH	Registration, Evaluation, Authorisation, and Restriction of Chemicals.
RMSE	root mean squared error.
RMSPE	root-mean-square percentage error.
ROS	reactive oxygen species.
RPi	Raspberry Pi.
RQ	research question.
RT	room temperature.

S. aureus	*Staphylococcus aureus*.
S. epidermidis	*Staphylococcus epidermidis*.
Si	silicon.
SiO_2	silicon dioxide.
SnO_2	stannic oxide.
SWCNT	single-walled carbon nanotubes.
TAS	total antioxidant status.
TBAR	thiobarbituric acid reactants.
TGME	triethylene glycol monoethyl ether.
Ti	titanium.
TiO_2	titanium dioxide.
UV	ultraviolet.
WE	working electrode.
WO_3	tungsten trioxide.
ZnO	zinc oxide.
ZrO_2	zirconium dioxide.

Colophon

This thesis was typeset with $\LaTeX\ 2_\varepsilon$. It uses the *Clean Thesis* style developed by Ricardo Langner. The design of the *Clean Thesis* style is inspired by user guide documents from Apple Inc.

Download the *Clean Thesis* style at `http://cleanthesis.der-ric.de/`.